Institut für Angewandte Physik

Fachrichtung Physik

Fakultät Mathematik und Naturwissenschaften

Technische Universität Dresden

Scattering Scanning Near-Field Optical Microscopy on Anisotropic Dielectrics

Dissertation

zur Erlangung des akademischen Grades

Doctor rerum naturalium

(Dr. rer. nat.)

vorgelegt von

Susanne C. Schneider

geboren am 30. Mai 1978 in Karlsruhe

Dresden   2007

To my family

Eingereicht am 19. April 2007

1. Gutachter: Prof. Dr. Lukas M. Eng

2. Gutachter: Prof. Dr. Jeremy Levy

3. Gutachter: Prof. Dr. Ramamoorthy Ramesh

Verteidigt am 31. August 2007

Abstract

Near-field optical microscopy allows the nondestructive examination of surfaces with a spatial resolution far below the diffraction limit of Abbe. In fact, the resolution of this kind of microscope is not at all dependent on the wavelength, but is typically in the range of 10 to 100 nanometers. On this scale, many materials are anisotropic, even though they might appear isotropic on the macroscopic length scale. In the present work, the previously never studied interaction between a scattering-type near-field probe and an anisotropic sample is examined theoretically as well as experimentally.

In the theoretical part of the work, the analytical dipole model, which is well known for isotropic samples, is extended to anisotropic samples. On isotropic samples one observes an optical contrast between different materials, whereas on anisotropic samples one expects an additional contrast between areas with different orientations of the same dielectric tensor. The calculations show that this anisotropy contrast is strong enough to be observed if the sample is excited close to a polariton resonance.

The experimental setup allows the optical examination in the visible and in the infrared wavelength regimes. For the latter, a free-electron laser was used as a precisely tunable light source for resonant excitation. The basic atomic force microscope provides a unique combination of different scanning probe microscopy methods that are indispensable in order to avoid artifacts in the measurement of the near-field signal and the resulting anisotropy contrast.

Basic studies of the anisotropy contrast were performed on the ferroelectric single crystals barium titanate and lithium niobate. On lithium niobate, we examined the spectral dependence of the near-field signal close to the phonon resonance of the sample as well as its dependence on the tip-sample distance, the polarization of the incident light, and the orientation of the sample. On barium titanate, analogous measurements were performed and, additionally, areas with different types of domains were imaged and the near-field optical contrast due to the anisotropy of the sample was directly measured.

The experimental results of the work agree with the theoretical predictions. A near-field optical contrast due to the anisotropy of the sample can be measured and allows areas with different orientations of the dielectric tensor to be distinguished optically. The contrast results from variations of the dielectric tensor components both parallel and perpendicular to the sample surface. The presented method allows the optical examination of anisotropies of a sample with ultrahigh resolution, and promises applications in many fields of research, such as materials science, information technology, biology, and nanooptics.

Kurzfassung

Die optische Nahfeldmikroskopie ermöglicht die zerstörungsfreie optische Untersuchung von Oberflächen mit einer räumlichen Auflösung weit unterhalb des klassischen Beugungslimits von Abbe. Die Auflösung dieser Art von Mikroskopie ist unabhängig von der verwendeten Wellenlänge und liegt typischerweise im Bereich von 10-100 Nanometern. Auf dieser Längenskala zeigen viele Materialien optisch anisotropes Verhalten, auch wenn sie makroskopisch isotrop erscheinen. In der vorliegenden Arbeit wird die bisher noch nicht bestimmte Wechselwirkung einer streuenden Nahfeldsonde mit einer anisotropen Probe sowohl theoretisch als auch experimentell untersucht.

Im theoretischen Teil wird das für isotrope Proben bekannte analytische Dipolmodell auf anisotrope Materialien erweitert. Während für isotrope Proben ein reiner Materialkontrast beobachtet wird, ist auf anisotropen Proben zusätzlich ein Kontrast zwischen Bereichen mit unterschiedlicher Orientierung des Dielektrizitätstensors zu erwarten. Die Berechnungen zeigen, dass dieser Anisotropiekontrast messbar ist, wenn die Probe nahe einer Polaritonresonanz angeregt wird.

Der verwendete experimentelle Aufbau ermöglicht die optische Untersuchung von Materialien im sichtbaren sowie im infraroten Wellenlängenbereich, wobei zur resonanten Anregung ein Freie-Elektronen-Laser verwendet wurde. Das dem Nahfeldmikroskop zugrunde liegende Rasterkraftmikroskop bietet eine einzigartige Kombination verschiedener Rastersondenmikroskopie-Methoden und ermöglicht neben der Untersuchung von komplementären Probeneigenschaften auch die Unterdrückung von mechanisch und elektrisch induzierten Fehlkontrasten im optischen Signal.

An den ferroelektrischen Einkristallen Lithiumniobat und Bariumtitanat wurde der anisotrope Nahfeldkontrast im infraroten Wellenlängenbereich untersucht. An eindomänigem Lithiumniobat wurden das spektrale Verhalten des Nahfeldsignals sowie dessen charakteristische Abhängigkeit von Polarisation, Abstand und Probenorientierung grundlegend untersucht. Auf Bariumtitanat, einem mehrdomänigen Kristall, wurden analoge Messungen durchgeführt und zusätzlich Gebiete mit verschiedenen Domänensorten abgebildet, wobei ein direkter nachfeldoptischer Kontrast aufgrund der Anisotropie der Probe nachgewiesen werden konnte.

Die experimentellen Ergebnisse dieser Arbeit stimmen mit den theoretischen Vorhersagen überein. Ein durch die optische Anisotropie der Probe induzierter Nahfeldkontrast ist messbar und erlaubt die optische Unterscheidung von Gebieten mit unterschiedlicher Orientierung des Dielektriziätstensors, wobei eine Änderung desselben sowohl parallel als auch senkrecht zur Probenoberfläche messbar ist. Diese Methode erlaubt die hochauflösende optische Untersuchung von lokalen Anisotropien, was in zahlreichen Gebieten der Materialwissenschaft, Speichertechnik, Biologie und Nanooptik von Interesse ist.

Contents

List of Figures

List of Tables

Nomenclature and Abbreviations

Variables I: Greek letters

$\widehat{\alpha}_t$	Polarizability tensor of the tip (complex value)
$\widehat{\alpha}_{t,j}$	Elements of the diagonal polarizability tensor of an anisotropic scatterer
$\widehat{\alpha}_{tot}$	Polarizability of the tip-sample system
β	Response function of the sample
δ	Azimuthal angle between the incident plane and the x axis
$\delta(x)$	Delta function
Δ	Frequency shift of the reference beam in heterodyne detection
Δf	Frequency shift of the cantilever oscillation
$\Delta\phi_{ref}$	Resulting phase oscillation amplitude in quasi-homodyne detection
Δr_{ik}	Difference of the reflection coefficients on an a and on a c domain (i,k=s,p)
$\Delta\varepsilon_j$	Strength of the Lorentz oscillator
ε_0	Permittivity of the vacuum ($8.854 \cdot 10^{-12}$ F/m)
ε_∞	High-frequency dielectric constant of the sample
ε_a	Dielectric constant perpendicular to the optical axis of a uniaxial material
ε_c	Dielectric constant along the optical axis of a uniaxial material
ε_m	Complex dielectric constant of the medium surrounding the tip
ε_s	Dielectric constant of the sample
ε_t	Dielectric constant of the tip
$\varepsilon_{t,j}$	Diagonal elements of the dielectric tensor of an aniso. sphere ($j = x, y, z$)
η	Anisotropy response function

η_i	Polarization of the refracted beams, i=o,eo
γ	Angle of incidence
γ_j	Linewidth of the j$^{\text{th}}$ infrared-active mode in the Lorentz oscillator model
$\gamma_{j,TO}$	Damping constant of the transverse optic mode
γ_p	Damping factor of the Lorentz oscillator
λ	Wavelength
ν_j	Frequency of the j$^{\text{th}}$ infrared-active mode in the Lorentz oscillator model
ω_p	Plasma frequency of a metal
ω_{ref}	Oscillation frequency of the reference mirror in quasi-homodyne detection
Ω	Frequency of the cantilever oscillation
Ω_{LO}	Longitudinal optical frequency
Ω_{TO}	Transverse optical frequency
$\Omega_{j,TO}$	Resonance frequency of the transverse optic mode
ϕ	Angle of the polar coordinate system with the tip in the center
φ	Polarization angle
ϕ_{het}	Optical phase measured with heterodyne interferometric detection
ϕ_{hom}	Optical phase calculated from homodyne detection measurements
ϕ_{ref}	Phase of the reference beam
$\phi_{ref,0}$	Phase offset of the reference beam
ϕ_{sca}	Phase of the scattered light
ρ	Density
σ	Image sheet charge in an anisotropic sample
$\widehat{\sigma}$	Complex scattering coefficient
σ'	Image line charge in a sample of weak anisotropy
τ	Opening angle of the image sheet charge
θ	Angle of the polar coordinate system with the tip in the center
θ_{het}	Phase difference in heterodyne interferometric detection

θ_{hom}	Phase difference between scattered light and reference beam
$\theta(x)$	Heaviside step function
ζ_i	Angle between **k** vector and Poynting vector of the refracted beam (i=o,eo)

Variables II: Latin letters

a	Tip radius (spherical tip)
a_j	Semiaxis of an ellipsoidal scatterer ($j = x, y, z$)
A	Oscillation amplitude of the AFM cantilever
A_{het}	Optical amplitude measured with heterodyne interferometric detection
A_{hom}	Optical amplitude calculated from homodyne detection measurements
C	Capacitance
C_Ω	Scattering cross section detected by a lens
C_{abs}	Absorption cross section
C_{sca}	Scattering cross section
$\frac{dC_{sca}}{d\Omega}$	Differential scattering cross section
d	Piezoelectric coefficient
d_{ik}	Tensor components of the piezoelectric coefficient
e	Eccentricity of a prolate ellipsoid
$\mathbf{e_0}$	Direction of the external electric field at the scattering-particle position
$\mathbf{e_p}$	Unit vector in the direction of p polarization
$\mathbf{e}_r$	Radial unit vector
$\mathbf{e_s}$	Unit vector in the direction of s polarization
E	Electric field
$\mathbf{E_0}$	External electric field at the position of the tip
E_c	Coercive electric field
$\mathbf{E_{inc}}$	Electric-field vector of the incident light
E_p	p component of the incident electric-field vector

$\mathbf{E_{ref}}$ electric-field vector of the reference beam

$\mathbf{E_{refl}}$ Electric-field vector of the light reflected at the sample surface

E_s s component of the incident electric-field vector

$\mathbf{E_{sca}}$ Scattered electric-field vector

f Quantity measured with the s-SNOM

f_0 Resonance frequency of the AFM cantilever

f_{dir} Quantity measured by direct detection of the scattered light

f_{het} Quantity measured by heterodyne interferometric detection

f_{hom} Quantity measured by homodyne interferometric detection

f_K Frequency of the ac voltage applied between tip and sample in KPFM

f_p Frequency of the ac voltage applied between tip and sample in PFM

f_r Resonance frequency of the damped AFM-cantilever oscillation

F Force

h Distance between tip dipole and sample surface

h_0 Turning point of the cantilever oscillation near the sample surface

h_1 Amplitude of the cantilever oscillation

H_n Fourier components for $n\Omega$ with n=1,2,3,...

$\widehat{I}$ Identity matrix

I Current

I_0 Intensity of the light at the position of the tip

I_{ref} Intensity of the reference beam

I_{sca} Scattered intensity

$\mathbf{k}$ Wave vector

k Spring constant of the AFM cantilever

k Wave number

$\widehat{K}$ Interaction matrix of tip-sample interaction

l Length of the AFM cantilever

L_j	Geometrical factors of an ellipsoidal particle ($j = x, y, z$)
m^*	Effective mass of the AFM cantilever
n	Relative index of refraction (complex value)
n_m	Index of refraction of the sample surrounding medium (complex value)
n_s	Index of refraction of the sample (complex value)
p	Dipole moment of a ferroelectric unit cell
p_{py}	Pyroelectric coefficient
P	Electric polarization of a ferroelectric sample
P_r	Remanent polarization of a ferroelectric sample
$\mathbf{P_s}$	Image dipole in the sample
P_s	Saturation polarization of a ferroelectric sample
$\mathbf{P_t}$	Tip dipole
$\mathbf{P_{tot}}$	Total dipole of the tip-sample system
q	Charge close to a sample surface
q'	Image point charge
r	Distance between scattering center and observation
r_i	Refraction angles, i=o,eo
r_{ik}	Reflection coefficients of an anisotropic sample (i,k=s,p)
r_p	Reflection coefficient on an isotropic sample for p-polarized light
r_s	Reflection coefficient on an isotropic sample for s-polarized light
S	Mechanical stress
S_j	Strength of the j$^{\text{th}}$ infrared-active mode in the Lorentz oscillator model
$\mathbf{T}$	Vector scattering amplitude
T	Temperature
t	Thickness of the AFM cantilever
t	Time
T_C	Curie temperature

U_{cpd} Contact potential difference

U_K Amplitude of the ac voltage applied between tip and sample in KPFM

$U_{K,0}$ Voltage applied in KPFM for compensating U_{cpd}

U_p Amplitude of the ac voltage applied between tip and sample in PFM

V Visibility

V_{aa} Optical contrast between differently oriented a domains

V_{ac} Optical contrast between a and c domains

V_{UC} Volume of a unit cell

w Width of the AFM cantilever

Abbreviations and Acronyms

4Q-PD   Four-quadrant photodiode

ac   Alternating current

a domain   Sample region with the optical axis parallel to the sample surface

AFM   Atomic force microscopy

Al   Aluminum

AM   Amplitude-modulated control of noncontact AFM mode

AOM   Acousto-optical modulator

a-SNOM   Aperture-type scanning near-field optical microscopy

Au   Gold

Ba   Barium

$BaTiO_3$ Barium titanate

c domain   Sample region with the optical axis perpendicular to the sample surface

dc   Direct current

eo   Extraordinary

FEL   Free-electron laser

FM   Frequency-modulated control of noncontact AFM mode

FTIR   Fourier transform infrared spectroscopy

FZD   Forschungszentrum Dresden-Rossendorf

HeNe   Helium-Neon

IP   In-plane

IR   Infrared

KPFM   Kelvin probe force microscopy

LIA   Lock-in amplifier

Li   Lithium

LiNbO$_3$ Lithium niobate

L-R   left-minus-right signal of the four-quadrant diode

MMP   Method of multiple multipoles

Nb   Niobium

O   Oxygen

o   Ordinary

OOP   Out-of-plane

PET   Polyethylene terephthalate

PFM   Piezoresponse force microscopy

PLL   Phase-locked loop

Pt-Ir5   Platinum-iridium

Pt   Platinum

Q factor Quality factor

SEM   Scanning electron microscopy

SiC   Silicon carbide

SI   International System of Units

Si   Silicon

SNOM   Scanning near-field optical microscopy

S/N   Signal-to-noise ratio

SPM   Scanning probe microscopy

s-SNOM   Scattering scanning near-field optical microscopy

STM   Scanning tunneling microscopy

T-B   Top-minus-bottom signal of the four-quadrant diode

Ti   Titanium

1   Introduction

The optical appearance of an object is its first property we observe with our own eyes. This might be the reason why the optical properties of materials are subject of the oldest and most common examination methods. Already in the ancient world, people discussed the origin of the "optike", which is the ancient Greek word for appearance or look [Wik07]. One opinion was that the eye sends out a beam which raster-scans the surrounding matter in order to form an image; another imagination was that a beam made of light atoms is sent out from the matter and reaches the eye (Demokrit, Aristoteles) [Tip94]. All these ideas had the linear propagation of light in common.

In the 17$^{\text{th}}$ century the question arised as to whether light is a particle beam (Isaac Newton) or a wave (Christian Huygens, Robert Hooke). Newtons reputation resulted in the refusal of the wave theory, until in 1801 Thomas Young explained interference phenomena by the wavelike properties of light. His explanation was confirmed ten years later by the work of Augustin Fresnel concerning interference, diffraction, and the theoretical description of light as a wave. In 1860, James Clerk Maxwell published his theory of electromagnetism, which was confirmed experimentally in 1887 by Heinrich Hertz as well as by Kirchhoff and others. The properties of light seemed to be properly described by the wave theory until Einstein showed that this model could not explain the photoelectric effect and he proposed the quantization of light into photons. Finally in 1920, Davisson, Germer, and Thompson observed the wavelike behavior of electrons which lead to the wave-particle dualism, which is still state-of-the-art.

In the last century, optics has continuously developed new fields. The laser, which was invented around 1960, opened many new fields of optical research and is used today in numerous applications, such as medical sciences and surgery, cutting and welding, as a pointer, and for scanning and printing. Optical fibers are used for high-speed data transfer, and many data storage devices such as CDs and bar-code labels are read by means of laser light. In order to achieve higher storage densities, strong efforts are being undertaken in order to scale down these data storage devices as well as integrated optics to the nanometer scale. The interaction of light with such small structures is described by evanescent waves, waves that recede over a distance smaller than the wavelength and are present in the very proximity of the matter.

These evanescent waves may be observed in so-called near-field optical microscopes and, as they carry information on the local sample properties, they allow the optical examination of samples way below the diffraction limit. The basic principle of near-field microscopy – as proposed by Synge in 1928 [Syn28] and realized experimentally for the first time in the 1970s [Ash72] – is the illumination of the sample through an aperture of subwavelength size. As only this very sample area is illuminated, one achieves a resolution which is no longer limited by the wavelength but by the size of the aperture. Another type of near-field microscope, which is used in the present work, is the scattering-type near-field optical microscope, in which the aperture is replaced by a scatterer being small compared with the wavelength and acting as a nanoscopic light source. A more detailed description of these methods is given in chapter 2.

As the resolution of near-field optical microscopes is no longer limited by the wavelength, these nondestructive methods are applied to many fields, such as materials science, biology, and nano-electronics. Even at IR wavelengths it is possible to reach a resolution on the nanometer scale, which opens a broad field of applications. Near-field optical microscopy is described with models assuming mostly isotropic samples or periodic structures of the sample. As most samples show anisotropies on the nanometer scale – even though they appear isotropic on the macroscopic scale – the question arises as to how this anisotropy influences the near-field signal and whether this anisotropy may be measured.

The present work examines the influence of optical anisotropy of a sample in s-SNOM. The work is divided in a theoretical part and an experimental part.

Theoretically, we extend a known model – applied to the s-SNOM examination of isotropic samples (see chapter 5) – to anisotropic samples and calculate a contrast caused by the anisotropy of a sample in addition to the well-known material contrast (see chapter 6). As the anisotropy contrast is expected to be fairly small, we find that a resonant excitation of the sample is necessary to measure this contrast experimentally.

As highly ordered and well-defined samples, we chose ferroelectric single crystals, which are optically uniaxial birefringent materials with an atomically flat surface. The basic properties of these sample are discussed in chapter 3.

An additional objective of the present work – in continuation of the preceding diploma thesis – is the design and assembly of a proper experimental setup (see chapter 8), which allows the examination of the anisotropy contrast. The basis is an atomic force microscope with additional illumination of the probe tip for optical investigations (for a short introduction to scanning probe microscopy in general see chapter 4). As the expected contrast is fairly small, we focus on the reduction of the characteristic artifacts scanning probe microscopy is known for, such as topographic or electrostatic cross-talk. The resulting unique setup is suitable for the visible and the IR wavelength regimes. As the samples show resonances in the IR regime and,

hence, the anisotropy contrast is highly enhanced for these wavelengths, we focus mainly on the measurements performed in the IR. As a light source we use the most powerful light source in the IR, namely a free-electron laser at the Forschungszentrum Dresden-Rossendorf, offering a wavelength regime of 4 to 22 μm at the time of this work, which has meanwhile been extended to a wavelength range up to 150 μm. As far as we know, the combination of a near-field optical microscope with a free-electron laser is unique in the world. It offers great application possibilities due to its precisely and continuously tunable wavelength.

In order to examine the resonantly excited ferroelectric samples with near-field optical microscopy, we use several complementary techniques such as spectroscopy, z scans, and lateral scans. For studying the anisotropy contrast mechanism, we analyze two different samples, namely lithium niobate and barium titanate, which show resonances at different wavelengths. We compare the results with theoretical calculations and find resonances at the predicted wavelengths. In order to examine the anisotropy contrast, we correlate the optical signals with the local anisotropy distribution of the samples and scan sample areas with different anisotropic properties. The results for lithium niobate and barium titanate are summarized in the chapters 9 and 10.

Part I

Fundamental Aspects

2   Near-Field Optical Microscopy

In this chapter we give a general introduction into near-field optical microscopy. Even though it is a rather new technique which has been fast-paced in the last decades, the principle idea is 80 years old. The history of near-field microscopy and the basic ideas of the different types are introduced as well as possible applications to several fields of science.

2.1   Near-field Optical Microscopy in General

Optical microscopy is one of the most commonly used examination methods in science, as it is fast, non-destructive and easy to interpret. In the last decades, the growth of nanotechnology has raised the need for high-resolution imaging techniques, followed by a boost of numerous scanning probe microscopy methods. Various properties of a sample can be imaged with ultrahigh resolution down to the atomic scale by using the appropriate techniques. In order to measure the optical properties below the diffraction limit, we examine the evanescent light bound to the material surfaces.

In 1928 Synge [Syn28] proposed that one could examine a sample optically with a resolution surpassing the diffraction limit of E. Abbe [Abb73, Abb83] by illuminating the sample locally. This can be realized by placing a screen with a hole small compared to the wavelength close to the sample of interest. The sample is illuminated only through this hole, which acts as a small light source, and thus any light collected from the sample has its origin at this small area (see figure 2.1a,b). Following Babinet's principle of complementary screens [Jac83], instead of the hole also the complementary inverted structure - i.e. a small scatterer - may be placed close to the sample surface, allowing the same resolution as the aperture (see figure 2.1c).

For Synge in 1928 it was not possible to prove his predictions in experiments, because, firstly, he was not able to prepare a small-enough aperture and, secondly, it was even more difficult to bring the aperture close enough to the sample surface. Almost 50 years later, in 1972, Ash and Nicholls for the first time reported a resolution of $\lambda/60$ with this technique by using microwaves of around $\lambda = 3$ cm and an aperture size of $a = 1.5$ mm$= \lambda/20$ [Ash72]. At visible wavelengths it was still not possible to observe a near-field effect, because the aperture could not be positioned
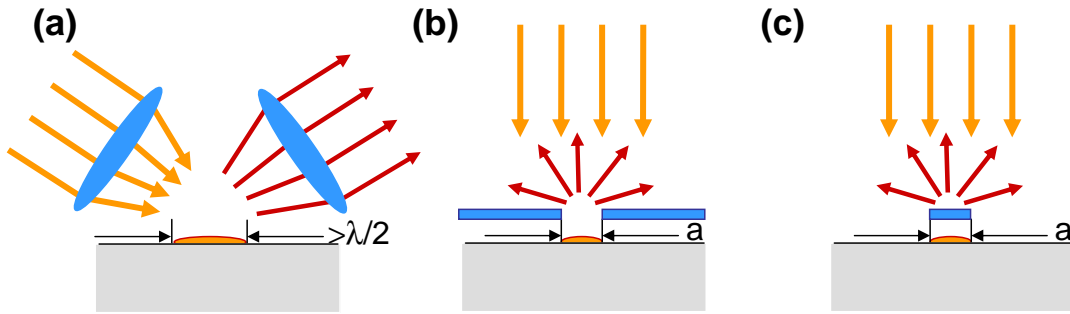
Figure 2.1: *(a) Classical optical examination of a sample, limited in resolution by the wavelength in accordance with Abbe's diffraction limit [Abb83]. (b) Illumination with evanescent waves through an aperture allows a resolution that is limited by the diameter of the aperture a only (Synge 1928) [Syn28]. (c) Following Babinet's principle of complementary screens, a particle of the same shape as the aperture in (b) should allow the same resolution.*

close enough to the sample surface.

With the advent of SPM, techniques were developed that allowed the experimenter to position a probe close to a sample surface with a dramatically improved precision. In, for example, STM and AFM the distance between the probe and the sample is kept constant at 1 to 50 nm with an accuracy better than 0.1 nm [Bin82, Bin86, Sar91]. In 1984, several groups reported the design and first results of scanning near-field optical microscopy at visible wavelengths, using small apertures to reach a resolution way below the diffraction limit. Lewis *et al.* reported the transmission through fixed apertures of different diameters as a pre-result showing the possible resolution of the scanning optical microscope down to $\lambda/10$ at $\lambda = 488$ nm [Lew84]. Only a couple of months later Pohl *et al.* reported first results of an "optical stethoscope", which consisted of an aperture with a diameter of less than 20 nm scanning over a sample surface, with a resolution of $\lambda/20$ at $\lambda = 488$ nm [Poh84]. The aperture scattering scanning near-field optical microscope (a-SNOM) was born.

Using a particle or a tip instead of an aperture in near-field microscopy was proposed by Wessel [Wes85] and first realized by Specht *et al.*. They excited a plasmon in a gold film and probed its near-field with a STM, achieving a resolution of 3 nm ($\lambda/200$) [Spe92]. Scattering the light directly at a metal tip placed close to a sample surface was for the first time reported in 1994 by Inouye and Kawata [Ino94]. Only a couple of months later Zenhäusern *et al.* showed a similar technique with a resolution of 3 nm ($\lambda/200$) [Zen94, Zen95]. Both groups modulated the tip-sample distance in order to suppress the background. With this, the first scattering scanning near-field optical microscopes (s-SNOM) had entered the stage. A couple of years later, in 1996, first s-SNOM measurements were performed at IR wavelengths (10.6 μm) with a resolution of 17 nm, showing clearly that the resolution does not depend on the wavelength but only on the radius of the tip apex [Lah96].
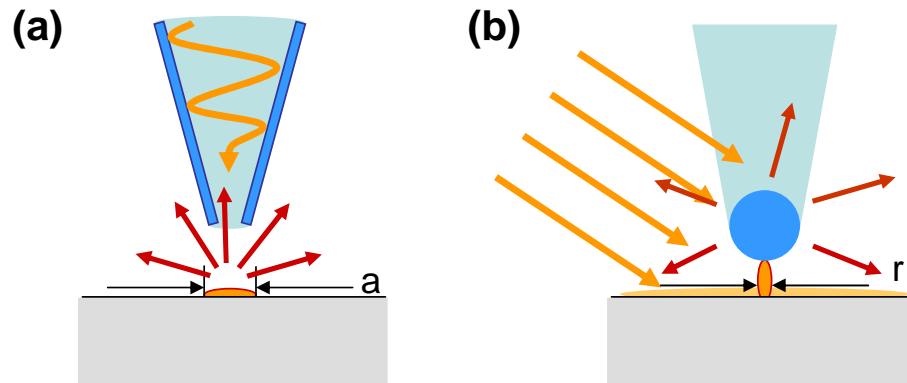
Figure 2.2: *Sketch of (a) aperture-type SNOM (a-SNOM) with near-field illumination of the sample through a fiber, (b) scattering-type SNOM (s-SNOM) with scattering of light at a tip with the sample within near-field reach.*

In the literature there are several abbreviations used for near-field optical microscopy such as SNOM [Bar96, Hil00, Lah96, Mag01, Ras05, Tau04a, Wur98], NSOM [Bet86, Bet91, DW06, Ham98, Ino94, Kar95, Mar96, Tal96, Zen94], NFOM [Bac94], and NFOS [Dür86, Fis88]. Because it is easiest to pronounce, in this work, we use the acronym SNOM. As the aperture-type SNOM was chronologically the first type and hence no separation from other types was needed, it is simply called SNOM or NSOM, while the apertureless or scattering-type SNOM has a prefix: AN-SOM [Hub98, Lev00], a-SNOM [Aub03, Bek06], or s-SNOM [Hil00, Ras05, Tau04a]. In order to differentiate clearly between the two types of SNOM, in the present work we call the aperture type "a-SNOM" and the scattering type "s-SNOM".

In the following sections we will discuss in detail the two variants of near-field microscopy, i.e. a-SNOM and s-SNOM, as sketched in figure 2.2.

2.2 Aperture Scanning Near-Field Optical Microscopy

In a-SNOM a small aperture is placed close to a sample surface. Historically this aperture was a hole in a screen or diaphragm [Fis85, Lew84, Syn28]. Today the method has been improved a lot and usually one uses pulled glass fibers with or without a metal coating [Bet92]. The metal coating decreases the aperture size at the end of the fiber, which can be as small as 70 nm [Buk97]. 20 years after the development of the first SNOMs, the basic physics of near-field microscopy are well understood. a-SNOM is no longer the matter of basic research only but is also a standard instrument which is even commercially available [Nan07a, Omi07, WiT07]. This illustrates clearly the high interest of the scientific community in high-resolution optical microscopy.

The different operation modes in a-SNOM are sketched in figure 2.3. The fiber
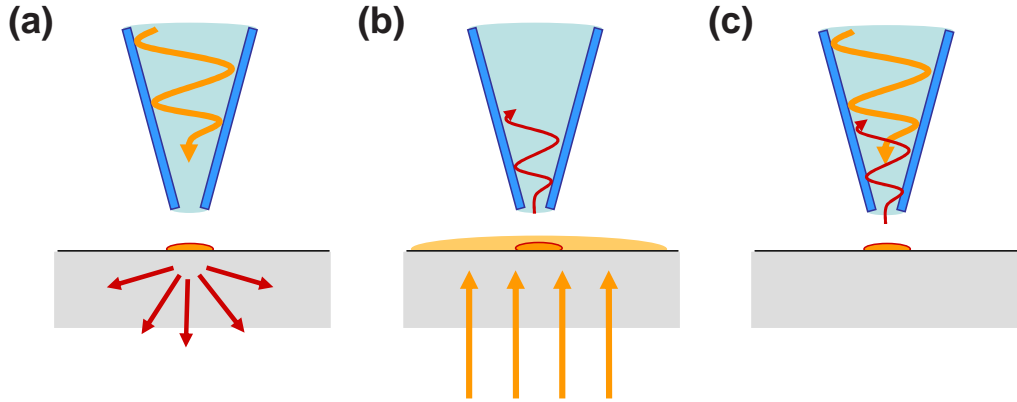
Figure 2.3: *Different illumination modes in aperture SNOM: (a) illumination through the fiber, (b) detection through the fiber and (c) illumination and detection through the fiber.*

can be used as a nanoscopic light source in that light is transmitted through the fiber while the light coming from the sample is collected by far-field optical elements (fig. 2.3a) [Dür86, Mur95, Sei01]. Conversely the sample may be illuminated through far-field optical elements while the near-field is detected by a fiber as illustrated in figure 2.3b. For far-field illumination, the sample is mostly placed on a prism and illuminated in total internal reflection [Cou89, Nov06], as also used for the excitation of surface plasmons in metal films [Kre71]. Finally, it is possible to both illuminate and detect through the fiber (see figure 2.3c), which is however done in rare cases only as the through-put of the aperture is very small.

For near-field microscopy it is important to control the distance between the probe and the sample in the range of a few nanometers. For fiber tips, this distance control is mostly done by so-called shear-force control. The fiber is oscillating and the interaction with the sample causes a damping of this oscillation. The oscillation may be detected optically by focusing a laser beam on the tip and measuring the signal modulated by the motion of the tip. For this detection method the light needs to be focused on the fiber close to the tip end, causing an additional illumination of the region of interest of the sample. Therefore, most groups use a nonoptical distance control, such as the method developed by Karrai and Grober [Kar95]. They mounted the fiber on one prong of a crystal quartz tuning fork. The fork is excited on resonance by an external piezo. Typically, the resonance frequency is about 33 kHz and the Q factor is about 1700. When the tip interacts with the surface, the system will be damped and thus the Q factor decreases. This can be detected as a change of the induced piezo-voltage at the electrodes of the fork. This method works quite well, but every new fiber tip needs to be attached separately to a tuning fork which requires a large preparation effort. Additionally, the high Q factors require slow scan rates [Bar96]. Barenz *et al.* attached the fiber tip to a four segmented piezotube that could be oscillated at frequencies of 10 kHz and higher. One segment

of the piezotube excited the fiber tip on resonance, while the other three segments detected the tip vibration, similar to a piezomicrophone. When the tip is damped by shear forces, the induced voltage at the three segments changes, which can easily be detected with a lock-in amplifier [Bar96]. A further detection method is based on a bent glass fiber used like an AFM cantilever [Mur95, Nan07a, Tal96, Tay97].

The main advantage of a-SNOM is clearly the small background field. Routinely a resolution of 100 nm can be achieved, the ultimate resolution being 20 nm.

The resolution in a-SNOM is in principle limited by the diameter of the aperture. However, as the light penetrates into the metal cladding, the effective aperture cannot be made smaller in diameter than approximately twice the skin depth of the metal coating, which is around 20 nm for aluminum. Additionally, a-SNOM struggles with low signal levels. Even highly sophisticated tips have a transmittance of no more than 10^{-3} for a 70-nm-diameter aperture [Buk97]. As high powers cannot be used, because the heating will cause the metal coating to flake off, a-SNOM is hence limited to very small signals [Lev00, Stä96].

Examining anisotropic samples such as ferroelectrics with an a-SNOM is realized usually by either examining the polarization dependence of the near-field signal by modulating the polarization of the incident light [McD98, Ram02], by modulating the electro-optical response of the sample by an external voltage [Hub98, Lev00, Ott04, Orl00], or by imaging second harmonic generation [Smo99, Smo01a, Smo01b, Xie01].

2.3 Scattering Scanning Near-Field Optical Microscopy

In scattering scanning near-field optical microscopy (s-SNOM) a scatterer is placed close to the sample surface. This scatterer can be a particle or a SPM tip. Light scattered by this probe contains information about the near-field interaction with the region of the sample next to the scatterer. Basically the near-field signal depends on the local dielectric constant, so that a contrast arises between regions of different optical properties.

In principle, it is possible to distribute many particles on the sample surface and to address optically one selected particle for reading a certain sample area. Unfortunately, the near-field signal depends strongly on the shape of the particle and hence the particles distributed on the sample would need to have precisely the same shape and size to deliver clear information rather than simply producing statistical data. Hence, it is more convenient to move one and the same particle over the sample and compare the scattering signals on different sample areas.

In scanning probe microscopy the scanning of the sample as well as the very delicate problem of distance control have already been solved. Using such an SPM-based s-SNOM one gets complementary information about various sample properties, such

as topography, mechanical hardness, or electrical properties. The s-SNOMs used today are based on STM [Spe92, Wes85] or AFM [Bre05, Hil00, Kei04, Lev00, Tau03, Wur98].

If the tip is placed close to the sample surface, meaning at distances h smaller than the radius a of the tip apex and much smaller than the wavelength λ, the resolution of the s-SNOM is only limited by the tip radius a. Typically, the resolution of the s-SNOM is in the order of the resolution of the underlying AFM. In particular, the resolution does not depend on the wavelength.

There are various modes of illumination in s-SNOM. The tip can be illuminated directly – from the side [Bek06] or the top [Bac94, Mar97] – or it can be illuminated through the sample in transmission mode [Mag01]. Many groups use an illumination in total internal reflection in order to reduce the background [Aub03, Ham98, Ino94, Wur03]. The interpretation of data measured in transmission mode is complicated, as the light is modified by the sample already before reaching the tip, even without any near-field interaction. Therefore we recommend the application of transmission mode for thin samples only. In particular for the thick polar samples used in the present work, an illumination in transmission mode is not advisable, as the birefringent sample changes the field distribution at the position of the tip.

For detection there are as well several possibilities. Some groups detect as much light as possible using an ellipsoidal mirror [Kno99a, Kno99b]. In principle all directions of detection are suitable, but one should keep in mind that a non-spherical tip shows a main scattering direction due to an antennalike behavior [GL99, Kni76]. Detection in forward direction has the disadvantage of increased background in the detected signal. In our setup we measure the backward-scattered light, the main advantage being that only one focus has to be adjusted [Bek06, Hil00]. The collection of the scattered light through the sample is possible as well, with the same restriction to thin and transparent samples as mentioned above for the transmission illumination mode [Mag01].

The main problem in near-field detection is to separate the small near-field signal from the huge background with an acceptable signal-to-noise ratio. A second task is to disentangle the amplitude and phase of the scattered wave.

First of all it is advisable to use a proper tip material and wavelength to excite the tip-sample system in a region where a large near-field signal is expected. For example a spherical gold particle as a scatterer shows plasmon resonances in the visible wavelength regime depending on the size of the particle [Kal04]. A detailed description of the wavelength dependence of the coupled tip-sample system is given in the theoretical part of this work (section 6.3). The background may be reduced by using an illumination geometry that by itself produces little background, for example total internal reflection. There is even one group that developed a near-field microscope without any light source to avoid the background completely – they measure the thermal infrared evanescent field emitted by the surface itself [DW06].
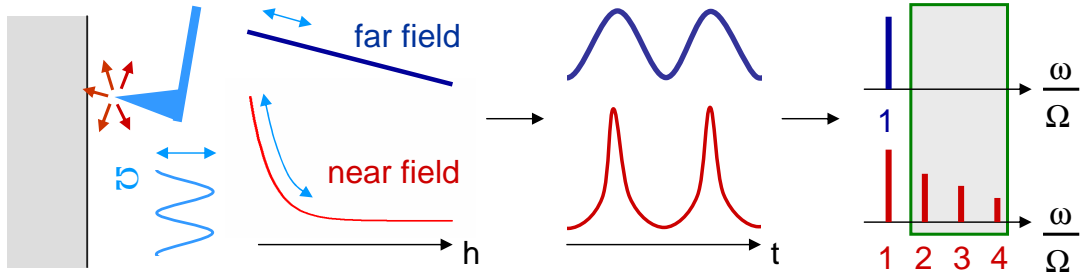
Figure 2.4: *Principle of higher-harmonic demodulation. Demodulation of the signal at $n\Omega$ with $n \geq 2$ allows the suppression of any far-field signal.*

Another possibility is to detect only the light from the very area of interest by using, for example, confocal detection [Wur03].

As already shown in the first s-SNOMs reported in the literature [Ino94, Zen94], one can use the distance dependence of the near-field signal to modulate the scattered light by vibrating the tip with a certain amplitude and frequency Ω close to the sample surface [Bek05, Lab00, Mag01]. In AFM such a cantilever oscillation is used for distance control in the so-called noncontact mode and, hence, it is easy to realize with a SPM-based setup. In order to avoid any cross talk between the mechanical tip-sample interaction and the near-field signal it is important to maintain a constant amplitude of this oscillation on different sample materials and regions. As the near-field signal depends strongly on the distance and the modulation amplitude [Tau05, Bek05], it is advised to use an additional amplitude controller to reduce topographical artifacts as reported in the literature [Bek06, Bil06, Lab00, Tau03]. For more details see the description of our experimental setup in chapter 8.

The method of so-called higher-harmonic demodulation allows us to separate the far-field from the near-field signal as illustrated in figure 2.4 [Hil01b]. As the far field depends essentially linearly on the distance, it is modulated at the tip oscillation frequency Ω and contains virtually no higher harmonics. On the other hand, as the near-field signal depends highly nonlinearly on the distance, it shows contributions to all higher harmonics. A more detailed discussion is given in the theoretical part of this work (section 5.3) as well as in the experimental part (chapter 8).

In order to separate the near-field optical amplitude and phase, an interferometric detection can be used to compare the scattered light with a reference beam having a fixed phase correlation to the incident light. Basically there are two different interferometric detection methods: homodyne and heterodyne detection.

In homodyne interferometric detection the reference beam has the same frequency as the light scattered by the tip. Basically the setup is a Michelson interferometer with the near-field microscope placed at the position of one mirror. The phase between the scattered beam and the reference beam depends on the pathlength difference. By performing two measurements at selected positions of the reference

mirror, we are able to calculate the optical amplitude and phase separately from the two measurements [Tau04b]. Another possibility is to modulate the relative phase by vibrating the reference mirror at a certain frequency [Ceb06, Oce06]. A detailed description is given in the theory part of this work in section 5.3. The main advantage of this method is that it is applicable at any wavelength. The principle works for visible wavelengths as well as in the IR - only the displacement of the reference mirror needs to be adjusted.

In heterodyne interferometric detection, the reference beam is shifted in frequency by Δ by means of, for example, an acousto-optical modulator (AOM). Hence, the interference of scattered beam and reference beam produces a beating signal with the beating frequency Δ. Using lock-in technique, one can directly measure the optical amplitude and phase of the scattered light. The reference amplitude can be used to increase the signal by a constant factor, which increases the signal-to-noise ratio. Additionally, the shift of the signal of interest to higher frequencies reduces background noise due to mechanical instabilities and electric noise. The main disadvantage is that the method is essentially restricted to visible wavelengths, as the AOM is limited to this wavelength range. A detailed description is given in the theoretical part of this work (section 5.3) and in the description of our experimental setup used at visible wavelengths (section 8.3).

s-SNOM has been applied at visible wavelengths to a wide range of materials reaching from anorganic structures – such as metal structures for data storage [Mar97] or plasmon excitation [Hil03, Wur03] – to organic materials [Hra02, Mar96]. The near field of light-emitting laser diodes has been examined [Bac98, Wur99] and spectroscopical studies on tobacco mosaic viruses have been performed [Mar96].

The resolution of s-SNOM is not limited by the wavelength. During the last ten years, there has been a rapid increase in the number of s-SNOM setups used in the IR regime. Many samples show interesting properties at IR wavelengths that have never before been examined optically with such an ultrahigh resolution about 1000 times higher than with classical optical microscopy. As a typical light source in the IR regime, most groups use a CO_2 laser with $\lambda \cong 10\ \mu m$ [Akh02, Hil04, Kno98, Kno99c, Lah96]. They report a resolution as good as 30 nm on structured metal films [Hil04, Kno99b]. Other samples examined by IR-s-SNOM were phonon-active materials such as SiC [Hil02b, Hub05, Hub06, Tau04b], Si_3N_4 [Hil04], and SiC with ion-beam-implanted structures [Oce04], as well as organic materials such as polymers [Tau04a], biological samples such as DNA strands [Akh02]. A line-tunable CO laser ($\lambda \cong 6\ \mu m$) was used for the IR spectroscopic mapping of tobacco mosaic viruses [Bre06b]. An alternative light source in the IR is the frequency comb laser offering simultaneously a set of discrete wavelengths between $\lambda = 9\ \mu m$ and $12 \mu m$ [Sch05b]. First measurements have been reported, allowing so-called "snapshots" of IR spectra [Bre06a], but the method still suffers from low-power signals. Combining s-SNOM with a FEL, as in the present work, is so far

unique in the world and offers access to a large wavelength range at high power.

The optical resolution in s-SNOM is not limited by the wavelength, but depends only on the size of the probe and possibly could be improved down to the atomic scale [Hil04, Tau03]. This wavelength independence facilitates many applications in biology, chemistry, materials science, as well as in basic research. For example near-field studies on diblock-copolymer nanostructures at IR wavelengths ($\lambda \cong 3.4\ \mu$m) are reaching intramolecular infrared spectroscopy [Ras05]. Very recently, examinations of specially designed metamaterials proved the superlensing effect [Pen00] at infrared wavelengths ($\lambda \cong 10.85\ \mu$m) [Tau06].

As these applications are heading towards ultrahigh optical resolution in near-field microscopy the question arises whether the model of an isotropic sample is still valid. On the nanometer scale nearly every sample shows local anisotropy even when it is isotropic on the macroscopic scale. The question how this anisotropy changes the near-field signal is the topic of the present work, with special reference to ferroelectric crystals. These samples show well-defined anisotropic structures while having an atomically flat surface and are thus the ideal samples for anisotropy investigations (see chapter 3).

2.4 Summary

In this chapter we have given a short overview of the history of scattering scanning near-field optical microscopy. We have illuminated the basic idea of Synge of optical resolution below the diffraction limit. Today there are two types of SNOMs using either an aperture or a scattering particle to examine the near-field properties of the sample of interest. The applications of s-SNOM fill a wide range due to the wavelength-independent ultrahigh resolution of the method.

3 Ferroelectrics

Ferroelectric single crystals are examined in the present work to study the influence of sample anisotropy on the near-field interaction with a scattering probe. We chose these samples because they show an atomically flat surface while having a well-defined domain distribution with different orientations of the optical axis and thus allow us to image a purely optically induced contrast without cross talk from the topography.

Ferroelectrics have many applications because of their unique material properties. In this chapter, a short introduction to ferroelectric materials is given, focussing on the materials and properties relevant for this work.

3.1 Basic Properties of Ferroelectrics

Pyroelectrics are materials showing a spontaneous electric polarization without an external electric field. If the direction of this polarization can be reoriented by an external electric field, the pyroelectric material is called ferroelectric. The name ferroelectricity comes from the analogy to ferromagnetic materials, which show a spontaneous magnetic polarization that is switchable by an external magnetic field [Was03].

The dependence of the polarization P on the external electric field E typically follows a hysteresis loop as shown in figure 3.1a [Was03]. At large electric fields the polarization is saturated at P_s. When the electric field is decreased to zero again, the polarization does not go to zero but a certain remanent polarization P_r remains. In order to reduce the polarization to zero, a coercive field E_c is necessary [Was03].

As ferroelectrics are pyroelectric (see figure 3.1b), a change of the temperature ΔT causes a change of the polarization of the material

$$\Delta P = p_{py}\Delta T \tag{3.1}$$

with p_{py} the pyroelectric coefficient. The change of the polarization generates charges on the sample surface which can be electrically detected as a current if electrodes are attached. This effect is used in some IR detectors at room temperature.

All pyroelectric materials are also piezoelectric (see figure 3.1b), i.e., an applied mechanical stress S changes the polarization of the material. For small changes of
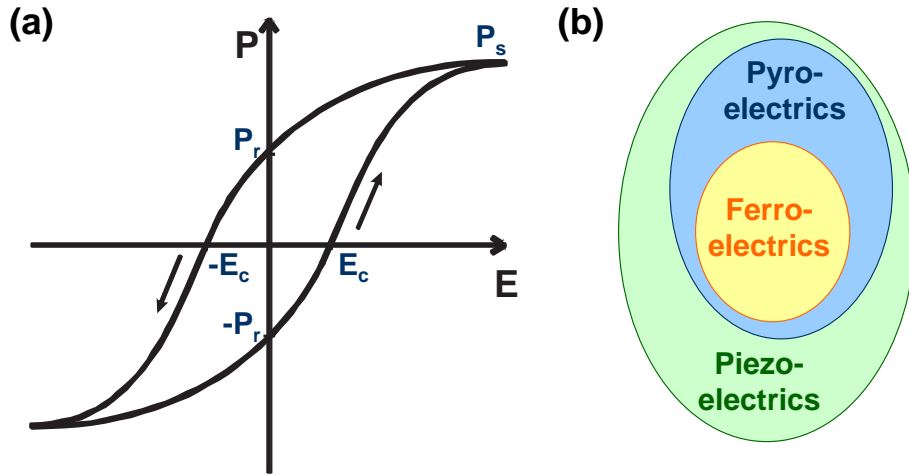
Figure 3.1: *(a) Hysteresis of the polarization P as a function of an external electric field E for ferroelectric materials: Maximal polarization is the saturation polarization P_s. The hysteresis curves cuts the ordinate at P_r, which is the remanent polarization. In order to reduce the polarization to zero, a coercive field E_c is necessary. [Was03]. (b) Classification of ferroelectric materials. Ferroelectrics are a subgroup of pyroelectrics, which again are a subgroup of piezoelectrics [Sch05a].*

S the polarization is given by

$$P = dS \tag{3.2}$$

with d the piezoelectric coefficient. Again the change of polarization can be measured as a current, which finds an application in, for example, mechanical sensors. The converse piezoelectric effect is the mechanical strain caused by an applied electric field. This effect is used in mechanical actuators. As the piezoelectric coefficient is a third-rank tensor, the resulting polarization is not necessarily oriented along the direction of the mechanical stress. Ferroelectric materials show a response in the parallel component d_{33} – meaning polarization and stress are in the same direction –, in the perpendicular component d_{31} – polarization perpendicular to the applied stress–, and in the shear component d_{15} - the reaction of the polarization when a shear stress is applied [Was03]. These components can be examined in piezoresponse force microscopy described below (see section 4.2).

Many properties of ferroelectric structures are unique and thus find applications in various fields. Their high dielectric constant over a wide temperature and frequency range makes ferroelectrics useful as dielectric in integrated or surface-mounted-device (SMD) capacitors. Due to their large piezoelectric coefficients they are also are used as electromechanical sensors, actuators, and transducers, while their large pyroelectric coefficients are used in IR sensors. The birefringence and nonlinear optical behavior of the crystals find applications in optical and electro-optical elements. The direction of the spontaneous polarization is directly used as the information-carrying quantity in nonvolatile memories [Auc98, Was03], for

example in the Sony PlayStation 2 [Son07].

Most ferroelectric materials are paraelectric above a certain transition temperature, the so-called Curie temperature T_C. The transition between different states can either be a second or a first-order transition, corresponding to the order parameter in the Ginzburg-Landau theory of ferroelectric phase transitions. Basically, in the second-order transition, the polarization as the order parameter diminishes continuously to zero at the phase transition temperature T_C, while in the first-order transition there is a discontinuous change [Kit05].

Ferroelectric materials may be divided into two main classes: the order-disorder class and the displacive class. The order-disorder class includes hydrogen-bonded systems such as KDP (potassium dihydrogen phosphate). The displacive class includes ionic crystal structures as the perovskites. As both ferroelectrics used in this work are ionic crystals, we will focus on the second class in the following.

Most ferroelectrics are ion crystals in which the centers of positive and negative ions are displaced against each other. Thus each unit cell of the crystal has a certain dipole moment p. The polarization of the crystal is the average dipole moment per unit volume. The possible directions of the polarization are limited by the crystal structure. For example in ferroelectrics with a tetragonal unit cell, there are six possible orientations The polarization can be along any of three orthogonal axes, pointing either in the forward or backward direction.

Regions with a uniform direction of the spontaneous polarization are called domains. The boundaries between different domains are called domain walls and are characterized by the angle between the polarization directions on either side of the wall. For example, a 180° domain wall is the boundary between domains with antiparallel polarizations, while a 90° domain wall separates, for example, two domains with up and a left polarization, respectively.

The formation of the domains is caused by electrical and mechanical boundary conditions. Most crystals form domains with opposite polarizations in order to minimize the electrical depolarization energy. In stable single crystals, the domain walls go straight through the crystal – the domain distribution on the surface represents the domain distribution in the whole crystal.

In the following, we will discuss the special properties of the ferroelectrics used in the present work, namely $BaTiO_3$ and $LiNbO_3$.

3.2   Barium Titanate

$BaTiO_3$ is a typical displacive ferroelectric crystal with a so-called perovskite structure as shown in figure 3.2. At high temperatures it is cubic in the paraelectric phase. The volume of the unit cell is $V_{UC} \cong 64 \cdot 10^{-24} cm^3$ corresponding to an edge
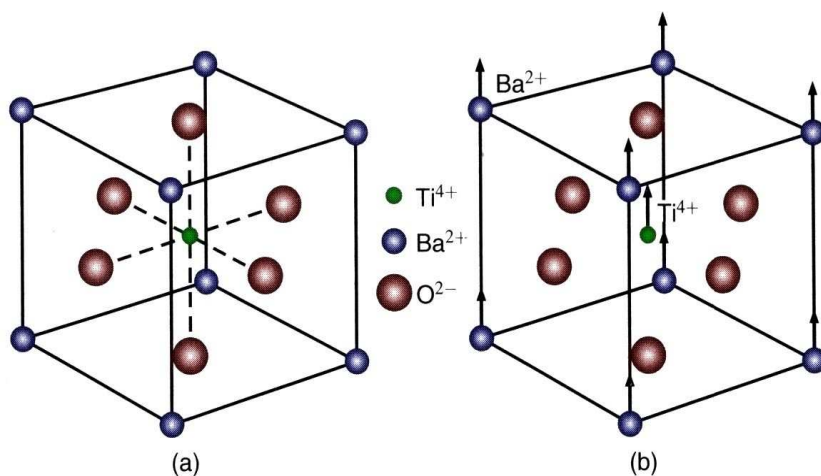
Figure 3.2: *Unit cell of BaTiO$_3$ (a) in the cubic phase above the Curie temperature and (b) in the tetragonal phase below T_C. The positive ions Ba^{2+} and Ti^{4+} are displaced with respect to the negative O^{2-}-ions, resulting in a polarization of the unit cell [Kit05].*
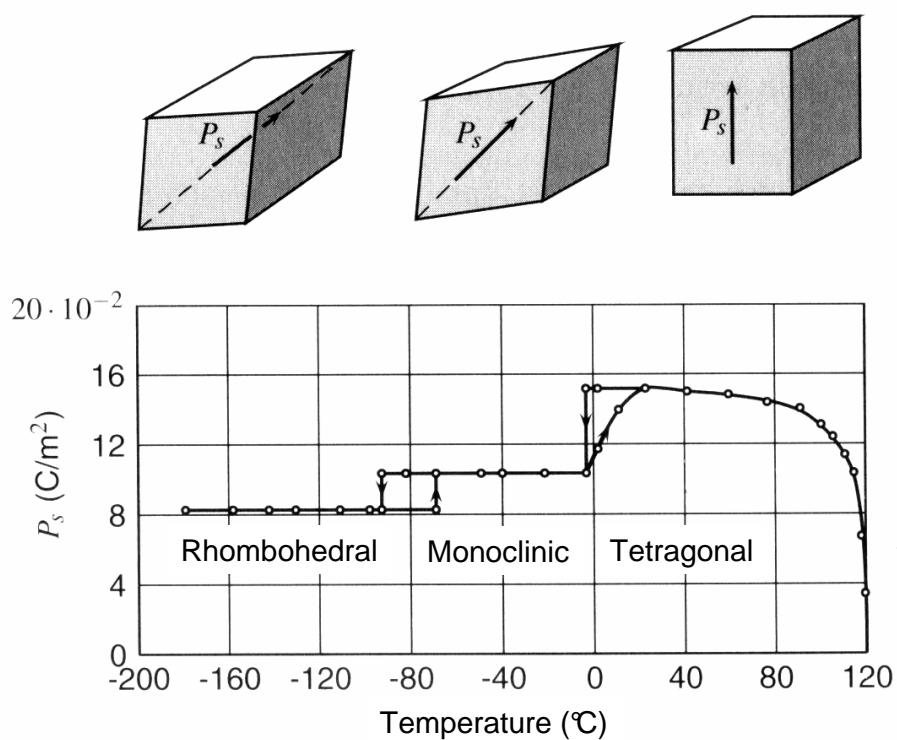
Figure 3.3: *Spontaneous polarization of BaTiO$_3$ as a function of temperature [Kit05].*
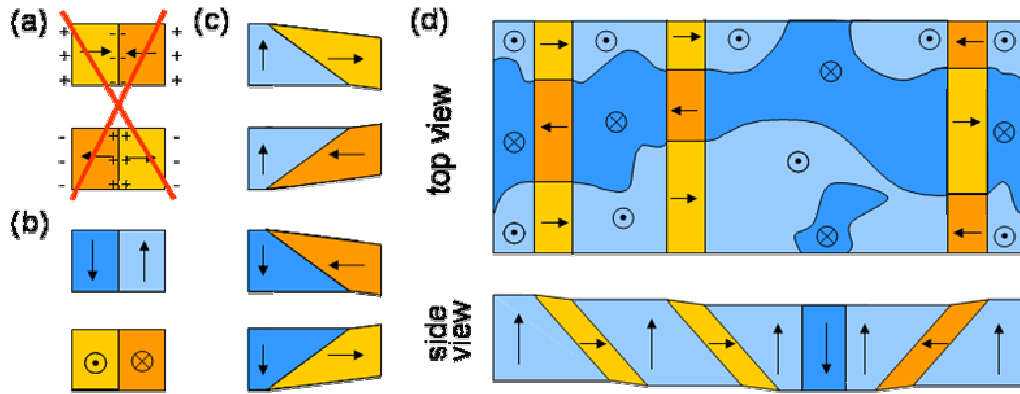
Figure 3.4: *(a) Combination of adjacent domains that are forbidden because of charged 180° domain walls. (b) Possible combinations of adjacent domains separated by 180° and (c) 90° domain walls, respectively. (d) Sketch of typical domain distribution in BaTiO₃ single crystals in top and side view. Subfigures (a)-(c) are correspond to side view.*

length of 4 Å. Below $T_C = 120°C$ it becomes ferroelectric with a tetragonally deformed unit cell with a displacement of $\delta \cong 0.1$ Å resulting in a spontaneous dipole moment of $p \cong 2 \cdot 10^{-29}$ Cm. At room temperature it is in this tetragonal phase [Kit05]. At lower temperatures, BaTiO₃ shows two more phase transitions leading to a orthorhombic and finally to a rhombohedral unit cell as shown in figure 3.3 [Jon62, Kit05]. All phase transitions are 1st -order transitions showing discontinuities in the spontaneous polarization.

In the tetragonal phase, BaTiO₃ is uniaxially birefringent with the optical axis parallel to the spontaneous polarization of the crystal. If the surface of the crystal is a (100) surface, the optical axis can be oriented either perpendicularly to the sample surface or lie within the surface plane along either of two axes at right angle to each other. The corresponding domains are called c domains for perpendicular orientation and a domains for parallel orientation.

The typical domain distributions of BaTiO₃ in the tetragonal phase are restricted to a limited set of possible combinations of domains, due to the crystal structure and because of charged domain walls being energetically unfavorable [Hip50, Mer54]. Two domains separated by a 180° wall have antiparallel polarizations. As the tetragonal distortion of the unit cell is in the same direction in both domains, all combinations sketched in figure 3.4a,b are possible from the crystallographic point of view. If the two polarizations are facing each other as sketched in figure 3.4a, then the domain walls are charged and thus the structure is not stable for energetic reasons. As the unit cell is only slightly tetragonally distorted, also 90° domain walls are possible. To compensate for the misfit of the unit cells on either side of the 90° domain wall, the surface of the a domain is tilted by typically 0.66° [Gru97a] with respect to the surface of the adjacent c domain. Furthermore due to the tetrago-

nality of the unit cell, the 90° wall runs through the crystal at an angle of 44.66° with respect to the polarization directions on either side. Avoiding again charged domain walls, four 90° domains walls are possible as sketched in figure 3.4c. Figure 3.4d shows a typical domain distribution of BaTiO$_3$ in top and side view. Due to the crystal structure, neighboring out-of-plane domains are typically separated by a meanderlike 180° domain wall, while the 180° domain walls between in-plane domains are always straight. In the side view sketch we observe the typical 44.66° angle of the 90° domain walls, while the 180° domain walls are perpendicular to the sample surface.

3.3   Lithium Niobate

LiNbO$_3$ shows large optical nonlinearities and is thus used in the field of electro-optic modulators, parametric oscillators, harmonic generators, etc. It is ferroelectric at room temperature and can be grown in the form of large optic-quality single crystals. It is uniaxial at all temperatures with only a single structural phase transition to the paraelectric phase, which is of second order, corresponding to a continuous change of the spontaneous polarization [Lin77]. It has a Curie temperature of $T_C = 1200°$C and the spontaneous polarization at room temperature is $P \cong 71$ μC/cm^2 [Kit05, Abr66]. The unit cell of LiNbO$_3$ has a size of about $(5.1 \times 5.1 \times 13.8)$ Å^3, which is much larger than the unit cell of BaTiO$_3$ [Vei02]. The displacement of the lithium and niobium ions in the ferroelectric phase is $\delta_{Li} \cong 0.9$ Å and $\delta_{Nb} \cong 0.5$ Å, respectively [Kit05].

LiNbO$_3$ shows a much more complex crystal structure than BaTiO$_3$ as shown in figure 3.5. It consists of planar sheets of oxygen atoms in approximately hexagonal close packing. The resulting octahedral interstices are one-third occupied by Nb^{5+} and one-third by Li$^+$, the remainder being vacant. Figure 3.5a shows the sequence of distorted octahedra along the polar c axis with Nb at the origin. The corresponding view along the polar axis is displayed in figure 3.5b, in which the Nb and Li ions are indicated within the outlined unit cell. The oxygen lattice has been idealized for simplicity [Abr66].

LiNbO$_3$ is uniaxially birefringent with $\Delta n \cong 0.1$ with the optical axis being parallel to the spontaneous polarization. Because of its crystal structure, there are only two possible directions of the polarization, which are antiparallel with respect to each other. Hence, only 180° domain walls are possible, separating the two types of domains.

Periodically poled lithium niobate is used to achieve quasi-phase-matching in nonlinear optics. Here, the ferroelectric domains point alternately in the +c and the -c directions, with a period of typically between 5 and 25 μm. The shorter periods are used in second-harmonic generation, while the longer ones are suitable for optical parametric amplification. The periodic poling is achieved by electrical poling with periodically structured electrodes.
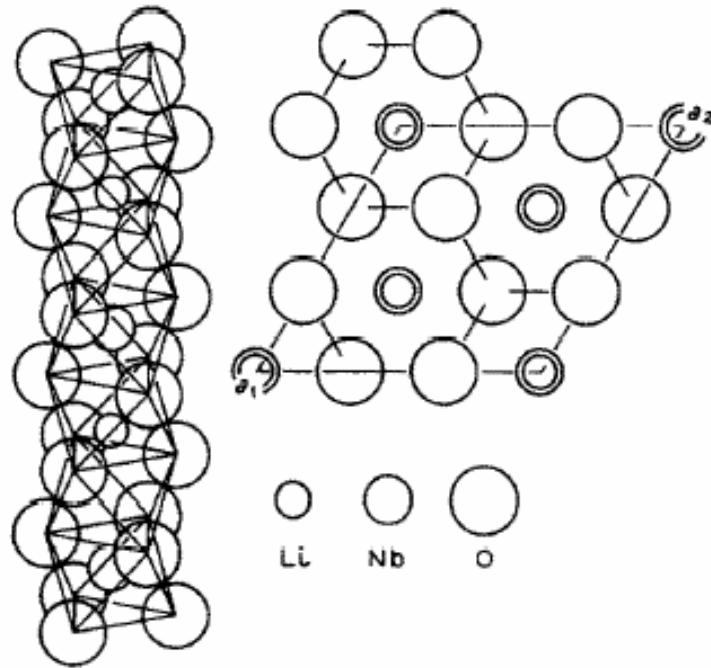
Figure 3.5: *Unit cell of LiNbO$_3$ [Abr66].*

3.4   Examination of Ferroelectric Domains

Ferroelectrics show various properties, which can be examined with numerous methods of which only some are mentioned here.

An easy and fast method is transmission optical microscopy with the ferroelectric sample placed between crossed polarizers [Jon62]. It allows the examination of the orientation of the optical axis of birefringent ferroelectrics. If the optical axis is oriented along the **k** vector of the incident light, then the polarization is not changed by the sample and the domain appears dark. The presence of a component of the optical axis perpendicular to **k** will lead to a rotated polarization, depending on the orientation and the thickness of the ferroelectric. Thus such regions appear bright.

The combination of optical microscopy and electric voltage allows the examination of the electro-optic response of the sample. For this the optical properties of the sample are mostly modulated by application of an ac voltage and imaged in the far field [Hub97, Hub00, Tik00] or in the near field [Ott04]. With this method, not only the domain distribution can be studied but also the mobility of the domain walls [Hub99].

Various methods transform the domain structure into a topographic information by, for example, selective etching or powder deposition. The topography can be examined with conventional methods such as optical microscopy in reflection, atomic force microscopy, or scanning electron microscopy. Chemical etching [Blu96, Jon62] happens at different rates on different domain ends and is used, for example, on

poled LiNbO$_3$. A clear disadvantage is the irreversible modification of the surface. Another possibility is to distribute a powder of charged particles on the sample in order to identify differently charged domain ends [Jon62]. These particles in general can be removed afterwards.

Several scanning probe microscopy methods (see chapter 4) allow the investigation of different properties of the ferroelectric domains. All methods discussed below were used in-situ with the s-SNOM experiments as discussed in the experimental part of this work (see section 8).

Some crystals show a domain-specific topography tilt due to unit-cell-misfit (see section 3.2). We can image this tilt directly by sensing the topography by an atomic force microscope. With this method we locate the position of 90° domain walls, but we cannot identify the domains further.

As the samples are piezoelectric, we can image the domain distribution by imaging the corresponding orientation of the piezoelectric tensor using piezoresponse force microscopy. For this we apply an alternating voltage between the tip and the sample which causes an alternating mechanical deformation of the unit cell. As tip and sample are in contact, the mechanical deformation causes a deflection of the cantilever. A deformation normal to the sample surface bends the cantilever, while a deformation of the sample parallel to the surface causes a torsion of the cantilever. With this method differently oriented domains can be identified precisely with a resolution on the nanometer scale.

As different domain ends carry different charges, we can image the electrostatic interaction of these charges with an AFM tip using Kelvin probe force microscopy or surface potential microscopy. Unfortunately, at ambient conditions, the surface charges may be screened and blurred by a water film on the sample surface.

3.5   Summary

In this chapter, we have given a short introduction into the classification, the basic properties, and the application of ferroelectrics. We have discussed the crystal structure and possible domain distributions in general as well as the specific properties of the ferroelectrics BaTiO$_3$ and LiNbO$_3$, which are the samples examined in this work. Finally, common examination methods have been specified.

4 Scanning Probe Microscopy

Since the invention of the first scanning probe instrument (SPM) – the scanning tunneling microscope (STM) – in 1982 by Binnig and Rohrer [Bin82] numerous scanning probe microscopes (SPM) have been developed. They are able to precisely position and scan a probe, such as the aperture or the scatterer in a SNOM (see chapter 2), in close proximity to a sample surface, thereby offering the possibility to image sample properties such as topography, piezoelectric properties, and surface charges. In this chapter, we will give a general description of all techniques used in the present thesis, namely atomic force microscopy (AFM) in contact and noncontact mode, piezoresponse force microscopy (PFM) and Kelvin probe force microscopy (KPFM).

4.1 Atomic Force Microscopy

The basis of all methods used in the present work is an AFM – being the second SPM developed by Binnig *et al.* in 1986 [Bin86] – which is used in contact or noncontact mode. For both methods a microfabricated tip on a cantilever is used as a probe, as shown in figure 4.1 [Nan07b, Wol91].

Typically, the probe is made of n-doped silicon and is for our applications coated with a 25-nm-thick metal film of platinum-iridium5 (Pt-Ir5)[1]. In order to be sensitive to small forces, the spring constant k of the cantilever has to be as small as possible ($k \cong 0.01..100$ N/m). On the other hand, the influence of acoustic waves and building vibrations should be minimized and the resonance frequency f_0 has to be high ($f_0 \cong 10 - 100$ kHz). The resonance frequency is given by [Lop00a, Mey92]

$$f_0 = \frac{1}{2\pi} \sqrt{\frac{k}{m^*}} \tag{4.1}$$

with m^* being the effective mass of the cantilever including the attached tip[2].

---

[1]The metal coating is necessary for in-situ PFM and KPFM measurements, as both techniques require an electrically conductive tip (see section 4.2 and 4.3). Additionally, a metal-coated tip exhibits a larger scattering cross section in the visible spectral range as well as a flat optical spectrum in the infrared regime, which is advantageous for the s-SNOM measurements (see section 8.1).

[2]The effective mass $m^* = m_c + 0.24m_d$ consists of the concentrated mass of the tip, $m_c \cong 10^{-12}$ kg, and the distributed mass, $m_d = lwt\rho$, of the cantilever with length l, width w, thickness t, and density ρ.
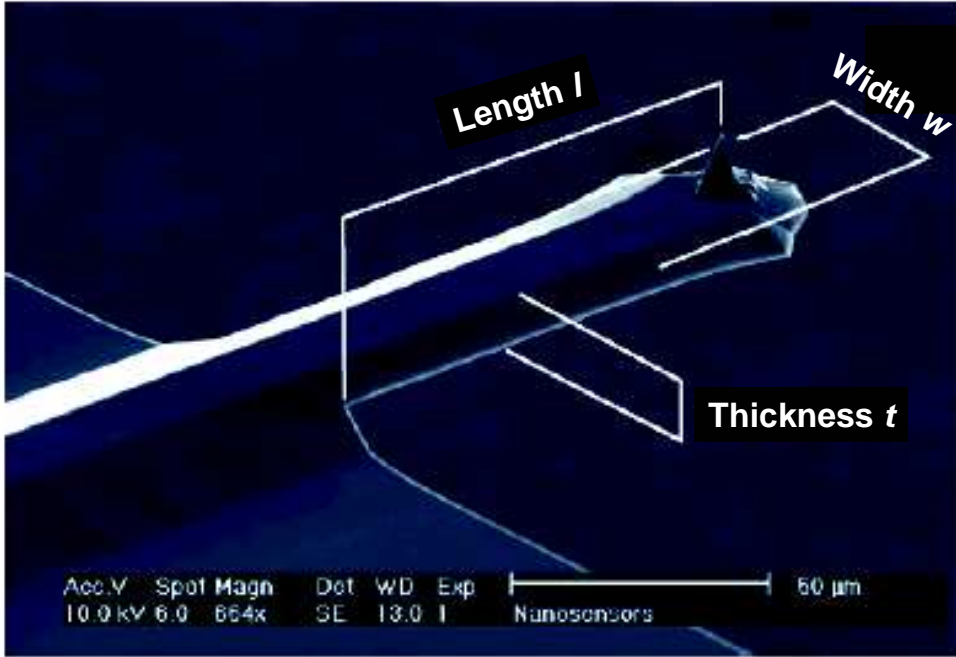
Figure 4.1: *Scanning electron microscopy picture showing a typical Pt-Ir5-coated AFM cantilever as used in this work, made of n-doped silicon. Additionally, the definitions of the cantilever dimensions and their typical scale are sketched: being thickness t, width w, and length l [Nan07b].*

Therefore, the mass of the cantilever has to be minimized by decreasing the dimensions of the cantilever [Mey92]. The typical thickness t, width w, and length l are $t \times w \times l = 7 \times 38 \times 225$ μm^3 for the cantilever type applied in the present work (see figure 4.1). The silicon cantilever (Young's modulus $E = 1,69 \cdot 10^{11}$N/m^2, density $\rho = 2.33 \cdot 10^3$kg/m^3) has thus a spring constant of [Wol91]

$$k = \frac{Et^3w}{4l^3} \cong 48 \text{ N/m} \tag{4.2}$$

and a resonance frequency of about $f_0 = 170$ kHz. The cantilever is attached to a support with a size of 1.5×3.5 mm having the same coating as the cantilever and the tip. The tip itself is shaped as a polygon-based pyramid with a height of about $10 - 15$ μm [Nan07b].

There are two different modes of operation in AFM, namely contact mode (or static mode) and noncontact mode (or dynamic mode).

In contact mode, the cantilever bends in response to the force F which acts on the probing tip, until the static equilibrium is established. As derived from Hooke's law, the deflection of the cantilever is proportionality to the force with the proportional constant being the spring constant k. By detecting the cantilever deflection, typical forces between 10^{-10} and 10^{-6} N can be measured.

While the tip is scanned across the surface, the deflection can be kept constant
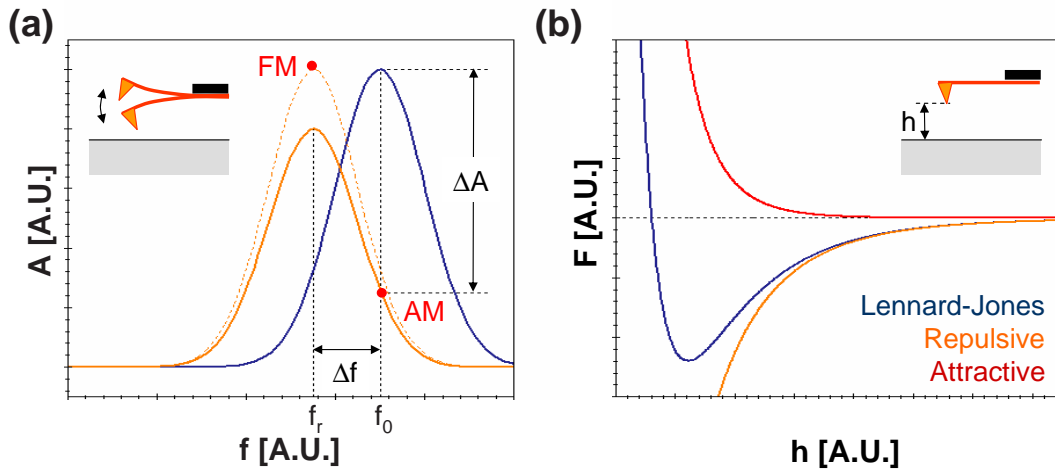
Figure 4.2: *(a) Resonance of an AFM cantilever with and without sample inter- action. The damping induced by the sample decreases the cantilever oscillation amplitude A at the resonance f_r. In FM mode, this amplitude might be con- trolled by an additional controller. The shift of the resonance towards lower frequencies corresponds to a positive slope of the force as function of the distance [Zer02]. The points of operation for FM and AM mode are marked by red dots. (b) Force calculated from the Lennard-Jones potential as a function of the dis- tance h between tip and sample [Sar91]. At small distances, the repulsive force is dominating, while for large distances the attractive force is.*

by regulating the height of the sample relative to the probing tip. This mode, called *equiforce mode*, is the most common mode. The height profiles are interpreted as reflecting the topography. As an alternative, the height position of the sample may be kept constant and the variations of the lever deflection recorded. This mode, called *variable-deflection mode*, allows high scanning speeds, but is only advised for samples with small height variations [Mey92].

In noncontact mode, the lever is oscillating close to its resonance frequency f_0. Any changes of the interaction force gradient $\partial F/\partial z$ between the tip and the sample change the resonance frequency. to first order[3], the new resonance frequency f_r of the cantilever can be described by an effective spring constant $k_{eff} = k - \partial F/\partial z$:

$$f_r = \frac{1}{2\pi}\sqrt{\frac{k_{eff}}{m^*}} \ . \tag{4.3}$$

A repulsive force ($F > 0$) increases the resonance frequency whereas an attractive force lowers it (see figure 4.2a). The shift of the resonance frequency is used to control the distance between tip and sample via a feedback loop. This loop ei-

---

[3]Here, we assume the cantilever oscillation amplitude to be small compared to the length scale on which the force gradient $\partial F/\partial z$ changes. For more detailed calculations using perturbation theory, see the work of Giessibl [Gie97].

ther ensures constant amplitude (amplitude-modulated (AM) control) or keeps the frequency constant (frequency-modulated (FM) control). Both methods keep the resonance curve of the cantilever at a fixed position while measuring profiles of constant gradient. For the AM mode, the excitation frequency is constant, while the shift of the resonance curve causes a decrease ΔA of the oscillation amplitude (see figure 4.2a). In the FM mode, the shift Δf of the resonance frequency is measured and the cantilever is always excited at its resonance f_r (see figure 4.2a). This technique allows the additional control of the oscillation amplitude by adjusting the excitation amplitude [Lop00a]. It is the FM mode that is able to keep the scattering conditions constant in s-SNOM and that is used throughout this thesis.

The interaction between tip and sample in AFM is given by intermolecular forces, mainly covalent forces, van der Waals forces, electrostatic forces, and magnetic forces. A good description is given by the Lennard-Jones potential, which combines the long-range attractive van der Waals and the short-range repulsive atomic potentials (see figure 4.2). A detailed overview is given in the literature [Mey92, Sar91].

There are various methods to detect the cantilever deflection. Besides the measurement of the capacitance, the tunnel current, or of an interferometric signal, the beam deflection method, as used in the present work, is the most common one [Mey92, Sar91]. For the latter one, a laser beam is focused on the back of the cantilever and is reflected back onto a four-quadrant photodiode [Ale89, Mey88a, Mey88b]. Any deflection of the lever causes a certain quadrant to collect more light than the others, which is measured electronically. The difference between the top and the bottom quadrants is called the top-minus-bottom (T-B) signal and is sensitive to changes of the deflection of the cantilever. On the other hand, the difference between the left and the right segments, the left-minus-right (L-R) signal, is sensitive to any torsion of the cantilever (see figure 4.3). For a more detailed description, we refer to the literature [Ale89, Mey88b, Sar91].

The AFM which was used in the present work is described in detail in section 8.1. For the s-SNOM investigations, we use the AFM in the noncontact mode. The distance modulation in this AFM mode causes a modulation of the highly distance-dependent optical signal, which allows us to separate the near- and far-field signals from each other using higher-harmonic demodulation (see section 2.3 and 5.3). In order to measure the domain distribution with complementary techniques, we perform in-situ KPFM as well as PFM. Because for PFM the AFM is used in contact mode, no simultaneous measurements are possible, but only an examination before or after the s-SNOM investigations.
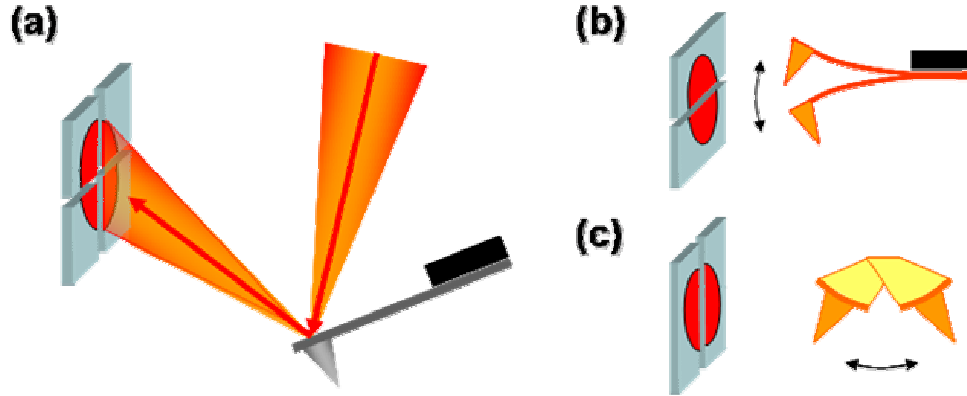
Figure 4.3: *Determination of the cantilever oscillation by the beam deflection method [Ale89, Mey88a, Mey88b]. (a) Sketch of the beam deflection setup. (b) The top-minus-bottom (T-B) signal represents the bending of the cantilever, while (c) the left-minus-right (L-R) signal reflects its torsion.*

4.2   Piezoresponse Force Microscopy

Since ferroelectrics are also piezoelectric (see section 3.1) and the orientation of the piezoelectric tensor is directly correlated with the direction of the spontaneous polarization, we can use piezoresponse force microscopy[4] to observe the local polarization of the crystal [Güt92]. For this, we monitor the local inverse piezoelectric effect, which reveals the three-dimensional distribution of the ferroelectric polarization [Was03].

We use an AFM in contact mode and apply an ac voltage between the conductive tip and an electrode on the back of the sample. The ac voltage has an amplitude of typically $U_p \cong 1$ to 5 V and a frequency $f_p \cong 20$ kHz [Abp98, Eng99a]. The adequate amplitude depends strongly on the sample properties and the proper frequency depends on the mechanical resonances of the AFM. The generated electric field at the tip causes a geometrical distortion of the sample by the inverse piezoelectric effect (see section 3.1). As the field is concentrated close to the tip-sample contact, we obtain the local piezoelectric response of this very area of the sample. The resolution is mainly limited by the tip radius and is comparable to the resolution of the AFM, being around 10 nm [Sch05a].

The response of the sample to the electric field is a geometrical distortion depending on the orientation of the polarization of the sample. In the following we assume the polarization of the sample to be oriented either perpendicularly (c domain) or parallel (a domain) to the sample surface, and we assume the applied electric field to be perpendicular to the sample surface. The electric field causes a deformation

---

[4]Also called voltage modulated scanning force microscopy [Eng99a] and
   dynamic contact electrostatic force microscopy [Lab00].

of the sample in z direction on a c domain (out-of-plane (OOP) deformation)

$$\Delta z = -d_{33}\mathrm{sgn}(P_z)U_p sin(2\pi f_p t) \tag{4.4}$$

and in x direction on an a domain (in-plane (IP) deformation)

$$\Delta x = -d_{15}\mathrm{sgn}(P_x)U_p sin(2\pi f_p t) \ . \tag{4.5}$$

These deformations are sensed by the cantilever as a deflection for Δz and a torsion or buckling for Δx. Deflection and buckling may be measured via the T-B signal of the 4-quadrant photodiode (see section 4.1), while the torsion gives a contribution to the L-R signal. The buckling vanishes if the polarization of the a domain is oriented perpendicularly to the cantilever axis. Hence, the two domains give only a contribution to one signal of the 4Q photodiode – namely the T-B signal for the c domain and the L-R signal for the a domain – and can hence be identified. Antiparallel orientations of the polarization are sensed via the sign of the geometric deformation, as indicated in equations 4.4 and 4.5. Hence, when demodulating the signal with a lock-in amplifier, we measure a phase shift of 180° between antiparallel domains.

In this work, we make use of the linear piezoelectric response of the sample, which is correlated with the piezoelectricity and the polarization. By sensing the 2nd-harmonic piezoelectric response of the sample at $2f_p$, one can additionally obtain information about the electrostriction and the permittivity of the sample [Fra94].

A typical PFM image of a BaTiO$_3$ crystal is depicted in figure 4.4. As we use the AFM in contact mode, we simultaneously measure the topography of the sample, which shows a meander shape typical to Remaika-grown BaTiO$_3$ crystals [Rem54], as depicted in figure 4.4a, which represents the domain structure during the growing of the crystal. Additionally, we observe steps in the topography as well as a corrugated surface. The corresponding PFM images are not correlated with the topography. The OOP signal 4.4b shows a similar meander structure of bright and dark areas corresponding to antiparallel c domains, interrupted by grey stripes being a domains. In the IP signal 4.4c, the c domains appear as grey areas, while the stripes that were grey in the OOP signal show antiparallel a domains as dark and bright areas [Eng98b, Eng99a]. In both PFM pictures we observe a cross talk from the complementary component, but we can clearly identify the domains. As discussed in section 3.2, on BaTiO$_3$ only 6 kinds of domains are possible – two antiparallel a domains in x and y and two antiparallel c domains – and the 90° domain walls are always straight lines.

In contact mode, it is also possible to manipulate the domain distribution by applying a dc voltage between the tip and the sample [Eng98a, Hu99, Hid96, Gru96]. As the electric field is oriented mainly perpendicularly to the sample surface, the poled area is usually a c domain with two possible states of polarization which can be switched by applying a dc voltage of opposite sign [Hu99, Gru97b]. This domain
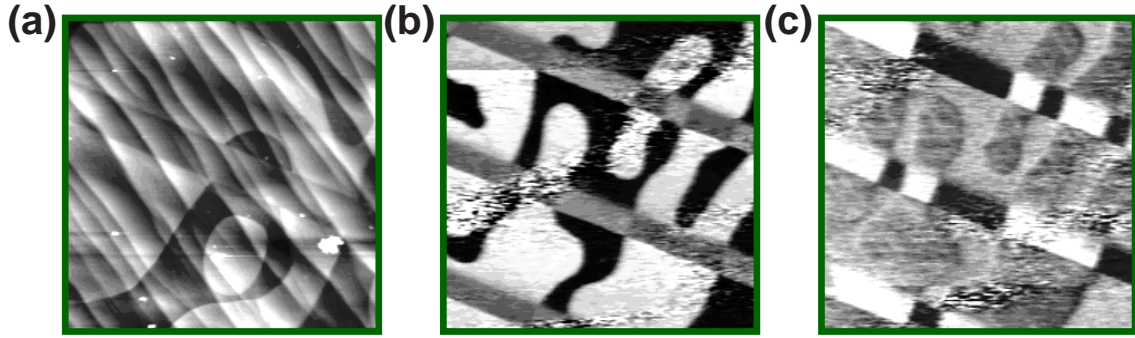
Figure 4.4: *PFM data of a BaTiO$_3$ single crystal (scan range: 10 µm). (a) Topography (z range: 55 nm), (b) PFM out-of-plane signal, and (b) PFM in-plane signal.*

writing may be used in data storage devices [Auc98, Was03].

For our s-SNOM investigations the AFM is used in noncontact mode and thus an simultaneously PFM measurement is not possible. Hence, we perform PFM measurements before and after the s-SNOM measurements to determine the domain structure of the examined area.

4.3   Kelvin Probe Force Microscopy

In Kelvin probe force microscopy (KPFM) [Lop04, Non91, Non92, Wea91], we determine the work function of a metal or the static surface charges on an isolating sample by measuring the electrostatic interaction between the tip and the sample.

KPFM is based on the capacitor method of Lord Kelvin, which he used to examine the contact potential difference of two metal plates [Kel98]. He compared the work functions of two parallel plates by interconnecting them electrically and moving one plate in the direction normal to the plates. This distance variation changes the capacitance C of the system, resulting in a current I

$$I = \frac{dC}{dt}U_{cpd} \tag{4.6}$$

with U_{cpd} being the contact potential difference. By applying an additional voltage $U_{K,0}$, the contact potential difference may be compensated and the current

$$I = \frac{dC}{dt}(U_{cpd} - U_{K,0}) \tag{4.7}$$

is nullified for $U_{K,0} = U_{cpd}$. As U_{cpd} corresponds to the difference of the work function of the two materials, knowing the work functions of one metal allows us to determine the work function of the sample plate.
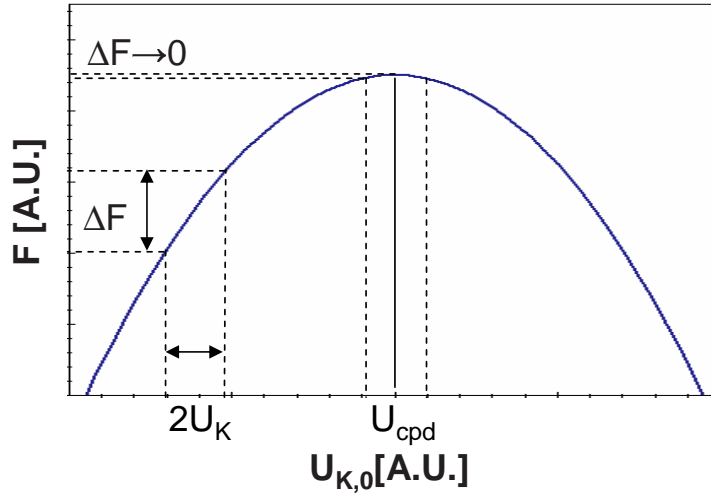
Figure 4.5: *Electrostatic force F as a function of the voltage $U_{K,0}$, showing the typical parabolic shape. For $U_{K,0} = U_{cpd}$, the force modulation is nullified.*

In an AFM, the metal-coated cantilever works as the reference part of the capacitor, interacting electrostatically with the sample. The resulting force

$$F = -\frac{1}{2}\frac{\partial C}{\partial z}U_{cpd}^2 \qquad (4.8)$$

may be measured as an additional modification of the cantilever oscillation in non-contact mode (see section 4.1) [Che02, Gie97, Lei03, Mar88, Sch05a, Wea91].

If an ac voltage U_K is applied between tip and sample with a typical amplitude $U_K \cong 0.5$ to 1.5 V and a frequency $f_K \cong 10$ kHz, the electrostatic interaction is modulated and can be detected by lock-in technique. Analogously to Lord Kelvin's method, applying an additional dc voltage $U_{K,0}$ allows us to compensate the potential difference between tip and sample and hence to nullify the modulation of the electrostatic interaction for $U_{K,0} = U_{cpd}$ [Non91, Non92, Wea91, Lop04, Zer02, Zer05]. Figure 4.5 shows the typical parabolic shape of the force F as a function of the applied dc voltage $U_{K,0}$

$$F = -\frac{1}{2}\frac{\partial C}{\partial z}(U_{cpd} - U_{K,0})^2 \; . \qquad (4.9)$$

Modulating the voltage by U_K causes a modulation of the force ΔF, except at the maximum of the parabola where the resulting modulation is zero. On a conductive sample, the compensating voltage can be correlated with the work function of the sample, while for insulating samples it represents basically the local electric potential on the sample surface due to static surface charges [Dur99, Sau90, Ter90].

On ferroelectric samples different polarizations in the sample generate different charges on the sample surface. By KPFM, we can identify antiparallel c domains as well as a domains on the sample. At room temperature these bound charges are

partly screened by adsorbates on the sample surface, such as water [Fel04, Jac98, Kit98]. Hence, the domain distribution is blurred in the KPFM picture. When irradiated by IR light, the water film might be vaporized and the domain structure can be observed more clearly [Sch07b].

During the s-SNOM measurements, we use KPFM as an simultaneous technique for domain imaging. But more importantly, we use KPFM to minimize the electrostatic interaction between tip and sample, which otherwise would influence the damping on different sample areas and hence the cantilever oscillating amplitude [Hon01], resulting in artifacts in the s-SNOM image, as reported in the literature [Bil06]. A detailed description of our setup is given in section 8.1.

Part II

Theory

5 Basic Theory of s-SNOM

In s-SNOM we scatter light off an AFM tip, which acts as a scatterer small compared with the wavelength. The interaction of this probe with the sample of interest makes the scattering characteristic of the coupled tip-sample system different from that of the tip alone. The coupling mechanism is a near-field interaction between tip and sample. The scattering process transforms the evanescent field, which is bound to the material surface, into a propagating wave. In the far field we are thus able to obtain optical near-field information on the local dielectric properties of a small sample area beneath the scatterer.

Theoretically, the quasi-electrostatic model of interacting dipoles in the tip and in the sample describes the scattering process as well as the interaction with the sample. This model is an easy-to-understand analytical model which explains the dependences in s-SNOM amazingly well. Comparison with numerical calculations confirms its results. The extension of this model to anisotropic samples is a main topic of this work and is described in the separate chapter 6.

5.1 Scattering by a Small Particle

Bohren and Huffman have treated in detail the scattering by small particles [Boh98]. For a particle small compared with the wavelength, the scattering process is well described by Rayleigh scattering, which is the quasi-electrostatic limit of the Mie theory [Mie08].

5.1.1 General Description

When a particle is illuminated, the incident light generates an external electric field $\mathbf{E_0}$ at the position of the particle.[1] The scattered light $\mathbf{E_{sca}}$ is correlated with the incident electric-field vector by the complex scattering coefficient $\widehat{\sigma}$ and, in the far field, can be described by its vector scattering amplitude $\mathbf{T}$:

$$\mathbf{E_{sca}} = \widehat{\sigma} \cdot \mathbf{E}_0 = \frac{e^{ikr}}{-ikr} \cdot \mathbf{T} \tag{5.1}$$

---

[1]In the theory chapters, all variables being vectors are typed bold and all tensors with a circumflex. If a parameter is complex valued, we simply mention this when introducing the parameter, but we do not use any special notation. We use the International System of Units (SI).

with k the wave number, being $2\pi/\lambda$,

      λ the wavelength, and

      r the distance between the scattering center and the point of observation.

Knowing the scattering amplitude $\mathbf{T}$, we can calculate measurable quantities such as the differential scattering cross section $\frac{dC_{sca}}{d\Omega}$, which specifies the angular distribution of the scattered light and which is given by

$$\frac{dC_{sca}}{d\Omega} = \frac{|\mathbf{T}|^2}{k^2 \cdot |\mathbf{E_0}|^2} \; . \tag{5.2}$$

By integrating the differential scattering cross section over the surface of an imaginary sphere around the scattering center, we get the total scattering cross section C_{sca} of the particle:

$$C_{sca} = \int_0^{2\pi} \int_0^{\pi} \frac{dC_{sca}}{d\Omega} \sin\theta d\theta d\phi \tag{5.3}$$

with θ, ϕ being the angles of the polar coordinate system with the particle in the center.

If the particle is small compared with the wavelength, we can use the electrostatic approximation of the Mie theory: The external electric field $\mathbf{E_0}$ induces a dipole moment $\mathbf{P_t}$ in the scattering particle given by

$$\mathbf{P_t} = \varepsilon_0 \varepsilon_m \cdot \widehat{\alpha}_t \cdot \mathbf{E_0} \tag{5.4}$$

with ε_0 the permittivity of the vacuum, being $8.854 \cdot 10^{-12}$ F/m,

      ε_m the complex dielectric constant of the surrounding medium, and

      $\widehat{\alpha}_t$ the polarizability of the particle.

In general, the polarizability is a complex tensor, which depends on the shape and material of the particle (see below). Knowing the dipole moment $\mathbf{P_t}$ induced in the particle, we can calculate the vector scattering amplitude $\mathbf{T}$:

$$\mathbf{T} = \frac{ik^3}{4\pi\varepsilon_m\varepsilon_0} \cdot \mathbf{e}_r \times (\mathbf{e}_r \times \mathbf{P}_t) \tag{5.5}$$

with $\mathbf{e}_r$ being the radial unit vector of the polar coordinate system with the dipole in the center. The scattering cross section is then given by

$$C_{sca} = \frac{k^4}{6\pi\varepsilon_0^2\varepsilon_m^2} \cdot \frac{|\mathbf{P}_t|^2}{|\mathbf{E_0}|^2} \; . \tag{5.6}$$

This cross section shows the typical $1/\lambda^4$ dependence of Rayleigh scattering, which is the electrostatic limit of Mie scattering. Furthermore, the cross section depends on the direction $\mathbf{e_0}$ of the external electric field $\mathbf{E_0}$ at the position of the particle

$$\mathbf{e_0} = \frac{\mathbf{E_0}}{|\mathbf{E_0}|} \tag{5.7}$$

and on the dipole $\mathbf{P_t}$ of the particle, i.e., its polarizability $\widehat{a}_t$ and the dielectric constant of the surrounding medium ε_m.

In the following parts of the present section we will discuss different particle shapes and materials and their polarizabilities. This is not absolutely necessary in order to understand the basic principles of s-SNOM, so if you want, you can take a shortcut to section 5.2.

5.1.2 Selected Particles

Isotropic sphere

For an isotropic sphere with radius a and dielectric constant ε_t the polarizability of the particle is a scalar given by [Jac83]

$$\alpha_t = 4\pi a^3 \frac{\varepsilon_t - \varepsilon_m}{\varepsilon_t + 2\varepsilon_m} \ . \tag{5.8}$$

The dipole $\mathbf{P_t}$ of the particle is parallel to the external electric field $\mathbf{E_0}$. The scattering cross section is given by

$$C_{sca} = \frac{k^4}{6\pi} \left| \alpha_t \right|^2 \tag{5.9}$$

and the corresponding absorption cross section C_{abs} is

$$C_{abs} = k\Im m(\alpha_t) \ . \tag{5.10}$$

Note that the cross sections depend only on the wave number k and on the polarizability $\widehat{\alpha}_t$ of the particle, i.e., on its size (radius a) and material (dielectric constant ε_t) as well as on the dielectric constant ε_m of the surrounding medium.

Figure 5.1 shows the two cross sections of the sphere as functions of the real and imaginary parts of its dielectric constant ε_t. At $\Re e(\varepsilon_t) = -2$ the polarizability has a resonance and both cross sections show a pronounced maximum. With increasing imaginary part, the resonance broadens and both maxima decrease. Far away from the resonance, the scattering cross section decreases with increasing imaginary part of the dielectric constant, while the absorption cross section increases. The absorption of the particle is determined by the imaginary part of its dielectric constant, while the corresponding real part defines the position of the resonance.

For an isotropic sphere the system is of spherical symmetry. This symmetry is reduced if the particle is anisotropic for geometrical or material reasons. Both cases will be discussed in the following.

Sphere made of an anisotropic material

We discuss the case of a sphere having a diagonal dielectric tensor with the elements $\varepsilon_{t,j}$ with $j = x, y, z$. The dipole moment of the particle is [Boh98]

$$\mathbf{P}_t = \varepsilon_0 \varepsilon_m \cdot \widehat{\alpha}_t \cdot \mathbf{E}_0 \tag{5.11}$$
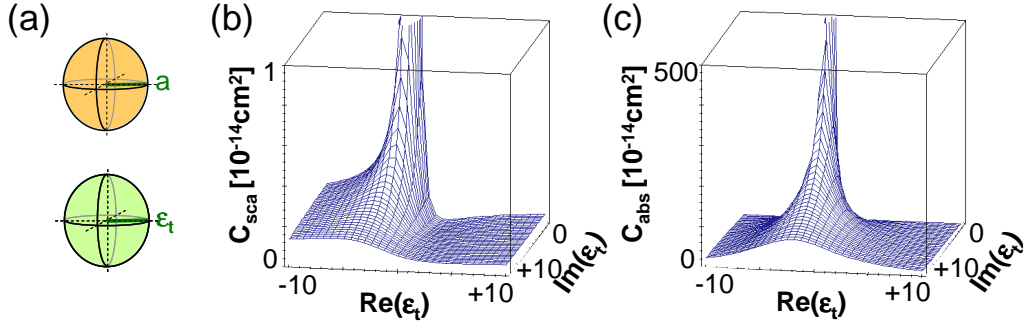
Figure 5.1: *(a) Sketch of the properties of an isotropic particle having a spherical shape (radius a) and a dielectric tensor of spherical symmetry (dielectric constant ε_t). Scattering cross section C_{sca}(b) and absorption cross section C_{abs} (c) of the isotropic sphere as functions of its dielectric constant ε_t (a = 10 nm, $\varepsilon_m = 1$, $\lambda = 633$ nm)*

with $\widehat{\alpha}_t$ being the diagonal polarizability tensor with the elements

$$\alpha_{t,j} = 4\pi a^3 \cdot \frac{\varepsilon_{t,j} - \varepsilon_m}{\varepsilon_{t,j} + 2\varepsilon_m} \tag{5.12}$$

Therefore the scattering cross section is given by

$$C_{sca} = \frac{k^4}{6\pi} \cdot \frac{|\widehat{\alpha}_t \cdot \mathbf{E}_0|^2}{|\mathbf{E}_0|^2} \ . \tag{5.13}$$

Compared to the former case, the symmetry of the system is reduced, as the scattering cross section of the anisotropic sphere depends additionally on the orientation of the external electric-field vector with respect to the dielectric tensor of the particle.

Figure 5.2 shows the scattering cross section of a uniaxial anisotropic sphere as a function of the real parts of its dielectric tensor elements. The two components of the dielectric tensor perpendicular to the anisotropy axis are equal ($\varepsilon_{t,1} = \varepsilon_{t,2} = \varepsilon_{t,a}$) and so are the corresponding elements of the polarizability tensor: $\alpha_{t,1} = \alpha_{t,2}$. The dielectric constant in the direction of the optical axis is $\varepsilon_{t,c}$, resulting in a polarizability $\alpha_{t,c}$. We plot the scattering cross section as a function of $\Re e(\varepsilon_{t,a})$ and $\Re e(\varepsilon_{t,c})$ for orientations of the external electric field parallel ($C_{sca,c}$) and perpendicular ($C_{sca,a}$) to the optical axis of the sphere. We observe that the scattering cross section has a maximum when the dielectric constant in the direction of the electric field equals -2. The dielectric constant perpendicular to the electric field does not influence the scattering cross section at all.

Ellipsoid made of an isotropic material

For an ellipsoid made from an isotropic material with semiaxes $a_x \leq a_y \leq a_z$ the components of the polarizability tensor in its diagonal form are given by [Boh98]

$$\alpha_{t,j} = 4\pi a_x a_y a_z \frac{\varepsilon_t - \varepsilon_m}{3\varepsilon_m + 3L_j \cdot (\varepsilon_t - \varepsilon_m)} \tag{5.14}$$
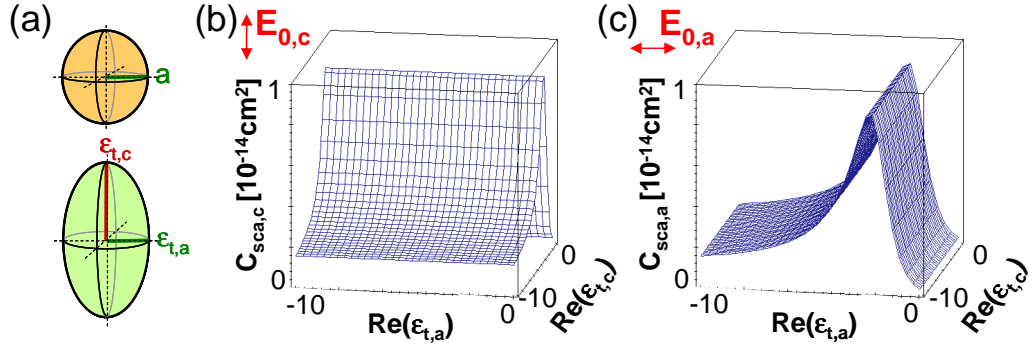
Figure 5.2: *(a) Sketch of the properties of a uniaxial anisotropic sphere with radius a and a dielectric tensor of cylindrical symmetry (dielectric constants $\varepsilon_{t,a}$ and $\varepsilon_{t,c}$). (b) and (c): Scattering cross sections of the uniaxial anisotropic sphere as functions of the real parts of its dielectric tensor elements $\varepsilon_{t,a}$ and $\varepsilon_{t,c}$ (a = 10 nm, $\varepsilon_m = 1$, $\lambda = 633$ nm, $\Im m(\varepsilon_{t,a}) = \Im m(\varepsilon_{t,c}) = 1$). (b) Scattering cross section when the external electric field is oriented along the optical axis of the sphere and (c) scattering cross section for perpendicular orientation.*

with L_j $(j = x, y, z)$ being geometrical factors:

$$L_j = \frac{a_x a_y a_z}{2} \int_0^\infty \frac{dq}{a_j^2 + q^2} \ . \tag{5.15}$$

Because of the relation

$$L_x + L_y + L_z = 1 \tag{5.16}$$

only two of the three geometrical factors are independent. Moreover, they satisfy the inequalities $L_x \geq L_y \geq L_z$. The scattering cross section is again given by equation 5.13.

For a prolate (cigar-shaped) ellipsoid, the two minor axes are equal $(a_x = a_y)$ and the two corresponding geometrical factors are

$$L_{x,y} = \frac{1 - e^2}{e^2} \cdot \left(-1 + \frac{1}{2e} \cdot \ln \frac{1 + e}{1 - e} \right) \tag{5.17}$$

and

$$L_z = 1 - 2 \cdot L_{x,y} \tag{5.18}$$

where e is the eccentricity given by

$$e^2 = 1 - \frac{a_x^2}{a_z^2} \ . \tag{5.19}$$

Figure 5.3 shows the scattering cross sections of such a cigar-shaped ellipsoid normalized to its volume, as functions of the real part of its dielectric constant ε_t and of the ratio of the major and minor axes. Similarly as for the anisotropic sphere, we plot C_{sca} for the cases when the external electric field is either parallel or perpendicular to the geometric axis of the particle. For an axis ratio of $c/a = 1$ we observe
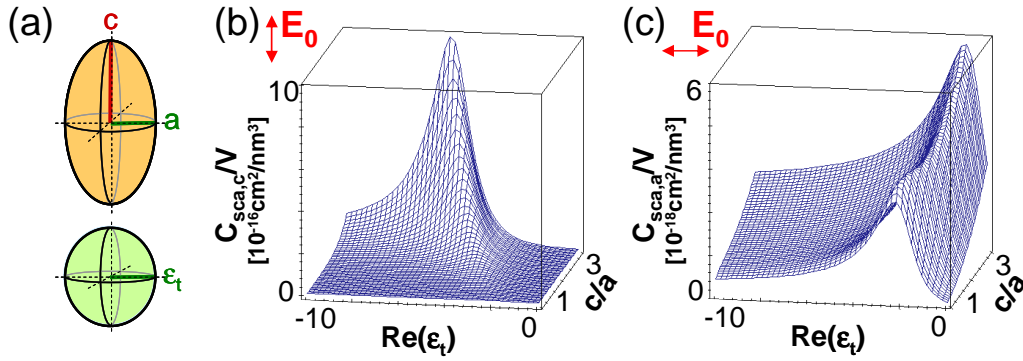
Figure 5.3: *(a) Sketch of the properties of a cigar-shaped ellipsoidal particle (axes a and c) made from an isotropic material (dielectric tensor has spherical symmetry, dielectric constant ε_t). (b) and (c): Scattering cross sections normalized to the volume V of the particle as functions of the dielectric constant and of the ratio between the two axes c/a (a minor axis, c major axis, $\varepsilon_m = 1$, $\lambda = 633$ nm). (a) Scattering cross section for orientation of the external electric-field vector along the major axis of the ellipsoid and (b) for perpendicular orientation.*

the resonance at $\Re e(\varepsilon_t) = -2$, which represents the limit of a spherical particle. With increasing axis ratio the scattering cross sections for the two orientations of $\mathbf{E_0}$ change differently: If $\mathbf{E_0}$ is oriented along the major axis, the resonance becomes dramatically stronger and shifts towards more negative values of $\Re e(\varepsilon_t)$. If $\mathbf{E_0}$ lies along a minor axis, the maximum increases only slightly and shifts towards larger $\Re e(\varepsilon_t)$.

The scattering cross section of the isotropic ellipsoid depends on the dimensions of the ellipsoid in all directions. Even when the external electric field is oriented along the minor axis of the ellipsoid, an increase of the major axis can be sensed. In contrast, for a sphere made of an anisotropic material an increase of the dielectric element along one axis is not sensed when the electric field is oriented perpendicularly to this axis.

5.1.3   AFM Tip as the Scatterer

In most s-SNOMs a typical AFM tip is used as the scatterer. The shape of such an AFM tip is well-defined by the fabrication process (see figure 4.1 and section 8.1). Still, it is very difficult to determine the size and shape of that part of the tip which contributes to the near-field signal.

As a first approximation, we can assume that the tip is an isotropic sphere. The shaft of the tip is neglected as well as its elongated shape, corresponding to the assumption that only the very end of the tip contributes to the near-field signal. This approximation works quite well as long as we choose the polarization of the incident light along the tip axis and thus perpendicular to the sample surface. Also,

we have begun to prepare improved tips with a metallic nanoparticle attached to the AFM tip [Wen07], which shows the spectrum of a spherical or elliptical single particle [Kal04].

In a more precise approximation we model the tip as a prolate ellipsoid with the major axis along the tip axis. With this method we take the different polarizabilities of the tip along and perpendicular to the tip axis into account. In most cases the cylindrical symmetry of the cigar-shaped particle corresponds quite well with the symmetry of the AFM tip.

As the symmetry of the tip-sample system is never higher than cylindrical, a tip shape of cylindrical symmetry with the corresponding axis perpendicular to the sample surface can be easily included in the model (see section 5.2). Any other tip shape is difficult to incorporate in the dipole model, because the symmetry of the coupled system is reduced and the formulae get much more complicated. In principle the dipole model holds for arbitrary tip shape as long as we can determine the polarizability of the tip.

5.1.4   Alternative Models

Using the dipole model to describe the scattering process in s-SNOM allows us to understand the interaction as well as the scattering process with simple formulae. The analytical model has the main advantage of clearly showing the various correlations.

Most other models describing the tip-sample interaction are numerical models, such as the method of multiple multipoles (MMP) [Haf90, Haf93, Nov97, Ren04]. This semianalytic boundary method expresses the electric and magnetic fields as a superposition of known exact solutions of Maxwell's equations, such as plane waves, multipole fields, or waveguide modes. By minimizing the error at the boundary, the code computes the expansion coefficients that best satisfy the boundary conditions. In this method only the boundary need to be discretized, which reduces the numerical effort and allows very accurate solutions [Ren04]. Within this model we are limited to isotropic materials as anisotropic materials may generate additional charges besides the considered surface charges. MMP calculations for spherical and ellipsoidal tips confirm the results of the dipole model. It has also been shown that at small distances the location of the point dipole in the tip is shifted towards the sample surface because of the strong gradient of the evanescent field [Ren05, Ren06]. Thus, in the dipole model it is necessary to use tip-sample distances which are smaller than the tip radius a to get the same results as in the numerical calculations. Comparison of measurements with theoretical data show that for our setup a distance of about $0.7a$ corresponds to the tip being essentially in contact with the sample (see chapter 9).

We can also think about a model describing the scattering as the tip acting as an antenna. This approach takes into account that the tip has a preferred scattering direction, as shown theoretically and experimentally for metal tips by several groups [GL99, Kni76]. The main disadvantage of this model is that it is very difficult to
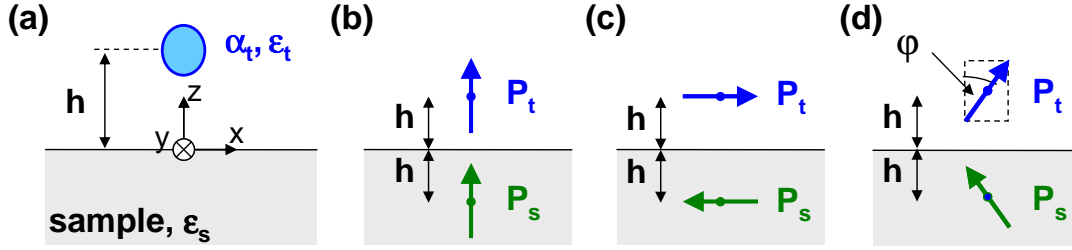
Figure 5.4: *(a) Definition of the cartesian coordinate system with the xy plane representing the sample surface. The origin is underneath the tip. Orientation of tip dipole $\mathbf{P_t}$ and sample image dipole $\mathbf{P_s}$ for the tip dipole being (b) perpendicular or (c) parallel to the sample surface as well as (d) arbitrarily oriented, as described by the polarization angle φ between the tip dipole and the sample normal.*

include the near-field interaction. Yet, most groups account for the antennalike behavior of the tip by choosing an appropriate angle of incidence in the experiments.

In the following section we describe the near-field interaction between an AFM tip and an isotropic sample using the dipole model. For simplicity we assume the tip to be an isotropic sphere. All formulae in the following section can be easily extended to a tip with one principal axis of the polarizability being perpendicular to the sample surface. Other tip shapes can be included by a more complicated extension of the model taking a tilt between the tip axis and the sample normal into account.

5.2   Tip-Sample Interaction in s-SNOM

In order to calculate the near-field interaction of tip and sample we assume the sample to fill the half-space next to the tip. The tip itself is placed outside the sample at a certain distance h to its surface. In the following calculations, the tip dipole is treated as a point dipole that is induced by an external electric field. The presence of the sample leads to a distortion of the electric field of the tip, which is calculated by the method of image charges. As the tip dipole is induced by the local electric field, the field distortion caused by the sample modifies the tip dipole. This model has been applied in the literature by several groups to calculate the optical near-field signal in s-SNOM [Kog97, Mad98, Kno99b, Kno00].

We define a cartesian coordinate system with its origin on the sample surface underneath the tip and with the sample surface located in the xy plane (see figure 5.4a). The distance h is assumed to be small compared to the wavelength, which allows us to neglect any retardation effects.

5.2.1   Method of Image Charges

The tip dipole induces charges on the sample, leading to a distortion of its electric field. Using the well-known method of image charges [Jac83], we calculate the electric field outside the sample by introducing an additional image dipole $\mathbf{P_s}$ in the sample at $(-h\mathbf{e_z})$ given by

$$\mathbf{P_s} = \beta \widehat{C} \cdot \mathbf{P_t} \ . \tag{5.20}$$

The factor β is the so-called response function of the sample:

$$\beta = \frac{\varepsilon_s - \varepsilon_m}{\varepsilon_s + \varepsilon_m} \tag{5.21}$$

with ε_s the complex dielectric constant of the sample. $\widehat{C}$ is the matrix

$$\widehat{C} = \begin{pmatrix} -1 & 0 & 0 \\ 0 & -1 & 0 \\ 0 & 0 & 1 \end{pmatrix} , \tag{5.22}$$

which accounts for the fact that the sample dipole is oriented differently depending on the orientation of the tip dipole: For a tip dipole perpendicular to the sample surface (z direction) the corresponding sample dipole is parallel to the tip dipole (see figure 5.4b), while for a tip dipole parallel to the sample surface (xy plane) the sample dipole is oriented antiparallel (figure 5.4c). Any mixed orientation is given by a superposition of the two cases and is defined by the polarization angle φ, which is the angle between the tip dipole and the sample normal (see figure 5.4d).

The electric field outside the sample is given by the superposition of the electric fields of the two electric dipoles $\mathbf{P_s}$ and $\mathbf{P_t}$. Observing this field far away from the tip, we can consider the two dipoles to be at the same position. The electric field is then given by a total tip-sample dipole $\mathbf{P_{tot}}$ being the sum of both dipoles.

5.2.2   Induced Tip Dipole

Because the tip dipole is induced by the local electric field $\mathbf{E_0}$, the distortion of the electric field by the sample changes the tip dipole. In addition to the external field, we have the field $\mathbf{E_s}$ of the sample dipole $\mathbf{P_s}$, which is situated at $\mathbf{r_0} = h\mathbf{e_z}$:

$$\mathbf{E_s} = \frac{3\mathbf{n}(\mathbf{P_s}\mathbf{n}) - \mathbf{P_s}}{4\pi\varepsilon_0 |\mathbf{r} - \mathbf{r_0}|^3}, \quad \mathbf{n} = \begin{pmatrix} 0 \\ 0 \\ 1 \end{pmatrix} . \tag{5.23}$$

Being the image of the tip dipole, the sample dipole is described by equation 5.20 and hence its field at the position of the tip is given by

$$\mathbf{E_s} = \widehat{K} \cdot \mathbf{P_t} \tag{5.24}$$

with the interaction matrix

$$\widehat{K} = \frac{1}{64\pi\varepsilon_0 h^3} \begin{pmatrix} 2\beta & 0 & 0 \\ 0 & 2\beta & 0 \\ 0 & 0 & 4\beta \end{pmatrix} . \tag{5.25}$$

The tip dipole given by equation 5.4 is modified by the electric field of the sample:

$$\mathbf{P_t} = \varepsilon_0 \varepsilon_m \widehat{\alpha}_t \left(\mathbf{E_0} + \mathbf{E_s}(\mathbf{P_t}) \right) . \tag{5.26}$$

Solving this equation for $\mathbf{P_t}$, we get

$$\mathbf{P_t} = (\widehat{I} - \varepsilon_0 \widehat{\alpha}_t \widehat{K})^{-1} \widehat{\alpha}_t \mathbf{E_0} = \widehat{\alpha}'_t \mathbf{E_0} \tag{5.27}$$

with the identity matrix $\widehat{I}$ and the modified tip polarizability $\widehat{\alpha}'_t$:

$$\widehat{\alpha}'_t = (\widehat{I} - \varepsilon_0 \widehat{\alpha}_t \widehat{K})^{-1} \widehat{\alpha}_t . \tag{5.28}$$

The total dipole moment of the tip-sample system is given by the sum of the modified tip dipole $\mathbf{P_t}$ and the corresponding sample dipole

$$\mathbf{P_{tot}} = \mathbf{P_t} + \mathbf{P_s} = \varepsilon_0 \varepsilon_m \widehat{\alpha}_{tot} \cdot \mathbf{E_0} \tag{5.29}$$

with the total polarizability $\widehat{\alpha}_{tot}$ of the tip-sample system being

$$\widehat{\alpha}_{tot} = \left(\widehat{I} + \beta\widehat{C} \right) \cdot \widehat{\alpha}'_t . \tag{5.30}$$

With this total tip-sample dipole, we can calculate any desired scattering parameter, as discussed for the single particle in section 5.1; e.g. the scattering cross section:

$$C_{sca} = \frac{k^4}{6\pi\varepsilon_0^2\varepsilon_m^2} \cdot \frac{|\mathbf{P}_{tot}|^2}{|\mathbf{E}_0|^2} . \tag{5.31}$$

If the tip is an isotropic sphere with a scalar polarizability α_t, the scattering cross section simplifies in that the external electric field $\mathbf{E_0}$ cancels. Still, the direction of the external electric field determines the size of the scattering cross section. The two special cases in which the external electric field is either perpendicular ($\perp$) or parallel ($\parallel$) to the sample surface are given by

$$C_\perp = \frac{k^4}{6\pi} \cdot \left| \frac{(1+\beta)\alpha_t}{1 - \frac{\alpha_t\beta}{16\pi h^3}} \right|^2 \text{ and} \tag{5.32}$$

$$C_\parallel = \frac{k^4}{6\pi} \cdot \left| \frac{(1-\beta)\alpha_t}{1 - \frac{\alpha_t\beta}{32\pi h^3}} \right|^2 .$$

In contrast to the tip alone, the scattering cross section of the coupled tip-sample system always depends on the polarization of the incident light. For a spherical tip the system is no longer of spherical, but of cylindrical symmetry. For such a
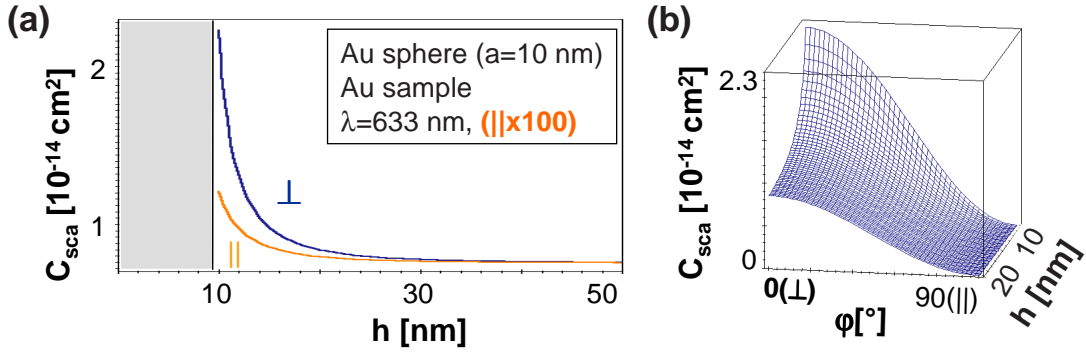
Figure 5.5: *(a) Distance dependence of the scattering cross section for different orientations of the tip dipole with respect to the sample surface. For easier comparison, the scattering cross section of the parallel-oriented tip dipole (∥) has been multiplied by 100. (b) Scattering cross section as a function of distance h and polarization angle φ as defined in figure 5.4d with φ = 0° and φ = 90° corresponding to ⊥ and ∥ orientation, respectively.*

system, figure 5.5a shows the characteristic distance dependence of the near-field-enhanced scattering cross section. In the calculations we assume the tip to be a gold sphere with radius $a = 10$ nm close to a gold sample with the excitation occurring at $\lambda = 633$ nm. Typically, the scattering cross section increases almost exponentially when the tip is approached to the sample. Note that the exponential decay length does not depend on the wavelength, but mainly on the tip radius, as long as the system is not excited at its resonance (see section 6.3). Figure 5.5a displays two curves referring to a parallel and perpendicular orientation, respectively, of the tip dipole with respect to the sample surface. We clearly observe a much larger scattering cross section for the perpendicular case, which results from the constructive superposition of the tip and sample dipoles, as they are oriented in the same direction. For the parallel orientation, the tip and sample dipoles are antiparallel to each other and therefore superpose destructively. Thus the signal is much smaller than for the perpendicular case (please note that in figure 5.5a the parallel component of the scattering cross section has been multiplied by 100 for easier comparison with the perpendicular component). Figure 5.5b shows the scattering cross section as a function of the distance h and the polarization angle φ as defined in figure 5.4d. Comparing again the signals for parallel ($\varphi = 90°$, ∥) and perpendicular orientation ($\varphi = 0°$, ⊥) of the external electric field, we see clearly that the signal is maximized for perpendicular orientation, while the parallel component of $\mathbf{E_0}$ produces almost no signal, even when the tip is very close to the sample surface.
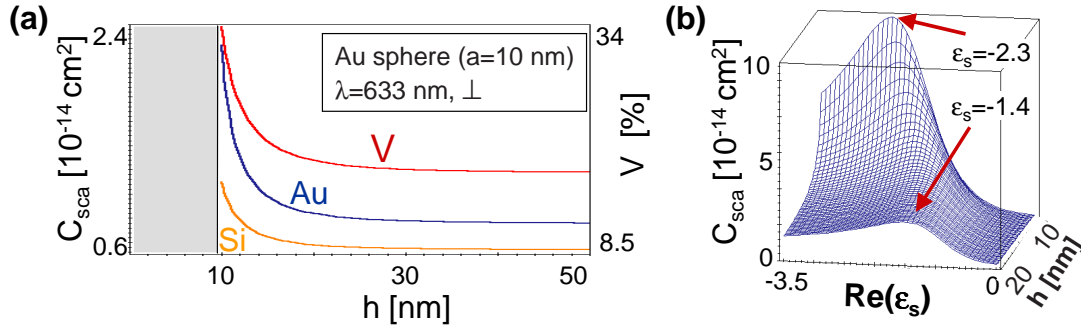
Figure 5.6: *(a) Distance dependence of the scattering cross section for different sample materials. The calculations were done for a spherical gold tip (radius $a = 10$ nm) with its dipole moment being perpendicular to the sample surface, and for $\lambda = 633$ nm. Additionally, the optical contrast V between gold and silicon is plotted as a function of the distance h. (b) Scattering cross section as a function of distance h and the dielectric constant ε_s of the sample.*

5.2.3 Optical Material Contrast

During a scan in s-SNOM, the tip properties, the wavelength, and the polarization of the incident light, as well as the distance between tip and sample can be considered constant. Therefore, the scattering cross section only depends on the dielectric constant ε_s of the sample. We thus expect to measure different signals on regions of the sample with different dielectric constants, i.e., different materials. Figure 5.6a shows the distance dependence of the scattering cross section on a gold (Au) and on a silicon sample (Si) at $\lambda = 633$ nm. The calculations were done for a spherical gold tip with $a = 10$ nm and an external electric field oriented perpendicularly to the sample surface. On both sample materials we observe an increase of the scattering signal close to the sample surface. For the gold sample the signal is much higher than for the silicon sample.

Figure 5.6b shows the dependence of the near-field signal on the distance h as well as on the dielectric constant ε_s of the sample. For each distance h, we observe a maximum in the scattering cross section. With decreasing distance, this maximum increases strongly while moving towards smaller dielectric constants of the sample. For large distances the maximum is located at $\Re e(\varepsilon_s) = -1$. This sample-induced resonance of the tip-sample system will be discussed in more detail for anisotropic samples in section 6.3.

The quantity that represents the difference in the measured signal between different sample areas A and B, is the complex optical contrast or visibility V, which is in general defined as

$$V(f) = \frac{f_A - f_B}{f_A + f_B} \; . \tag{5.33}$$

with f representing the measured quantity, which is different for different detection methods (see section 5.3). If, for example, the absolute scattering cross section is

measured, the visibility V is given by

$$V(C_{sca}) = \frac{C_{sca,A} - C_{sca,B}}{C_{sca,A} + C_{sca,B}} \; . \tag{5.34}$$

In figure 5.6a this cross section contrast between gold and silicon is plotted as a function of the distance between tip and sample. We observe that the optical contrast increases dramatically with decreasing distance. When the tip touches the sample surface, we expect a contrast of about 34% between gold and silicon.

Because this contrast is caused by spatial variations of the dielectric constant of the sample, we call it a material contrast. In chapter 6 we will introduce an additional contrast mechanism caused by variations of the anisotropy of the sample.

5.2.4   Reflection at the Sample Surface

Illuminating a tip close to a sample surface in a real experiment is not possible without reflection at the sample surface. This reflection changes the external electric field $\mathbf{E_0}$ at the position of the tip, which determines all scattering parameters discussed in section 5.1. Here we analyze how this external electric field is connected to the electric field $\mathbf{E_{inc}}$ of the incident light .

Without restriction, we choose the x axis of the coordinate system defined above to be parallel to the plane of incidence. The incident electric field is given by

$$\mathbf{E_{inc}} = E_s \mathbf{e_s} + E_p \mathbf{e_p} \tag{5.35}$$

with E_s and E_p denoting the s- and p-polarized components of the electric field defined by the unit vectors

$$\mathbf{e_s} = \begin{pmatrix} 0 \\ -1 \\ 0 \end{pmatrix} \;\; , \;\; \mathbf{e_p} = \begin{pmatrix} \cos\gamma \\ 0 \\ \sin\gamma \end{pmatrix} \;\; , \tag{5.36}$$

where γ is the incident angle, defined as the angle between the $\mathbf{k}$ vector of the incident light and the negative z axis, which is normal to the sample surface (see figure 5.7a).

The reflection at the surface of a material with index of refraction[2] n_s is given by the Fresnel reflection coefficients r_s and r_p [Fow89]:

$$r_s = \frac{cos(\gamma) - \sqrt{n^2 - sin^2(\gamma)}}{cos(\gamma) + \sqrt{n^2 - sin^2(\gamma)}} \;\; , \tag{5.37}$$

$$r_p = \frac{n^2 cos(\gamma) - \sqrt{n^2 - sin^2(\gamma)}}{n^2 cos(\gamma) + \sqrt{n^2 - sin^2(\gamma)}}$$

---

[2]The index of refraction n of a material is correlated to its dielectric constant ε by $n^2 = \varepsilon$.
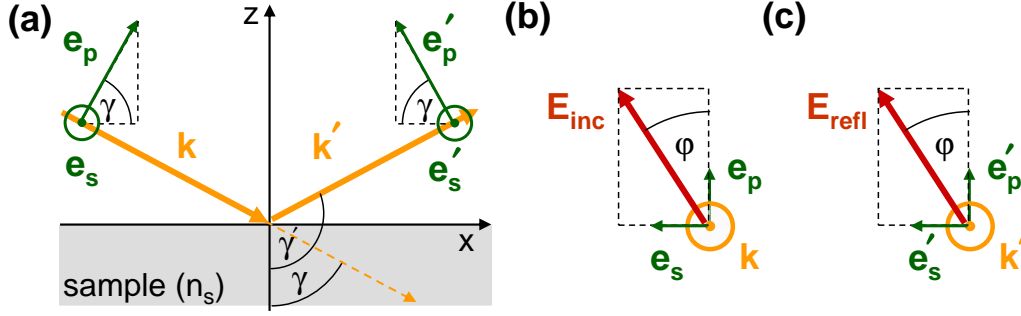
Figure 5.7: *Definitions of the incident angle γ, of the unit vectors $\mathbf{e_s}$ and $\mathbf{e_p}$ used to describe the incident polarization, and of the corresponding quantities referring to the reflected wave (γ', $\mathbf{e'_s}$, and $\mathbf{e'_p}$). View in the plane of incidence (a) and in a plane perpendicular to the $\mathbf{k}$ vector of the incident light (b) or of the reflected light (c).*

with the relative index of refraction n given by the ratio of the indices of refraction of the sample material (n_s) and of the surrounding medium (n_m):

$$n = \frac{n_s}{n_m} \; . \tag{5.38}$$

Note that some textbooks prefer to define r_p with the opposite sign [Fow89] because of a different definition of the unit vectors by which the reflected-light polarization is described.

Figure 5.8a shows the reflection coefficients as functions of the incident angle γ for a silicon sample. For easier comparison with the literature, we plot $-r_p$. For $\gamma = 0°$ both components E_s and E_p of the incident electric-field vector are parallel to the sample surface and hence the corresponding reflection coefficients are equal. The s component decreases with γ to more negative values and reaches -1 at $\gamma = 90°$, while r_p increases with γ, crosses zero at Brewster's angle, and reaches $+1$ at $\gamma = 90°$. At Brewster's angle the reflected light is purely s polarized [Fow89].

Knowing the reflection coefficients r_s and r_p, we can calculate the reflected electric field $\mathbf{E_{refl}}$ according to

$$\mathbf{E_{refl}} \;=\; r_s E_s \mathbf{e_s} + r_p E_p \widehat{C} \mathbf{e_p} \tag{5.39}$$

with $\widehat{C}$ given by

$$\widehat{C} = \begin{pmatrix} -1 & 0 & 0 \\ 0 & -1 & 0 \\ 0 & 0 & 1 \end{pmatrix} \; . \tag{5.40}$$

Knowing the electric fields of both the incident and the reflected light, we can calculate the external electric field $\mathbf{E_0}$ at the position of the tip. For small distances h between tip and sample it is given by the sum

$$\mathbf{E_0} = E_s(1 + r_s)\mathbf{e_s} + E_p(\widehat{I} + r_p \widehat{C})\mathbf{e_p} \; . \tag{5.41}$$
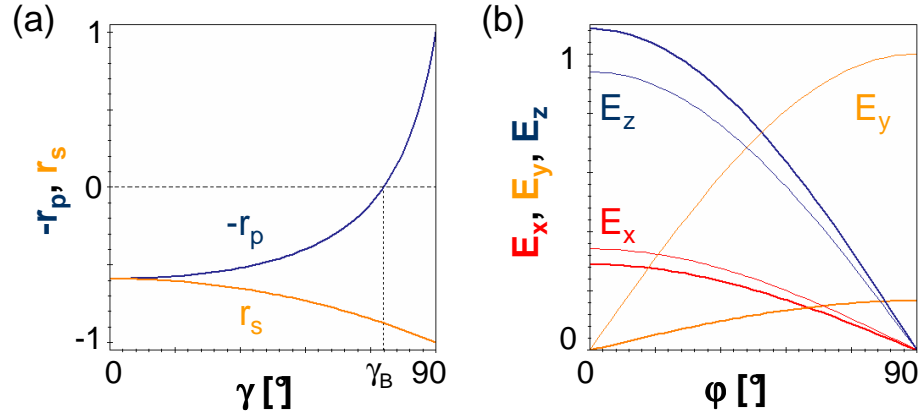
Figure 5.8: *(a) Reflection coefficients $-r_p$ and r_s as functions of the incident angle γ for a silicon sample with $\varepsilon_s = 15$. At Brewster's angle $\gamma_B \cong 75.5°$, the reflected light is purely s polarized as r_p is zero. (b) Electric-field components normalized to the electric-field strength of the incident light at the position of the tip as functions of the incident polarization φ for an incident angle of $\gamma = 70°$ as used in the experiments. The thick lines show the components along the x, y, and z axis with the reflection at the sample taken into account. For comparison, the thin lines of the corresponding color show the electric field of the incident light.*

Figure 5.8b shows the resulting electric-field components at the position of the tip as functions of the polarization angle φ of the incident light for an incident angle of $\gamma = 70°$ as used in the experiments. For comparison, we plot the corresponding electric-field components of the incident wave as thin lines of the same color. For p-polarized light ($\varphi = 0°$), we have components along the x and the z axis, which are slightly modified in their magnitudes by the reflection at the sample surface. Both components decrease with φ and are zero for s-polarized light. The most drastic change is observed for the y component, which is the direction of the s polarization. It is zero at $\varphi = 0°$ and increases with the polarization angle. The y component of the incident light reaches 1, while the field vectors of the light reflected at the sample surface is antiparallel to the incident one and, hence, decreases it such that it reaches a value of less than 0.2 at $\varphi = 90°$.

In figure 5.9 we compare the scattering cross sections with and without reflection at the sample surface taken into account. As an example we assume the tip to be a gold sphere next to a silicon sample and depict the scattering cross sections as functions of the incident angle γ and the polarization angle φ of the incident light.

In figure 5.9a the reflection at the sample surface has been neglected and the external electric field at the position of the tip is assumed to be the electric field of the incident light. For p-polarized light and an incident angle of $\gamma = 90°$ the electric-field vector at the tip is perpendicular to the sample surface. We observe a maximum in the scattering cross section corresponding to a maximized constructive superposition of the tip and the sample dipoles. With increasing polarization angle φ, the parallel
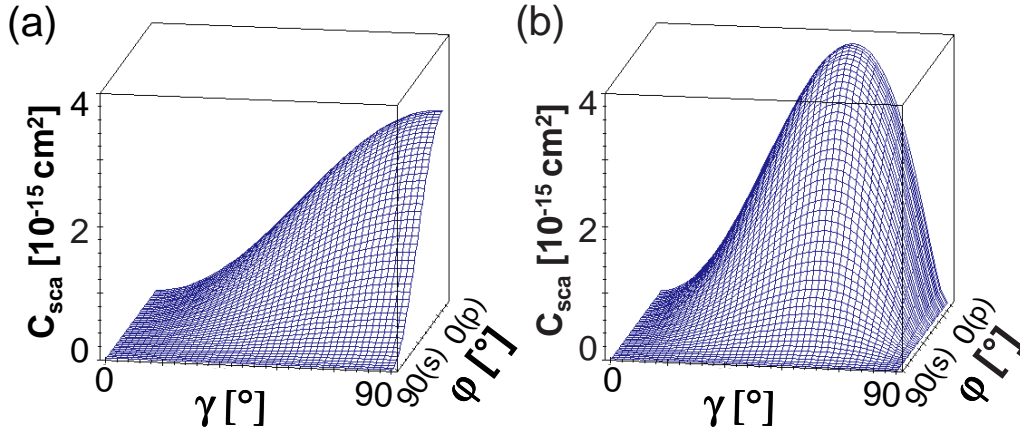
Figure 5.9: *Scattering cross section of a spherical gold tip (radius $a = 10$ nm) next to a silicon sample ($h = 10$ nm) as a function of the incident angle γ and the polarization angle φ of the incident light. In (a) reflection at the sample surface is neglected, while it is included in (b).*

component of the tip dipole increases. This component has an antiparallel image dipole and hence the signal decreases. For smaller incident angles γ, the p-polarized part of the incident electric field has not only a component perpendicular to the sample surface but also a parallel component. Hence, the scattering cross section decreases again.

In figure 5.9b the scattering cross section with reflection at the sample surface included is plotted for the same parameters. In contrast to figure 5.9a, we observe a maximum at $\gamma \cong 67°$, which is about 30 % higher due to the additional contribution of the reflected field parallel to the incident electric field. At Brewster's angle of $\gamma_B \cong 75°$ the reflected field has no p component and the cross section has about the same size as without reflection as the contribution from the s component is negligible. For $\gamma > \gamma_B^\circ$, the reflected field is antiparallel to the incident field and the cross section is smaller than in figure 5.9a. At $\gamma = 90°$ the z component is zero and so is the cross section except for a negligible contribution from the s-polarized component.

These pictures show clearly the influence of reflection at the sample surface. On anisotropic samples the impact is even higher, because the polarization of the light is changed by the reflection at the sample surface (see chapter 6).

In the following section we will discuss different possibilities of collecting the scattered light. Different methods allow us to measure different quantities of the scattering process.

5.3   Demodulation and Detection

The detection of the optical near-field signal is crucial for the results we obtain. The easiest method is to detect the scattered light directly as it is done in our IR setup (see section 8.4). We will describe the method of direct detection in the first part of this section.

The maybe most delicate point in measuring near-field signals is the separation of the very small near-field signal from the huge background signal. For all types of detection, this discrimination can be realized by higher-harmonic demodulation. The underlying principle is discussed in section 2.3, while in this section we will describe the method theoretically as it applies in the case of direct detection.

As the near-field signal is very small, many groups use homodyne or heterodyne interferometric detection to enhance the signal-to-noise ratio. In addition, interferometric detection allows us to distinguish between the amplitude and phase of the complex near-field signal.

5.3.1   Direct Detection of the Scattered Light

One of the main problems in detecting the scattered light directly is the small amount of backscattered light. The signals are still large enough to be measured with an ordinary detector, but what we want to measure are tiny changes of this small signal. It does not help very much to collect as much light as possible with, for example, an ellipsoidal mirror [Kno99a, Kno99b] to take advantage of the full scattering cross section of about 10^{-14} cm^2, because it is difficult to find a mirror that fits the special setup and because the adjustment is delicate. This is the reason why most groups simply use a lens to collect the scattered light. For a lens with a numerical aperture of 0.25 we expect the effective scattering cross section to be about 10^{-16} cm^2. Direct detection with a lens is sketched in figure 5.10a.

With the direct-detection method we collect and measure the power of the scattered light, which is proportional to its intensity I_{sca} given by the square modulus of the scattered electric field $\mathbf{E_{sca}}$

$$I_{sca} = |\mathbf{E_{sca}}|^2 \ .$$
(5.42)

The power scattered in a certain direction is directly proportional to the differential scattering cross section (see equation 5.2) multiplied by the actual intensity at the tip $I_0 = |\mathbf{E_0}|^2$:

$$I_{sca} \sim \frac{dC_{sca}}{d\Omega} I_0 \ .$$
(5.43)

The particular cross section C_Ω detected by a lens can be calculated by integrating the differential cross section over the solid angle covered by the lens

$$C_\Omega = \int \int \frac{dC}{d\Omega} \sin\theta d\theta d\phi \, .$$
(5.44)
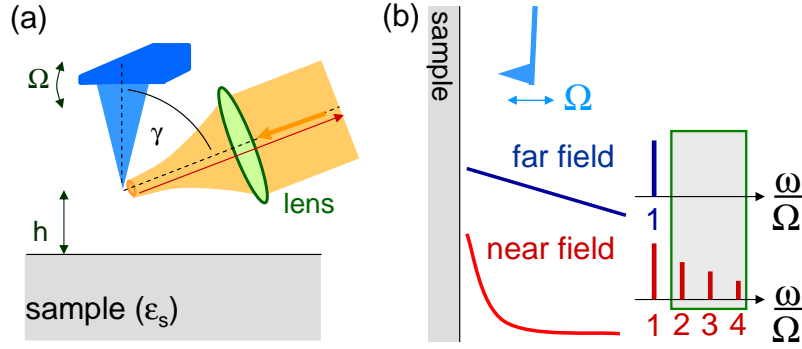
Figure 5.10: *(a) Sketch of direct detection with incident angle γ and distance h between tip and sample. (b) Background suppression by higher-harmonic demodulation: As a result of the cantilever oscillating at a frequency Ω, the far-field signal, which depends linearly on h, is modulated at Ω, while the near-field signal contains a whole spectrum of frequencies $n\Omega$.*

Determining a realistic sector of detection is difficult as we do not know the exact orientation of the tip-sample dipole with respect to the incident **k** vector. Furthermore, the real tip-sample system does not show a pure dipole radiation pattern. Even though the tip-sample interaction is well described by the electrostatic approximation, a real tip exhibits a mixture of dipole and antenna properties (see section 5.1). Studies on more needle-shaped tips have clearly shown this antenna characteristic [GL99, Kni76]. In our experimental setup we account for this behavior by illuminating the tip at the proper angle of incidence ($\gamma = 70°$) corresponding to the main lobe of the antenna pattern. As we measure the backscattered light at the same angle, we expect the lens to collect a radiation maximum. In view of the above uncertainties, we use the total power radiated into the upper half-space as a measure of the signal to be expected when direct detection is used. This power corresponds to half the total scattering cross section:

$$f_{dir} = \frac{1}{2}C_{sca} \ .$$ (5.45)

The optical contrast (equation 5.33) is then given by

$$V_{dir} = \frac{C_{sca,A} - C_{sca,B}}{C_{sca,A} + C_{sca,B}} \ .$$ (5.46)

With the method of direct detection we measure signal changes caused by the amplitude of the scattered wave. We are not sensitive to any variations of its phase and thus we lose that piece of information about the near-field interaction. Measuring both signals is possible with interferometric detection methods described in the sections below.

Please note that in this section the direct detection has been described as an ideal system in which the detector only collects light that is scattered by the tip. In the corresponding experiments, one usually has backreflections from optical elements

such as mirrors, lenses, and beamsplitters, but also from the tip-sample junction. As these backreflected beams interfere with the scattered beam, the measured signal is in fact sensitive to both the amplitude and phase of the scattered wave [Bla03]. Interferometric detection suppresses these terms and replaces them by controlled interferences with a well-defined reference beam.

Before discussing how to distinguish between optical amplitude and phase by using interferometric detection, we detail how to suppress the huge far-field signal, such that the small near-field signal becomes accessible. This can be realized with the method of higher-harmonic demodulation.

5.3.2   Higher-Harmonic Demodulation

In the experiment, the light scattered by the tip contains not only the near-field signal but also a contribution due to reflections at the tip shaft as well as far-field interferences between different light paths. To single out the small near-field signal from this background, we use the method of so-called higher-harmonic demodulation.

In noncontact mode, the cantilever is oscillating at a certain frequency Ω and thus the distance between the tip and the sample is modulated. As the near-field signal depends strongly on the distance, it is modulated at the cantilever frequency as well. In fact, the nonlinear distance dependence causes a modulation not only at the cantilever frequency Ω, but also at multiples $n \cdot \Omega$ with $n = 1, 2, 3, ...$, which are the so-called higher-harmonic frequencies (see figure 5.10b). As the far-field background exhibits only a weak, essentially linear dependence on the distance between tip and sample, the modulation of the background occurs only at Ω. Hence, when demodulating the signal at one of the higher harmonics using lock-in technique, we measure a pure near-field signal (see figure 5.10b).

The different higher harmonics can be calculated by Fourier transformation of the signal. We will discuss this for the example of direct detection.

The signal measured by direct detection is proportional to the scattering cross section (see equation 5.43). For simplicity we assume the tip to have a scalar polarizability α_t and the external electric field at the tip to be oriented perpendicularly to the sample surface. Hence, the measured signal is given by (see equation 5.32)

$$f(h) = \frac{k^4}{2 \cdot 6\pi} \left| \frac{\alpha_t (1 + \beta)}{1 - \frac{\alpha_t \beta}{16\pi h^3}} \right|^2 . \tag{5.47}$$

If the tip oscillates in z direction at the frequency Ω and with the amplitude h_1, the distance h as a function of time is given by

$$h(t) = h_0 + h_1 (1 + cos(\Omega t)) . \tag{5.48}$$

with h_0 being the distance at the turning point of the oscillation at the surface.

After inserting this formula for h in equation 5.47, we can calculate the contributions to the nth higher-harmonic signal by calculating the respective Fourier
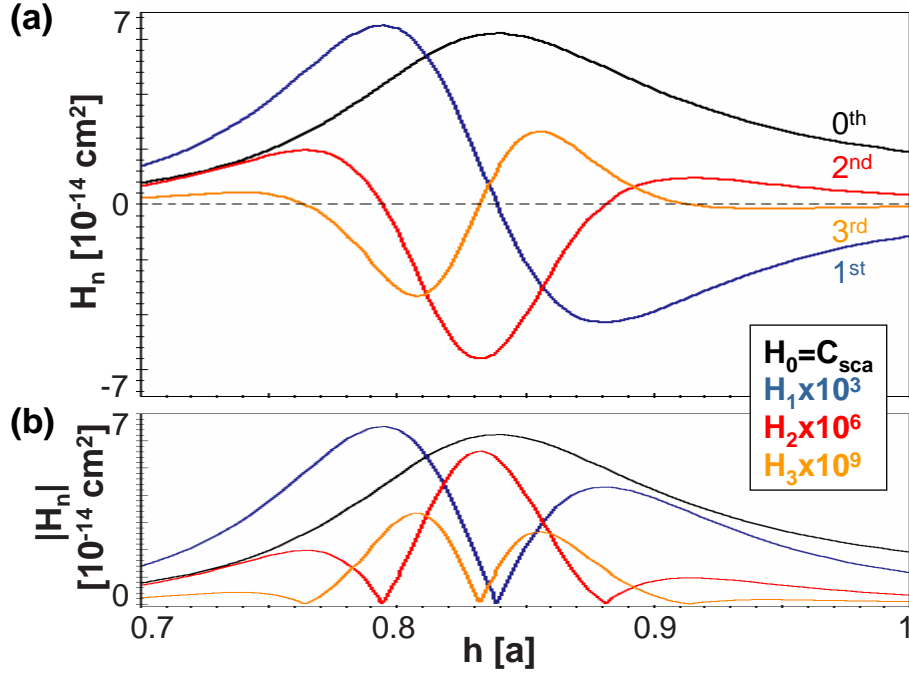
Figure 5.11: *(a) Higher harmonics of the directly detected near-field signal as functions of the tip-sample distance h. The tip is assumed to be a metal sphere (a = 10 nm) far from any resonance ($\alpha_t \cong 4\pi a^3$) at $\lambda = 633$ nm. (b) shows the absolute values of the signals as measured by lock-in technique in the experiments shown below.*

coefficient H_n

$$H_n = \frac{\Omega}{\pi} \int_0^{2\pi/\Omega} f(h(t)) \cos(n\Omega t) \mathrm{d}t \ . \tag{5.49}$$

For modulation amplitudes small compared with the tip radius a ($h_1 \ll a$), the nth Fourier component is given by the nth derivate of f with respect to the distance h [Hil01a], corresponding to the nth coefficient of a Taylor expansion.

Figure 5.11a shows the higher-harmonic signals as functions of the tip-sample distance h for a nonresonant spherical tip next to a resonantly excited sample with $\varepsilon_s = -4$ (see section 6.3). The 0th order is positive for all h and has a maximum at $h_{max} \cong 0.8a$. The 1st harmonic, corresponding to the derivate of the 0th-order signal is positive for $h < h_{max}$, crosses zero at $h \cong h_{max}$, and is negative for $h > h_{max}$. This harmonic shows two extrema, a positive maximum and a negative minimum. Accordingly, the 2nd harmonic, reflecting the derivate of the 1th harmonic, shows 3 extrema, the 3rd harmonic has 4 extrema, and so on. The corresponding functions are plotted in figure 5.11a. The signal decreases dramatically with increasing order. For easier comparison, we have depicted the nth harmonic multiplied with the factor 10^{3n}. Figure 5.11b shows the absolute values of the higher-harmonic signals which are the quantities measured by lock-in technique in the experiment. When demodulating the signal at $n\Omega$, we only have two possible phases - reflecting the sign of the
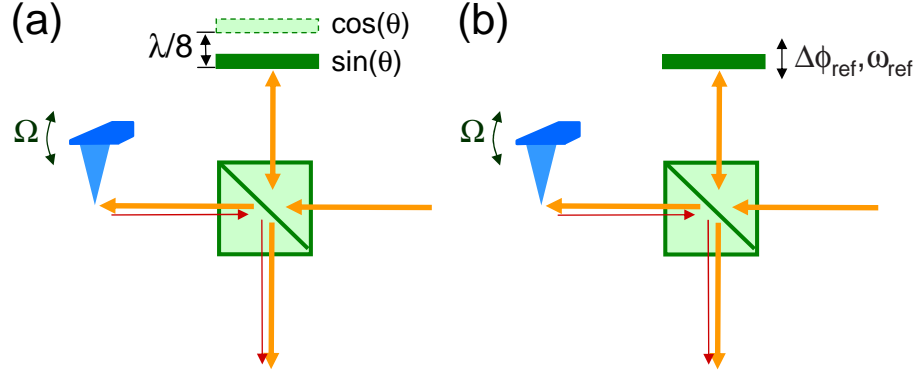
Figure 5.12: *Sketch of homodyne interferometric detection showing (a) a static method and (b) a dynamic method to separate optical amplitude and phase.*

corresponding higher harmonic. Usually in the experiments, we collect the amplitude of the harmonics and measure the corresponding phase only for completeness.

The calculations of higher harmonics, as shown here for direct detection, can easily be extended to any arbitrary signal f, as long as we can determine the distance dependence of the measured quantity. In the following parts we will discuss the methods of homodyne and heterodyne interferometric detection.

5.3.3   Homodyne Interferometric Detection

For homodyne interferometric detection, we make the scattered wave interfere with a reference wave having a fixed phase correlation to the incident laser light. A beam splitter is used to split the laser beam into a reference beam and the beam illuminating the tip. The same beam splitter recombines the scattered light and the reference wave on the detector. This setup corresponds to a Michelson interferometer with the s-SNOM replacing the mirror in one of the branches of the interferometer (see figure 5.12a). The total power as measured by the detector is given by[3] [Fow89]

$$f_{hom} = |\mathbf{E_{sca}} + \mathbf{E_{ref}}|^2 = |\mathbf{E_{sca}}|^2 + |\mathbf{E_{ref}}|^2 + 2\,|\mathbf{E_{sca}}|\,|\mathbf{E_{ref}}|\cos\theta_{hom} \qquad (5.50)$$

with $\mathbf{E_{sca}}$ the electric-field vector of the scattered light (see eq. 5.1),
         $\mathbf{E_{ref}}$ the electric-field vector of the reference beam,

and the phase difference θ_{hom} between the scattered light and the reference beam

$$\theta_{hom} = \phi_{ref} - \phi_{sca} \qquad (5.51)$$

with ϕ_{ref} the phase of the reference beam and
         ϕ_{sca} the phase of the scattered light.

---

[3]Please note that, for simplicity, we assume $\mathbf{E_{sca}}\|\mathbf{E_{ref}}$.

The phase of the reference beam is fixed with respect to the phase of the incident light, while the phase of the scattered light might be changed by the scattering process as well as the near-field interaction.

In comparison with direct detection, the detected power has increased by the power of the reference beam $I_{ref} = |\mathbf{E_{ref}}|^2$, and additionally we measure an interference term which includes contributions of both reference beam and scattered light. This interference term is proportional to the quantity of interest $|\mathbf{E_{sca}}|$ multiplied by a constant factor being twice the reference beam amplitude $|\mathbf{E_{ref}}|$. Also, the interference term is sensitive to the phase between the two beams. Thus, changes of the detected signal can result from either an amplitude or a phase change of the scattered wave.

In order to separate amplitude and phase of the near-field signal, usually heterodyne interferometry is used, as described in the next subsection. In principle, it is also possible to separate the optical amplitude and phase by means of homodyne interferometry. Taubner *et al.* [Tau04b], for example, measure the homodyne signal (eq. 5.50) twice for each point on the sample surface, first at an arbitrary mirror position and then at a position shifted by $\lambda/8$, which corresponds to a phase shift of $\Delta\phi_{ref} = \pi/2$ (see figure 5.12a). The corresponding data f_1 and f_2 are proportional to $\cos(\theta)$ and to $\sin(\theta)$, respectively. After substraction of the offset $I_0 = |\mathbf{E_{sca}}|^2 + |\mathbf{E_{ref}}|^2$, the equations for the optical amplitude and phase measured with this method are given by

$$A_{hom} = \quad \sqrt{(f_1 - I_0)^2 + (f_2 - I_0)^2} \quad = 2\,|\mathbf{E_{sca}}|\,|\mathbf{E_{ref}}| \ , \ \text{and} \qquad (5.52)$$

$$\phi_{hom} = \quad \arctan\frac{f_2 - I_0}{f_1 - I_0} \quad = \phi_{ref} - \phi_{sca} \ . \qquad (5.53)$$

This method works correctly only if the offset I_0 is chosen properly. Furthermore, every data point has to be measured twice, which leads to a longer aquisition time and hence to a decreased signal-to-noise ratio because of stability problems.

Separating the optical amplitude and phase in a homodyne interferometric setup is also possible by vibrating the reference mirror at a certain frequency ω_{ref}. This oscillation causes a well-defined modulation of the reference phase ϕ_{ref}

$$\phi_{ref} = \phi_{ref,0} + \Delta\phi_{ref}\cos\left(\omega_{ref}t\right) \qquad (5.54)$$

Two different methods using such a phase-modulated homodyne interferometer have been reported in the literature: In the first method, the mirror oscillates with a large amplitude, which generates a whole spectrum of interference terms. By demodulating these terms by lock-in technique the optical amplitude and phase can be calculated [Oce06]. In the second method, a rather small mirror oscillation amplitude is used together with an additional controller that keeps the average phase shift between reference beam and scattered beam constant by displacing the reference mirror. With this method the optical amplitude and phase can be measured directly [Ceb06]. Both methods allow the separation of amplitude and phase. They are in principle applicable for arbitrary wavelengths, but are quite complex in comparison to the heterodyne interferometer described in the following.
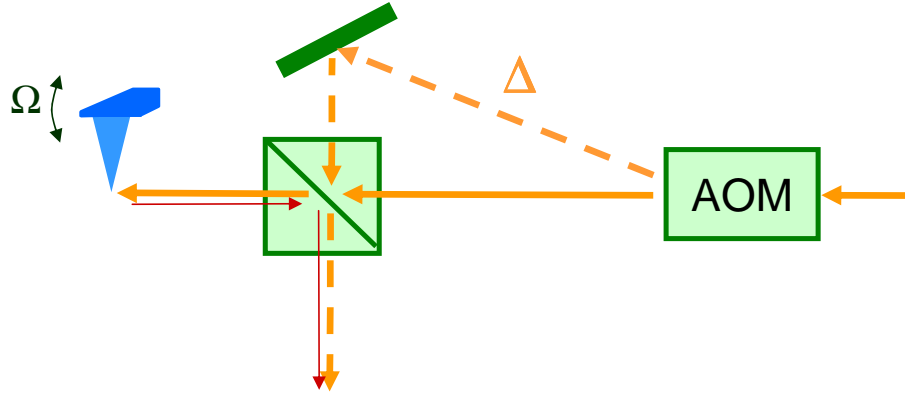
Figure 5.13: *Sketch of heterodyne interferometric detection including a frequency shift Δ of the reference beam (dashed lines) by an AOM, scattering at an AFM tip oscillating at the frequency Ω and interference after the beam splitter cube.*

5.3.4   Heterodyne Interferometric Detection

For heterodyne interferometric detection as used in our setup at visible wavelengths, the measured quantity is again the interference term between the scattered wave and a reference wave. In contrast to homodyne interferometric detection, the two interfering beams have slightly different frequencies, which allows us to directly separate amplitude and phase of the scattered light. Also, the method improves the signal-to-noise ratio by transforming the signal to a higher frequency.

For heterodyne detection part of the incident beam is frequency shifted to act as the reference beam which is superimposed on the scattered light (see figure 5.13). The measured signal f_{het} includes the interference between the fields of the reference beam $\mathbf{E}_{ref}$ and of the scattered light $\mathbf{E}_{sca}$:[4]

$$f_{het} = |\mathbf{E}_{ref}|^2 + |\mathbf{E}_{sca}|^2 + 2\,|\mathbf{E_{ref}}|\,|\mathbf{E_{sca}}|\cos\theta_{het} \; , \qquad (5.55)$$

where the phase relation between the two fields θ_{het} is given by

$$\theta_{het} = \Delta \cdot t + \phi_{ref} - \phi_{sca} \qquad (5.56)$$

with Δ the frequency shift of the reference beam and
         t the time.

Due to the different frequencies of the two beams, the interference term is a beating signal. This beating signal can be demodulated by a lock-in amplifier, which allows us to measure its phase as well as its amplitude:

$$\begin{aligned} A_{het} &= 2\,|\mathbf{E_{ref}}|\,|\mathbf{E_{sca}}| \;\; \text{and} \\ \phi_{het} &= \phi_{ref} - \phi_{sca} \; . \end{aligned} \qquad (5.57)$$

---

[4]Please note that, for simplicity, we assume $\mathbf{E_{sca}}\|\mathbf{E_{ref}}$.

Hence, this detection scheme is able to disentangle the phase ϕ_{sca} and the amplitude $|\mathbf{E_{sca}}|$ of the scattered wave. Similarly to homodyne detection, the reference amplitude enters the signal as a factor, so we may increase the signal by using a more intense reference beam. At the same time, the method of heterodyne interferometric detection has several advantages over homodyne detection: The signal amplitude does not depend on the absolute reference mirror position. Unlike in phase-modulated homodyne detection, no additional controller is needed to control the reference phase. Moreover the beating shifts the signal to higher frequencies. If we use an acousto-optical modulator (AOM) to shift the frequency of the reference beam, we can typically achieve $\Delta \simeq 80$ MHz. In this regime, there is almost no mechanically or electronically induced noise. We thus expect a much higher signal-to-noise ratio.

5.4   Summary

In this chapter we have described the theory of s-SNOM of isotropic samples, using the well-known electrostatic dipole model. We assume the AFM tip to be small compared with the wavelength. For a given tip polarizability we can calculate scattering parameters such as the vector scattering amplitude and the scattering cross section. The shape and material of the tip determine its polarizability and lead to a certain polarization dependence of the scattered signal.

The method of image charges is used to include the interaction between tip and sample in the model. The sample distorts the electric field of the tip and decreases the symmetry of the system. The tip-sample interaction enhances the scattering, when the tip is brought close to the sample surface. We expect a material contrast in the s-SNOM signal between isotropic sample materials with different dielectric constants.

We have theoretically described different detection methods that are commonly used in s-SNOM, such as direct detection, homodyne interferometric detection, and heterodyne interferometric detection. We found that with interferometric detection it is possible to separate the optical amplitude from the phase of the scattering signal, while direct detection yields only the amplitude. For all detection methods we can use the method of higher-harmonic demodulation to suppress far-field signals, thereby gaining access to the pure near-field signal.

6   Anisotropic Samples in s-SNOM

In chapter 5 we discussed the theoretical description of scattering scanning near-field optical microscopy of isotropic samples. The scattering by the tip is described by the electrostatic limit of the Mie theory, being basically Rayleigh scattering, while the near-field interaction between the scattering tip and the isotropic sample is described by the electrostatic dipole model. This model is well established for isotropic samples.

In this chapter we extend the model to anisotropic samples, e.g. ferroelectric materials. We are interested in the optical contrast induced by the anisotropy of the sample. In ferroelectric materials a contrast can arise between ferroelectric domains in which one and the same dielectric tensor is oriented differently.

The anisotropy of the sample disturbs the symmetry of the system. This can be described by a modified image dipole. Moreover, the reflection at the surface of an anisotropic sample depends strongly on the orientation of the dielectric tensor. As the reflected light contributes to the electric field at the position of the tip (see section 5.2), this reflection strongly influences the optical signal. How to include these modifications in the dipole model is described in section 6.1. In section 6.2, the possible optical contrast between regions in a uniaxial sample differing by the orientation of the dielectric tensor is discussed for selected tip shapes. In order to enhance this anisotropy contrast, the coupled tip-sample system may be excited close to its resonances. These resonances can be induced by resonant excitation of either the tip or the sample. We calculate the scattering occurring when a gold tip is excited at its plasmon resonance in the visible wavelength regime or when a sample is excited close to a phonon resonance in the IR. Finally we discuss the two samples used in our experimental work, $LiNbO_3$ and $BaTiO_3$, both showing multiple phonon resonances in the IR regime. Close to these phonon resonances the scattering cross section as well as the optical contrast between different domains are strongly enhanced (see section 6.3).

6.1   Anisotropic Samples in s-SNOM

In this section we extend the known dipole model to anisotropic samples. We introduce the corresponding method of image charges, the extended dipole interaction, as well as the modified Fresnel formulae describing the reflection at anisotropic samples.

6.1.1   Method of Image Charges for Anisotropic Samples

In section 5.1 we calculated the distorted field of the scatterer close to an isotropic sample by introducing a dipole in the sample according to the well-known method of image charges. The image charge problem was solved for an anisotropic sample in 1996 when Ismo Lindell *et al.* presented first calculations for an anisotropic half-space slightly deviating from transverse isotropy [Lin96]. One year later, they reported that arbitrary anisotropic samples can be treated [Lin97] by introducing - in addition to the image point charge in the case of an isotropic sample [Jac83] - an image sheet charge in the sample accounting for the anisotropy. In this work, we restrict ourselves to samples having a diagonal dielectric tensor $\widehat{\varepsilon}_s$ with one principal axis being perpendicular to the sample surface

$$\widehat{\varepsilon}_s = \begin{pmatrix} \varepsilon_x & 0 & 0 \\ 0 & \varepsilon_y & 0 \\ 0 & 0 & \varepsilon_z \end{pmatrix} . \tag{6.1}$$

For the electrostatic calculations of Lindell, the elements ε_j $(j = x, y, z)$ are assumed to be real and nonnegative numbers. Without restriction, the x axis is the direction of the largest dielectric constant within the surface plane $(\varepsilon_x \geq \varepsilon_y)$.

For an anisotropic sample the image charge of a point charge situated at $z = h$ above the surface is the superposition of a point charge q' at $z = -h$ and a sheet charge distribution σ (see figure 6.1a). Similarly to the isotropic case, the point charge is given by

$$q' = \beta q \tag{6.2}$$

with q the charge outside of the sample at $z = h$ and
        β the response function of the sample.

For an anisotropic sample the response function is given by

$$\beta = \frac{\sqrt{\varepsilon_z \varepsilon_y} - 1}{\sqrt{\varepsilon_z \varepsilon_y} + 1} . \tag{6.3}$$

The sheet charge fills an angular sector in the xz plane below the position of the image point charge, $z = -h$, (see figure 6.1a) with an opening angle τ, which depends on the degree of anisotropy parallel to the sample surface:

$$\tau = \arctan \sqrt{\frac{\varepsilon_x - \varepsilon_y}{\varepsilon_y}} . \tag{6.4}$$

The sheet charge is given by [Lin97]

$$\begin{aligned}
\sigma \quad &= -q \quad \frac{2\sqrt{\varepsilon_z}(\varepsilon_x - \varepsilon_y)|z+h|}{\pi\sqrt{(\varepsilon_x - \varepsilon_y)(z-h)^2 - \varepsilon_y x^2}} \frac{\varepsilon_z[(\varepsilon_x - \varepsilon_y)(z+h)^2 - \varepsilon_y x^2] - x^2}{(\varepsilon_z[(\varepsilon_x - \varepsilon_y)(z+h)^2 - \varepsilon_y x^2] + x^2)^2} \\
&\quad \cdot \delta[y]\theta[(\varepsilon_x - \varepsilon_y)(z+h)^2 - \varepsilon_y x^2]\theta[-(z+h)] \quad .
\end{aligned} \tag{6.5}$$
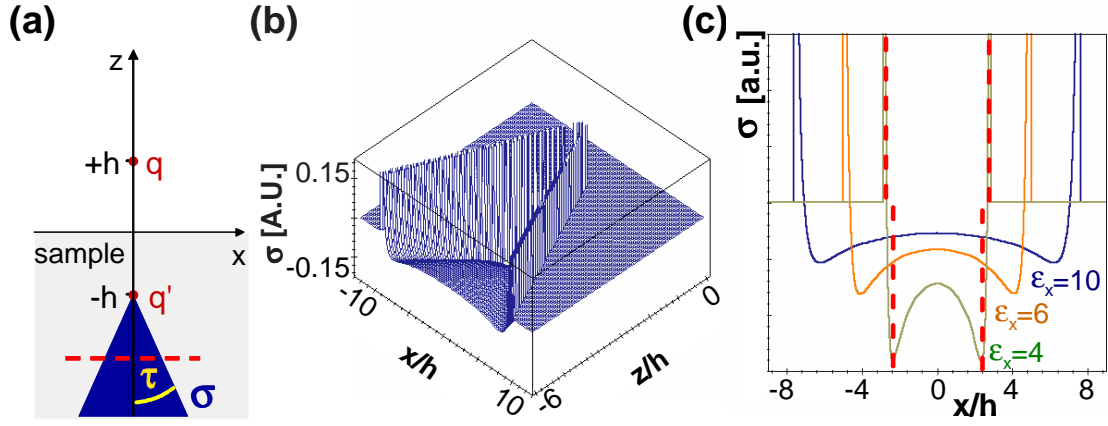
Figure 6.1: *(a) Schematic figure of a point charge q and its image charge distribution consisting of a point charge q' and a two-dimensional charge distribution σ [Lin97]; (b) sheet charge distribution for $\varepsilon_x = 10$, $\varepsilon_y = 3$, $\varepsilon_z = 2$; the half angle of the sector is $\tau = 57°$. (c) Profile of the sheet charge distribution at $z = -2h$ [see dashed line in (a)] for $\varepsilon_y = 3$ and $\varepsilon_z = 2$ and for different values of ε_x. As ε_x comes closer to ε_y the sheet charge distribution becomes narrower and more and more resembles a quadrifilar line charge as indicated by the dashed lines in (c).*

with $\quad\delta(x)\quad$ the delta function and
$\qquad\theta(x)\quad$ the Heaviside step function $\theta(x) = \int_{-\infty}^{x} \delta(t)\mathrm{d}t$.

Figure 6.1b shows the sheet charge as a function of the xz position for a sample with $\varepsilon_x = 10$, $\varepsilon_y = 3$, and $\varepsilon_z = 2$, and hence with a half angle $\tau = 57°$. At the borders of the sector, the sheet charge is positive, while in the center it is negative. At any distance z from the sample surface the integral of σ across x is 0. For a sample being isotropic in the plane parallel to the sample surface ($\varepsilon_x = \varepsilon_y$) the sheet charge vanishes ($\sigma = 0$).

In order to determine the interaction between the tip and the sample in the dipole model, we need to calculate the field of the image dipole at the position of the tip dipole. The field of the image charge distribution σ is given by [Jac83]

$$E_\sigma(\mathbf{r}) = \frac{1}{4\pi\varepsilon_0} \int \sigma(\mathbf{r}') \frac{\mathbf{r} - \mathbf{r}'}{|\mathbf{r} - \mathbf{r}'|^3} d^3\mathbf{r}' \ . \qquad (6.6)$$

In general, this integral is not solvable for anisotropic samples, but it may be solved for samples showing weak anisotropy with

$$\tau \cong \tan\tau \cong \sqrt{\frac{\varepsilon_x - \varepsilon_y}{\varepsilon_y}} \ll 1 \ . \qquad (6.7)$$

In this case the sheet charge reduces to a quadrifilar line charge σ' described by

$$\sigma \to \sigma' = -2q\eta(z + h)\partial_x^2 \delta[x]\,\delta[y]\,\theta[-(z + h)] \qquad (6.8)$$

with the anisotropy response function

$$\eta = \frac{\sqrt{\varepsilon_z \varepsilon_y} \cdot (\varepsilon_x - \varepsilon_y)}{2\varepsilon_y \cdot \left(\sqrt{\varepsilon_z \varepsilon_y} + 1\right)^2} \; . \tag{6.9}$$

Figure 6.1c illustrates the structure of the line charge. We plot a cross section of the sheet charge at $z = -2h$ for several sets of dielectric constants. For small in-plane anisotropy the angle τ decreases and the sheet charge becomes narrower until only 4 line charges are left as indicated by the dashed lines. The typical structure of the sheet charge is reflected by the four line charges being positive, negative, negative, and positive with equal absolute values. Mathematically, the lines are described by the second derivation of the delta function $\partial_x^2 \delta[x]$. The δ function in y and the Heaviside function $\theta(-(z+h))$ limit the charges to $y = 0$ and $z \leq -h$, respectively. Away from $z = -h$ the absolute value of the four line charges increases linearly along the z axis.

From the point of view of symmetry, a point charge next to an isotropic sample generates circular lines of equal potential on the sample surface. The system is of cylindrical symmetry and the electric field can be described by adding an image point charge. For a sample being anisotropic in the plane parallel to the sample surface, these circular lines are distorted to ellipses with the major axis in the direction of the larger dielectric constant. The sheet charge or - in the case of weak anisotropy - the quadrifilar line charge generates this distortion of the equipotential lines.

In the following section we apply this method of image charges for anisotropic samples to the dipole model.

6.1.2   Dipole Model for Anisotropic Samples

On the basis of the above-described method of image charges we can extend the dipole model to anisotropic samples. We assume the anisotropy of the sample to be small (eq. 6.7) so that equation 6.8 applies.

As in section 5.2 we assume the tip dipole to be a point dipole induced by an external electric field. The electric field of the tip dipole in the presence of an anisotropic sample is given by the superposition of the fields of the tip dipole and of the image charge distribution in the sample. At distances r large compared with the distance h between tip and sample, the total electric field is the field of the total tip-sample dipole $\mathbf{P_{tot}}$ given by (see eq: 5.29)

$$\mathbf{P_{tot}} = \widehat{\alpha}_{tot} \varepsilon_0 \mathbf{E_0} \tag{6.10}$$

with

$$\widehat{\alpha}_{tot} = \left(\widehat{I} + \beta \widehat{C}\right) \cdot \widehat{\alpha}'_t \tag{6.11}$$

and

$$\widehat{\alpha}'_t = (\widehat{I} - \varepsilon_0 \widehat{\alpha}_t \widehat{K})^{-1} \widehat{\alpha}_t \; . \tag{6.12}$$
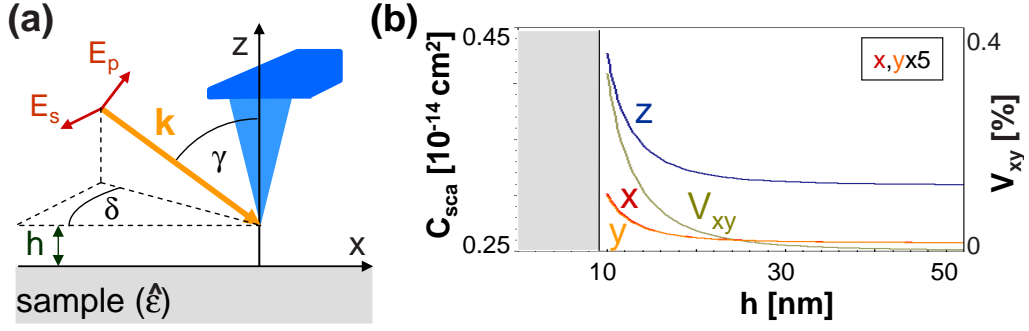
Figure 6.2: *(a) Sketch of the tip-sample system for anisotropic samples. In addition to the isotropic case, we define the angle δ between the plane of incidence and the x axis. The x axis is defined as the principal axis with the larger in-plane dielectric constant of the sample. (b) Distance dependence of the scattering cross section of a gold sphere ($a = 10$ nm) next to an anisotropic sample ($\varepsilon_x = 3.5$, $\varepsilon_y = 3$, $\varepsilon_z = 2$) for different orientations of the tip dipole with respect to the sample surface. For better comparability the two scattering cross sections for orientation of the tip dipole along the directions x or y are multiplied by a factor of 5. In order to stress the difference between these two components, their mutual visibility V_{xy} is plotted additionally.*

For an anisotropic sample the response function β of the sample is given by equation 6.3 and the interaction matrix $\widehat{K}$ is modified by the anisotropy response function η:

$$\widehat{K} = \frac{1}{64\pi\varepsilon_0 h^3} \begin{pmatrix} 2\beta + 3\eta & 0 & 0 \\ 0 & 2\beta + \eta & 0 \\ 0 & 0 & 4\beta + 4\eta \end{pmatrix}. \qquad (6.13)$$

Note that the image sheet charge, which is characterized by the anisotropy response function η, modifies the tip dipole via α'_t, but does not contribute to the dipole moment of the sample. This is because the symmetry of the sheet charge makes its dipole moment vanish so that it does not contribute directly to the radiated field.

The tip-sample system for anisotropic samples is no longer of cylindrical symmetry. This is reflected by the polarizability of the system having different x and y components. Hence, in order to describe the system for anisotropic samples, we define an additional angle δ, which is the azimuthal angle between the incident plane and the x axis, which we have defined as the direction with the largest in-plane dielectric constant of the sample (see figure 6.2a).

In figure 6.2b the scattering cross sections are plotted as functions of the distance h for three possible orientations of the tip dipole along the x, y, or z axis above an anisotropic sample with $\varepsilon_x = 3.5$, $\varepsilon_y = 3$, and $\varepsilon_z = 2$. As for isotropic samples, the scattering is much stronger when the tip dipole is along the z axis than when it is parallel to the surface. In figure 6.2 the scattering cross sections for the latter case have been multiplied by five for better legibility. The difference between the x and

the y directions is depicted as the visibility $V_{xy} = (C_{sca,x} - C_{sca,y})/(C_{sca,x} + C_{sca,y})$, which turns out to be smaller than 0.4 %. The difference may be increased by selected tip shapes (see section 6.2) or by resonant excitation of the sample (see section 6.3).

All the samples examined experimentally in this work are optically uniaxial with only a few possible orientations of the optical axis (see chapter 3). In the following we discuss the simplifications of the model that apply to these specific samples.

6.1.3   Uniaxial Anisotropic Samples

For optically uniaxial crystals the dielectric tensor $\widehat{\varepsilon}_s$ is diagonal with two identical elements ε_a perpendicular to the optical axis and a different element ε_c along the optical axis (c axis). As our calculations above are restricted to a diagonal dielectric tensor with one axis perpendicular to the sample surface, there are two possible orientations of the optical axis: either perpendicular (c domain) or parallel (a domain) to the sample surface. The corresponding dielectric tensors $\widehat{\varepsilon}_s^a$ and $\widehat{\varepsilon}_s^c$ in the xyz coordinate system read

$$\widehat{\varepsilon}_s^a = \begin{pmatrix} \varepsilon_a & 0 & 0 \\ 0 & \varepsilon_c & 0 \\ 0 & 0 & \varepsilon_a \end{pmatrix}, \ \widehat{\varepsilon}_s^c = \begin{pmatrix} \varepsilon_a & 0 & 0 \\ 0 & \varepsilon_a & 0 \\ 0 & 0 & \varepsilon_c \end{pmatrix} . \tag{6.14}$$

In ferroelectric samples we call regions having these orientations of the dielectric tensor a domains and c domains (see section 3.2).

In c domains the sample is isotropic within the surface plane and thus of cylindrical symmetry. This results in

$$\eta_c = 0 \tag{6.15}$$

as in the isotropic case, while the factor β becomes

$$\beta_c = \frac{\sqrt{\varepsilon_a \varepsilon_c} - 1}{\sqrt{\varepsilon_a \varepsilon_c} + 1} . \tag{6.16}$$

The situation is very similar to that of an isotropic sample. Clearly, the symmetry of the tip-sample system on a c domain is cylindrical and thus the scattering cross section does not depend on the azimuthal angle δ.

On the other hand, for an a domain with $\varepsilon_a > \varepsilon_c$ the optical axis coincides with the y axis according to the convention that the x axis is the axis with the largest dielectric constant in the surface plane. The anisotropy factor is given by

$$\eta_a = \frac{\sqrt{\varepsilon_a \varepsilon_c}(\varepsilon_a - \varepsilon_c)}{2\varepsilon_c(\sqrt{\varepsilon_a \varepsilon_c} + 1)^2} , \tag{6.17}$$

whereas β remains unchanged:

$$\beta_a = \beta_c = \frac{\sqrt{\varepsilon_a \varepsilon_c} - 1}{\sqrt{\varepsilon_a \varepsilon_c} + 1} . \tag{6.18}$$
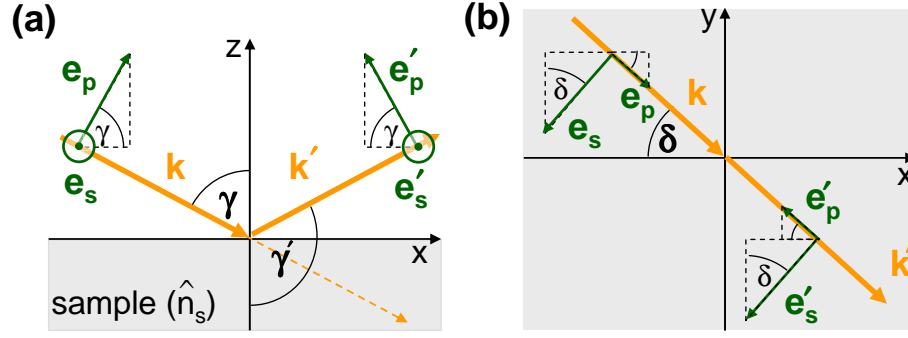
Figure 6.3: *Definition of the unit vectors* $\mathbf{e_s}$ *and* $\mathbf{e_p}$ *for the incident beam and the beam reflected on the anisotropic sample surface (marked with dash) (a) Side view, projection on the plane of incidence and (b) top view, projection on the sample surface.*

On an *a* domain, the cylindrical symmetry of the system is lost and the scattering cross section depends on the angle δ between the plane of incidence and the x axis.

In the following we discuss the reflection at an anisotropic sample, which shows a strong dependence on the orientation of the dielectric tensor.

6.1.4   Reflection at Anisotropic Samples

Unlike in the case of an isotropic sample, reflection at the surface of an anisotropic sample leads to partial transformation of p into s polarization and vice versa. Mathematically this can be expressed by introducing mixed reflection coefficients r_{sp} and r_{ps} in addition to the Fresnel coefficients r_s and r_p. The field reflected by an anisotropic sample is thus given by

$$\mathbf{E_{refl}} = (r_{ss}E_s + r_{sp}E_p)\mathbf{e_s} + (r_{pp}E_p + r_{ps}E_s)\widehat{C}\mathbf{e_p} \ , \tag{6.19}$$

with E_s and E_p being the s and p components of the incident electric-field vector, defined as the components along the directions given by the unit vectors (see figure 6.3

$$\mathbf{e_p} = \begin{pmatrix} \cos\delta\cos\gamma \\ -\sin\delta\cos\gamma \\ \sin\gamma \end{pmatrix} \quad \text{and} \quad \mathbf{e_s} = \begin{pmatrix} -\sin\delta \\ -\cos\delta \\ 0 \end{pmatrix} . \tag{6.20}$$

In 1928 Szivessy calculated these coefficients for arbitrary anisotropy [Szi28][1]. The derivation for the most general and for the special case of uniaxial anisotropy is reported in appendix A. The results for a *c* domain and for two specific orientations of an *a* domain are discussed here.

---

[1]For reflection at a sample showing weak anisotropy, see also the work of Grafström [Gra06].
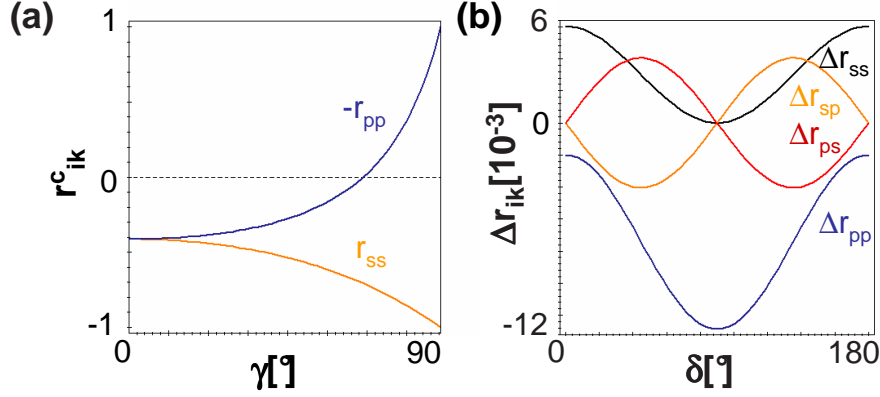
Figure 6.4: *Fresnel coefficients r_{ik} of anisotropic BaTiO$_3$. (a) $(-r_{pp}^c)$ and r_{ss}^c of a c domain as functions of the incident angle γ ($r_{sp}^c = r_{ps}^c = 0$). (b) Differences of the Fresnel coefficients between an a and a c domain for $\gamma = 70°$ as functions of the azimuthal angle δ. The variation with δ is due to the a domain, since on the c domain, the coefficients are constant: $r_{pp}^c = -0.053$, $r_{ss}^c = -0.733$, and $r_{ps}^c = r_{sp}^c = 0$. The small negative value of r_{pp} indicates that γ is slightly above Brewster's angle.*

For a *c* domain the reflection coefficients are given by

$$
\begin{aligned}
r_{pp}^c &= \frac{n_a n_c \cos(\gamma) - n_m \sqrt{n_c^2 - n_m^2 \sin^2(\gamma)}}{n_a n_c \cos(\gamma) + n_m \sqrt{n_c^2 - n_m^2 \sin^2(\gamma)}} \\
r_{ss}^c &= \frac{n_m \cos(\gamma) - \sqrt{n_a^2 - n_m^2 \sin^2(\gamma)}}{n_m \cos(\gamma) + \sqrt{n_a^2 - n_m^2 \sin^2(\gamma)}} \\
r_{sp}^c &= r_{ps}^c = 0
\end{aligned}
\tag{6.21}
$$

with $n_a = \sqrt{\varepsilon_a}$, $n_c = \sqrt{\varepsilon_c}$ the indices of refraction of the *a* and the *c* direction of the crystal and $n_m = \sqrt{\varepsilon_m}$ the index of refraction of the surrounding medium. As the *c* domain is of cylindrical symmetry, the coefficients r_{ik}^c do not depend on the azimuthal angle δ. In figure 6.4a their dependence on the incident angle γ is plotted for a *c* domain of BaTiO$_3$ ($n_a = 2.36$, $n_c = 2.412$ at $\lambda = 633$ nm [Zgo94]). For easier comparison with textbooks, we have plotted $(-r_{pp})$. The different sign in our calculation is caused by the different definition of $\widehat{C}$ in equation 6.19 as compared to Szivessy. For $\gamma = 0°$ both coefficients have the same value of $(1-n_a)/(1+n_a) \cong -0.4$. With increasing γ $-r_{pp}$ increases, crossing zero at Brewster's angle [Fow89] of about $70°$ and rising further until reaching 1 at $\gamma = 90°$. On the other hand, r_{ss} decreases with increasing γ, reaching -1 at $\gamma = 90°$. The behavior of the reflection coefficients of a *c* domain is very similar to that found for an isotropic material. As r_{sp} and r_{ps} are zero, there is no transformation of *p* into *s* polarization or vice versa.

For an *a* domain the reflection coefficients are much more complex as they depend additionally on δ. For an *a* domain with the optical axis perpendicular to the plane

of incidence, corresponding to $\delta = 0°$, the coefficients are given by

$$
\begin{aligned}
r_{pp}^{a,0} &= \frac{n_a^2 \cos(\gamma) - n_m \sqrt{n_a^2 - n_m^2 \sin^2(\gamma)}}{n_a^2 \cos(\gamma) + n_m \sqrt{n_a^2 - n_m^2 \sin^2(\gamma)}} \\
r_{ss}^{a,0} &= \frac{n_m \cos(\gamma) - \sqrt{n_c^2 - n_m^2 \sin^2(\gamma)}}{n_m \cos(\gamma) + \sqrt{n_c^2 - n_m^2 \sin^2(\gamma)}} \\
r_{sp}^{a,0} &= r_{ps}^{a,0} = 0 \; .
\end{aligned}
\tag{6.22}
$$

while for $\delta = 90°$ they are

$$
\begin{aligned}
r_{pp}^{a,90} &= \frac{n_a n_c \cos(\gamma) - n_m m \sqrt{n_a^2 - n_m^2 \sin^2(\gamma)}}{n_a n_c \cos(\gamma) + n_m m \sqrt{n_a^2 - n_m^2 \sin^2(\gamma)}} \\
r_{ss}^{a,90} &= \frac{n_m \cos(\gamma) - \sqrt{n_a^2 - n_m^2 \sin^2(\gamma)}}{n_m \cos(\gamma) + \sqrt{n_a^2 - n_m^2 \sin^2(\gamma)}} \\
r_{sp}^{a,90} &= r_{ps}^{a,90} = 0 \; ,
\end{aligned}
\tag{6.23}
$$

with

$$
m = \left| \frac{n_a^2 n_c^2 - (n_a^2 - n_c^2) n_m^2 \sin(\gamma)^2}{n_a^2 n_c^2 + (n_a^2 - n_c^2) n_m^2 \sin(\gamma)^2} \right| \; .
\tag{6.24}
$$

In general, for an a domain, the mixed coefficients r_{sp}^a and r_{ps}^a have to be taken into account as functions of δ (see appendix A). For $\delta = 0°$ or $\delta = 90°$ they are both zero.

The differences of the Fresnel coefficients Δr_{ik} between an a and a c domain of BaTiO$_3$ are plotted in figure 6.4b for an incident angle of $\gamma = 70°$ as functions of the azimuthal angle δ. As the coefficients are constant on the c domain, the variation with δ is due to the a domain.

Knowing the reflection coefficients, we can calculate the external electric field at the position of the tip from he superposition of the electric-field vectors of the incident and of the reflected wave

$$
\begin{aligned}
\mathbf{E}_0 &= E_p \cdot \mathbf{e}_p + (r_{pp} E_p + r_{ps} E_s) \cdot \widehat{C} \cdot \mathbf{e}_p + \\
&\quad E_s \cdot \mathbf{e}_s + (r_{sp} E_p + r_{ss} E_s) \cdot \mathbf{e}_s.
\end{aligned}
\tag{6.25}
$$

The polarization of the external electric field at the position of the tip may be changed significantly by the reflection at the sample surface. This polarization change depends strongly on the orientation of the dielectric tensor of the sample. Hence, we expect an additional contrast due to the reflection. In the following section, we will discuss this influence on the contrast for different tip shapes for nonresonant excitation.

6.2 Optical Contrast Arising from Anisotropy

In this section we study the optical contrast between regions characterized by different orientations of the dielectric tensor of the sample for a nonresonant tip-sample
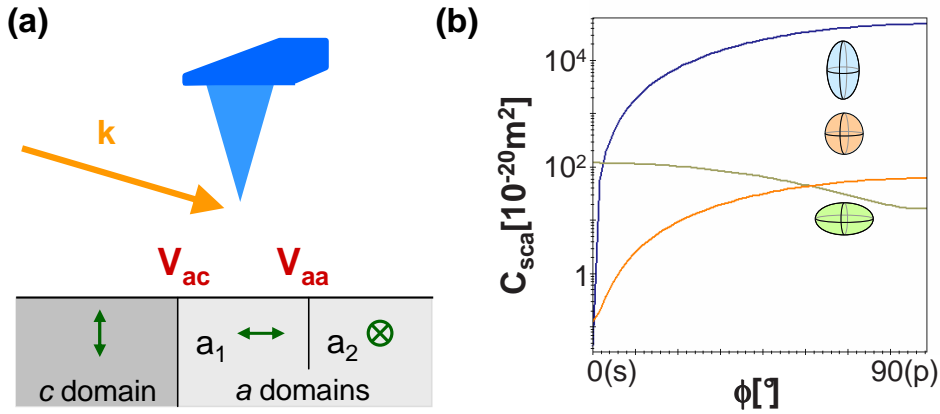
Figure 6.5: *(a) Sketch of the possible orientations of the optical axis of a uniaxial crystal, e.g. $BaTiO_3$ with three possible types of domains. For such a sample system we expect two different kinds of contrast: V_{ac} between different types of domains and V_{aa} between differently oriented a domains. (b) Scattering cross section as a function of the incident polarization φ for scatterers of different shape touching the surface of a c domain of $BaTiO_3$: sphere (red) with a radius of 10 nm, prolate ellipsoid (axis ratio 10:3) with the long axis normal to the sample surface (blue) or perpendicular to the plane of incidence (green). The prolate ellipsoids were adjusted in size to have the same volume as the sphere.*

system. As the anisotropic sample lowers the symmetry of the system, we expect the scattering to be highly sensitive to the polarization of the incident light as well as to the tip geometry. Therefore, we will not only discuss the contrast for a spherical tip, but also for a cigar-shaped tip with its major axis being oriented either parallel or perpendicularly to the sample surface.

In the following we assume the sample to be uniaxial with the optical axis either perpendicular or parallel to the sample surface (see section 6.1). In analogy to the possible domains in $BaTiO_3$ we consider – in addition to the *c* domain – two possible *a* domains with their optical axes at right angle to each other as sketched in figure 6.5a. For such a sample we expect a contrast V_{ac} between different types of domains as well as a contrast V_{aa} between differently oriented *a* domains (see figure 6.5a).

In the following we discuss the optical contrast between domains of ferroelectric $BaTiO_3$ for selected tip shapes as a function of the azimuthal angle δ and the polarization φ of the incident light. For all calculations we assume an incident angle $\gamma = 70°$, a wavelength $\lambda = 633$ nm, and a gold tip with radius $a = 10$ nm touching the sample surface $(h = a)$ [Sch05c].
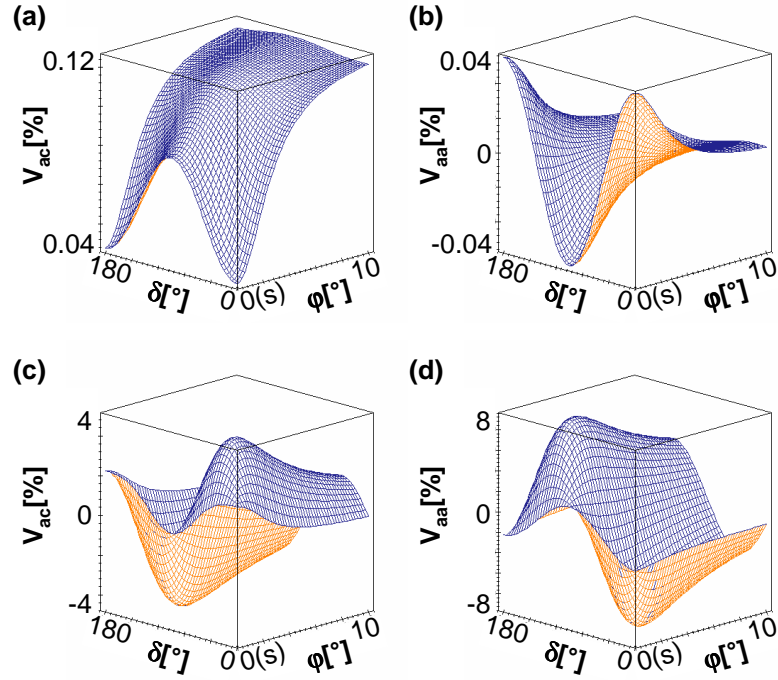
Figure 6.6: *Optical contrast between ferroelectric domains in BaTiO$_3$ probed with a gold sphere touching the surface: the contrast V_{ac} between an a and a c domain is illustrated in (a) and (c), while (b) and (d) depict the contrast V_{aa} between two a domains of different orientation. The contrast is shown as a function of the azimuthal angle δ and the polarization angle φ in the region close to s polarization. The two contributions to the contrast are displayed separately: the contrast caused by the probe-sample interaction is shown in (a) and (b), and the contribution due to the Fresnel coefficients is plotted in (c) and (d).*

6.2.1   Spherical Tip

First we discuss the contrasts between a and c domains (V_{ac}) as well as between differently oriented a domains (V_{aa}) for a spherical tip. In figure 6.6 these contrasts are plotted as functions of the polarization of the incident light and of the azimuthal angle δ. The two contributions to the contrast discussed in section 6.1 are displayed separately: The contrast caused by the probe-sample dipole interaction is shown in (a) and (b) and the contribution due to reflection at the sample surface is plotted in (c) and (d). As it needs only a small normal field component to make the perpendicular dipole dominate the scattering, a behavior similar to that observed for pure p polarization is obtained already at fairly small angles φ. Therefore, only a limited range of φ close to s polarization is displayed. Furthermore, reversing the sign of φ has the same effect as replacing δ by $180° - \delta$. Hence, we can restrict the discussion to positive φ.

The anisotropy causes only a small change in the tip-sample interaction such that the resulting contrast is no more than a fraction of a percent, far too small

to be measured. The domain-dependent Fresnel coefficients – which are depicted in figure 6.4b – on the other hand lead to a much more pronounced contrast of up to several percent. In all cases discussed in the following it is a general feature that the dipole interaction between tip and sample gives rise to negligible contrast only. Therefore, we concentrate on the discussion of the contribution stemming from the Fresnel coefficients. Nevertheless, for completeness the dipole contribution is included also in figures 6.7 and 6.8 as subfigures (a) and (b).

Let us first discuss the *ac* contrast V_{ac} depicted in figure 6.6c. For *s* polarization both the Fresnel coefficients r_{ss} and r_{ps} contribute. If the electric field points along the y axis ($\delta = 0°$, or equivalently $180°$), the dielectric constant sensed by the incident wave is ε_a on the *c* domain and ε_c on the *a* domain. This leads to a difference in r_{ss} causing an *ac* contrast of 2.2%. For $\delta = 90°$ any difference in reflectivity vanishes ($\Delta r_{ss} = \Delta r_{ps} = 0$) and so does the corresponding contrast. The coefficient r_{ps} is always zero on the *c* domain. On the *a* domain, this coefficient vanishes at $\delta = 0°$ and $90°$ but reaches a maximum positive or negative value at $\delta = 45°$ and $135°$, respectively. Here, part of the light is transformed to *p* polarization so that a dipole perpendicular to the surface arises. As such a dipole is more efficiently excited than a dipole parallel to the surface (see sections 5.2 and 6.1) this leads to stronger scattering on the *a* domain resulting in a small positive contribution to the *ac* contrast.

If now the polarization is rotated slightly so that the incident wave contains a *p*-polarized component, the influence of r_{ps} is such that the normal field component is enhanced around $\delta = 45°$, whereas it is reduced around $\delta = 135°$. This leads to an increase or decrease of the scattered power on the *a* domain, respectively, resulting in positive and negative extrema of the *ac* contrast of $\pm 4\%$ for a polarization angle $\varphi \approx 2°$. For larger angles φ outside the region displayed in Fig. 6.6(c), the contrast becomes more and more dominated by the difference in r_{pp} between the two domains, which is largest for $\delta = 90°$, where it gives rise to $V_{ac} = -1.4\%$ for pure *p* polarization. Unlike r_{ps}, the Fresnel coefficient r_{sp} – despite being equal to r_{ps} in absolute magnitude – has little impact on the contrast, as the resulting dipole parallel to the sample surface contributes only weakly to the scattering.

Concerning the *aa* contrast, we first note the general feature that replacing δ by $\delta + 90°$ simply interchanges the two domains and, hence, leads to sign reversal of V_{aa}. Again, the Fresnel coefficients represent the main source of contrast (see figure 6.6d). For pure *s* polarization, r_{ps} has no influence on V_{aa} since it is equally effective on both domains. The contrast is then most pronounced at $\delta = 0°$ and $90°$, where it amounts to $\pm 2.2\%$. However, as soon as the polarization deviates from $\varphi = 0°$, r_{ps} comes into play in a similar way as for V_{ac}, because its sign is different on the two domains. This again gives rise to extrema in the contrast close to *s* polarization, this time reaching a value of $\pm 8\%$. Pure *p* polarization provides a maximum contrast of $\pm 1.2\%$ for $\delta = 0°$ and $90°$ as a consequence of r_{pp}.
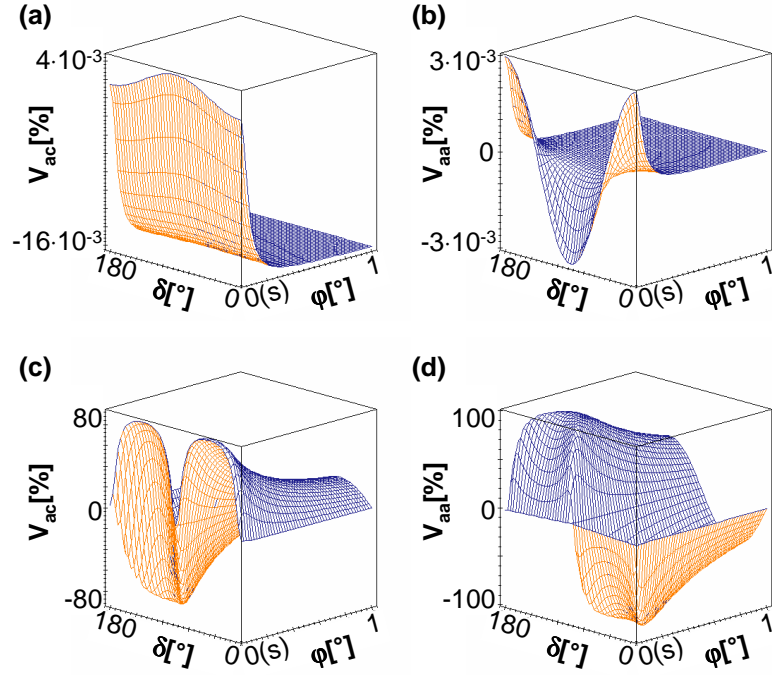
Figure 6.7: *Same as Fig. 6.6 but calculated for a prolate (cigar-shaped) scatterer in contact with the BaTiO₃ surface, having its long axis aligned with the surface normal. The axis ratio was set to 10:3.*

6.2.2   Ellipsoidal Tip

Real experiments commonly use a metal tip as the scatterer. The elongated geometry leads to larger polarizability along the tip axis than in the xy plane. To model such a situation we may replace the sphere by a prolate (cigar-shaped) ellipsoid having its long axis aligned with the sample normal. As an example we take a gold ellipsoid with an axis ratio of 10:3. In this case, the polarizability along the particle is more than 40 times larger than in the transverse direction [Boh98]. This strongly enhances the influence of r_{ps} on the contrast for φ close to s polarization. Here, both V_{ac} and V_{aa} are increased to almost $\pm 100\%$ around $\delta = 45°$ and $135°$ (see figures 6.7c and 6.7d). These extrema now move very close to $\varphi = 0°$. On the other hand, the behavior for pure p polarization is essentially the same as for the spherical probe.

As follows from the discussion above, one may gain in relative contrast (as expressed by V_{ac} and V_{aa}) by choosing φ close to s polarization. However, this benefit is obtained only at the expense of an extreme loss in absolute signal level, as indicated by the scattering cross section of the sphere and the prolate ellipsoid shown in Fig. 6.5(b) (red and blue curve, respectively). The two probes were assumed to have the same volume and to touch the surface of a c domain. For the sphere, the scattered power obtained with s polarization is two orders of magnitude smaller than with p polarization. For the cigar-shaped particle the difference is even five orders of magnitude. Therefore, one has to make a trade-off between signal strength and
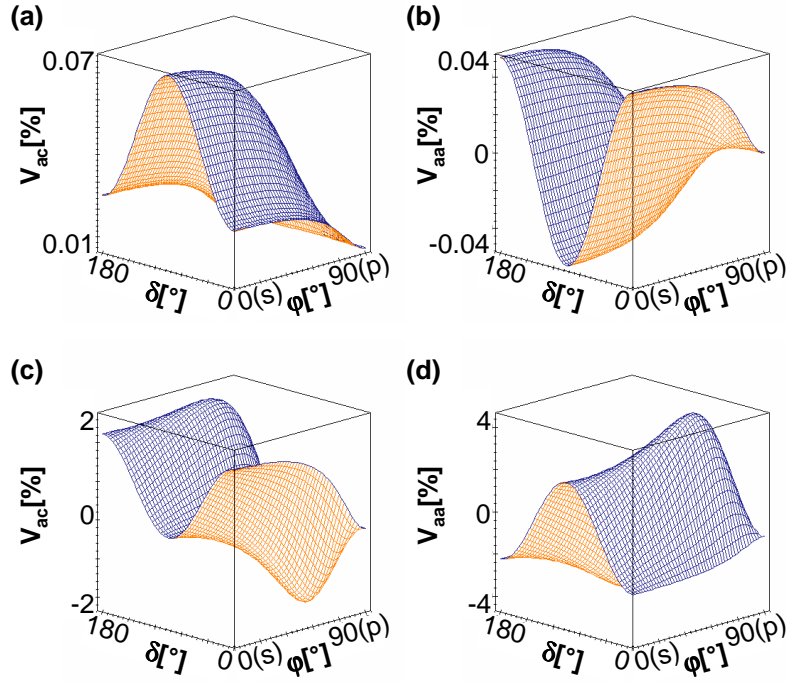
Figure 6.8:   *Same as Fig. 6.6 but for a prolate scatterer (axis ratio 10:3) in contact with the surface, with its long axis perpendicular to the plane of incidence. Note that in these plots the full range of polarization angle is displayed.*

contrast to find the optimal conditions providing the best signal-to-noise ratio.

If the prolate ellipsoid is aligned with its long axis perpendicular to the plane of incidence instead, excitation of the dipole parallel to the sample surface by the *s*-polarized component of the field is strongly promoted. This results in a much weaker dependence of the scattering cross section on polarization (see figure 6.5b, green curve). At the same time, the contrast V_{ac} and V_{aa} amounts to $\geq 2\%$ over a broad range of polarization angles if the azimuthal angle is chosen properly (figure 6.8c,d). In this case, r_{sp} plays a prominent role in that it produces maximum contrast of up to $\pm 4\%$ close to *p* polarization ($\delta \approx 80°$).

As illustrated in this chapter, in principle we can achieve a contrast of up to 100 % between differently oriented *a* domains and of 80 % between *a* and *c* domains even for off-resonant excitation. This contrast is only possible if we choose a proper tip shape and control the polarization as accurately as 0.1 °. However, the corresponding scattering cross sections are very small. Orientation of the tip ellipsoid with its major axis perpendicular to the plane of incidence causes a contrast of around 4 % with a scattering cross section of measurable size which is not that sensitive to the polarization of the incident light. Both results do not allow much variation of the parameters and are thus not very attractive for experimental examinations.

Another possibility to enhance both relevant quantities – scattering cross section and optical contrast – is to excite the tip-sample system close to its resonance, which will be discussed in the following section.

6.3 Resonant Tip-Sample System

The scattering cross section discussed for isotropic samples in chapter 5 and for anisotropic samples in section 6.1 represents the coupled tip-sample system. Both parts of the system, tip and sample, can be excited resonantly which leads to a resonance of the coupled system. For a typical metallic tip this resonance corresponds to the excitation of a surface plasmon in the tip at visible wavelengths. The sample excitation depends strongly on the sample material. The ferroelectric samples show a resonance corresponding to the excitation of a phonon in the IR regime.

First, the conditions for a resonant excitation of the tip-sample system will be discussed in general. Furthermore, we describe a tip-induced resonance for a metal tip. Finally, a sample-induced resonance is illustrated for an isotropic sample with a single phonon resonance in the IR as well as for the anisotropic ferroelectrics $LiNbO_3$ and $BaTiO_3$ showing multiple phonon resonances in the IR regime.

6.3.1 General Description

The scattering cross section C_{sca} depends on the tip polarizability ($\widehat{\alpha}_t$), the sample response (β and η), the distance h between tip and sample, and the wavelength λ. Under the assumption that the tip dipole is oriented perpendicularly to the sample surface (z direction), the scattering cross section is given by (see equations 5.31 and 6.10)

$$C_{sca}^z = \frac{k^4}{6\pi} \left| \frac{(1+\beta)\alpha_t}{1 - \frac{\alpha_t(\beta+\eta)}{16\pi h^3}} \right|^2 \tag{6.26}$$

with k the wave number, being $2\pi/\lambda$,

α_t the tip polarizability,

being $\alpha_t = 4\pi a^3 \frac{\varepsilon_t-1}{\varepsilon_t+2}$ for a spherical tip (radius a),

β the response function of the sample $\beta = \frac{\sqrt{\varepsilon_z\varepsilon_y}-1}{\sqrt{\varepsilon_z\varepsilon_y}+1}$,

η the anisotropy sample response function $\eta = \frac{\sqrt{\varepsilon_z\varepsilon_y}\cdot(\varepsilon_x-\varepsilon_y)}{2\varepsilon_y\cdot\left(\sqrt{\varepsilon_z\varepsilon_y}+1\right)^2}$, and

h the distance between tip and sample,

being typically in the order of a for near-field investigations.

This scattering cross section has a pole at

$$\alpha_t(\beta + \eta) = 16\pi h^3 \ . \tag{6.27}$$

If the tip dipole is parallel to the sample surface, we find analogous formulae for the poles, namely

$$\alpha_t(2\beta + 3\eta) = 64\pi h^3 \tag{6.28}$$
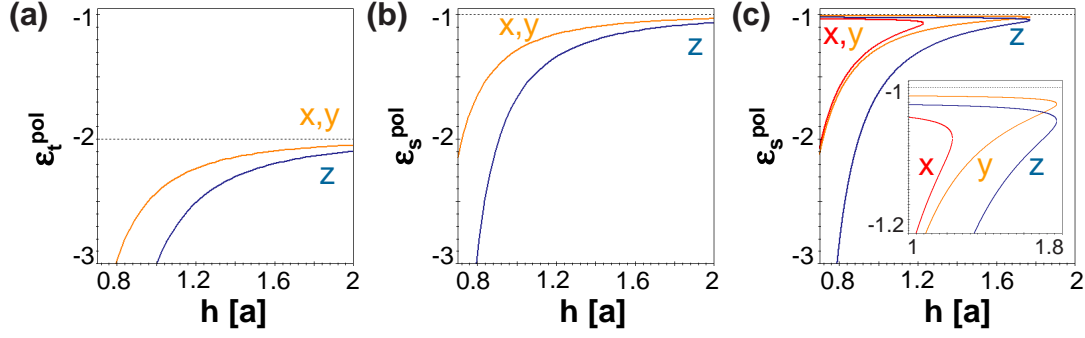
Figure 6.9: *Distance dependence of the dielectric constants ε^{pol} that result in a resonant excitation of the coupled tip-sample system. (a) Tip-induced resonance of a spherical tip (radius a) next to a nonresonant sample. (b),(c) Sample-induced resonance of a nonresonant spherical tip next to an (b) isotropic sample and (c) next to a uniaxial anisotropic sample (optical axis along y axis) with $\varepsilon_s^{pol} = \overline{\varepsilon_s} = \sqrt{\varepsilon_a \varepsilon_c}$ and $\tau = \sqrt{(\varepsilon_a - \varepsilon_c)/\varepsilon_c} = 0.3$.*

for x orientation and

$$\alpha_t(2\beta + \eta) = 64\pi h^3 \tag{6.29}$$

for the y direction. Basically there are two possibilities to excite the system at these poles: a proper polarizability of the tip α_t or a matching sample response β. Accordingly, we call the resonance tip-induced or sample-induced.

In both cases the resonant conditions are fulfilled when the corresponding quantity is excited close to its uncoupled resonance. In general, the interaction between tip and sample shifts these resonance only slightly, depending on the distance h.

For a spherical tip we expect a maximum of the polarizability when the real part of its dielectric constant is -2 (see section 5.1):

$$\Re e(\varepsilon_t) = -2. \tag{6.30}$$

The interaction with the sample shifts the corresponding tip-induced resonance of the tip-sample system slightly towards smaller dielectric constants of the tip. The resonances are located at $\varepsilon_{t,j}^{pol}$ $(j = x, y, z)$

$$\varepsilon_{t,x}^{pol} = \varepsilon_{t,y}^{pol} = -2 - \frac{3}{\frac{16h^3}{(2\beta+\eta)a^3} - 1} \quad \text{and} \tag{6.31}$$

$$\varepsilon_{t,z}^{pol} = -2 - \frac{3}{\frac{4h^3}{(\beta+\eta)a^3} - 1}$$

for the tip dipole oriented along the x, y, and z axis, respectively. These poles are depicted in figure 6.9a as functions of the tip-sample distance h for a nonresonant isotropic sample with $\beta \cong 1$. On the isotropic sample the system is of cylindrical symmetry and, hence, the poles in x and y direction coincide. These parallel poles and the z pole converge towards -2 for large h. For small h both components split

while they shift towards more negative values with decreasing h. As the scattering cross section is directly correlated with the square of the absolute value of the polarizability of the tip, we expect a highly enhanced scattering cross section when the tip is excited at its resonance.

The sample contribution to the scattering cross section of the tip-sample system is mainly given by the response function β. For large β the image dipole in the sample is much larger than the original tip dipole itself. In fact, for very large $\beta \gg 1$ the tip dipole can be neglected.

For an isotropic sample ($\eta = 0$), we expect a maximum in the response function β when the real part of its dielectric constant is -1:

$$\Re e(\varepsilon_s) = -1. \tag{6.32}$$

As for the tip-induced resonance, the interaction with the tip shifts the spectral position of the sample-induced resonance slightly towards smaller dielectric constants of the sample. Hence we expect poles of the coupled tip-sample system at ε_s^{pol}

$$
\begin{aligned}
\varepsilon_{s,x}^{pol} = \varepsilon_{s,y}^{pol} &= -1 - \frac{2}{\frac{32\pi h^3}{\alpha_t} - 1} \\
\varepsilon_{s,z}^{pol} &= -1 - \frac{2}{\frac{16\pi h^3}{\alpha_t} - 1}
\end{aligned}
\tag{6.33}
$$

for the tip dipole being oriented along the x, y, and z axis, respectively[2]. Figure 6.9b shows these poles as functions of the distance h, for the case when the tip is an isotropic sphere excited far from its resonance. As the tip-sample system is again of cylindrical symmetry, the x and y components coincide. Both poles are located at $\varepsilon_s = -1$ for large distances h. With decreasing h the resonances split while shifting towards more negative values.

For anisotropic samples, the formulae for the sample-induced poles are much more complicated, as $\eta \neq 0$ and as the resonance might be induced by poles along different crystallographic directions of the sample. However, for a uniaxial sample with weak optical anisotropy the poles can be calculated from the above equations 6.27, 6.28, and 6.29. The resonant conditions deviate only slightly from the poles of an isotropic sample, if we replace the sample dielectric constant by the geometric mean $\bar{\varepsilon}_s = \sqrt{\varepsilon_a \varepsilon_c}$ of the two components of the dielectric tensor of the sample. Figure 6.9c shows the corresponding poles as functions of h. As the system is not of cylindrical symmetry any more, the x and y components lead to different poles. Also, there are two solutions for each h to excite the system at its resonance,

---

[2]Please note that the applied method of image charges (see section 6.1.1) is valid only for weakly anisotropic samples with real and nonnegative elements of the dielectric tensor. Hence, for a resonantly excited sample, these formulae can only be used to estimate the dipole contribution to the near-field signal. The additional calculations for the reflection on the sample surface as discussed in section 6.1.4 hold for the resonant case.
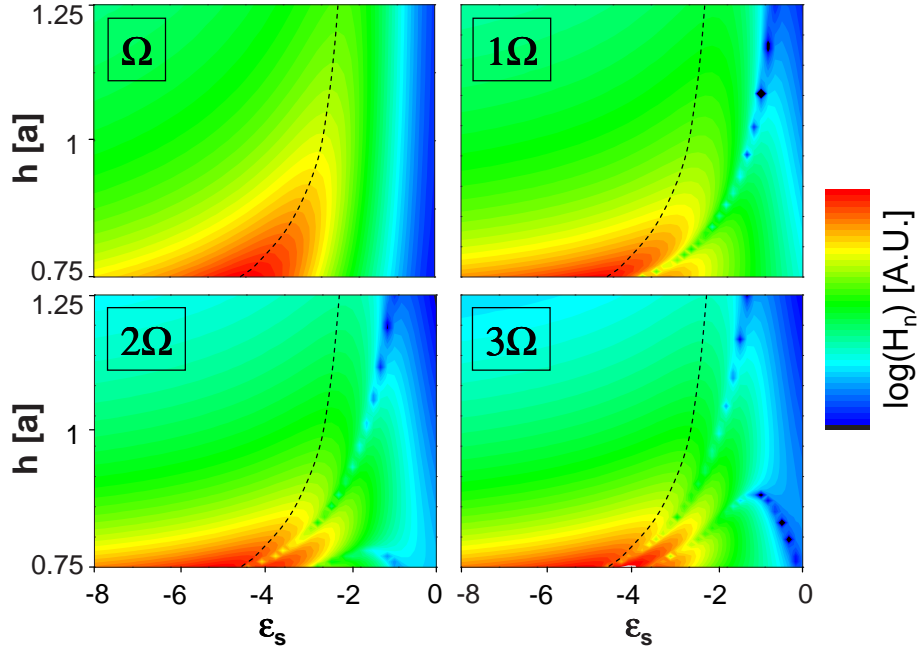
Figure 6.10: *Higher-harmonic signals at the sample-induced resonance as functions of the distance h and the dielectric constant ε_s of an isotropic sample for a tip-dipole perpendicular to the sample surface. The 0th harmonic represents the scattering cross section itself, while the nth higher harmonic is the corresponding n^{th} Fourier component.*

one which is shifted towards smaller dielectric constants as for isotropic samples and a second one close to $\varepsilon_s = -1$, which is related to the anisotropy factor η. As the scattering cross section at the latter pole is small compared with the first resonance, it can be neglected for samples with nonzero damping.

In order to obtain pure near-field signals, we measure so-called higher harmonics of the near-field signal (see section 5.3.2). These higher harmonics are generated by distance modulation and are demodulated by lock-in technique (see chapter 8). For a sample-induced resonance of a system with the tip dipole perpendicular to the sample surface, figure 6.10 shows the expected signals of the 0th to 4th harmonics as functions of the distance h and the dielectric constant of an isotropic sample. The 0th harmonic represents the scattering cross section itself as denoted in eq. 6.26. The nth higher harmonic represents the nth Fourier component and is in first approximation proportional to the nth derivation of the scattering cross section with respect to h. For large distances, all harmonics show a maximum around $\varepsilon_s = -2$. With decreasing h, this resonance shifts towards smaller dielectric constants as discussed above and as indicated by the dashed lines in fig. 6.10. As the resonance broadens for smaller distances, the signal has a characteristic, lobelike shape in the images displayed in figure 6.10. The corresponding n^{th} harmonic shows typically n lobes with the most pronounced one at about the same position as the lobe seen in the
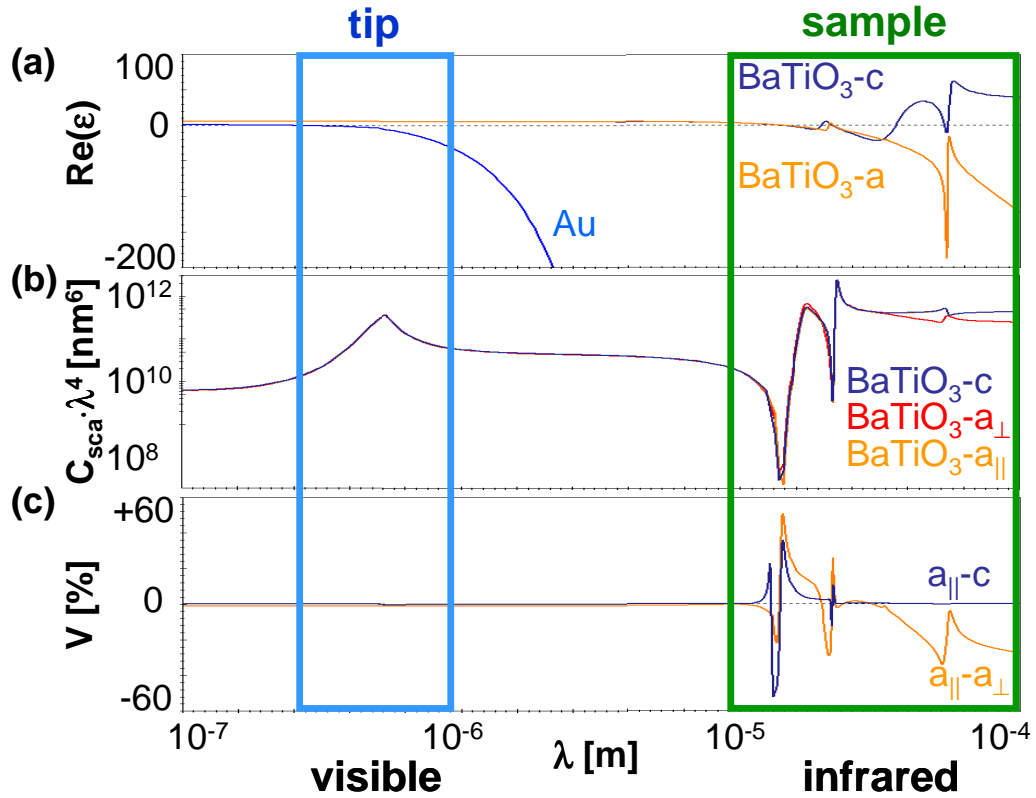
Figure 6.11: *(a) Real parts of the dielectric constants of gold (Au) [Lid92] and of BaTiO$_3$ (ordinary and extraordinary dielectric constants) [Ser80]. (b) Scattering cross sections of a gold sphere (a = 10 nm, $\Im m(\varepsilon_t) = 2$) next to the domains of uniaxial BaTiO$_3$ for a tip dipole oriented perpendicularly to the sample surface. The indices $\perp$ and $\parallel$ of the a domain indicate the direction of the optical axis with respect to the plane of incidence. (c) Corresponding contrast V_{ac} and V_{aa}.*

scattering cross section (compare dashed lines).

Figure 6.11 shows the real parts of the dielectric constants of the spherical gold tip and the BaTiO$_3$ sample, the scattering cross sections of the coupled system, as well as the optical contrasts between ferroelectric domains as functions of the wavelength. In the scattering cross section we clearly observe the resonances of the system, which are located in the visible wavelength regime, corresponding to a tip resonance, and in the IR regime for the sample resonance. The contrast is clearly enhanced at certain wavelengths in the IR regime due to the sample-induced resonance, while at the tip-induced resonance the optical contrast is smaller than 1 %. A more detailed discussion is given in the following.

6.3.2   Tip-Induced Resonance

In a metallic tip we can excite a resonance corresponding to a surface plasmon. For noble metals the plasmon can typically be excited in the visible wavelength regime. It gives rise to a maximum of the polarizability of the tip. The spectral position

depends on the tip material as well as on its shape.

The dielectric constant of a metal is determined by the density of free electrons in the metal. The classical model describing the resulting optical properties is the *Drude model* [Boh98]. Within this model the dielectric function of the free electrons in the metal is given by

$$\varepsilon_t = 1 - \frac{\omega_p^2}{\omega^2 + i\gamma_p\omega} \tag{6.34}$$

with ω_p the plasma frequency of the metal,

ω the angular frequency ($\omega = ck$), and

γ_p the damping constant.

For gold, the *Drude model* yields a good description of the dielectric constant only for a very limited wavelength range. Hence, we use experimental data from [Lid92] for our calculations. The plasma frequency of gold, by means of $\Re e(\varepsilon) = 0$, is around $\lambda_p \cong 220$ nm [Lid92]. In the wavelength range $\lambda = 350$ to 600 nm $\Re e(\varepsilon_t)$ varies between -1 and -6, which is the range where the tip-induced resonance of the sample system can be excited.

Figure 6.12 shows the behavior of a coupled system consisting of a resonantly excited gold tip ($a = 10$ nm) touching a BaTiO$_3$ ($h = 0.75a$). In order to calculate the sample influence properly, we take into account the reflection at the sample surface as well as the response functions β and η representing the dipole interaction. The resulting scattering cross sections and the expected contrasts are shown for *p*- and for *s*-polarized incident light. For *p*-polarized light (fig. 6.12a and c), the scattering cross section is highly enhanced around 562 nm, which corresponds to the excitation of the pole $\varepsilon_{t,z}^{pol} \cong -4.5$ at $h = 0.75$ nm (see figure 6.9a). For the tip-induced resonance, the scattering cross section on the different types of domains is enhanced by the same factor. Hence, the expected optical contrast (fig. 6.12c) is only slightly affected by the resonance and is smaller than 1 %. For *s*-polarized light, the resonance is located at $\lambda = 531$ nm, corresponding to the pole $\varepsilon_{t,x}^{pol} \cong -3.2$ parallel to the sample surface. The scattering cross section for *s*-polarized light is 3 orders smaller in magnitude than the signal for *p*-polarized light. The corresponding optical contrasts are slightly larger than for *p*-polarized light, but still smaller than 2.5 %.

The tip-induced resonance of the system clearly increases the scattering cross section. Unfortunately, the anisotropy contrast V_{aa} between differently oriented *a* domains is not influenced, while the contrast V_{ac} between different types of domains is enhanced only in a very narrow wavelength regime. Similarly as for the special tip shapes discussed in section 6.2, it is not possible to enhance both relevant quantities – the scattering cross section and the optical contrast – by tip-induced resonant excitation of the tip-sample system.

In the following, we will discuss the sample-induced resonance for an isotropic sample in general and for specific anisotropic samples, namely the ferroelectrics
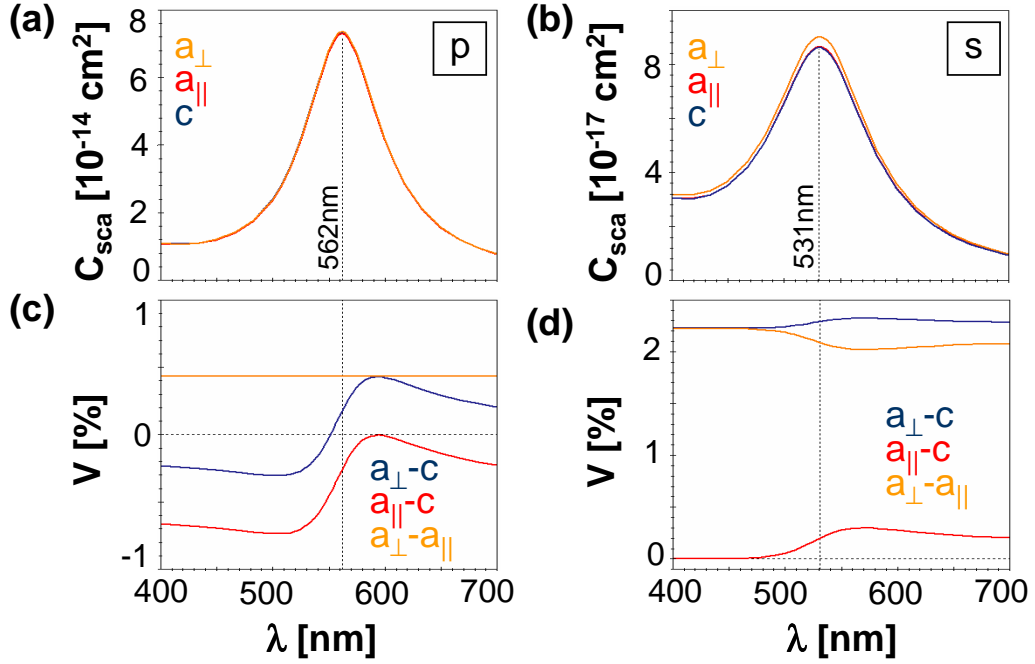
Figure 6.12: *Scattering cross sections and optical contrasts for different polarizations for a tip-sample system consisting of a gold tip (radius a, $\Im m(\varepsilon) = 2$) touching a BaTiO$_3$ surface ($h = 0.75a$, $\varepsilon_a = 5.82$, $\varepsilon_c = 5.57$ [Zgo94]). In (a) and (b) the scattering cross sections are depicted for p- and for s-polarized incident light, while (c) and (d) show the corresponding optical contrasts. The indices $\perp$ and $\parallel$ of the a domain indicate the direction of the optical axis with respect to the plane of incidence.*

LiNbO$_3$ and BaTiO$_3$.

6.3.3   Resonant Isotropic Sample

As the tip resonance increases the scattering cross section but not the anisotropy contrast, we will now discuss the sample-induced resonance. We assume the tip polarizability to be $\alpha \cong 4\pi a^3$ corresponding to a metal at IR wavelengths, where metals have large negative dielectric constants. First, we discuss the basic properties of the sample-induced resonance of an isotropic sample exhibiting one phonon resonance in the IR regime. Later, we will show calculations for the anisotropic ferroelectrics BaTiO$_3$ and LiNbO$_3$, which have multiple phonon resonances.

The dielectric constant of an ionic crystal is determined by the ions in the lattice and their interaction. The optical excitation of lattice vibrations can be described by the well-known Lorentz oscillator model. In general, the dielectric constant is given by [Kit05]

$$\varepsilon = \varepsilon_\infty \left(1 + \frac{\Omega_{LO}^2 - \Omega_{TO}^2}{\Omega_{TO}^2 - \omega^2 - i\gamma\omega} \right) \tag{6.35}$$

with ε_∞ the high-frequency dielectric constant,
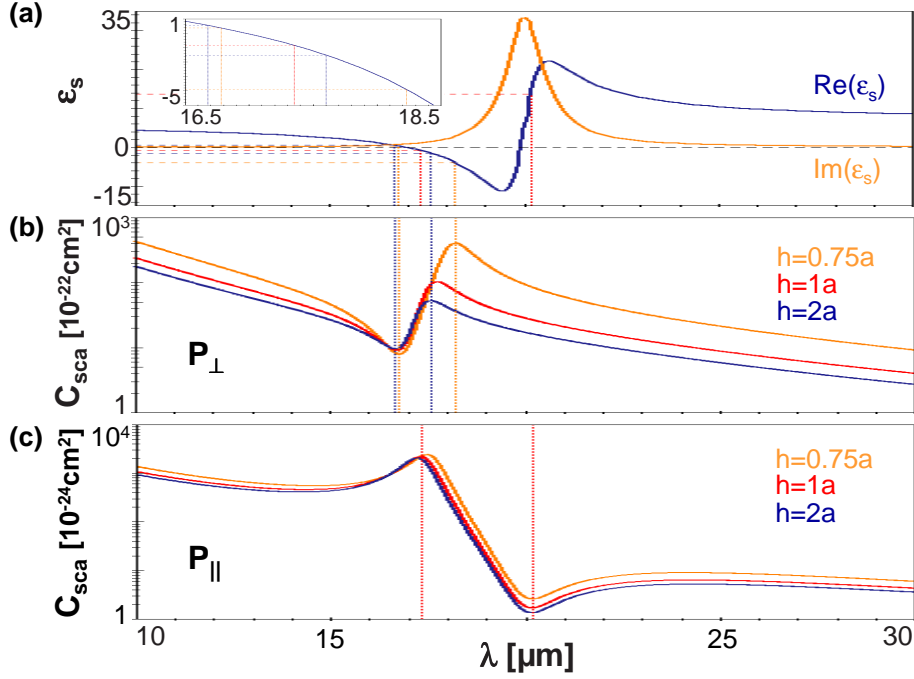
Figure 6.13: *(a) Dielectric constant of an isotropic sample close to its phonon resonance at λ = 20 μm. (b),(c) Scattering cross section of a metal sphere (a = 10 nm) touching the sample, with the tip-sample dipole being normal (b) or parallel (c) to the sample surface.*

Ω_{LO} the longitudinal optical-phonon frequency,

Ω_{TO} its transverse optical-phonon frequency, and

γ the damping constant.

Figure 6.13a shows the dielectric constant of an isotropic sample with $\varepsilon_\infty = 5$, $\Omega_{LO} = 592$ cm^{-1}, $\Omega_{TO} = 500$ cm^{-1} and $\gamma = 35$ cm^{-1}.[3] We observe a maximum in the imaginary part of the dielectric constant around $\lambda = 20$ μm ($FWHM = 1.25$) corresponding to the phonon resonance of the sample at $\lambda_{res} = 1/\Omega$. The real part of the dielectric constant is 5 for large frequencies, i.e., for small wavelengths. It first decreases with λ and crosses zero at $\lambda = 1/\Omega_{LO} \cong 17$ μm. It decreases further and reaches a minimum of -11.2 at $\lambda \cong 19.4$ μm. Around the phonon resonance at 20 μm, it crosses zero again an reaches a positive maximum of 22.2 at $\lambda \cong 20.6$ μm. After that, it decreases and approaches 8 for large λ. In the range of 17 to 20 μm the real part is negative and a sample-induced resonance of the tip-sample system may be induced in the range of 17.3 μm ($\Re e(\varepsilon_s) \cong -0.7$) to 18.5 μm ($\Re e(\varepsilon_s) \cong -5.4$) (see figure 6.9b).

In figure 6.13b we depict the scattering cross section of a metallic sphere ($a = 10$ nm) next to this sample for selected distances h and for the tip dipole oriented

---

[3]In spectroscopy, typically one uses the wavenumber notation $\nu = 1/\lambda$ with the unit cm^{-1} instead of the frequency $\omega = (2\pi c)/\lambda$. As the constant factor $(2\pi c)$ is canceled in all formulae (e.g. eq. 6.35), we will use this spectroscopic notation in the following.

perpendicularly to the sample surface. The scattering cross section shows a resonance on the high-frequency side of the phonon resonance. It has a minimum at around $\lambda \cong 16.7$ μm ($\Re e(\varepsilon_s) \cong 0.5$), which shifts only very slightly with the distance h. This corresponds to a destructive superposition of the tip dipole and the sample dipole, which are antiparallel ($\beta < 0$) in the range $-1 \leq \varepsilon_s \leq 1$. For larger wavelengths the scattering cross section has a maximum which increases towards smaller distances while shifting to larger λ. For $h = 2a$ it is located at $\lambda \cong 17.6$ μm ($\Re e(\varepsilon_s) \cong -1.5$) and for $h = 0.75a$ at $\lambda \cong 18.2$ μm ($\Re e(\varepsilon_s) \cong -3.9$). This affirms the above findings that the sample-induced resonance occurs at small negative dielectric constants of the sample and shifts towards smaller (more negative) dielectric constants for smaller h (see section 6.3.1).

Figure 6.13c shows the scattering cross section for a tip dipole oriented parallel to the sample surface. For nonresonant near-field interaction (not shown here), the scattering is negligible in this case, but for the resonant system it is only one order of magnitude smaller than the normal component. For $\varepsilon \cong -1$ the sample dipole becomes much larger than the tip dipole. Thus the parallel component has a maximum at $\lambda \cong 17.3$ μm ($\Re e(\varepsilon_s) \cong -0.9$) followed by a minimum at $\lambda \cong 20.2$ μm ($\Re e(\varepsilon_s) \cong 13.8$) close to the maximal absorption of the sample.

For small negative values of the dielectric constant, the sample-induced resonance enhances the scattering cross section for both possible orientations of the tip dipole, parallel and perpendicular to the sample surface. This offers the possibility to measure the different components of the tip-sample anisotropy (see section 6.1) by using different polarization of the incident light. Please note that this is only possible for the case of a sample-induced resonance. For a tip-induced resonance and for nonresonant excitation, the parallel component is several orders of magnitude smaller than the perpendicular component and is hence not measurable.

In the following we discuss the more complex system of an anisotropic sample with multiple resonances for two specific examples, namely ferroelectric $LiNbO_3$ and $BaTiO_3$.

6.3.4   Resonant Sample $LiNbO_3$

As first anisotropic sample, we chose ferroelectric $LiNbO_3$, which is a uniaxial crystal with phonon resonances in the IR regime. It has a hexagonal unit cell (see section 3.3) with different resonances of the a and the c direction of the crystal. Due to its crystallographic structure, $LiNbO_3$ single crystals show only antiparallel domains with 180° domain walls. As these domains are optically identical as long as no electric voltage is applied, we assume $LiNbO_3$ to be a uniaxial single crystal with the optical axis oriented either perpendicularly or parallel to the sample surface.

The optical properties of $LiNbO_3$ were examined with FTIR measurements in transition and reflection. As discussed in the experimental part of the thesis (see section 9.1), the results are in good accordance with the theoretical reflection spectra calculated from dielectric constants found in the literature. As ferroelectric $LiNbO_3$

j	S_j	Ω_j [cm^{-1}]	γ_j [cm^{-1}]	λ_j [μm]
E-type modes, $\mathbf{E}\perp$ opt. axis (ordinary ray), $\varepsilon_{a,\infty} = 5$				
1	0.2	670	47	13.2
2	3.3	586	35	17.1
3	0.18	431	12	23.2
4	2.3	363	33	27.5
5	2.2	322	11	31.1
6	5.5	265	12	37.7
7	0.8	236	12	42.4
8	22	152	14	65.8
A_1-type modes, $\mathbf{E}\parallel$ opt. axis, $\varepsilon_{c,\infty} = 4.6$				
1	0.13	692	49	14.5
2	2.55	628	34	15.9
3	0.16	307	25	32.6
4	1	274	14	36.5
5	16	248	21	40.3

Table 6.1: *Strengths, frequencies, and linewidths of the phonon resonances in LiNbO$_3$ according to equation 6.36 [Bar67]. The corresponding wavelengths are quoted for easier comparison with figure 6.14.*

shows several resonance in the IR regime, we have multiple oscillators in the crystal resulting in a sum of Lorentz oscillators. The dielectric constant of our samples is well described by [Bar67]:

$$\varepsilon = \varepsilon_\infty + \sum_j \frac{S_j \Omega_j^2}{\Omega_j^2 - \omega^2 + i\omega\gamma_j} \tag{6.36}$$

with ε_∞ the high-frequency dielectric constant,
S_j the strength of the j$^{\text{th}}$ infrared-active mode,
Ω_j the frequency of the j$^{\text{th}}$ infrared-active mode, and
γ_j the linewidth of the j$^{\text{th}}$ infrared-active mode

with the parameters given in table 6.1

Figure 6.14 shows the dielectric constants of the two directions of the LiNbO$_3$ crystal. Both functions show several resonances corresponding to the phonon modes of table 6.1. For the c direction, the dielectric constant is dominated by the resonances at 15.9 μm and 40.3 μm, while for the a direction all 8 resonances of table 6.1 contribute significantly. Additionally, we depict the reflectivity of LiNbO$_3$ crystals for an incident angle of $\gamma = 0°$, which can be directly compared with the experimental FTIR data (see section 9.1). Due to higher absorption around the phonon resonances, the reflectivity at the corresponding wavelengths is decreased.
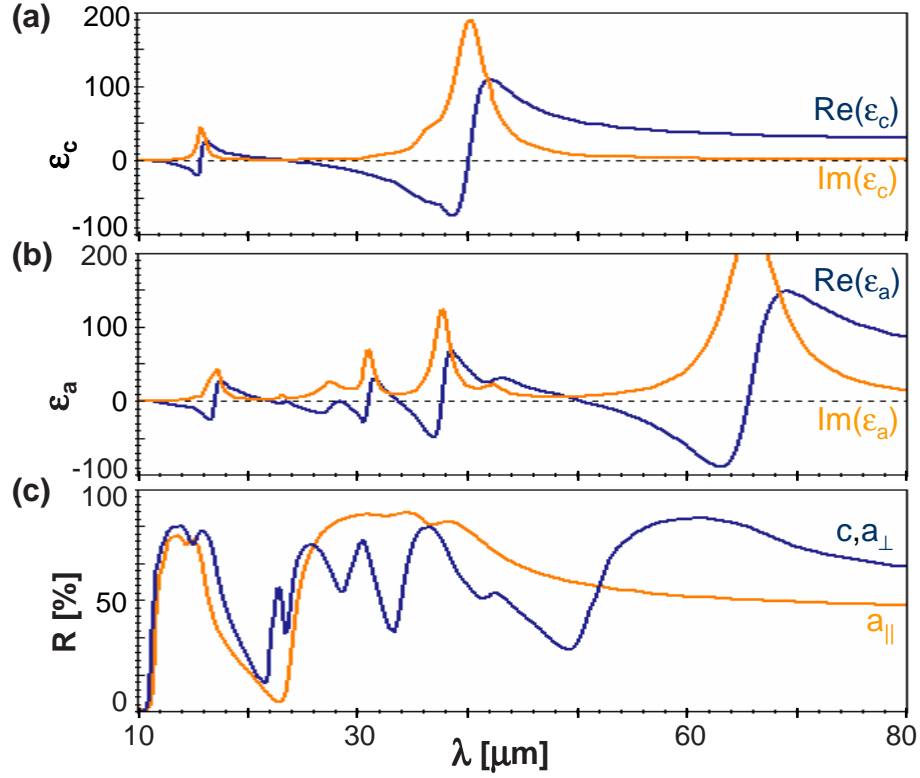
Figure 6.14: *Dielectric constants of a LiNbO$_3$ crystal calculated by the Lorentz oscillator model for the two different crystallographic directions in the single crystal (a) along the optical axis (ε_c) and (b) perpendicular to it (ε_a) [Bar67]. (c) Corresponding reflectivities for perpendicularly incident light, being R_c for a c domain crystal and $R_{a,\parallel}$, $R_{a,\perp}$ for an a domain crystal with the optical axis parallel and perpendicular, respectively, to the electric field of the incident light.*

On the high-frequency side of the phonon resonances of LiNbO$_3$ in the IR regime, its dielectric constant is close to $\Re e(\varepsilon_s) = -1$. As discussed above in detail, in this regime, the near-field-coupled tip-sample system shows a resonance. As we are limited in the experiment to a wavelength range of 4 to 25 μm we will focus on the resonance around 16 μm in the following discussion.

Figure 6.15 shows the scattering cross sections on all possible types of domains as functions of the wavelength λ for two different polarizations of the incident light. In order to compare the difference, we additionally plot the corresponding optical contrast, even though this contrast is not directly measurable on the single domain crystals.

For p-polarized incident light (fig. 6.15a,c), we observe a distinct resonance of the scattering cross section at 13.3 μm ($\varepsilon_a = -3.9 + i0.9$, $\varepsilon_c = -3.9 + i1.2$) on all types of domains. A second maximum at 24.2 μm ($\varepsilon_a = -3.9 + i4.2$, $\varepsilon_c = -0.5 + i1.1$) is observable on the a domains, corresponding to the phonon mode E_3 around $\lambda = 23.2$ μm (see table 6.1). These resonances correspond to poles along the z axis of the system. The excited in-plane poles are much weaker in magnitude. They are
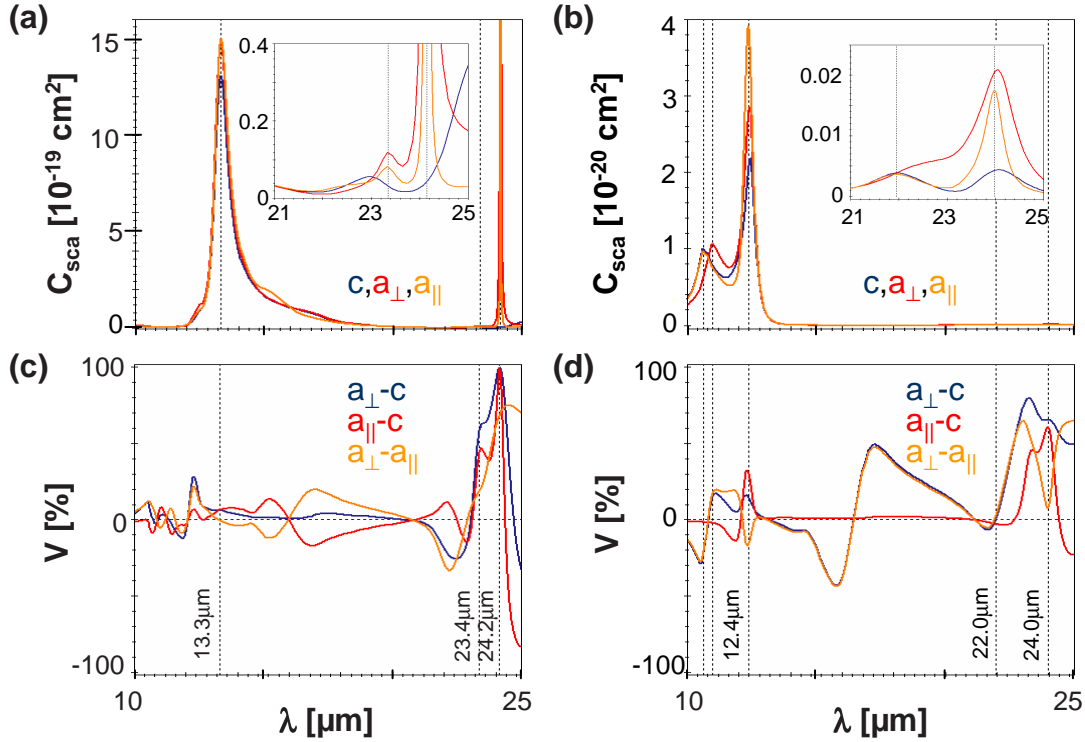
Figure 6.15: *Scattering cross sections on resonantly excited LiNbO$_3$ for p-polarized (a) and s-polarized (b) incident light ($\gamma = 70°$). (c) and (d) show the corresponding optical contrast between different domains. The indices $\perp$ and $\parallel$ of the a domain indicate the direction of the optical axis with respect to the plane of incidence.*

observable at around 12.5 μm ($\varepsilon_a = -2.0 + i0.5$, $\varepsilon_c = -1.6 + i0.6$) as a shoulder of the large resonance and at around 23.4 μm ($\varepsilon_a = -0.2 + i7.4$, $\varepsilon_c = +0.6 + i1.0$) next to the narrow resonance. The corresponding optical contrasts show a small maximum of about ± 30 % at the shoulder of the first resonance. At the resonance itself we expect a contrast of about 8 %. Around 24 μm we observe an additional maximum in the optical contrast of up to 100 %, as the corresponding resonance is only excitable on the a domains.

For the experiments, both parameters, scattering cross section and optical contrast, need to be enhanced. First of all we need a signal of measurable size. For our measurements discussed in chapter 9, we chose the resonance around 13.3 μm as it is broad and has a large magnitude.

For s-polarized light, we observe a distinct maximum at 12.4 μm ($\varepsilon_a = -1.8 + i0.5$, $\varepsilon_c = -1.4 + i0.5$) for all domain types due to dipole interaction. For smaller wavelength, we observe a maximum at 10.65 μm ($\varepsilon_a = +0.7 + i0.2$, $\varepsilon_c = +1.1 + i0.2$) for the c and the $a_\parallel$ domain and at 11 μm ($\varepsilon_a = +0.4 + i0.2$, $\varepsilon_c = 0.7 + i0.2$) for the $a_\perp$ domain. This maximum corresponds to a maximal reflection at the sample surface (see section 6.1.4). Again we observe a second maximum at 24 μm which is about 2 orders smaller than the first maximum. The corresponding optical contrasts

shows several maxima and contrast reversals. Around 12.4 μm we expect a contrast of 30 %, while at 24 μm it is up to 80 %.

The sample-induced resonance on LiNbO$_3$ affects the optical contrast between all types of domains, at the same time providing a scattering cross section of measurable size. While the contrast in the visible regime was mainly caused by different reflection on the different domains (see section 6.2), the contrast for the sample-induced resonance is generated by both dipole interaction and reflection.

6.3.5   Resonant Anisotropic Sample BaTiO$_3$

As second anisotropic sample we chose the ferroelectric BaTiO$_3$, which has a well known and simple crystal structure. In BaTiO$_3$ single crystals, there are 6 different domains possible, with the optical axis either along the x, y, or z direction with two possible orientations of the permanent dipole moment in each case (see section 3.2). As antiparallel domains show the same optical properties as long as no electric field is applied, we do not include the electric dipole in the model and limit our calculations to 3 types with the optical axis in x, y, or z direction. As for LiNbO$_3$, the optical properties of BaTiO$_3$ were examined by FTIR measurements in transmission and reflection. As discussed in the experimental part of the thesis, the results are in good accordance with the theoretical reflection spectra (see section 10.1).

As for LiNbO$_3$, ferroelectric BaTiO$_3$ shows several resonances in the IR regime resulting in a dielectric constant which may be described by a sum of Lorentz oscillators [Ser80]

$$\varepsilon_s = \varepsilon_\infty + \sum_j \Delta\varepsilon_j \cdot \frac{\Omega_{j,TO}^2}{\Omega_{j,TO}^2 - \omega^2 + i\gamma_{j,TO}\omega}. \tag{6.37}$$

with $\Delta\varepsilon_j$ the strength of the j$^{\text{th}}$ oscillator,
       $\Omega_{j,TO}$ the resonance frequency of the TO mode of the j$^{\text{th}}$ oscillator, and
       $\gamma_{j,TO}$ the corresponding damping constant.

The set of parameters used for the following calculations is given in table 6.2.

Figure 6.16a,b shows the real and imaginary parts of the calculated dielectric constants ε_a and ε_c as functions of the wavelength. In the range 10 to 70 μm we observe basically two resonances in both components, one at around 20 μm and the second one at around 55 μm. These resonances correspond to the TO modes around $\Omega_{TO} = 482$ cm^{-1} and $\Omega_{TO} = 306$ cm^{-1} for the a direction and around $\Omega_{TO} = 507$ cm^{-1} and $\Omega_{TO} = 280$ cm^{-1} for the c direction. For both directions the phonon mode around 35 μm is barely visible. We expect an additional resonance around $\lambda = 300$ μm for the a direction, which is indicated by the further decreasing real part of the corresponding dielectric constant. The real part of the dielectric constant of the c direction is nearly constant for large wavelengths. As we are limited in the experiment to a wavelength range of 4 to 25 μm we will focus on the resonance

j	$\Omega_{j,TO}$ [cm^{-1}]	$\gamma_{j,TO}$ [cm^{-1}]	$\Delta\varepsilon_j$	λ_j [μm]
E-type modes, $\mathbf{E}\perp$ optical axis (ordinary ray), $\varepsilon_{a,\infty} = 5.82$				
1	482	21	0.4	20.8
2	306	9	0.05	32.7
3	181.8	2.8	1.4	55.0
4	34	100	2000	294.1
A$_1$-type modes, $\mathbf{E}\parallel$ optical axis, $\varepsilon_{c,\infty} = 5.57$				
1	507	45	1.1	19.7
2	280	120	22	35.7
3	180	4	3.6	55.6

Table 6.2: *Oscillator strengths, frequencies, and damping constants of the TO mode used for the calculation of the dielectric constants according to equation 6.37 [Ser80, Zgo94]. For easier comparison with the following, we list the corresponding wavelengths λ_j.*

around 20 μm. In addition we plot the corresponding reflectivity in figure 6.16c for normal incidence, calculated for comparison with the FTIR measurements in section 10.1. Due to higher absorption around the phonon resonances, the reflectivity around 20 μm and 55 μm is decreased.

In figure 6.17 the scattering cross sections on all possible domains of BaTiO$_3$ and the corresponding contrasts are plotted as functions of the wavelength λ. We assume the tip to be a metal sphere touching the BaTiO$_3$ surface at $h = 0.75a$ and the incident light to be either p or s polarized at $\gamma = 70°$.

For p-polarized light (fig. 6.17a), the scattering cross sections show a resonance around 18.1 μm ($\varepsilon_a = -3.0 + 1.5i$, $\varepsilon_c = -6.5 + 4.4i$) which is slightly shifted for the different domains. The signal on the $a_{\parallel}$ domain is enhanced by a factor of 2 due to a larger reflection coefficient. An additional maximum on all domains is observable at 23.8 μm ($\varepsilon_a = -5.4 + 3.2i$, $\varepsilon_c = -5.8 + 7.9i$), being about one order smaller in its magnitude than the first resonance. The corresponding contrasts are up to 38 % and 13 % at the resonance wavelengths of 18.1 μm and 23.8 μm, respectively, and reach a maximum value of 45 % at around 16.5 μm.

For s-polarized light, we observe a broad maximum consisting of at least two peaks around 13.6 μm ($\varepsilon_a = 1.2 + 0.6i$, $\varepsilon_c = 0.8 + 0.8i$) and 15.6 μm ($\varepsilon_a = -0.3 + 0.9i$, $\varepsilon_c = -1.4 + 1.5i$) for the $a_{\perp}$ domain and at 14.5 μm ($\varepsilon_a = 0.5 + 0.7i$, $\varepsilon_c = -0.1 + 1.1i$) and 15.6 μm for c and $a_{\parallel}$ domains. A second maximum is located around 22 μm ($\varepsilon_a = -2.1 + 3.5i$, $\varepsilon_c = -1.8 + 6.8i$) with an about 2 orders of magnitude smaller magnitude. The corresponding contrast of up to 42 % is mostly negative corresponding to a brighter c domain. At 15.6 μm the contrasts are expected to be $15 - 30$ % and around 22 μm they are about 12 %.

Close to the maximum of the sample-induced resonance of the tip-sample system both relevant quantities, the scattering cross section as well as the optical contrasts, are enhanced sufficiently under resonant excitation of the sample. Their spectral
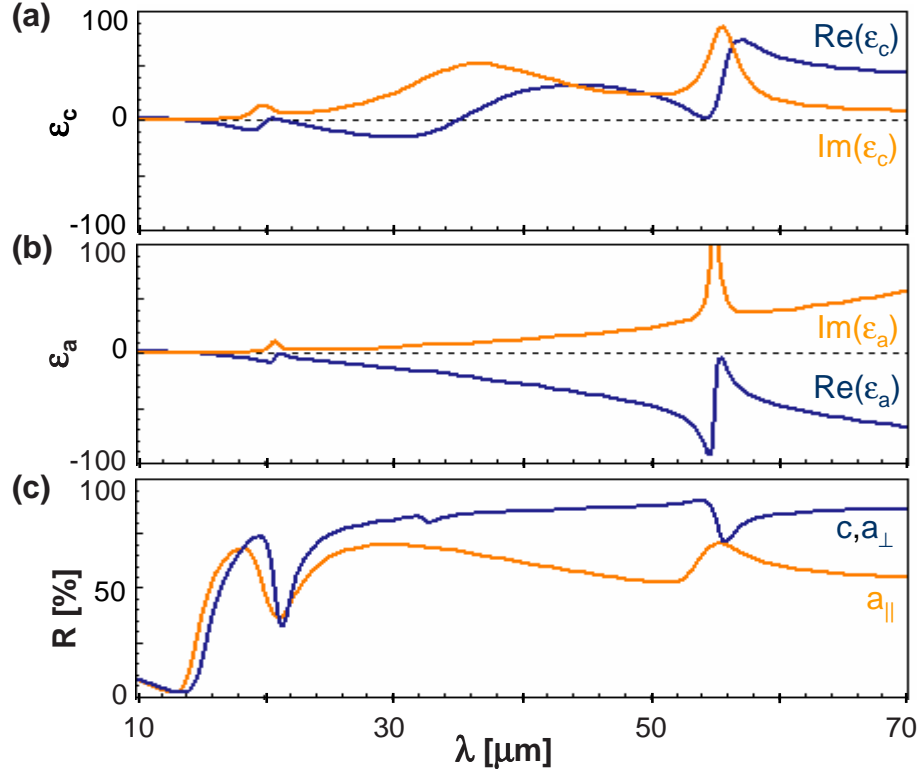
Figure 6.16: *Calculated dielectric constants of a $BaTiO_3$ crystal calculated by the Lorentz oscillator model for the two different crystallographic directions in the single crystal (a) along the optical axis (ε_c) and (b) perpendicular to it (ε_a) [Ser80]. (c) Shows the corresponding reflectivities for perpendicularly incident light, being R_c for a c domain crystal and $R_{a,\parallel}$, $R_{a,\perp}$ for an a domain crystal with the optical axis parallel and perpendicular, respectively, to the electric field of the incident light.*

behavior is determined by both reflection and dipole interaction.

6.4   Summary

In this chapter we have extended the known dipole model to anisotropic samples. We have included a modified method of image charges in order to describe the tip-sample interaction as well as extended Fresnel formulae for reflection at an anisotropic sample surface. As the anisotropy reduces the symmetry of the tip-sample system compared to a system with an isotropic sample, it is much more sensitive to the polarization of the incident light as well as to the tip shape.

For uniaxial samples we defined 3 types of contrast corresponding to the possible orientations of the optical axis either perpendicular or parallel to the sample surface. Analogously to ferroelectric domains in $BaTiO_3$, we call these orientations c domains and a domains. In the near-field-coupled system we expect a contrast between a and c domains as well as between different a domains with their optical axes at right
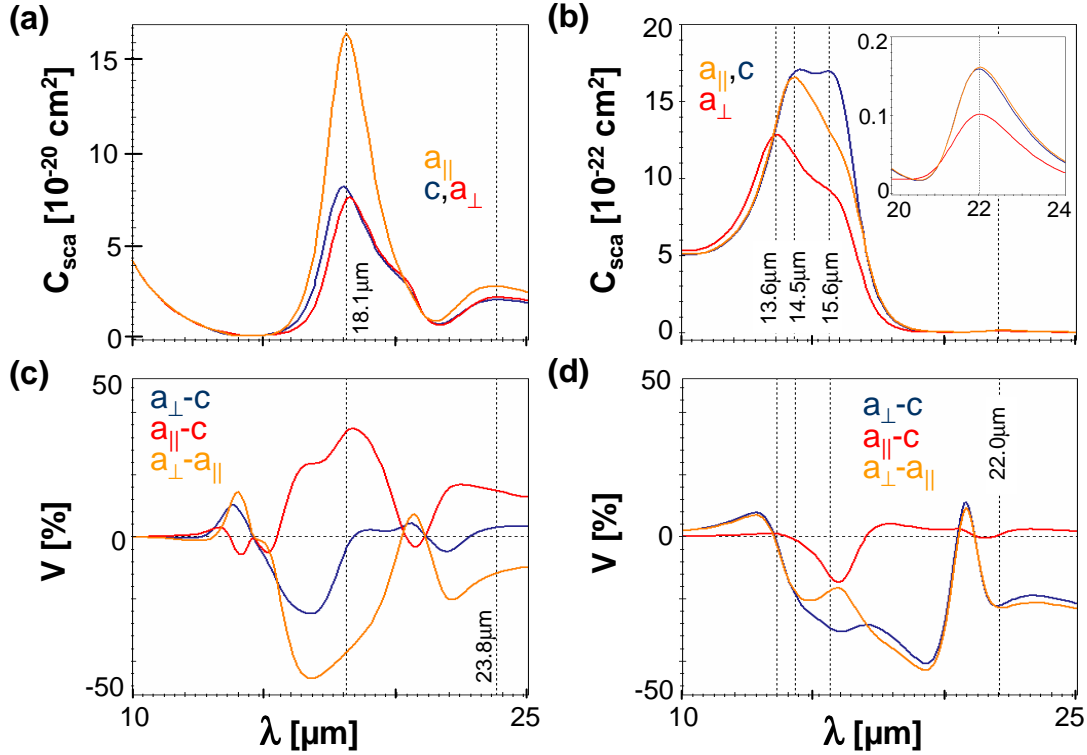
Figure 6.17: *Scattering cross sections on resonantly excited BaTiO₃ for p-polarized (a) and s-polarized (b) incident light ($\gamma = 70°$). (c) and (d) show the corresponding optical contrast between different domains. The indices $\perp$ and $\parallel$ of the a domain indicate the direction of the optical axis with respect to the plane of incidence.*

angle to each other.

The influence of the tip shape on the contrast were discussed for the nonresonant tip-sample system. We found that the optical contrast is highly enhanced for a certain tip shape and a certain polarization of the incident light. Unfortunately the corresponding scattering cross section is rather small.

Exciting the system at its resonances is possible by exciting either the metallic tip close to its plasmon frequency or the sample close to its phonon resonance. Both possibilities enhance the scattering cross section, but only the sample-induced resonances also enhance the optical contrast. Calculations for the ferroelectrics BaTiO₃ and LiNbO₃ are directly comparable with the experiments shown in the experimental part of this work.

In general, the calculations for anisotropic samples predict a contrast between domains with different orientations of the dielectric tensor of the sample. The optical signal does not only carry information about the dielectric component perpendicular to the sample surface, but is also sensitive to the parallel component. Hence, we are able to measure the in-plane and out-of plane dielectric constants of the resonantly excited sample.

7   Conclusion: Theory

The near-field interaction between a probe and the sample is described by the dipole model which is well known for isotropic samples. The light scattered by the probe is modified by the presence of the sample and hence includes information about the local optical properties of the sample. The scattering process transforms the information of the near-field interaction into a propagating wave which may be measured in the far field.

This far field may be detected directly or with interferometric detection. For all detection methods higher-harmonic demodulation allows the separation of the small near-field signal and the huge far-field signal, which is due to reflection at the tip shaft and to interferences between different light paths. The interferometric detection methods additionally allow us to increase the small near-field signal by a constant factor and, much more importantly, they allow us to measure the optical scattering amplitude and the scattering phase separately. These parameters may be correlated with complementary information about the sample, such as dielectric properties and absorption.

The shape and material of the tip influence strongly the scattering properties of the probe. As the probe is assumed to be constant in experiments, we expect the tip properties to influence mainly the absolute value measured in s-SNOM, but not the contrast. This is true for isotropic samples showing a material contrast between regions with different dielectric constants.

The extension of the dipole model to anisotropic samples is a main topic of the present work. A modified dipole interaction is included as well as the reflection at the anisotropic sample, which may change the polarization of the light. In addition to the material contrast for isotropic samples, we found an anisotropy contrast due to different orientations of the dielectric tensor in one and the same sample. This contrast depends strongly on the polarization of the incident light, the orientation of the sample, and the tip geometry. Only when controlling all these parameters, we expect a contrast of noticeable size for a nonresonant tip-sample system.

On the other hand, the coupled tip-sample system shows resonances which can be induced by the tip or by the sample. Tip-induced resonances can be excited close to the plasmon resonance of the typically metallic probe. Close to this resonance the scattering cross section is highly enhanced, but the anisotropy contrast stays small. As the properties of the tip are constant during the experiment, the scattering

properties are enhanced similarly on different sample regions.

When the sample is excited at its resonance, not only the scattering cross section is enhanced, but usually also the anisotropy is more pronounced, i.e. the difference between different crystallographic directions. Hence, the corresponding anisotropy contrast is much larger and of measurable size. As the different crystallographic directions of the anisotropic sample in general show resonances at different wavelengths, we can spectroscopically differ between these regions and identify, for example, different ferroelectric domains.

Calculations for our ferroelectric samples, which show multiple phonon resonances in the IR regime, predict two different types of contrast on the crystals corresponding to the out-of-plane and the in-plane component of the dielectric tensor. The latter seems surprising as the large field enhancement is known to be perpendicular to the sample surface. The calculations showed that this is only the case for nonresonant excitation. For resonant excitation of the sample, the sample influence is enhanced such that also the in-plane component may be sensed.

Part III

Experimental Setup and Results

8 Experimental Setup

The s-SNOM setup used in this work was specially designed for the examination of polar sample materials such as ferroelectrics. It is a unique combination of different scanning probe microscopy methods such as AFM, PFM, KPFM (see chapter 4), and s-SNOM (see section 2.3). This ensures the optical examination without cross-talk from mechanical or electrostatic interactions. For the optical measurements we illuminate the AFM tip with laser light in the visible and IR regimes, and measure the light scattered off the tip-sample junction in the backward direction.

In this chapter we schematically describe this setup used in the visible and IR regimes, but then complement our findings with first results obtained in the visible wavelength range.

8.1 Atomic Force Microscope

The basis of our s-SNOM setup is a home-built AFM which is specifically designed for the examination of polar materials using SNOM methods as well as complementary techniques allowing domain imaging of ferroelectric materials (see section 3.4 and chapter 4). In designing this setup we mainly focussed on the following aspects:

The AFM provides good mechanical stability while at the same time the tip is accessible by optical focussing elements. A frequency-modulated (FM, see section 4.1) electronic controls the distance between tip and sample, while an additional controller stabilizes the cantilever oscillation amplitude to minimize the cross-talk between the mechanical and near-field interactions [Bil06]. For comparison with the results of other groups, it is also possible to use alternative AFM control modes such as amplitude control (see section 4.1). A third controller minimizes the electrostatic interaction between the tip and the sample by compensating for surface charges on the polar sample (KPFM). This method moreover allows us to locate and identify ferroelectric domains through charge mapping. A more precise imaging of the ferroelectric domain distribution is possible with the complementary technique of PFM. In order to ensure constant scattering conditions at the oscillating tip, it is kept at a fixed position in the laser focus during the experiments, while the sample is scanned for imaging. Also, the sample can be changed without moving the tip. The birefringence of the thick ferroelectric samples used in this work limits the possible modes of illumination, as any transmission through the polar sample causes changes
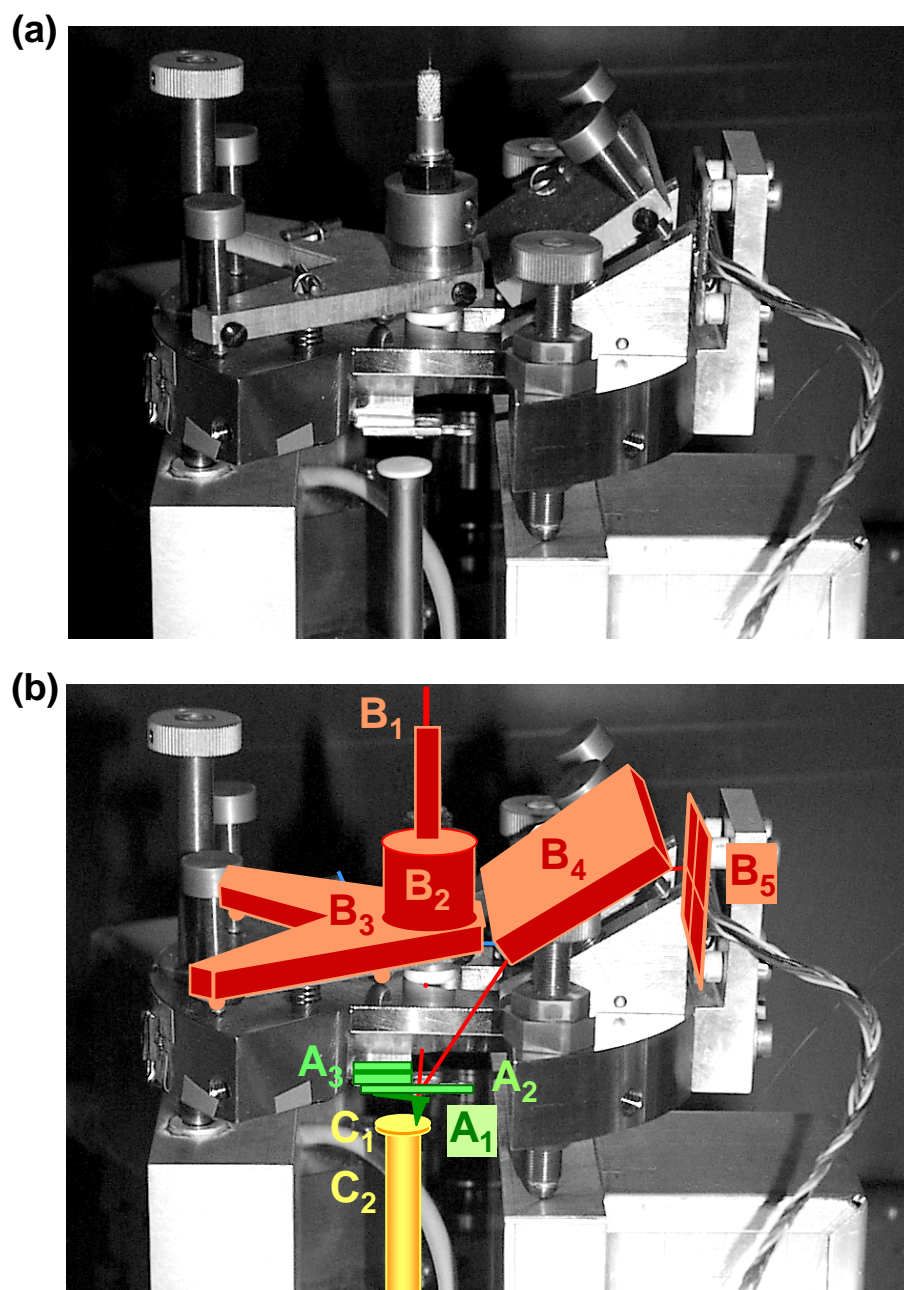
(a)

(b)

Figure 8.1: *(a) Picture of the home-built AFM including head, post, and sample holder with piezoelectric scanner tube. (b) Sketch of the main elements of the AFM with (A) the AFM cantilever and its excitation piezo, (B) the beam deflection unit, and (C) the sample holder.*

of the optical signal, that are correlated with the domain structure but not due to near-field interaction. Therefore illumination or collection through the sample, as used by other groups [Ino94, Mag01], is not appropriate. We illuminate the sample from the side and detect the light scattered in backward direction [Hil00].

AFM head and sample holder

A picture of the AFM head is shown in figure 8.1. In our group, several compatible scan heads of the same design have been built for numerous applications. They are all made out of 15-mm-thick stainless steel and very compact to ensure high mechanical stability and stiffness.

In the following, the parts of the scan head are described in detail with reference to the numbering in figure 8.1b: The cantilever (A_1) is attached at an angle of 15° via a commercial cantilever holder clip[1] (A_2) with the counterpart fixed to the AFM head. The cantilever is excited via a piezoelectric shaker plate placed between two insulating pieces[2] (A_3). It is possible to apply a voltage to the cantilever holder and thus to the cantilever tip itself, e.g., for PFM or KPFM measurements. For those SPM techniques a conductive cantilever is mandatory[3]. Therefore, we use commercially available platinum-iridium-coated cantilever tips[4] (see section 4.1). We measure the deflection of the cantilever by so-called beam deflection: The light of a laser diode is coupled into a glass fiber (B_1) and then focused onto the back of the cantilever via a lens (B_2). The fiber end together with the lens can be positioned with a home-built kinematic mount (B_3). A mirror (B_4) directs the reflected light onto a four-quadrant photodiode (4Q-PD) (B_5). The deflection of the cantilever is measured via the displacement of the laser spot on the 4Q-PD. The vertical displacement of the reflected spot corresponds to the bending of the cantilever and is measured via the difference signal between the two top segments and the two bottom segments of the 4Q-PD, which is called the top-minus-bottom signal (T-B). Conversely, the difference between the two segments on the left and the two segments on the right is called the left-minus-right signal (L-R) and is sensitive to a torsional motion of the cantilever.

The sample is mounted below the tip on a magnetic sample holder (C_1) attached to a piezoelectric scanner tube (C_2). The piezotube D_2 has a xy scan range of 14 μm×14 μm and a z range of 1.6 μm. For optimal positioning of the sample, the piezotube is mounted on a 3D translation stage[5]. With this stage not only the xy position can be adjusted over a range of 13 mm with a precision of 1 μm[6], but also the coarse approach of the sample to the tip in z direction can be accomplished via

---

[1]Omicron, S308301-S [Omi07]

[2]Macor®, machinable glass ceramics by Corning Inc. [Cor07]

[3]Metal-coated tips also offer a higher scattering cross section in the visible wavelength regime as discussed in section 2.3, chapter 5, and section 8.2.

[4]Nanosensors, PPP-NCLPt [Nan07b]

[5]Newport, ULTRAlign Model 561D [New07]

[6]Newport, SM-13 [New07]
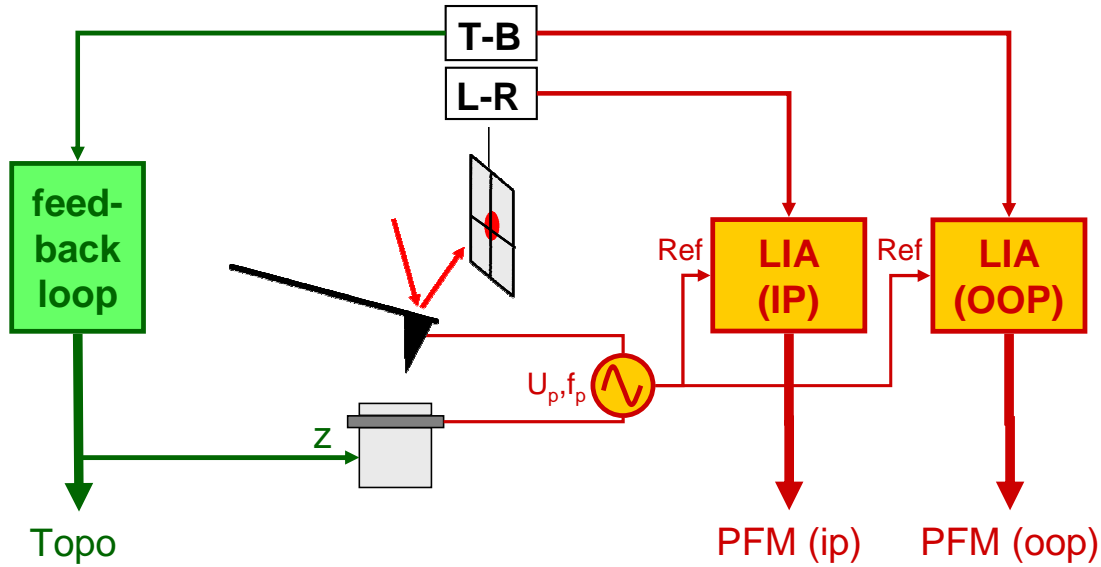
Figure 8.2: *The left-hand side illustrates the AFM contact mode with the T-B signal of the 4Q photodiode used for distance control. On the right-hand side the additional components needed for piezoresponse force microscopy (PFM) are shown: the T-B and L-R signals are used to measure the out-of-plane and in-plane components of the piezoelectric tensor of the sample.*

a high-precision micrometer screw[7] with a coarse travel of 8 mm and a fine travel of 0.3 mm providing an accuracy of 20 nm.

Contact mode

When the AFM is used in contact mode, the sample is approached to the tip until the desired deflection of the cantilever is measured by the 4Q-PD (see section 4.1 for general description). The (T-B) signal is kept constant via a control loop regulating the sample height (see left-hand side in figure 8.2).

A common technique to image ferroelectric domains is PFM (see section 4.2 for general description). The electronic setup for PFM is shown on the right-hand side in figure 8.2. An additional ac voltage with a frequency f_p in the kHz range and an amplitude U_p depending strongly on the sample is applied. For $BaTiO_3$ bulk crystals we typically use $U_p \simeq 5$ V_{pp}. The applied voltage causes a mechanical distortion due to the inverse piezoelectric effect (see section 3.1), which can be recorded as a bending or torsion of the cantilever at the applied frequency. By demodulating the (T-B) or (L-R) signal of the 4-segment diode at f_p using a lock-in amplifier[8] (LIA), we are able to measure the out-of-plane (OOP) or in-plane (IP) component of the piezoelectric properties of the sample.

A typical PFM picture of ferroelectric $BaTiO_3$ (one of the samples examined in the IR, see section 10.5) is shown in figure 8.3. The OOP and IP components,

---

[7]Newport, DS-4F [New07]
[8]Stanford Research Systems, SR830 [Sta07]
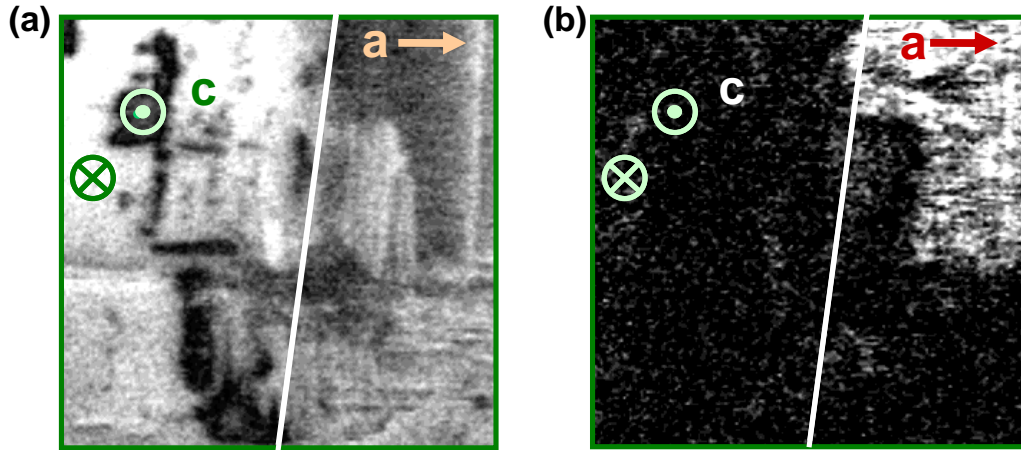
Figure 8.3: *PFM measurements of a ferroelectric BaTiO$_3$ sample. (a) Out-of-plane component showing oppositely oriented c domains ($\odot$ and $\otimes$) as bright and dark areas, while the a domain on the right-hand side appears as a grey area. (b) In-plane component showing the a domain as bright area and no difference between different c domains. The white line is drawn for easier comparison of the two pictures as well as of the corresponding s-SNOM images shown in figure 10.12. The line marks the position of a topographic edge at a typical 0.6° surface tilt as expected between a and c domains (see section 3.2).*

deliver complementary information about the domain distribution of the sample [Eng99a, Eng00]. On the left-hand side the OOP component clearly shows dark and bright areas with meandering boundaries corresponding to the two different types of *c* domains with the remanent electric polarization either pointing towards or away from the sample surface ($\odot$ and $\otimes$). On the right-hand side of the OOP image we again observe bright areas as well as grey regions corresponding to *a* domains. The IP component shows the corresponding *a* domain distribution. We observe one bright area corresponding clearly to an *a* domain of characteristic shape. Besides the *a* domain, the sample appears uniformly dark in the IP component, in particular, there is no difference between the antiparallel *c* domains ($\odot$ and $\otimes$) observed in the OOP component. The shape of the *a* domain is not typical for BaTiO$_3$, where the boundaries between *a* and *c* domains as well as between differently orientated *a* domains normally are straight due to their crystallographic structure (see sections 3.2 and 4.2). We therefore assume that the crystal structure is disturbed by crystal defects. Irrespectively of such defect, the PFM technique allows us to specify all types of domains and their spatial distribution [Eng99b].

Noncontact mode

For s-SNOM imaging, the AFM is operated in the true noncontact mode (fig. 8.4) [Lop00b]. Therefore, the cantilever is excited at its resonance frequency (for oscillation in free space: $f_0 \simeq 170$ kHz) with a given amplitude of $A = 2 - 50$ nm.
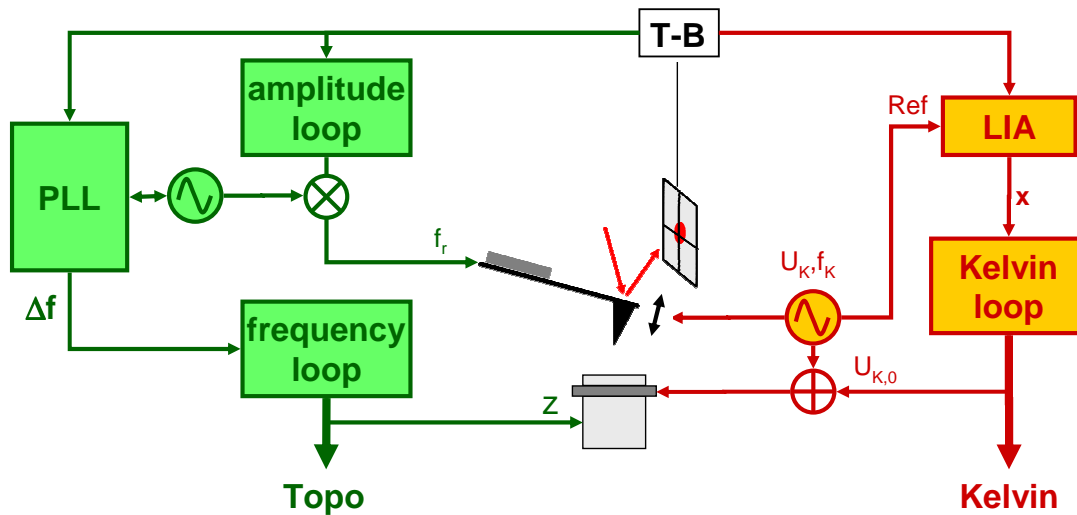
Figure 8.4: *Sketch of the AFM in noncontact mode using a PLL and an additional amplitude control loop (left hand side). On the right-hand side the additional control electronics for KPFM measurements is shown [Wea91].*

A phase-locked-loop system[9] (PLL) excites the cantilever at its true resonance frequency f_r, which may be shifted due to tip-sample interaction (see section 4.1 for general description) [Lop98, Lop00a]. A frequency feedback loop keeps this resonance shift constant by controlling the distance between tip and sample. At the same time, a second feedback loop keeps the oscillation amplitude at a constant value by adjusting the driving voltage. This is mandatory to avoid that amplitude variations produce artifacts in the s-SNOM image due to the strong dependence of the optical signal on the tip-sample distance and the oscillation amplitude [Bil06]. Moreover only a constant oscillation amplitude at a constant average tip-sample distance ensures that the conditions for the scattering by the tip remain constant and, hence, the results are quantitative and comparable.

On ferroelectric materials different domains regions have different surface charge densities resulting in an additional electrostatic interaction. To avoid crosstalk to the mechanical interaction between tip and sample, the Kelvin probe force microscopy (KPFM) (see section 4.3) is used to compensate for the surface charges and thus to minimize the electrostatic interaction between tip and sample [Ter90]. The principle setup used for KPFM is shown on the right-hand side in figure 8.4. An ac voltage ($f_K \simeq 10$ kHz, $U_K \simeq 3$ V$_{pp}$) with an adjustable dc offset ($U_{K,0}$) is applied between tip and sample. Due to electrostatic interaction, the tip-sample distance and thus the deflection of the cantilever is modulated at f_K unless the electric potentials of tip and sample are equal. An additional loop is used to adjust $U_{K,0}$ such that the modulation of the cantilever deflection is nullified and thus the electrostatic interaction is minimized.

---

[9]Nanosurf, easyPLL plus [nan07c]

8.2   Cantilever Tip as the Scatterer in s-SNOM

For s-SNOM measurements, the AFM is operated in the noncontact mode as described in section 8.1. At visible wavelengths we use a helium neon (HeNe) laser at $\lambda = 632.8$ nm as the light source and a heterodyne detection system. A tunable infrared light source is provided by the free-electron laser (FEL)at the Forschungszentrum Dresden-Rossendorf (FZD) close to Dresden.

For all optical measurements we use platinum-iridium(Pt-Ir5)-coated silicon cantilevers[10] (see figure 4.1) for several reasons: First of all, compared to other metal coatings such as gold, Pt-Ir5 is mechanically very stable. Thus, we do not expect big changes of the tip geometry and scattering behavior. Second, having an electrically conductive tip coating is indispensable for performing PFM and KPFM measurements. Third, these cantilevers are also used by other groups [Tau03] for the visible and IR wavelength regimes, which allows direct comparison with their results. Fourth, at visible wavelengths the metal coating increases the scattering cross section of the probe because of surface plasmon resonances. Therefore, the signal-to-noise ratio (S/N) is increased. And finally, fifth, in the IR wavelength regime we spectroscopically examine phonon resonances of the sample. Here, any wavelength dependence of the tip would distort the near-field signal. The metal coating exhibits an optically flat response in the IR regime.

Figure 8.5 shows optical reflection spectra of commercially available AFM tips with different coatings. These data were taken with a FTIR spectrometer[11] by focussing the light onto the cantilever support of the AFM tips coated within the same procedure as the tips. The reflectivities of all metal coatings (Pt-Ir5, Al, Au, and Pt) are flat in the IR regime. For comparison, we also examined the uncoated support, which shows clear resonances of the n-doped silicon. Note that the absolute values are not comparable, because the size as well as the position of the FTIR spot on the support are different for each measurement.

For all setups the tip is illuminated from the side at 90° with respect to the cantilever axis and at 70° with respect to the tip axis . The angle of 70° takes the antenna behavior of the tip into account [Kni76] (see section 5.1) and additionally allows the tip to be illuminated without shading by the sample.

The backscattered light is collected with the same lens (or parabolic mirror for the IR) as used for illumination. The detection method is different for the two setups: In the visible regime, we use a heterodyne interferometer, while in the IR we detect the light directly. These special setups are described in the following sections 8.3 and 8.4. The detected light is demodulated at higher harmonics, i.e., at multiples of the cantilever frequency (see section 2.3 and 5.3). A frequency mixer generates the reference signal for the LIA from the cantilever oscillation frequency measured via the 4-segment diode. This ensures a fixed phase of the reference signal with respect

---

[10]Nanosensors, PPP-NCLPt [Nan07b]
[11]Bruker, Equinox 55 [Bru07]
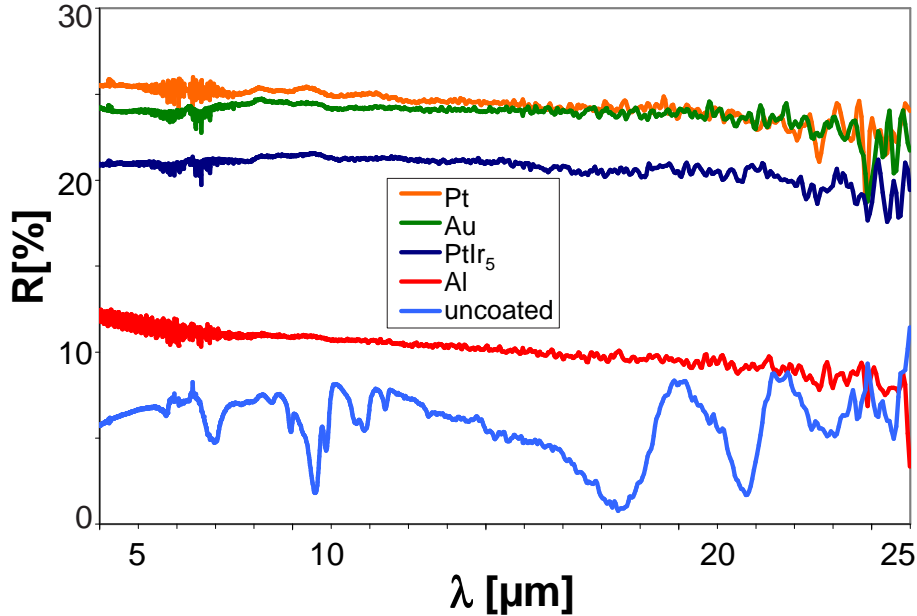
Figure 8.5: *FTIR reflection spectra of commercially available AFM tips with different coatings: Pt-Ir5, Al, Au, Pt. For comparison, we show the spectrum of an AFM tip with no coating. The absolute values are not comparable because of different sizes and positions of the illumination spot on the AFM cantilever support.*

to the oscillation.

8.3   Setup in the Visible Wavelength Regime

A schematic of the setup as used at visible wavelengths is shown in figure 8.6. We use a heterodyne interferometric detection system as described in the sections 2.3 and 5.3 [Hil01a, Hil00].

The light of a HeNe laser[12] ($\lambda = 632.8$ nm) passes a Faraday optical isolator[13] (FOI) to avoid destabilization of the HeNe laser by backreflected light. An acousto-optical modulator[14] (AOM) diffracts the beam into several beams with their frequencies shifted by $n \cdot \Omega$ ($\Omega \simeq 70$MHz, $n = 0, 1, 2, ...$) and the diffraction angles being $n \cdot 13.5$ mrad with respect to the 0th-order beam. The AOM is aligned in the way that the Bragg condition is fulfilled for the 1st order. Hence, mostly 0th and 1st order are transmitted with about equal intensities, but also higher orders with less intensity. The polarization of all orders is rotated by a $\lambda/2$ plate, placed right behind the AOM. An iris diaphragm (id) blocks all higher orders, transmitting only the 0th - and one 1st-order beam. The 0th-order beam is the main beam and is di-

---

[12]Polytec PL-750-P, Power P=5 mW, [Pol07]
[13]Leysop Type FOI 5/57 [Ley07]
[14]Isomet Corp., Type 1205C-2 [Iso07]
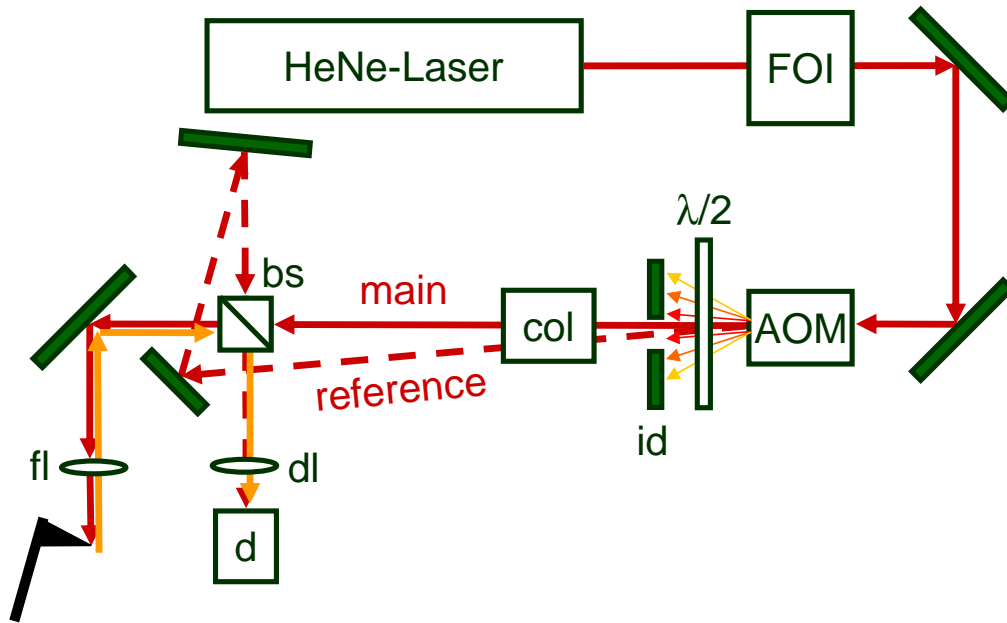
Figure 8.6: *Optical setup for illumination and detection at visible wavelengths, including a helium-neon laser, a Faraday optical isolator (FOI), an acousto-optical modulator (AOM), an iris diaphragm (id), a collimator (col), a beam splitter cube (bs), two focussing lenses (fl, dl), and a detector (d).*

rected onto the AFM tip, while the 1st-order beam is used as a reference. A two-lens system (col) collimates both beams and increases their diameters by a factor of 5.2 to allow full illumination of the focussing lens (fl). The 0th-order beam, passes a polarization-independent 50:50 beam splitter cube[15] (bs) and is then reflected at an angle of 20° towards the table to illuminate the tip at an angle of 70° with respect to the tip axis. The light is focussed on the tip by an aspheric lens[16]. The backscattered light is collected by the same lens, reflected by the beam splitter cube (bs), and focussed by the detector lens (dl) on a high-speed photodetector[17] (d). The 1st-order beam – the reference beam – is reflected by two mirrors before passing the beam splitter cube (bs) to them overlap the scattered light. It interferes with the scattered beam and is also focussed by the detector lens (dl) on the detector (d).

Every part of the illumination and detection systems was analyzed in detail, especially concerning their polarization dependence. The FOI rotates the polarization by 45°. To minimize depolarization by the mirrors and by the highly-polarization dependent AOM, we adjust the laser and the FOI such that the light exiting the AFOM is polarized perpendicularly to the optical table. After the AOM, no polarization dependent elements are used. Therefore we place the $\lambda/2$-plate directly

---

[15]Thorlabs, BS-013 [Tho07]

[16]Thorlabs, aspheric lens 350220-A [Tho07]

[17]Thorlabs, Det210/M [Tho07],

In earlier measurements we used a passive photodiode to avoid any power supply noise: Hamamatsu, Si PIN Photodiode S5972 [Ham07]
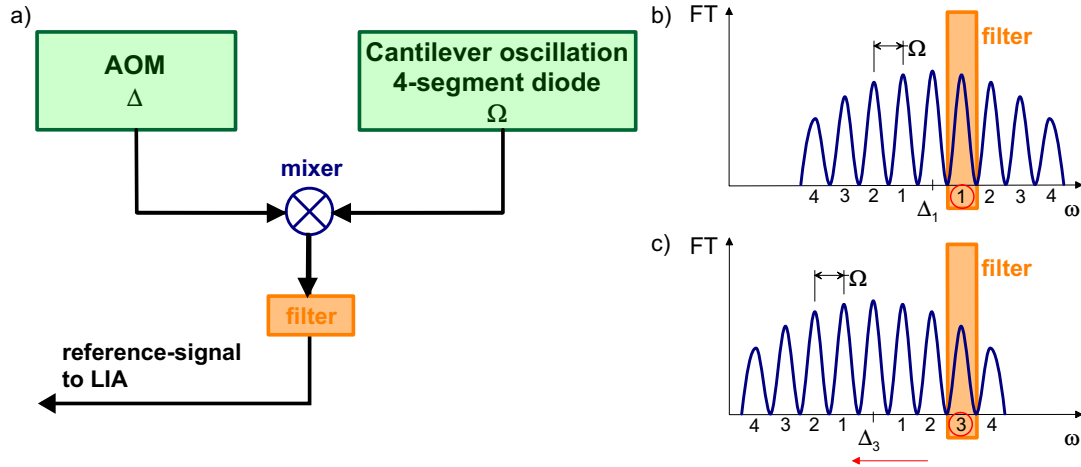
Figure 8.7: *Schematic of the reference frequency generation: (a) signal gener-ation, signal-to-filter correlation for (b) the 1ˢᵗ- and (c) the 3ʳᵈ-harmonic signal generation*

behind the AOM to adjust the polarization of both the main and the reference beam in the same way.

In principle, a heterodyne interferometer as described in section 2.3 does not depend on the retardation between the reference and the main beam. In a real setup it is still advisable to make both paths similar in length, not only because of the divergence of the beams, but also to avoid destructive superposition of different longitudinal laser modes.

For measuring higher harmonics of the near-field signal, we demodulate the signal at the sideband of the beating term $(\Delta \pm n \cdot \Omega)$. To produce the reference signal for the LIA[18], we mix[19] the AOM frequency $\Delta \simeq 70\text{MHz}$ with the cantilever frequency Ω measured by the 4-quadrant photodiode. We use a crystal filter[20] to isolate one distinct order, which is then used as the reference signal. As the filter has a fixed frequency, we adjust the AOM frequency to shift the frequency spectrum in such a way that the desired higher harmonic coincides with the filter frequency (see figure 8.7).

Figure 8.8 shows approach curves on aluminum. On the left-hand side we display the signal demodulated at the cantilever frequency: Even for distances of up to 600 nm the amplitude is large and shows a clear periodic variation with distance. This typical behavior can be attributed to interference terms, i.e., it represents a pure far-field signal. Only very close to the sample surface we can observe some deviation from this periodic shape. On the right-hand side, we see the optical amplitude of the 3ʳᵈ-harmonic signal. For distances larger than 100 nm, we observe a constant signal, while for smaller distances, the signal changes dramatically, due to near-field interaction between tip and sample. These measurements clearly show

---

[18]Stanford Research Systems, SR844, up to 80 MHz [Sta07]

[19]mixer: minicircuits ZP-5MH [Min07]

[20]Kinseki MXF70-30B [Kin07]
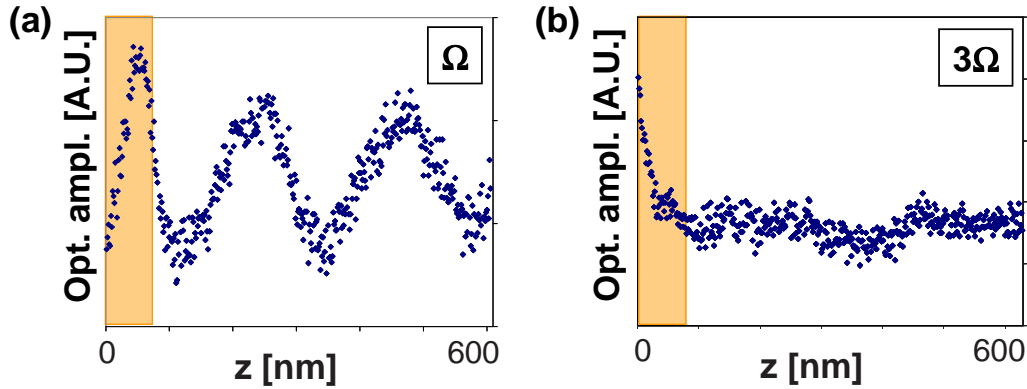
Figure 8.8: *Approach curves on an aluminum sample for two different harmonics: For demodulation at Ω, a periodic far-field signal is observed with only a very small deviation close to the sample surface. In the 3rd-harmonic signal (3Ω) we see no far-field signal any more, but a clear near-field signal for distances smaller than 80 nm.*

the suppression of far-field contributions in the higher-harmonic signals, leading to a pure near-field measurement. The observed distance dependence and far-field suppression look very similar to those seen in approach curves measured by other groups on gold samples [Hil00, Bek06].

For comparison with the results of other groups, we examined so-called Fischer patterns, i.e., projection patterns named after U. Fischer [Fis81, Fis02]. To produce such patterns, latex spheres are distributed in a dense-packed monolayer on a glass substrate. This structure is covered by about 15 nm of vapor-deposited aluminium, and afterwards the latex spheres are removed. This leaves only the aluminum on the surface that passed through the gaps between the spheres to directly wet the surface of the substrate. These islands of trianglelike shape reflect the hexagonal structure of the dense monolayer of spheres.

Figure 8.9 shows s-SNOM images of such a structure at $\lambda = 633$ nm. Figure 8.9a shows the topography of the sample with some of the bright triangular aluminum islands being separated while others are or connected to form larger island. In figure 8.9a the corresponding near-field signal is depicted, as demodulated at the 2nd harmonic (2Ω). The metal islands are bright in the optical signal on the dark glass substrate. In comparison to measurements on a similar pattern reported in the literature [Bek06, Hil02a, Bre05], the near-field signal at the second harmonic looks much noisier. At the third harmonic, the signal-to-noise ratio of our s-SNOM is too low to perform a reproducible optical scan. We believe that the weak signal is mainly caused by difficulties in the adjustment of the tip in the laser focus. Moreover, any mechanical cross-talk is minimized and no topographical induced contrast is measured. This can also be observed in figure 8.9b as no edge-enhanced signal is measured of the kind discussed in [Bek06], which is due to our more sophisticated feedback control system.
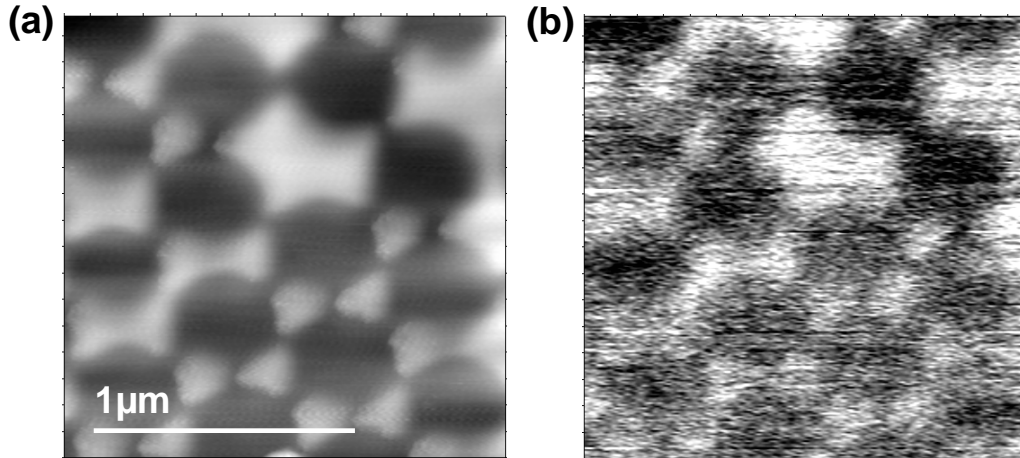
Figure 8.9: *Scan on a Fischer pattern showing (a) the topography ($\Delta z = 25$ nm) and (b) the corresponding optical amplitude demodulated at the 2nd harmonic (2Ω).*

With our setup for the visible wavelength regime, we studied the general behavior of the near-field signal on metal samples such as gold or aluminum. We focussed on the dependence of the different harmonics on the polarization of the incident light and the amplitude of the cantilever oscillation, and on how the different modes of our control system influence the optical signal [Sch07b]. We performed these measurements not only for the near-field signal, but also for the far-field interferences observed at large distances of up to 5 μm [Sch07a]. These examinations showed the excellent reproducibility and stability of our s-SNOM setup.

As we focus on ferroelectric systems in this work, we will not go into the details here. We also tried some near-field measurements with visible light on a BaTiO$_3$ sample. Unfortunately the signal was very weak and was dominated by far-field interference patterns. Also, the contrast between the ferroelectric domains is expected to be very small. This is the reason why we use the free-electron laser in Rossendorf as a light source for near-field investigations on ferroelectric crystals. The setup used for the IR measurements is described in the following section.

8.4 Setup in the Infrared Wavelength Regime

Using near-field microscopy to image the optical anisotropy of the samples meets with mainly two problems: small signals in general and small optical contrast. Both parameters can be increased if the sample is excited at a resonance (see chapter 6). Ferroelectrics, which are the materials we are interested in, show phonon resonances in the IR regime. These resonances are slightly different for different crystal axes due to the anisotropy of the ferroelectric. This can be used to increase the optical contrast, which we measure by using a FEL as an IR light source. In this section the setup used for these examinations will be described.
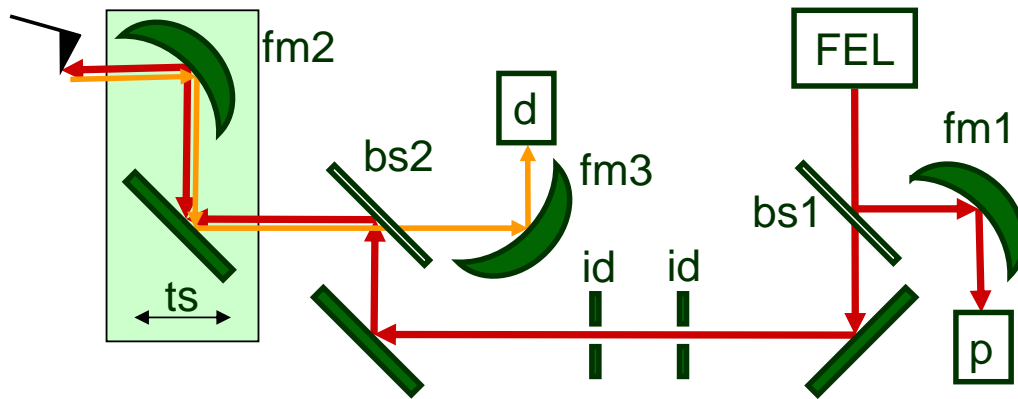
Figure 8.10: *Setup for the infrared wavelength regime, including power measurement, focussing on the AFM tip, and direct detection of the backscattered light*

The free-electron laser at the Forschungszentrum Dresden-Rossendorf (FZD) produces IR light with a wavelength that can be tuned to any value from 4 to 22 μm[21] with a spectral width of about 100 nm [Mic04]. The wavelength is determined by the electron energy and the gap width between the permanent magnets of the undulator, i.e., the magnetic field. For spectroscopic purposes it is possible to sweep the wavelength by increasing or decreasing the undulator gap without changing the electron energy [FZD07]. Changing the wavelength by such a gap scan takes about 2 s and can be done directly from the user lab. In this way, a wavelength range of $\Delta\lambda = 2 - 3$ μm around a preset center wavelength is accessible. This was used for the spectroscopic measurements presented in chapters 9 and 10.

The beam of the free-electron laser is delivered to the user laboratory through a vacuum beam line. When entering the lab, it is polarized parallel to the optical table, but can be switched to perpendicular orientation. In our experiments, these two polarizations correspond to *s*- and *p*-polarized light, respectively, with respect to the plane of incidence at the sample. The setup using either incident light polarizations is shown in figure 8.10 and described in the following.

First we split off part of the laser light by a beam splitter foil[22] (bs1) to measure the current laser power with a powermeter[23]. This is essential, because the power may change drastically during the gap scan. The light transmitted through the beam splitter foil (bs1) passes two iris diaphragms (id) serving for easier alignment, and is reflected by a second beam splitter foil (bs2, Mylar). This part of the laser light is focussed on the AFM tip by a parabolic mirror (fm2). The parabolic mirror and an additional plane mirror are mounted on a translation stage (ts) by which the two mirrors and, hence, the focus can be moved along the line of the beam hitting the AFM tip. The light backscattered by the tip is collected with the same parabolic

---

[21]A larger wavelength regime up to 150 μm will be accessible for users starting in 2007

[22]Biaxially oriented polyethylene terephthalate(PET) film called Mylar® by DuPont [DuP07].

[23]Melles Griot, 13PEM001 Broadband Power and Energy Meter [Mel07]
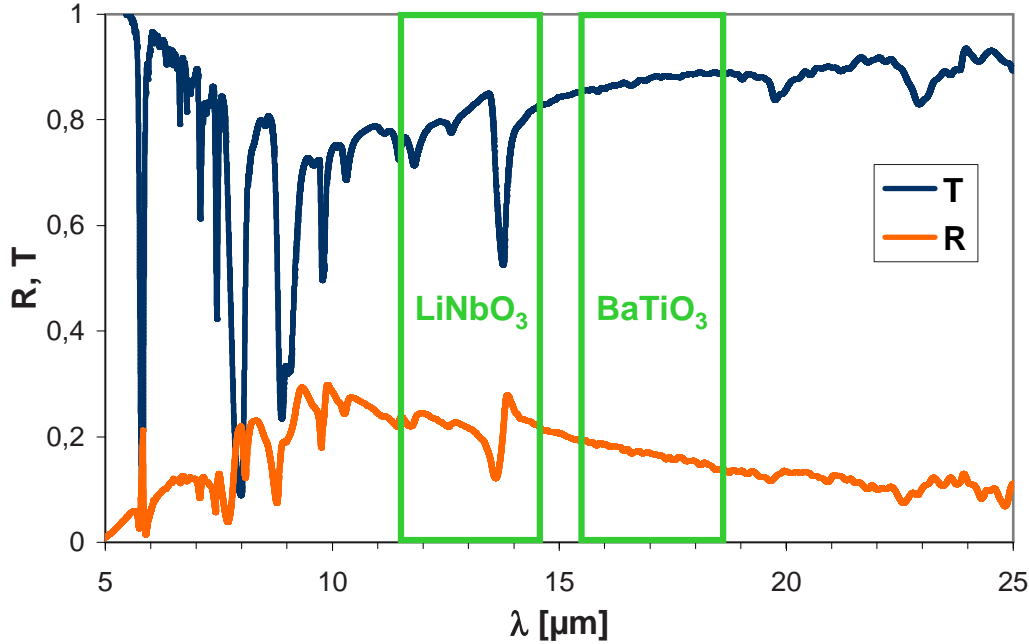
Figure 8.11: *FTIR spectra of Mylar foil as used in the beam splitters, showing the reflectance (R) and transmittance (T) as functions of wavelength. The green-marked areas correspond to the wavelength ranges used for near-field examination of LiNbO$_3$ and BaTiO$_3$.*

mirror, transmitted through the beam splitter foil (bs2), and focussed by a second parabolic mirror (pm2) on a detector (d)[24]. The signal is demodulated at higher harmonics (up to the 4th) by a LIA[25], which has an internal reference mixer. The reference input of the LIA is the cantilever oscillation signal as measured by the 4-segment diode.

As the laser beam passes through beam splitters made of Mylar foil several times, it is important to know their properties. FTIR spectra of the foil are shown in figure 8.11. The wavelength regimes used for the examination of the ferroelectric samples, 11.5 to 14.5 μm for LiNbO$_3$ and 15.5 to 18.5 μm for BaTiO$_3$, are marked in the figure. In the regime applying to LiNbO$_3$ the beam splitter has a pronounced absorption line around 13.7 μm[26], while in the range relevant to BaTiO$_3$ the spectra are rather flat. The wavelength dependence of the beam splitter needs to be taken into account in the analysis of the near-field data, especially of their spectral dependence. Therefore, we measured in detail the spectral dependence of the beam splitter (bs1) of the setup across the wavelength range used in the near-field measurements.

Focussing an invisible beam on an AFM tip is a nontrivial problem. To make sure that the tip is placed accurately in the focus, we apply the following procedure.

---

[24]Liquid-nitrogen-cooled mercury cadmium telluride (HgCdTe) detector J15D16 by Judson Technologies [Jud07]

[25]EG&G model 5302 [EGG07]

[26]The absorption A may be calculated from the data shown in figure 8.11 by $A = 1 - R - T$.
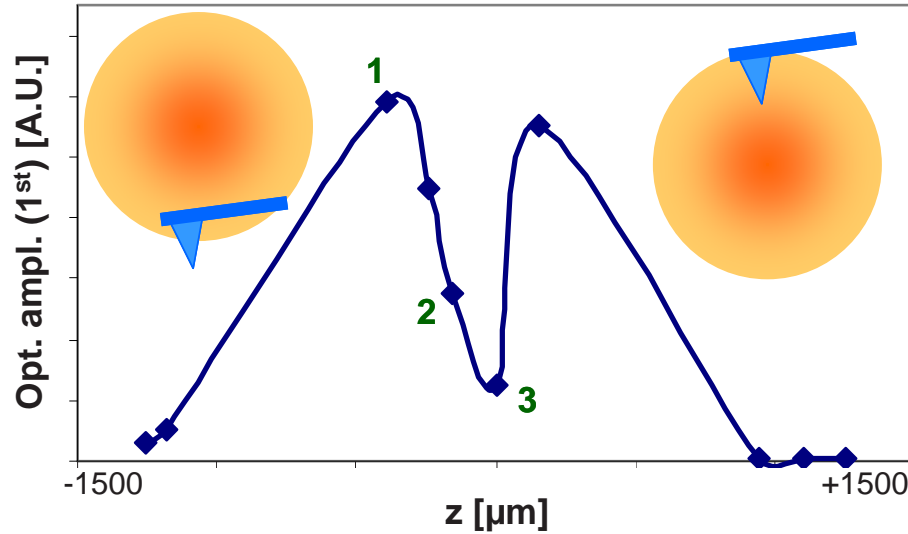
Figure 8.12: *Scattered power as a function of the z position of the tip in the focus ($\lambda = 12.8$ μm).*

First we use the red light of a semiconductor laser for preadjustment. To position the tip in the focus, we use both the translation stage (ts) and the kinematic mount of the focussing mirror (fm2) as well as the screw on the AFM adjusting the tip height. With the free-electron laser, we then measure the 1st-harmonic signal for different z positions of the AFM tip, which is made to oscillate at its resonance frequency with an amplitude of about 50 nm. The result is shown in figure 8.12. We see the optical amplitude as a function of the z position of the tip. The signal increases until a maximum is reached, which is followed by a minimum going down to nearly the noise level and a second maximum of nearly the same height as the first maximum. Demodulation at the 1st harmonic yields a nonzero signal only if the scattered power is modulated by the tip oscillation. This happens only if the intensity has a gradient across the tip. The focus of the FEL is homogeneous in intensity in the center but has a large gradient at the borders. We thus believe that the two maxima in figure 8.12 correspond to the edges of the focus whereas the minimum corresponds to the center. Note that variation of the z position is much larger than the amplitude of the cantilever oscillation. The focus spot is expected to be a few hundred micrometers in diameter while the cantilever oscillation amplitude is around 50 nm.

We now take approach curves for selected z positions and different harmonics on a reference sample (150 nm-gold film on glass). The result is depicted in figure 8.13 for the z positions (1) to (3) marked in figure 8.12. For point (1) (focus more on the cantilever than on the tip) we observe a small far-field signal in the 1st harmonic, which is zero at the sample surface. The 2nd- and 3rd-harmonic signals are very weak and show only a slight distance dependence, which could be correlated with the far-field signal. At point (2) we see a much larger far-field signal in the 1st harmonic
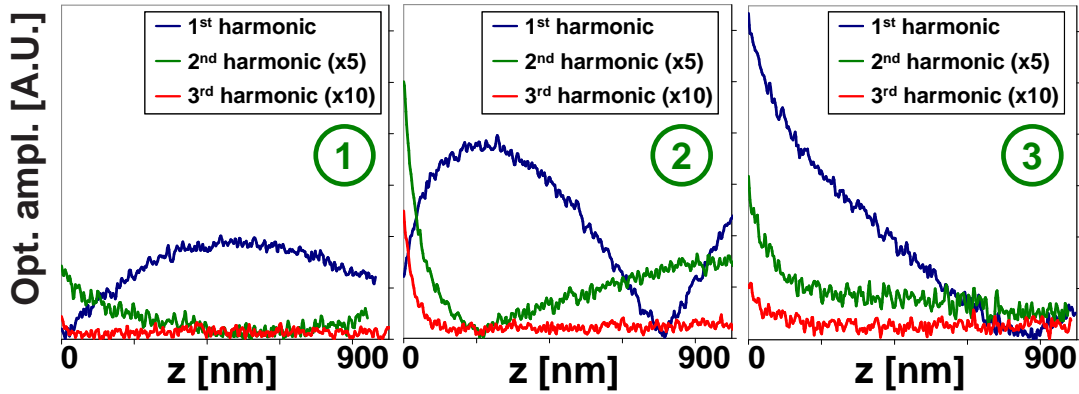
Figure 8.13: *Approach curves on a reference sample for different positions of the tip in the focus of the FEL beam. The approach curves were measured at different harmonics, showing the separation of near-field and far-field signals.*

with a small deviation close to the sample surface. The 2nd harmonic still contains some contribution of the far field even at distances of about 900 nm, but exhibits a strong increase of the signal for distances smaller than about 200 nm. In the 3rd-harmonic signal there is no obvious contribution of the far field any more, but a clear near-field signal at distances smaller than 80 nm. At point (3) the far-field signal looks much different. At a distance of 600 nm, all harmonics vanish. The second- and 3rd-harmonic signals show a similar distance dependence as the 1st harmonic, but have smaller absolute values. For z positions close to the second maximum in figure 8.12 the dependence looked the same as for (3), but the amplitude decreased dramatically. These approach curves confirm the above interpretation concerning the focal spot. We thus believe that the tip is in the middle of the focus at the minimum in figure 8.12 between point (2) and (3). The approach curves are consistent with s-SNOM measurements using a CO_2 laser as IR light source [Tau04b, Akh02].

With the direct detection method used in the IR setup, we measure the amplitude of the near-field signal (see section 5.3. To additionally obtain information on the near-field optical phase, an interferometric detection is being planned also for measurements in the IR (see section 2.3, 5.3). This will be part of the PhD thesis of Marcus Cebula.

8.5   Summary

In this chapter, the experimental setup used in this work has been described and discussed in detail. The basic AFM is home-built and designed especially for the examination of polar materials. It can be used in contact mode, mainly to image ferroelectric domains via PFM, as well as in noncontact mode as needed for s-SNOM and KPFM. The noncontact mode, which allows the signal to be demodulated at higher harmonics and hence the far- and near-field signals to be separated,

was used for all s-SNOM measurements. For the visible wavelength regime, we use a heterodyne-interferometric detection system, while for the IR, we measure the backscattered light directly.

Measurements in the visible regime demonstrated how higher-harmonic demodulation suppresses the far-field signal, and provided a clear near-field contrast on a Fischer pattern. For the IR we discussed the dependence of the optical signal on the position of the tip in the focus for a reference sample. The near-field investigation of ferroelectric samples will be discussed in the following chapters 9 and 10.

9   Results on Single-Domain LiNbO$_3$ Single Crystals

In this chapter, we present experimental results achieved by the excitation of the tip-sample system close to the phonon resonances of the ferroelectric LiNbO$_3$ sample at infrared wavelengths. We examine the resonance of the coupled tip-sample system as a function of the tip-sample distance and the wavelength. By comparing the signals obtained with different sample orientations, we prove that the in-plane dielectric properties of the sample contribute to the optical near-field signal. Finally, it is shown that the spectral response of the sample depends characteristically on the polarization of the incident light.

9.1   LiNbO$_3$: Sample Description

LiNbO$_3$[1] is a ferroelectric crystal described in detail in section 3.3. We chose it for near-field investigations, because, being a uniaxial single-domain single crystal, it is as close as possible to the ideal system used for the calculations. In addition it has – due to its high mechanical and chemical stability – a perfectly flat surface with nearly no scratches or defects. The examined sample is highly oriented with its optical axis lying in the plane of the sample surface, i.e. it is a y- cut, or a domain crystal. Hence, when turning the sample macroscopically around the surface normal, we change the orientation of its in-plane optical properties, while the component of the dielectric tensor perpendicular to the sample surface remains unaffected. s-SNOM measurements on this sample were performed for parallel ($a_\parallel$) and perpendicular ($a_\perp$) orientation of the optical axis with respect to the plane of incidence (see figure 9.1a).

As the sample is a single-domain crystal, the optical properties on the nanometer scale are expected to be similar to the macroscopic ones, which are well known from far-field studies. Far-field Fourier transform infrared (FTIR) spectroscopy measurements on our sample are shown in figure 9.2. Reflection and transmission spectra were taken for two different sample orientations with the optical axis either parallel (Fig. 9.2a) or perpendicular (Fig. 9.2b) to the incident electric-field vector. The measured spectra agree very well with the theoretical data obtained

---

[1]Crystal Technologies [Cry07]
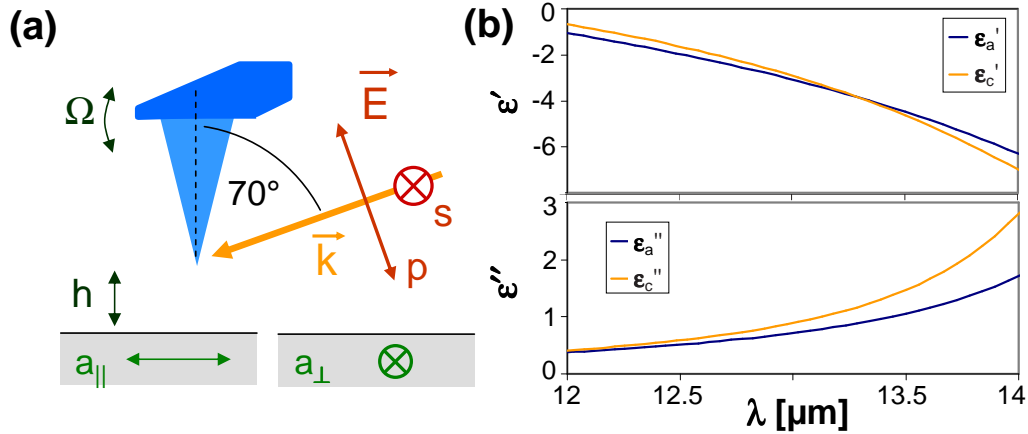
Figure 9.1: (a) Excitation geometry of the s-SNOM setup. Measurements on a domain LiNbO₃ were performed for two different orientations of the anisotropic sample, with the in-plane optical axis being either parallel ($a_\parallel$) or perpendicular ($a_\perp$) to the plane of incidence. (b) Real (ε') and imaginary (ε'') parts of the dielectric function of LiNbO₃ in the relevant wavelength regime.

from the dielectric constants of LiNbO₃ reported in the literature [Bar67] (see section 6.3). From the known components of the dielectric tensor of the sample, we expect to observe phonon resonances in the wavelength range accessible by the FEL around $\lambda = 14.5$ and $15.9\ \mu m$ for the electric field along the optical axis and around $\lambda = 13.2, 17.1$, and $23.2\ \mu m$ for the perpendicular component (see table 6.1). On the high-frequency side of these phonon resonances, the real part of the dielectric constant ε' is close to -1. In this regime, the near-field-coupled tip-sample system shows a resonance due to excitation of a surface polariton in the sample (see section 6.3).

The dielectric constants of the different crystal directions are shown in figure 9.1b for the relevant wavelength range. For both directions the real parts decrease nearly linearly with wavelength and they cross at about 13.3 μm, while the imaginary parts and their difference rise strongly. We expect the region from $\lambda = 12.6$ to 13.6 μm ($\varepsilon = -2$ to -5) to be the relevant one where the polariton can be excited (see section 6.3.1). At 13 μm the dielectric constants differ by $\Delta\varepsilon \simeq 0.2 + i0.2$ corresponding to a relative difference of about 6 % (see figure 9.1). Even though the anisotropy is very small, we expect to measure an optical contrast (see section 6.3.4), which is mainly caused by differences in the imaginary part of the dielectric constant.

9.2   Distance-Dependent Near-Field Spectra

Measuring the characteristic distance dependence of the near-field signal at different wavelengths provides a spectroscopic fingerprint of the coupled system. The signals measured at several higher harmonics form a unique set of data which can be clearly compared to theoretical predictions.
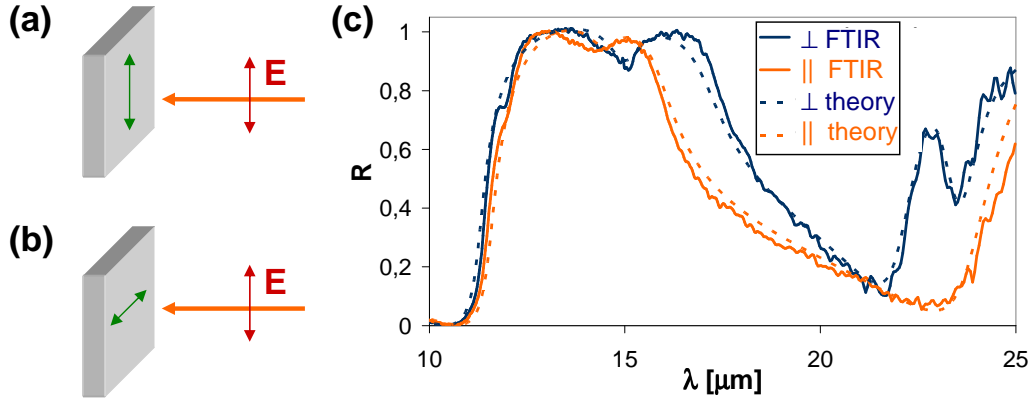
Figure 9.2: *FTIR examination of a LiNbO$_3$ sample. Orientation of the sample with respect to the polarization of the incident light: (a) parallel orientation and (b) perpendicular orientation. (c) Reflection spectra obtained for the two orientations. The solid lines show the normalized measured data, while the dotted lines show normalized theoretical spectra.*

For the distance-dependent near-field spectra we take several approach curves above one and the same sample region at different wavelengths. We usually start at the largest wavelength and then decrease it by widening the undulator gap (see section 8.2). The approach curves were taken by decreasing the tip-sample distance until the damping became 5% higher than under active stabilization of the tip-sample distance by the feedback loop. This corresponds to an additional decrease of the distance by $\Delta h \cong 10 - 20$ nm. During the approach, the PLL, the amplitude controller, and the Kelvin controller are still active to avoid cross talk between the mechanical or electrostatic interaction and the near-field signal (see section 8.2).

During the approach we record the scattered power – demodulated at multiples of the cantilever oscillation frequency (see section 5.3.2)–, the corresponding phase, the mechanical damping, and the current laser power (see figure 8.10). The measurements are repeated at least once for each wavelength to ensure reproducibility. We perform these measurements at several higher harmonics to collect a data set that can be clearly compared to the theoretical data.

Figure 9.3 shows the optical signal measured on the LiNbO$_3$ sample with the optical axis perpendicular to the plane of incidence (see figure 9.1a). The second- and 3$^{\text{rd}}$-harmonic signals shown here represent raw data, whereas the 1$^{\text{st}}$-harmonic data have been corrected: as the signal at 1Ω still contains a large amount of background, we extrapolated the weakly varying background signal measured at somewhat larger distances and subtracted it from the measured data.

In the 1$^{\text{st}}$-harmonic signal we observe a near-field signal at distances smaller than 130 nm. At $h' = 100$ nm, maximum near-field signal is obtained at $\lambda = 12.9$ μm. This maximum shifts towards larger wavelengths for smaller tip-sample distances, being located at $\lambda = 13.05$ μm for $h' \cong 50$ nm and at $\lambda = 13.2$ μm for $h' \cong 20$ nm. In the 2$^{\text{nd}}$-harmonic signal, we observe zero amplitude at points of a phase change
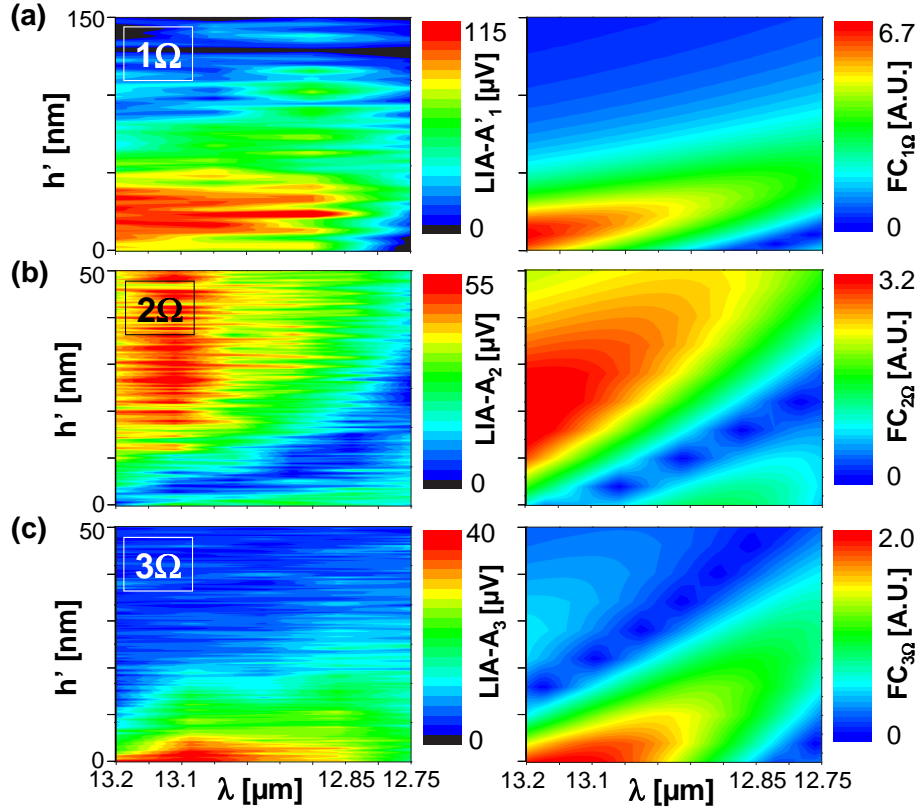
Figure 9.3: *Distance-dependent near-field spectra of LiNbO₃ as demodulated at 1Ω (a), 2Ω (b), and 3Ω (c) measured with a cantilever oscillation of $A \simeq 50$ nm (left column). The optical axis of the crystal was oriented perpendicularly to the plane of incidence. The second- and third-harmonic data represent raw data, whereas the 1st-harmonic data have been corrected by subtracting a linear far-field contribution. The right column shows the corresponding theoretical data as calculated within the dipole model for an isotropic sample with the dielectric constant being $\varepsilon_s = \sqrt{\varepsilon_a \varepsilon_c}$. $h' = 0$ is the smallest measured distance between tip and sample and corresponds to $h \cong 0.7a$ in the calculations (see section 5.1).*

by 180° of the optical signal. This characteristic point moves to larger wavelengths for smaller distances, being located at 13.2 μm for $h' = 0$ nm. The 3rd-harmonic signal has a maximum at about 13.1 μm for $h' = 0$ nm, which moves slightly towards smaller wavelengths for larger distances. The characteristic shift of the resonance with distance as well as the concentration of the signal at the sample surface are typical for the near-field-coupled system as discussed in detail in section 6.3.1. It has also been reported for other systems, such as SiC, which shows a resonance at around 10.5 μm [Tau04b].

In order to compare these results with theoretical data, we calculate the Fourier components of the near-field signal corresponding to the different higher harmonics. As the wavelength range is narrow, we may assume the real and imaginary parts of the dielectric constant to be linearly dependent on the wavelength. The difference

in the optical signal due to the anisotropy of the sample is expected to be small compared to the absolute values. Therefore, in the model calculations we assume the sample to be isotropic with a dielectric constant $\varepsilon = \sqrt{\varepsilon_a \varepsilon_c}$ representing the geometric mean of the components of the dielectric tensor.

We plot the calculated optical amplitude as a function of the wavelength λ and the distance h in units of the tip radius. In order to compensate for a constant far-field contribution in the 2nd harmonic signal we added an offset of 1.5 to the corresponding theoretical data set. Knowing both the real cantilever oscillation amplitude and the total distance moved during the approach, we are able to determine the size of the part of the tip contributing to the near-field signal to be around 600 nm. This does not directly represent the radius of the tip apex, but rather the part effectively contributing to the higher-harmonic signal [Sch07c].

We find that the calculations fit the measured data quite well for all harmonics. The positions of the resonance as well as the correlation between the different higher harmonics are alike. Having a closer look at the scale bars of the plotted data, we see that even the ratios between the different harmonics are the same for experiment and theory. The correlation of experiment and theory indicates clearly that we have found the sample-induced resonance of the system. In the following section we discuss the influence of the in-plane anisotropy on the near-field signal.

9.3   LiNbO$_3$: Anisotropy Contrast V_{aa}

In order to examine the influence of the anisotropy of the LiNbO$_3$ sample, we perform measurements for two different orientations of the sample with respect to the plane of incidence as shown in figure 9.1a. While the sample is turned by 90°, the tip is not moved at all and thus remains at the same focus spot. As the LiNbO$_3$ sample is a highly uniform single-domain crystal, the data obtained with the two different orientations are comparable even though they were not taken on exactly the same spot on the sample. We cannot exclude changes of the far-field signal due to a slightly different tilt of the sample. However, the spectral behavior of the near-field signal should not be affected by this. Turning the sample leaves the out-of-plane dielectric constant unchanged, whereas the optical axis is rotated from perpendicular to parallel orientation with respect to the plane of incidence. Theoretical calculations have predicted that this will change the near-field signal due to the in-plane anisotropy (see section 6.3.4).

In figure 9.4, distance-dependent near-field spectra of the 2nd- and 3rd- harmonic signals are shown for the two different sample orientations. These data were acquired across a much larger wavelength range than the data displayed in figure 9.3. We observe a clear difference between the two cases in the spectral dependence as well as in the distance dependence and in the intensities.

For perpendicular orientation of the optical axis with respect to the plane of incidence ($a_\perp$, fig. 9.4a,b), the distance-dependent near-field spectrum shows the
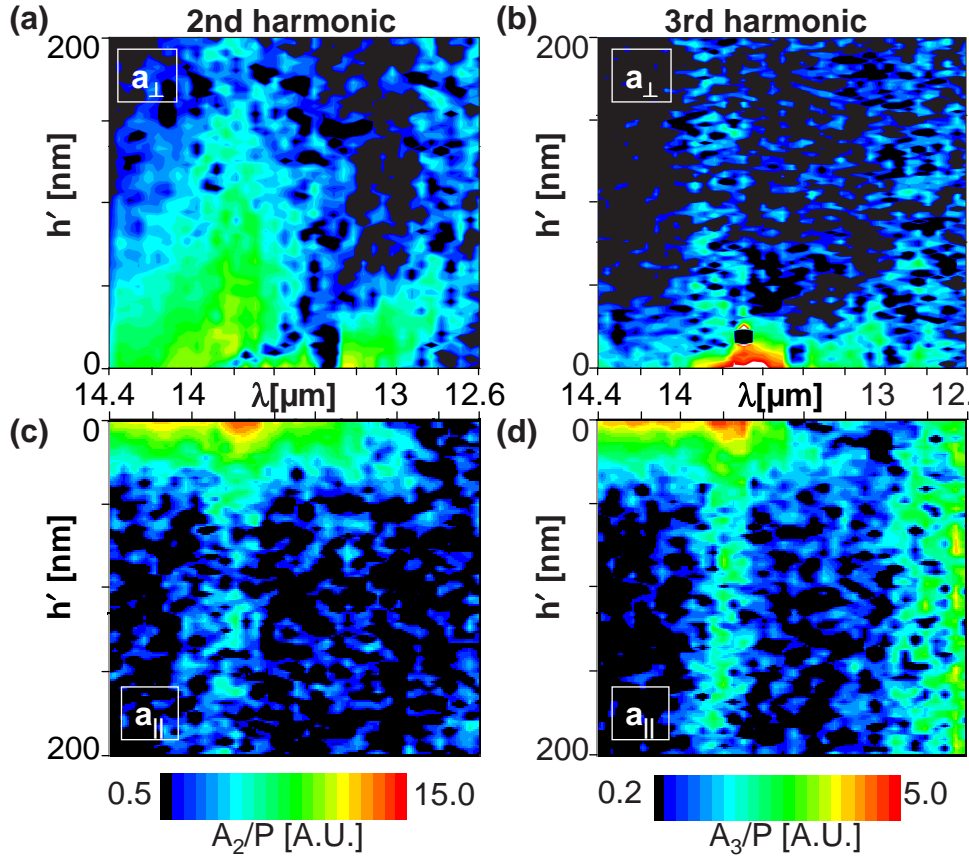
Figure 9.4: *Distance-dependent near-field spectra at the 2ⁿᵈ and 3ʳᵈ harmonics (p-polarized light) for different orientations of a LiNbO₃ single crystal with the c axis either (a), (b) perpendicular ($a_\perp$) or (c), (d) parallel ($a_\parallel$) to the plane of incidence. The data have been normalized to the corresponding laser power and corrected for the spectral dependence of the beam splitter and of the detector sensitivity. The bright lines around 13.8 µm correspond to an absorption line of the beam splitter (see fig. 8.11) which increases the noise level upon normalization of the data.*

typical near-field shape of the higher harmonics with lobelike resonances shifting to larger wavelength with decreasing h (see section 6.3.1). In the 2ⁿᵈ-harmonic signal we clearly observe two maxima, one around 14 µm and a smaller one at around 13.2 µm for $h' = 0$ nm. The 3ʳᵈ-harmonic signal is fairly small, but still shows correlative information. Comparing the results with theoretical predictions, we find that the signal on the $a_\perp$ domain is well described by the dipole model. From theory we expect a maximum scattering cross section at around 13.3 µm for $h \cong 0.7a$ (see section 6.3.4). Compared to that value, the measured spectrum is slightly shifted to larger wavelengths by $\Delta\lambda \cong 0.5$ µm. This shift might be caused by an offset of the signal which changes the ratio between the two lobes or it might be caused by a deviation of the local dielectric constant. Determining the absolute value of the dielectric constant is up to now not possible, as a statistically significant number of

reference measurements is not available yet.

When the optical axis is parallel to the plane of incidence ($a_\parallel$, fig. 9.4c,d), the signal looks completely different: In the 2$^{\text{nd}}$-harmonic signal we observe an enhancement close to the sample surface for wavelengths larger than 13 μm. There is no distinct shift of this resonance with distance in contrast to the former case. As this data is reproducible and as the corresponding 3$^{\text{rd}}$ harmonic signal shows the same spectral behavior, we are sure that this is a true near-field signal. For this sample orientation, the dipole model predicts a near-field signal which is very similar to the one on the $a_\perp$ domain, as the dielectric constants differ only slightly. A maximum is expected at around $\lambda \cong 13.3$ μm as well. Neither the reflection at the sample surface nor a tilt of the sample surface affects the signal in the way the measured data show. An explanation for the blurred spectrum could be that the signal is a complex superposition of the two near-field components, namely parallel and perpendicular to the sample surface, and of the reflection. A theoretical proof of this assumption could not be achieved yet.

The measurements above clearly show a change in the optical near-field signal due to the in-plane anisotropy of the sample. These are the first experimental results confirming the theoretical prediction that changes of the in-plane dielectric constant are measurable.

Additionally, in the case of a resonant sample, the parallel modes of the near-field-coupled system are expected to be sufficiently enhanced to be of measurable size (see section 6.3). In the following we examine the spectral response of the different components of the near-field-coupled system by using different polarizations of the incident light.

9.4   Polarization Dependence of Near-Field Spectra

In order to study the correlation between near-field spectra as shown in figure 9.4 and the orientation of the dielectric tensor of the sample, we perform measurements for different polarizations of the incident light (s and p). The orientation of the electric field of the incident light defines the directions of the tip dipole and of its corresponding image dipole in the sample.

The dipole model predicts different spectral positions of the tip-sample resonances for the tip dipole being oriented perpendicularly or parallel to the sample surface (see section 6.3). For an anisotropic medium with $\tan\tau = \sqrt{(\varepsilon_a - \varepsilon_c)/\varepsilon_c} = 0.3$ we expect a splitting of the parallel component. Assuming $h = 0.7a$ and with the definition $\varepsilon_s^{pol} = \sqrt{\varepsilon_a \varepsilon_c}$, the poles are located at $\varepsilon_x^{pol} = -2.07$, $\varepsilon_y^{pol} = -2.12$, and $\varepsilon_z^{pol} = -6.23$ for x, y, and z orientation of the tip dipole, respectively (see section 6.3.1). For p-polarized light, the incident electric field and, hence, the induced tip dipole have components perpendicular as well as parallel to the sample surface in the plane of incidence. For parallel-oriented LiNbO$_3$ ($a_\parallel$), we expect to excite the resonances at ε_z^{pol} and ε_y^{pol}, which occur at different wavelengths. The spectrum is
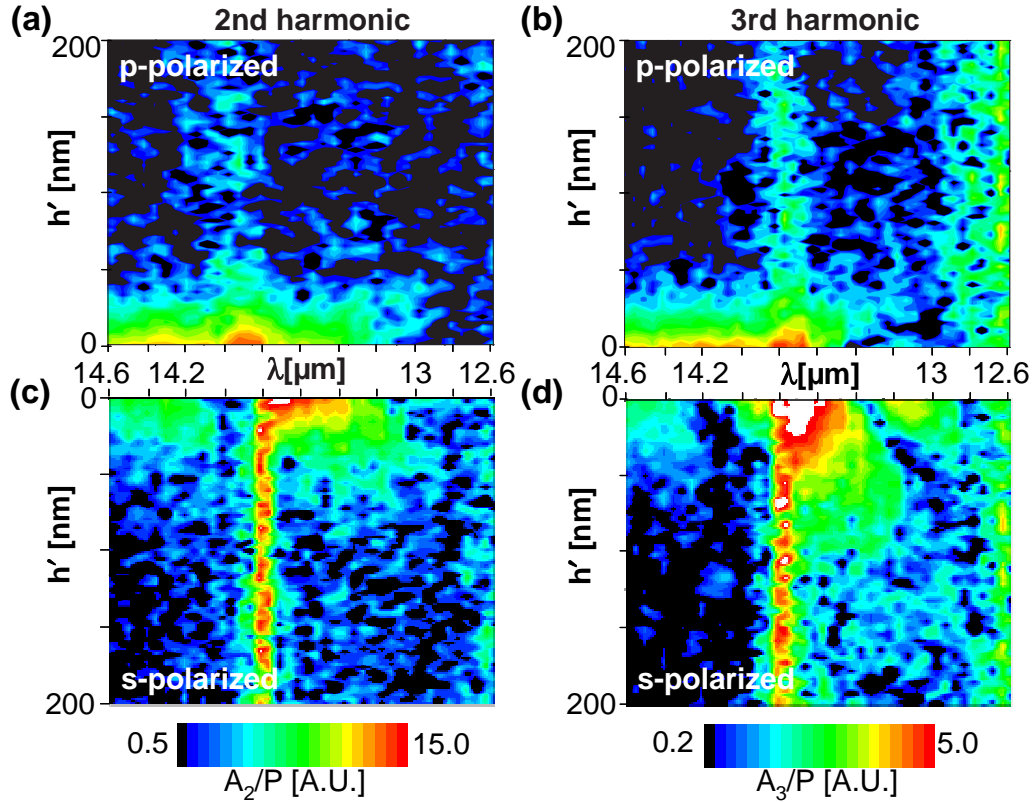
Figure 9.5: *Distance-dependent near-field spectra at the 2ⁿᵈ and 3ʳᵈ harmonics for a parallel-oriented LiNbO₃ single crystal (a₍ₗ₎) and different polarizations of the incident light. For different polarizations we observe different spectral behaviors. The acquired data have been normalized to the corresponding laser power and corrected for the spectral dependences of the beam splitter and of the detector sensitivity. The bright lines around 13.8 µm correspond to an absorption line of the beam splitter (see fig. 8.11) which increases the noise level upon normalization of the data.*

a superposition of the two individual resonances. In comparison, *s*-polarized light produces a field that is purely parallel to the sample surface and perpendicular to the plane of incidence, corresponding to the pole ε_x^{pol}. As we only excite one resonance with *s*-polarized light, the spectrum is expected to show the typical lobelike shape as discussed in section 6.3.1.

Figure 9.5 shows the measured near-field spectra of the 2ⁿᵈ- and 3ʳᵈ-harmonic signals for the orientation of the optical axis parallel to the plane of incidence $(a_{\parallel})$. Figures 9.5a,b show the signals for *p*-polarized incident light, the same data as depicted above in figure 9.4. As discussed above, the spectra do not show the characteristic lobelike dependence of the near-field signals. Instead, we observe a spectrally broad signal enhancement close to the sample surface for wavelengths larger than 13 µm. This behavior could be caused by a superposition of the poles in y and z direction as well as an additional contribution from the reflection at the

Orientation	Polarization	Excitable Poles	Contribution to r_{ik}
$\parallel$	s	ε_x^{pol}	ε_a
$\parallel$	p	ε_y^{pol}, ε_z^{pol}	ε_a, ε_c
$\perp$	s	ε_y^{pol}	ε_c
$\perp$	p	ε_x^{pol}, ε_z^{pol}	ε_a

Table 9.1: *Possible combinations of sample orientation and polarization of the incident light for LiNbO$_3$: Excitable poles expected from dipole-dipole interaction with $\varepsilon_{pole} = \sqrt{\varepsilon_a \varepsilon_c}$ (see section 6.3) as well as contributions to the reflection coefficient r_{ik}, i.e. r_{pp} for p-polarized light and r_{ss} for s-polarized light.*

sample surface.

For s-polarized incident light (figures 9.5c,d), we observe exactly the spectral behavior expected from the dipole model. We observe several maxima with opposite phases in both harmonics (see section 5.3.2). In the 2nd-harmonic signal (fig. 9.5c), we measure two maxima at 14.2 μm and 13.5 μm for $h' = 0$ nm. The 3rd harmonic, being in first approximation the derivation of the 2nd harmonic, shows three maxima at 14.5, 13.7, and 13.1 μm. From theory, we expect the resonance to be located at around 12.4 μm. The deviation of about $\Delta\lambda \cong 1$ μm is much larger than for p-polarized light, and not fully understood yet. However, the spectral lobelike behavior as well as the magnitude of the signal correspond to the expected values. As expected for the sample-induced resonance of the system, the magnitude of the in-plane component of the tip-sample dipole is on the same order of magnitude as for the out-of-plane component.

At the wavelengths at which the s-component has a maximum, the corresponding p-polarized data also show a clear near-field signal. This indicates that, in principle, the latter could include a contribution of the in-plane component superposed with an out-of-plane component and reflection effects as assumed above.

The measurements for a parallel-oriented sample ($a_\parallel$, fig. 9.5) showed the influence of the polarization on the near-field signal. According to the orientation of the electric field, we assume that with s-polarized or p-polarized light, we excite one pole ε_x^{pol} or two poles ε_y^{pol} and ε_z^{pol}, respectively. For a perpendicularly oriented sample ($a_\perp$), we expect to excite the same pole ε_z^{pol} with the z component of the p-polarized light. The poles parallel to the sample surface are expected to be interchanged, due to the rotation of the sample by 90°, resulting in ε_x^{pol} for the parallel component of the p-polarized light and in ε_y^{pol} for s polarization (see table 9.1). As the parallel poles are located at nearly the same dielectric constant $\varepsilon_x^{pol} \cong \varepsilon_y^{pol} \cong -2.1$, the dipole model predicts the spectra of the two orientations to look very similar and to be only slightly shifted in the frequency. Additionally, we have to take the reflection at the sample surface into account, which depends on the orientation of the sample and on the polarization of the incident light (see section 6.1.4). The components of the dielectric tensor that contribute to the reflection coefficient are additionally listed in table 9.1.
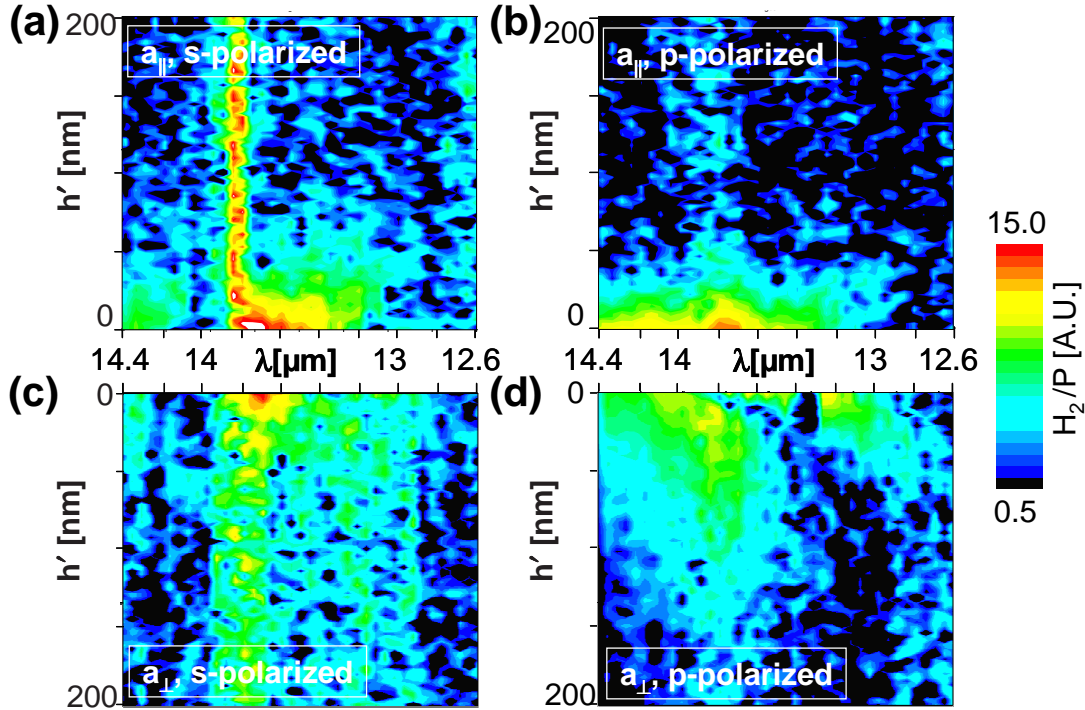
Figure 9.6: *Distance-dependent near-field spectra acquired with 2nd-harmonic demodulation for all possible combinations of polarization and orientation of the a domain LiNbO₃ sample.*

In figure 9.6 we compare the distance-dependent spectra for all the possible combinations of sample orientation and polarization listed in table 9.1. Both spectra for *s*-polarized light (fig. 9.6a,c) show the typical spectral behavior of a single sample resonance as expected from the dipole model. The signal for the perpendicularly oriented sample is weaker, which can be explained by a slightly smaller reflectivity. The spectra for *p*-polarized light look very different (fig. 9.6b,d): The parallel-oriented sample shows a mixed spectrum as discussed above, while the spectrum for the perpendicular orientation looks like a single-resonance spectrum, which is even more distinct than for *s*-polarized light. Although both orientations should be characterized by a superposition of parallel and perpendicular poles, a blurred resonance appears only for the parallel-oriented sample. We propose that this behavior, which cannot be explained by the simple dipole model, is caused by reflection at the sample surface: As shown in table 9.1 and as specified in section 6.1.4, only for the $a_\parallel$ domain and for *p*-polarized light, we expect a reflection that depends on both elements of the dielectric tensor and which is additionally correlated with the degree of anisotropy of the sample (eq: 6.24).

Even though the interpretation of the data is very difficult, we believe that the model of superposed poles describes the data adequately. Furthermore, we will study the polarization dependence also on BaTiO₃ to confirm the results by using a different sample (section 10.2).
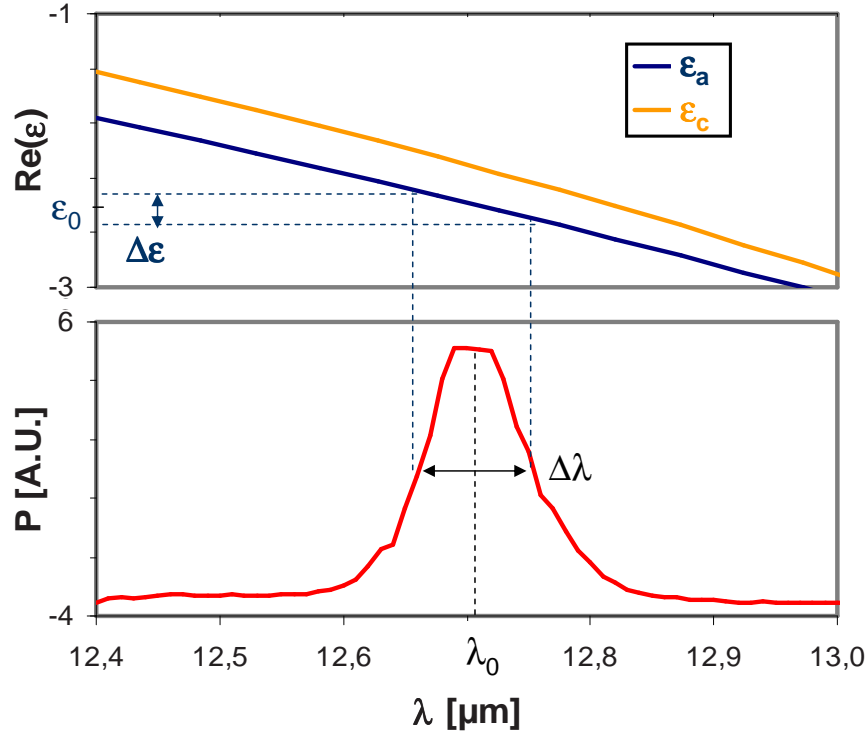
Figure 9.7: *Spectral width $\Delta\lambda$ of the free-electron laser at $\lambda_0 \cong 12.71 \ \mu m$. $\Delta\lambda$ causes an uncertainty $\Delta\varepsilon$ of the corresponding dielectric constant ε_0.*

9.5   Resolution in Distance-Dependent Near-Field Spectra

The spectral resolution of the distance-dependent near-field spectra is mostly limited by the spectral width of the laser light, but also by the accuracy of the distance between tip and sample.

Figure 9.7 shows the laser intensity as a function of the wavelength. The center wavelength of the depicted spectrum is $\lambda_0 \cong 12.71 \ \mu m$ and the corresponding width $\Delta\lambda \cong 100$ nm. This behavior is typical in the wavelength range used for the near-field examination of $LiNbO_3$ and $BaTiO_3$. As the laser line has a certain width, also the corresponding dielectric constant ε_0 has an uncertainty $\Delta\varepsilon$, which is 0.25 in the example of figure 9.7.

Zero distance between tip and sample is defined by the condition applied to terminate the acquisition of the approach curve, namely a certain damping of the cantilever oscillation. This position is reproducible with an accuracy of 5 nm for a typical approach length of 1 μm. Decreasing this length increases the accuracy. During the approach, the distance is changed by the piezoelectric tube used also for scanning. Any errors arising from the applied control voltage or from the piezoelectric response of the piezotube are negligible compared to the uncertainty caused by the determination of $h = 0$ nm.

9.6   Summary

On LiNbO$_3$ we studied the near-field signal close to the resonance of the tip-sample system induced by a sample phonon polariton. The observed resonances show the expected spectral behavior, including the characteristic shift of the resonance to larger wavelengths when the tip-sample distance is decreased. The experimental data match the theoretical prediction very well. On the LiNbO$_3$ single crystal we studied the influence of different orientations of the dielectric tensor by macroscopically rotating the sample. We were able to measure a clear difference between two orientations of the sample. Furthermore, polarization-dependent measurements were performed for different orientations of the sample, showing a characteristic that is explainable by the dipole model provided that reflection at the sample surface is taken into account. The measurements for the first time confirmed the influence of the in-plane anisotropy on the near-field signal.

10 Results on Multi-Domain BaTiO$_3$ Single Crystals

On BaTiO$_3$ we measure distance-dependent near-field spectra on different domains of the sample. An anisotropy contrast is observed between different types of domains having an orientation of the optical axis either parallel or perpendicular to the sample surface. Hence, the optical contrast is not only caused by in-plane changes of the dielectric tensor, but also by changes perpendicular to the sample surface. The dependence of the near-field spectra on the polarization is examined, showing the coupling of the electric field to different components of the dielectric tensor.

As the multi-domain sample shows a certain domain structure, it is possible to measure so-called line-scan near-field spectra: While scanning along a line on the sample surface that crosses several domains, we measure the near-field spectrum. Hence, we can correlate the near-field resonances at different wavelengths with the lateral domain distribution of the sample. Systematic studies are done for various harmonics, s and p polarization, as well as different amplitudes of the cantilever oscillation. At selected wavelengths we perform two-dimensional scans showing clearly the domain distribution in the near-field signal. By choosing the wavelength carefully, we are able not only to maximize the contrast between the domains but even to reverse this contrast at a characteristic wavelength.

10.1 BaTiO$_3$: Sample Description

The ferroelectric BaTiO$_3$ samples used in this work are single crystals[1] with a polished (100) surface. Due to the mechanical polishing procedure, the surface is slightly rougher than the surface of LiNbO$_3$. The samples used show a striped structure of alternating a and c domains. The orientation of this structure with respect to the plane of incidence is shown in figure 10.1a: the domain walls on the surface are oriented perpendicularly to the plane of incidence. Due to the crystallographic structure, the topography is not flat, but shows a small tilt of the surface of typically 0.6° between a and c domains [Gru97a]. This tilt is indicated in fig. 10.1a as well as the fact that the 90° domain walls between a and c domains run through the crystal

---

[1] BaTiO$_3$ standard quality crystals, MaTeck GmbH [Mat07]
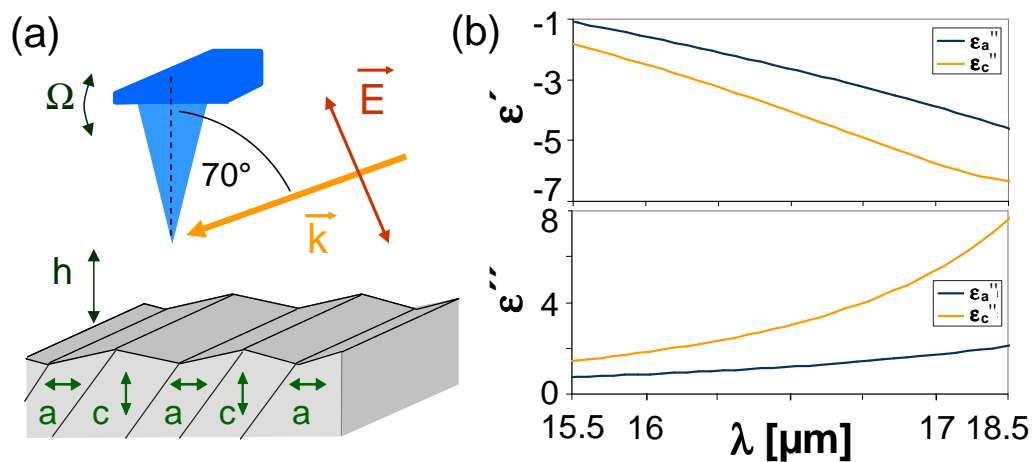
Figure 10.1: *(a) Excitation geometry of the s-SNOM setup for the examination of BaTiO₃. Measurements on BaTiO₃ were performed for orientation of the 90° domain walls perpendicular to the plane of incidence. For such an orientation, the optical axis of the a domain is oriented parallel to the plane of incidence. The optical axis of the cylindrically symmetric c domains is always oriented perpendicularly to the sample surface, i.e., parallel to the plane of incidence. (b) Real and imaginary parts of the dielectric function of BaTiO₃ in the relevant wavelength range.*
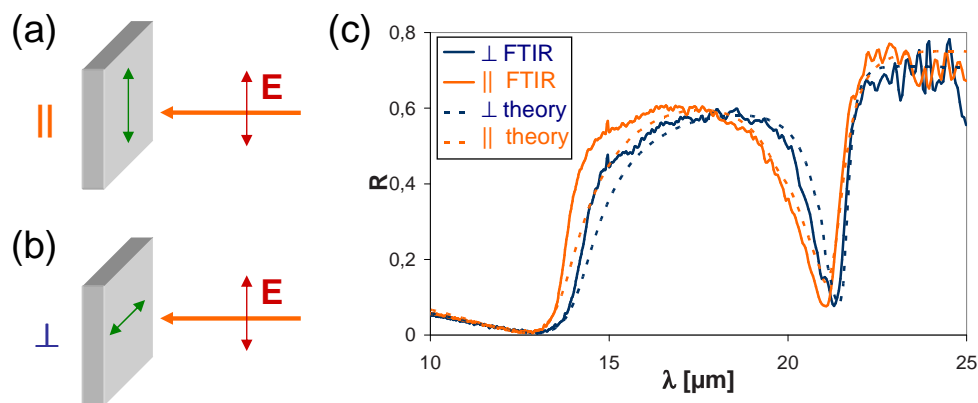
Figure 10.2: *FTIR examination of BaTiO₃ sample. Orientation of the sample with respect to the polarization of the incident light: (a) parallel orientation and (b) perpendicular orientation. (c) Reflection spectra obtained for the two orientations. The solid lines show the normalized measured data while the dotted lines show normalized theoretical spectra.*

(a) Topo

(b) KPFM
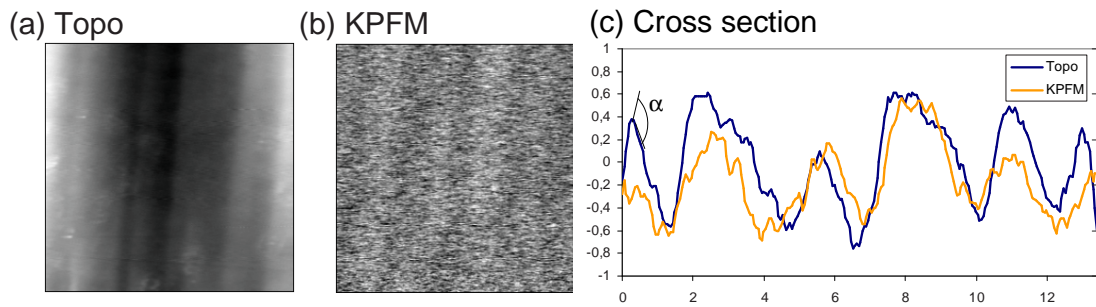
(c) Cross section

Figure 10.3: *(a) AFM and (b) simultaneous KPFM measurements on BaTiO$_3$ with a scan range of $(13.4 \ \mu m)^2$ and a z range of 10 nm. The graph in (c) shows a cross section of the topography with an angle of $\alpha \cong 0.14°$ between a and c domains, and the corresponding KPFM data averaged over about 50 lines to decrease the noise.*

at an angle of 45° with respect to the (100) sample surface (see also section 3.2).

As for LiNbO$_3$, the optical properties were studied with Fourier transform infrared (FTIR) spectroscopy in transmission and reflection. Figure 10.2 shows the reflection spectra for two different orientations of a single-domain BaTiO$_3$ crystal, which was bought from the same company [Mat07] as the multi-domain crystal. The orientation of the optical axis with respect to the polarization of the incident light is either parallel (fig. 10.2a) or perpendicular (fig. 10.2b). We compare the measured spectra with those calculated from theoretical values of the dielectric constant (see section 6.3, [Ser80]). In all curves we observe a minimum in the reflection at around 21 μm. The position of this minimum agrees very well with the theoretical data. For smaller wavelengths, the theoretical data are slightly different from the measured curves, which may be attributed to our sample being doped. However, we expect the theoretical data to represent the sample properties very well in the relevant wavelength range around 18 μm.

As for the LiNbO$_3$ sample, close to the phonon resonance of the sample, the real part of the dielectric constant is negative and therefore fulfills the resonance conditions of the near-field-coupled tip-sample system. The dielectric constants in the relevant wavelength range are shown in figure 10.1b. Both real parts are negative and decrease with larger wavelengths, while the imaginary parts increase. The difference between the two crystallographic directions is much larger than for LiNbO$_3$. In the interesting regime, the real parts differ by up to 50 % and the imaginary parts even by up to 200 %.

The domain structure is well known from scanning probe microscopy images of topography (AFM), surfaces charges (KPFM), and piezoelectric response (PFM) (see section 4), which were taken before, during, and after the acquisition of the s-SNOM pictures.

Figure 10.3a shows AFM and KPFM measurements of the same sample area that is examined also optically by s-SNOM. In both pictures we can faintly discern the
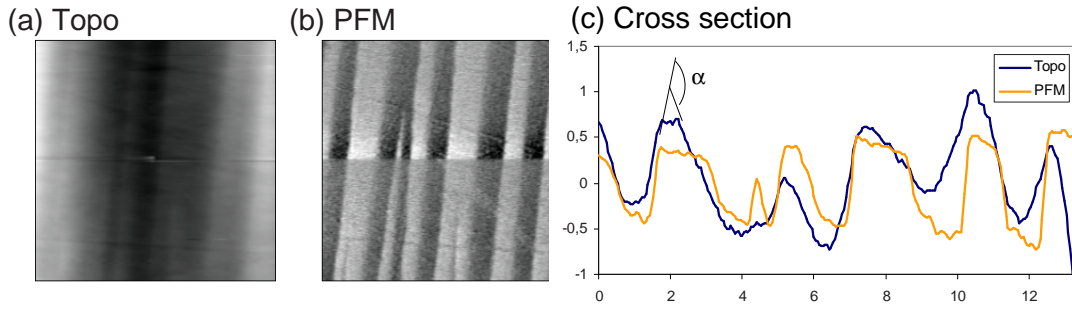
Figure 10.4:   *(a) Topography and (b) simultaneous out-of-plane PFM-measurement on BaTiO₃ with a scan range of (13.4 μm)². We observe the typical striped domain structure of alternating* a *and* c *domains. (c) Cross sections of the topography and of the corresponding PFM data showing again the angle of α ≅ 0.13° as in figure 10.3 and respectively a pronounced difference between* a *and* c *domains. Please note that the horizontal line in the PFM image is caused by the interaction of the tip with a particle which is imaged at the same position in the topographic image. The line is not correlated with the piezoelectric properties of the sample.*

stripelike domain structure. In the AFM picture we see the typical tilt of the surface, described in detail in section 3.2. In the KPFM picture we observe the difference in surface charge between different domains. The charge distribution is blurred most likely because of the presence of a water film on the sample under ambient conditions (see section 4.3). Figure 10.3c shows a cross section of the topographical and KPFM pictures. The slope change between a and c domains was analyzed to be about 0.14°. This is much smaller than the expected typical angle of 0.6° reported in the literature [Gru97a]. This indicates that the surface of the BaTiO₃ single crystal is not exactly a (100) surface but slightly tilted by about 0.4° due to the polishing procedure. This explains also the the needle shape of some of the domains [Eng07]. In a perfect crystal, no needles should be formed, but perfectly parallel stripes. The KPFM data seems to reproduce the topography more than the charge distribution.

PFM offers a more direct examination method of the domain distribution (see section 4.2). Although it requires the AFM to be operated in the contact mode and therefore cannot be performed in parallel with SNOM, but only before and afterwards, it is the most common and certain way to know the exact domain distribution of the sample. Figure 10.4 shows a PFM and a topography image taken in AFM contact mode. The topography again reflects the typical tilt of the surface, while the piezoresponse image shows the striped domain distribution. From additional experiments including switching of the domains it follows that the bright stripes correspond to c domains, while the dark stripes are a domains. In figure 10.4c cross sections of the AFM and PFM images are depicted. Again we observe an angle of 0.13° between different types of domains, confirming the measurements in noncontact mode. The PFM cross section shows basically two levels of the signal coinciding

with positive or negative slopes, respectively, in the AFM picture. This agrees very well with the assumption that the bright areas are c domains, while the dark areas are a domains.

Knowing the domain distribution of the sample and the direction of the surface tilt allows us to also derive the direction of the 90° domain walls within the bulk crystal. As already sketched in figure 10.1a it runs through the crystal at an angle of 45° with respect to the sample surface and 125° with respect to the incident k vector. This will play a role in the interpretation of the scan data discussed in sections 10.4 and 10.5.

In the following studies we always perform additional PFM measurements to unambiguously correlate the optical data to the domain pattern. While measuring the s-SNOM signals, we perform KPFM at the same time, not only in order to image the domain distribution but, even more importantly, in order to minimize the electrostatic interaction between tip and sample (see section 4.3).

In the next section we will discuss the results of the distance-dependent near-field spectra on BaTiO$_3$.

10.2   Distance-Dependent Near-Field Spectra

On the BaTiO$_3$ samples we perform distance-dependent spectroscopy studies. A general description of this method is given in section 9.2 for LiNbO$_3$. Here we perform the same kind of measurement in another wavelength range, close to a phonon resonance of the BaTiO$_3$ sample. We took distance-dependent near-field spectra for the 1st to 4th harmonics on both a and c domains.

In figure 10.5 the experimental results are shown for the 2nd to 4th harmonics (left-hand side) in comparison with theoretical calculations (right-hand side). Even more pronounced than on LiNbO$_3$, maxima appear in the spectrum of the near-field signal. They shift to larger wavelengths when the distance between tip and sample is decreased. This is observed in all higher harmonics: In the 2nd-harmonic signal we measure a near-field signal at distances of up to 140 nm at around 16.6 μm. This resonance broadens close to the sample and at the same time moves to larger wavelengths, reaching 17.5 μm at zero distance. In the 3rd-harmonic signal, we observe a maximum at a distance of about 90 nm at around 16.8 μm which moves to 17.6 μm at zero distance. The 4th harmonic shows two maxima with opposite phase, one moving from 17.2 μm at a distance of 50 nm to 17.7 μm at the surface, and the second moving from 16.3 μm at 10 nm distance to 16.6 μm at the surface.

Again the experimental data match very well the theoretical spectra for all harmonics. As the results again show the predicted dependences, we believe that our method is working quite well.

In the following section we compare spectra on different domains for selected polarizations of the incident light.
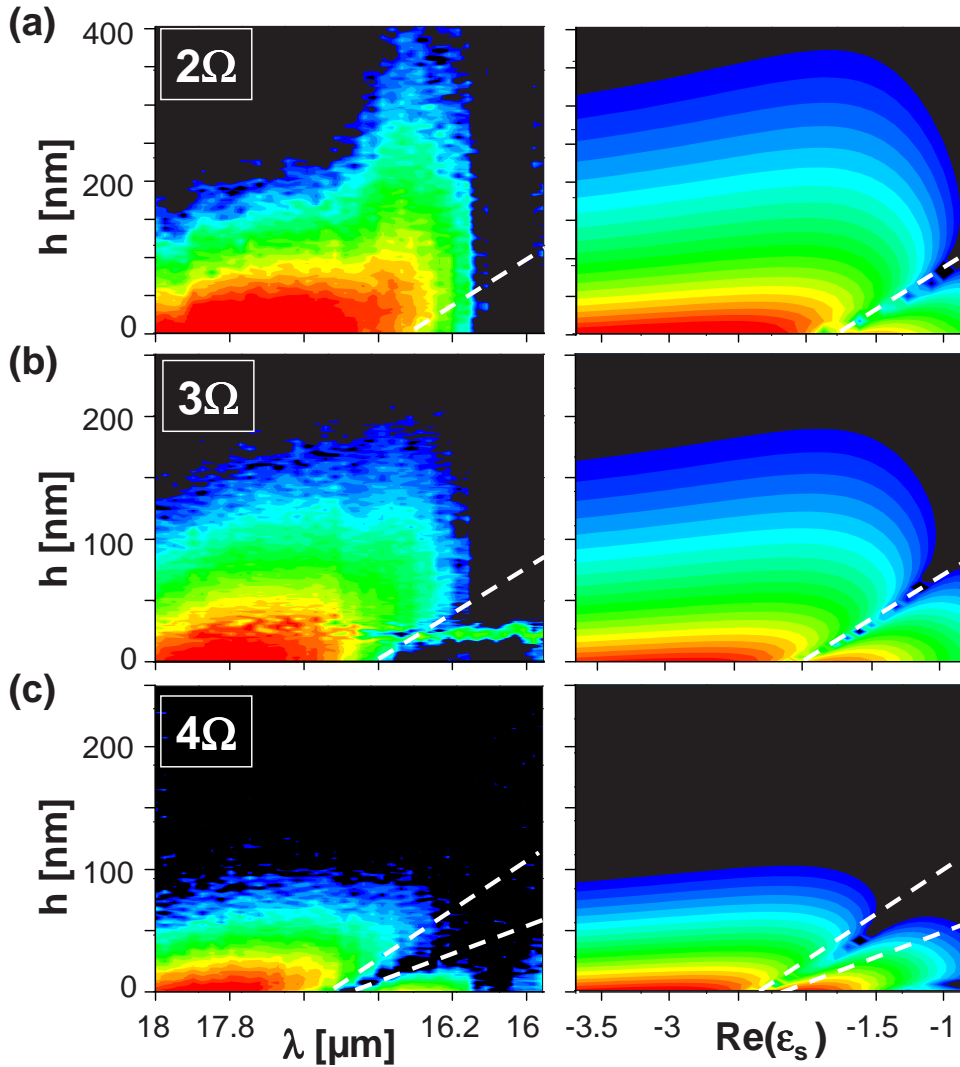
Figure 10.5: *Distance-dependent near-field spectra of BaTiO₃ with the optical axis oriented perpendicularly to the sample surface (c domain) and p-polarized incident light (left column). The near-field signal was demodulated at (a) 2Ω, (b) 3Ω, and (c) 4Ω. All data represent raw data, normalized to the current laser power. The right column shows the corresponding theoretical data as calculated within the dipole model. The dashed lines are shown for easier comparison of the data in the left and in the right column.*

Domain	Polarization	Excitable Poles	Contribution to r_{ik}
c	s	$\varepsilon_{x,c}^{pol}$	ε_a
c	p	$\varepsilon_{x,c}^{pol}$, $\varepsilon_{z,c}^{pol}$	ε_a, ε_c
a	s	$\varepsilon_{x,a}^{pol}$	ε_a
a	p	$\varepsilon_{y,a}^{pol}$, $\varepsilon_{z,a}^{pol}$	ε_a, ε_c

Table 10.1: *Possible configurations of domains on the BaTiO$_3$ sample and polarizations of the incident light and the corresponding excitable poles expected from dipole-dipole interaction with $\varepsilon_s^{pol} = \sqrt{\varepsilon_a \varepsilon_c}$ (see section 6.3). Additionally, we list the elements of the dielectric tensor contributing to the corresponding reflection coefficient r_{ik}: r_{pp} for p-polarized light and r_{ss} for s-polarized light.*

10.3   BaTiO$_3$: Anisotropy Contrast V_{ac} in Distance-Dependent Near-Field Spectra

As the sample is oriented as shown in figure 10.1a, the electric field may excite the following poles of the tip-sample system (see table 10.1). For s-polarized light, it has a component along the x axis of the sample on both a and c domains, corresponding to poles at $\varepsilon_{x,a}^{pol}$ and $\varepsilon_{x,c}^{pol}$, respectively, (see section 6.3.1)[2]. For p-polarized light, the tip dipole has components both perpendicular and parallel to the sample surface. In both cases, one component is along the c axis, namely the perpendicular component on the c domain and the parallel component on the a domain. The corresponding excitable poles are $\varepsilon_{z,c}^{pol}$ and $\varepsilon_{y,c}^{pol} = \varepsilon_{x,c}^{pol}$ for the c domain and $\varepsilon_{z,a}^{pol}$ and $\varepsilon_{y,a}^{pol}$ for the c domain (see table 10.1). As for LiNbO$_3$, the reflection at the sample surface contributes as well to the near-field signal. The correlation of reflection coefficients and the elements of the dielectric tensor depends on the domain type and on the polarization of the incident light (see table 10.1).

In figure 10.6 the distance-dependent near-field spectra for 2$^{\text{nd}}$- and 3$^{\text{rd}}$-harmonic demodulation are shown for p-polarized incident light on the c domain (fig. 10.6a,b) and the a domain (fig. 10.6c,d). We observe a distinct spectral behavior with distance-dependent resonances. Even for the third harmonic we have a clear signal up to 50 nm above the sample. For both harmonics, we observe two maxima, at around 17.7 μm and 16.7 μm for the smallest distance between tip and sample, which corresponds very well with the resonance around 18.1 μm expected from the dipole model (see section 6.3.5). The two maxima are 180° phase-shifted and the corresponding zero crossing is located at around 17 μm. No strong blurring of the spectra due to reflection is observed as it was the case on LiNbO$_3$. The only anomaly in the spectra of both harmonics is a small dip in the near-field intensity at around 17.9 μm on the c domain and at 17.7 μm on the a domain (arrows in figure 10.6). As these dips are reproducible and as they are located at different wave-

---

[2]The indices a and c at indicate that the anisotropy factors on the a and on the c domain are different (see section 6.1.3).
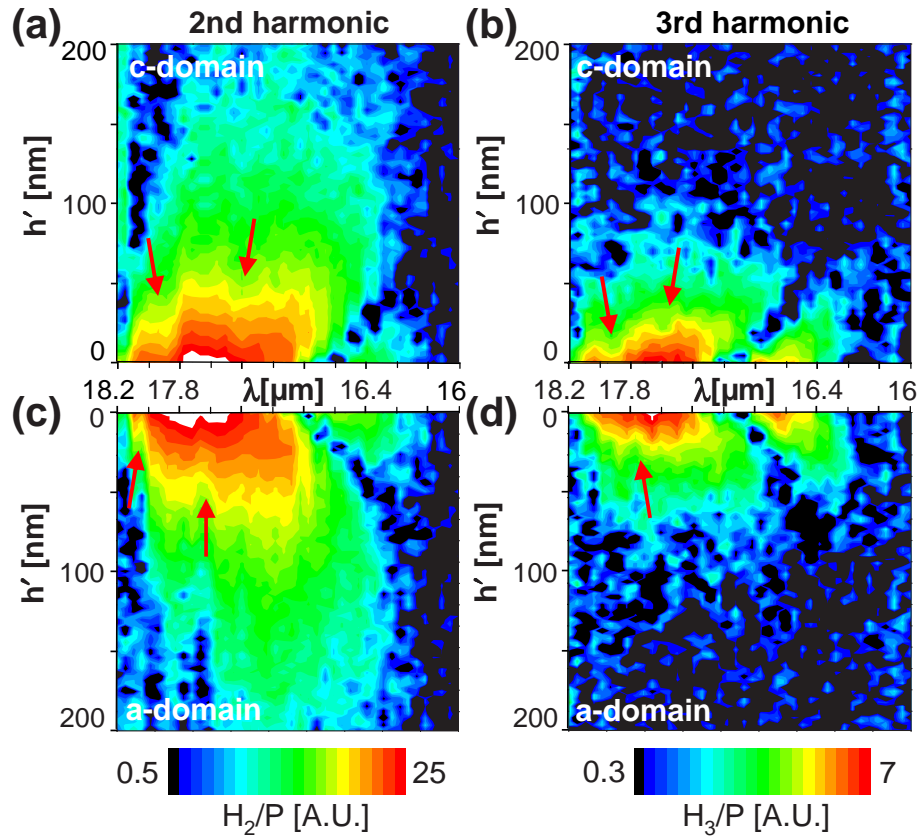
Figure 10.6: *Distance-dependent near-field spectra of the 2nd- and 3rd-harmonic signals on different domains of the BaTiO₃ sample for p-polarized incident light. The upper two pictures show the data on a c domain with the optical axis perpendicular to the sample surface, while the lower two data sets were taken on an a domain with the optical axis parallel to the sample surface and to the plane of incidence. The arrows mark dips which may correspond to the superposition of two excited poles.*

lengths for the two different domains, it seems to be a true near-field effect, which may correspond to the superposition of the two poles perpendicular and parallel to the sample surface. The pole at larger λ corresponds to a more negative dielectric constant and is thus most likely the pole perpendicular to the sample surface, while the pole at smaller wavelength is also observable for s-polarized light as discussed in the following paragraph.

Figure 10.7 shows the corresponding spectra for s-polarized incident light on the two different domain types for the 2nd and 3rd harmonics. Again we observe a clear near-field signal with two maxima: For the smallest distance between tip and sample, one is located at around 17.4 μm and the other at around 16.4 μm. Both maxima are located at much larger wavelength than expected from the dipole model, which predicts a resonance at 15.6 μm. Again the maxima are of opposite phase and the corresponding zero crossing is located at around 16.8 μm.
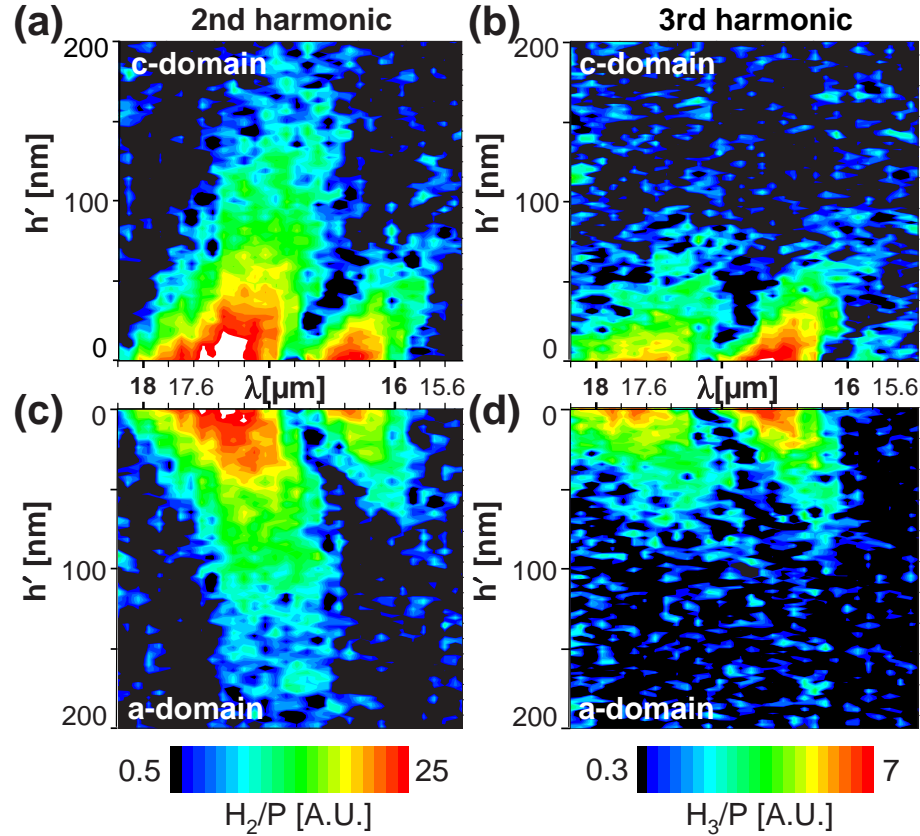
Figure 10.7: *Distance-dependent near-field spectra on different domains of $BaTiO_3$ for 2nd- and 3rd-harmonic demodulation and for s-polarized incident light.*

The spectra differ only slightly between the two kinds of domains. Only on a closer look can we observe a slight shift of the spectra as well as a small difference in the intensity. To study the possible contrast, we calculate the visibility $V = (C_c - C_a)/(C_c + C_a)$ from the measured data sets for p-polarized incident light (see figure 10.6) and show the results in figure 10.8 for selected distances between tip and sample. The visibility has a value of -0.8 to +0.8 with negative values corresponding to a domains being brighter than the c domains and positive values corresponding to brighter c domains. For the second harmonic, we observe a dip in all three visibility spectra at around 17.9 μm. This dip as well as the maxima next to it at around 17.7 μm do not depend on the distance and both are thus most likely no near-field effects. Starting at 17.5 μm, we observe an increase in the red curve (the spectrum for $h = 0$ nm). The signal rises until a maximum of about 0.55 around 16.9 μm. Then it decreases strongly until a negative minimum of -0.85 at around 16.7 μm is reached. After this minimum it increases again gently and approaches zero. The red curve shows two zero crossings corresponding to points of contrast reversal: one at around 17.5 μm and one at around 16.85 μm. For larger distances (green curve for $h = 25$ nm and blue curve for $h = 50$ nm) we observe the same qualitative behavior
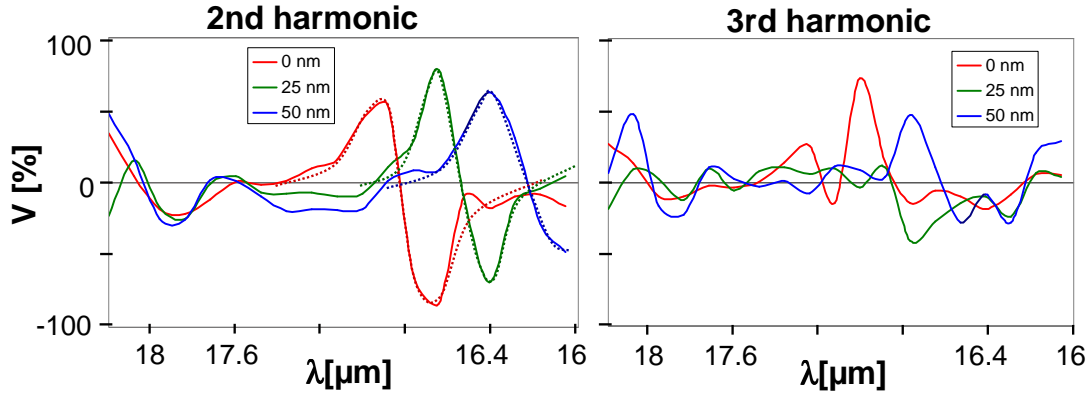
Figure 10.8: *Contrast V_{ac} on the BaTiO$_3$ sample calculated by $V = (f_a - f_c)/(f_a + f_c)$ from the measured data sets shown in figure 10.6. Depicted are the 2nd- and 3rd-harmonic contrasts for p-polarized incident light and for selected distances h. Positive and negative contrasts correspond to a brighter a or c domain, respectively.*

but shifted towards smaller wavelengths. The positive maximum (bright c domains) is located at 16.7 μm for the green and at 16.4 μm for the blue spectrum, while the negative minimum (bright a domain) is at 16.4 μm and below 16 μm, respectively, in the two cases. The zero crossings are also shifted to smaller wavelengths, namely 16.95 μm and 16.55 μm for the green, and 16.9 μm and 16.25 μm for the blue curve. Also, for both curves at larger distance we observe an additional broad negative minimum (bright a domains) between 17 and 17.4 μm. The distance dependence of the visibility spectra shows a typical spectral near-field shift. From these data, we expect a maximum contrast of 80% and contrast reversals around 16.85 μm and 17.5 μm for $h = 0$. The visibility spectra for the 3rd-harmonic signal are very noisy and show no obvious near-field characteristics. Anyway, they are shown for completeness in figure 10.8.

In conclusion, the measured distance dependence spectra show a very similar near-field signal on the two types of domains for both polarizations of the incident light. An enhanced signal with a typical lobelike character is observed around the wavelength expected from the dipole model. On a closer look, a small shift of the two spectra is observable, with the c domain resonance at slightly smaller wavelengths compared to the a domain. In the corresponding visibility spectra, we observe maximum contrast between the a and the c domain of up to 80 % as well as contrast reversals at characteristic wavelengths. Both maxima and contrast reversal shift with the wavelength, which indicates the near-field-coupled character of the signal.

As the sample shows two different types of domains, we can now measure the optical contrast or visibility directly by scanning the sample. This was done in 2-dimensional scans at selected wavelengths (section 10.5) as well as in so-called line-scan near-field spectra discussed in the following section.
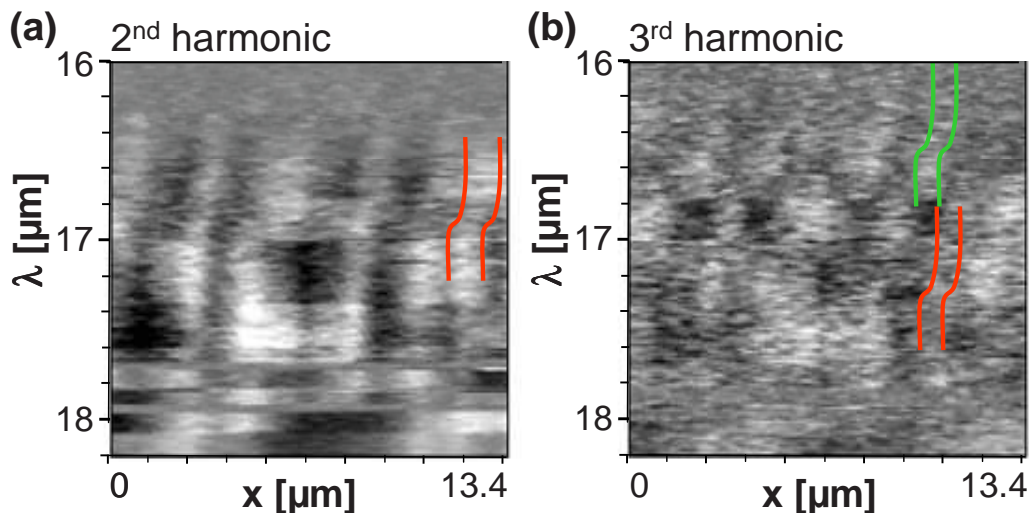
Figure 10.9: *Line-scan near-field spectra on a BaTiO$_3$ sample for (a) 2nd- and (b) 3rd-harmonic demodulation. The length of the scanned line was 13.4 μm (horizontal direction in the images) while the wavelength was varied from 18.2 μm to 16 μm in steps of $\Delta\lambda = 120$ nm (vertical direction).*

10.4 Line-Scan Near-Field Spectra on BaTiO$_3$

In addition to the distance-dependent near-field spectra, we measured spectra under feedback control of the tip-sample distance while scanning along a single line on the sample surface. Knowing the domain distribution of the sample, we chose a line crossing both domain types several times to avoid random errors. We start scanning the line at large wavelengths and then decrease the wavelength by increasing the undulator gap (see section 8.2) in steps of typically $\Delta\lambda \cong 100$ nm. For each wavelength we make 10 scans each in forward and backward direction. At each wavelength, the laser power changes strongly during the first scan, which can be observed easily in the measurement. After reaching the last wavelength, we switch back to the first one to make a reference scan, which takes about one minute. For all the measurements shown here, these reference scans reproduce the signal at the starting wavelength and are thus not depicted here. The reference scans as well as the corresponding topography scans ensure that there is no drift of the sample for all measurements which are presented here.

Figure 10.9 shows the measured data for 2nd- and 3rd-harmonic demodulation using *p*-polarized incident light. For both harmonics we see a stripy contrast along the scanned line – the horizontal direction of the picture – which changes with wavelength. For describing the data, we proceed from large to small wavelengths (bottom to top), which was the scan direction also in the experiment.

In the 2nd-harmonic signal at 18.2 μm we see two bright lines with a lateral distance of about 9 μm that move to the right at the next wavelength step. We believe that these maxima correspond to far-field interference maxima at the sample

surface. At smaller wavelengths, we observe a substructure consisting of 5 bright lines. First, the positions of these bright lines do not change when we change the wavelength until reaching $\lambda \cong 17.0$ μm. Then, the intensity of the bright lines decreases, while the intensity of the dark lines increases until the contrast is reversed. Surprisingly, the lines seem to move to the right before the contrast reverses (see red marks in the picture). We believe that this movement is caused by the near field probing a certain depth in the sample. As the 90° domain wall runs through the crystal at an angle of 45° with respect to the sample surface, there are certain regions with an *a* domain on the sample surface and the *c* domain underneath or vice versa (see figure 10.1a). At these domain-mixed intersections, the distance between e.g. the tip and the *c* domain underneath the *a* domain is larger than on a pure *c* domain and hence the spectral response is shifted to smaller wavelengths. Knowing the domain distribution, we can identify the domains. The lines which are bright at larger wavelengths correspond to *a* domains, while the dark areas are *c* domains. The contrast reversal takes place at about 16.8 μm.

In the 3rd-harmonic signal we see again the two bright lines at large wavelengths, which are much weaker than for the 2nd harmonic. This confirms the assumption that this is a far-field effect. Again, for smaller wavelengths we observe a substructure of 5 bright and dark lines which reverse in the contrast at a certain wavelength ($\lambda \cong 17.3$ μm) with the same movement to the right as observed for the 2nd harmonic (see red mark). When the wavelength is decreased further, the contrast jumps back to the former contrast at 16.7 μm, corresponding to the 180° phase shift of the higher-harmonic signals discussed above (see section 5.3.2). Then, the contrast reverses again with a similar movement to the right (see green marks) at $\lambda \cong 16.4$ μm.

Comparing these observations with the distance-dependent near-field spectra shown in figure 10.6 we can estimate the distance between tip and sample during the scan. We may assume that the number of contrast reversals correlates with the number of maxima in the distance-dependent near-field spectra. The region where the 2nd harmonic shows only one contrast reversal, while the 3rd harmonic shows two, is limited to a distance of about $h' = 45$ to 55 nm in the corresponding distance-dependent spectra (see figure 10.6). This is a realistic value for the distance, considering the smaller frequency shift of the cantilever oscillation during the scan due to distance control. For *p*-polarized light and a distance of 50 nm the visibility between *a* and *c* domains is depicted in figure 10.8. Here the 2nd harmonic shows contrast reversals at 16.8 μm as well as 16.25 μm, which matches perfectly the observations of the lateral scan. The visibility of the 3rd-harmonic signal as depicted in figure 10.8 is too noisy to find any accordance to the lateral-scan data.

Distance dependence

Knowing the distance-dependent near-field spectra, we can test the agreement with the line-scan near-field spectra by measuring at a different distance between tip and sample. In noncontact AFM mode this can be realized by changing the amplitude of
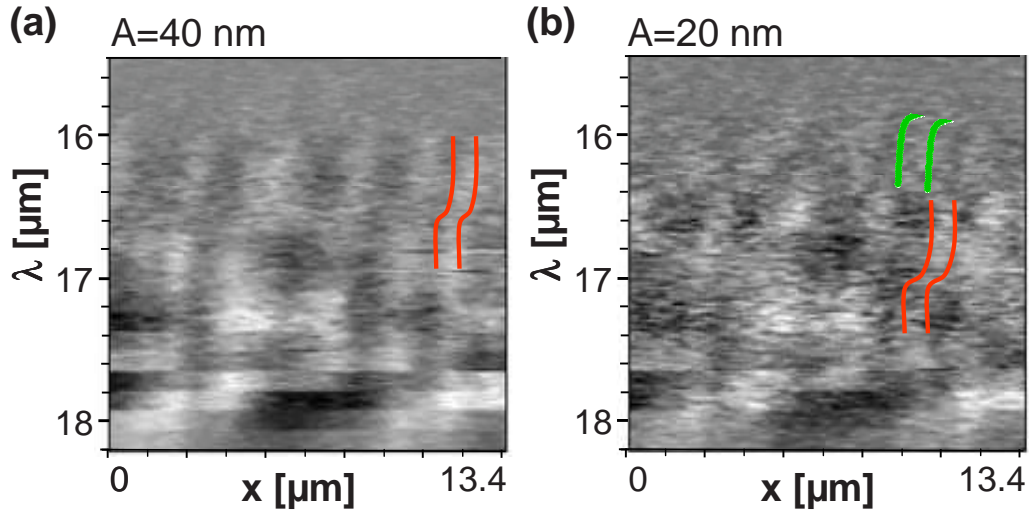
Figure 10.10: *Line-scan near-field spectra of the 2nd-harmonic signal on BaTiO$_3$ for different amplitudes of the cantilever oscillation. The length of the scanned line was 13.4 μm (horizontal direction), while the wavelength was changed from 18.2 μm to 15.44 μm in steps of 140 nm (vertical direction).*

the cantilever oscillation. Taking half the amplitude corresponds to a good approximation to half the distance. Closer to the sample surface we expect the contrast reversal to happen at larger wavelengths, because the resonances on both domain types are shifted to larger wavelengths. The absolute value of the optical signal should be smaller because of the smaller modulation amplitude, while the lateral resolution of the signal is expected to be higher [Wur99, Tau05].

The result of such a measurement is shown in figure 10.10 for 2nd-harmonic demodulation: The spectrum taken at an amplitude of about 40 nm is shown on the left-hand side and its counterpart acquired at half the amplitude on the right-hand side. Both spectra were taken along the same line on the sample surface. The half-amplitude image is much noisier due to less optical signal. At large wavelengths both spectra are dominated by far-field contributions, which shift to the right when the wavelength is decreased. At about 17.8 μm we observe the stripelike substructure of the ferroelectric domains in both pictures. First, they do not move when the wavelength is reduced further. For the large amplitude we observe a contrast reversal (red lines in fig. 10.10a) at about 16.6 μm, which is in good accordance to the earlier measurement. For half the amplitude this contrast reversal happens at a clearly larger wavelength, namely at about 17.1 μm (see red lines in fig. 10.10b). The signal for half the amplitude is noisier, but we can clearly observe a second contrast reversal at about 16.0 μm (green lines in fig. 10.10b).

Comparing the results with the distance-dependent near-field spectra, we observe all expected features: For smaller oscillation amplitudes, the spectra are shifted towards larger wavelengths. Due to the smaller distance between tip and sample, we observe a second phase-inverted maximum around 16.0 μm in the 2nd-harmonic
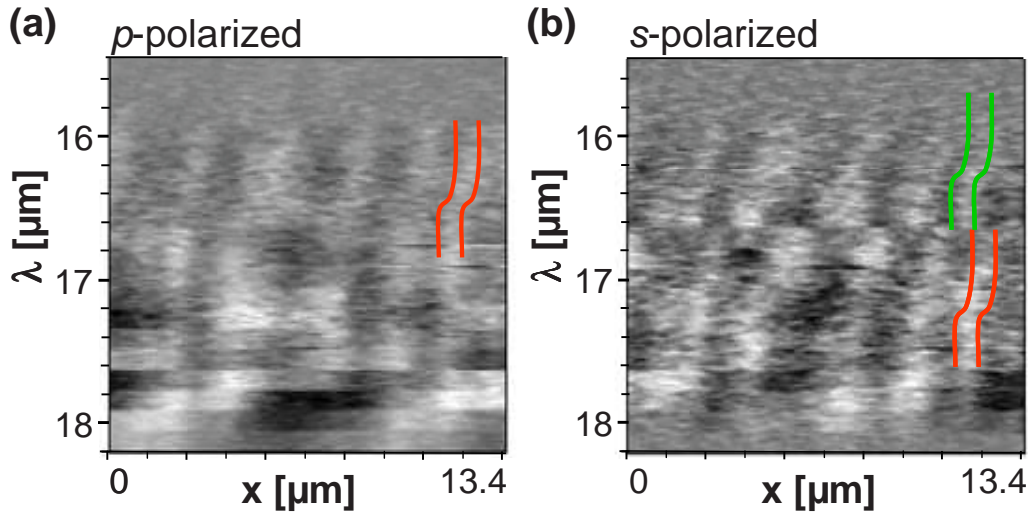
Figure 10.11: *Line-scan near-field spectra of the 2nd-harmonic signal on BaTiO₃ for different polarizations of the incident light. The length of the scanned line was 13.4 µm (horizontal direction), while the wavelength was changed from 18.2 µm to 15.44 µm in steps of 140 nm (vertical direction).*

signal. These observations fit to the distance-dependent near-field spectra shown in figure 10.6, if we assume the distance between tip and sample to be smaller than 40 nm. Comparing these results with the visibility plots of figure 10.8, we find a good agreement with the visibility at $h = 25$ nm, where the contrast is shifted by about 300 nm towards larger wavelengths. The second point of reversal cannot be found in the visibility curve. Note that the corresponding distance-dependent near-field spectra were taken at larger amplitudes and therefore cannot serve for quantitative comparison.

Polarization dependence

We know from the distance dependent measurements that the near-field signal depends strongly on the polarization of the incident light. Therefore we also acquire line-scan near-field spectra for different polarizations of the incident light.

In figure 10.11 you see the line-scan near-field spectra demodulated at the 2nd harmonic for p- and s-polarized incident light. The measurement with p-polarized light reproduce the measurements discussed before and shown in figure 10.9, which were taken on a different day and with slightly different FEL settings. Again the contrast reversal occurs at a wavelength of about 16.85 µm. For s-polarized light, we observe two contrast reversals, one at around 17.05 µm and a second one at around 16.3 µm. As for the 3rd harmonic depicted in figure 10.9, we observe a jump between the two lines at around 16.6 µm. This agrees with the distance-dependent near-field spectra depicted in figures 10.6 and 10.7 if we again assume that the distance between tip and sample during the line scan was about 45 nm.

In conclusion, the method of line-scan near-field spectra is a good complementary method to the distance-dependent near-field spectra. It affirms the results of the latter if we assume the distance during the scan to be about 45 nm larger than the smallest distance in the approach curves. All measurements at different harmonics, selected amplitudes, and *s*- and *p*-polarized incident light coincide completely with the results from the distance-dependent near-field spectra. The line-scan near-field spectrum in general provides a fast spectral and spatial examination of the sample at one single tip-sample distance. In particular, it is very helpful in finding the right wavelength that yields the maximal contrast in spatial two-dimensional scans, which are discussed in the following section.

10.5   Scans at Selected Wavelengths with Contrast Reversal

The above results show the principle of s-SNOM based on a tunable light source at IR wavelengths. The comparison with theory facilitates the interpretation of the data and the usage of the method for spectroscopic examinations. In this section we will discuss the additional application of s-SNOM in the IR as an imaging technique at selected wavelengths.

As the deviation of the anisotropic dielectric tensor from a scalar in most ferroelectric samples is too small to be imaged at visible wavelengths with a common tip, many groups have used the electro-optic properties of the ferroelectric sample to extract optical information [Hub98, Lev00, Ott04, Orl00]. Close to the phonon resonance of the sample, s-SNOM allows a purely optical examination of ferroelectric domains.

For imaging a ferroelectric domain distribution (or any other structure showing spatial variations of the optical anisotropy), the wavelength should be chosen such that the optical contrast is as large as possible. The lateral scans discussed in section 10.4 are a good preliminary investigation to find the right wavelength. From those measurements we know the point of contrast reversal and the points of maximal optical contrast before and after the contrast reversal.

Scans at selected wavelengths

Figure 10.12 shows a whole set of scans at several fixed wavelengths on a sample region where we have a *c* domain to the left and an *a* domain to the right (separated by the white line in the images). The first and second rows show measurements of the 2nd- and 3rd-harmonic signals, respectively. From left to right the wavelength increases from 15.9 μm to 17.4 μm. For wavelengths smaller than 16 μm, we see no contrast between the domains. When increasing the wavelength, we see first some far-field features. At about 16.6 μm the *c* domain is clearly brighter than the
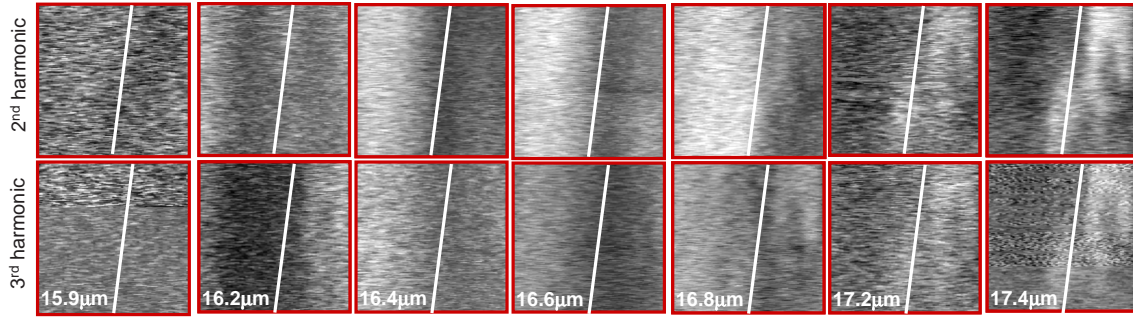
Figure 10.12: *Scans on BaTiO$_3$ single crystal at selected wavelengths (2nd and 3rd harmonic). The white line indicates the 90° domain wall between a c domain to the left and an a domain to the right side. For the corresponding PFM picture see figure 8.3.*

a domain in both harmonic signals. This contrast is maximal at about 16.8 μm. At about 17 μm the contrast reverses and the a domain gets brighter than the c domain. This contrast increases for larger wavelengths and has its maximum at about 17.4 μm.

In the scans at selected wavelengths we can clearly observe the domain structure. The characteristically shaped a domain, which is deformed most likely due to defects in the crystal, can easily be identified. The corresponding PFM picture was shown earlier in figure 8.3. Please note that – as expected from theory – no contrast is observed between antiparallel c domains ($\odot$ and $\otimes$ in fig. 8.3a). At the domain wall, we see some additional features which we do not understand completely yet. Due to the edge in the topography, we surely have some scattering effects, which modify the appearance of the domain wall at some wavelengths – e.g. at 17.4 μm in the lower part of the 2nd-harmonic image. These effects seem to be weaker in the 3rd-harmonic signal. Additionally, the transition of the optical signal between the two domains is displaced laterally with respect to the location of the domain wall as measured by PFM, which is marked by a white line in the picture. This effect is stronger for the a-resonant case at 17.4 μm than for the c-resonant case at 16.8 μm. We believe that this displacement is caused by the near field probing a certain depth in the sample. As discussed earlier, the 90° domain wall runs through the crystal at an angle of 45° with respect to the sample surface (see figure 10.1a). Thus the scattering signal measured above the domain wall, contains information on the c domain as well as the a domain, the latter being located at different depths underneath the tip. For the measurements shown here, this effect cannot be clearly examined, because the ferroelectric structure is not well-defined due to defects in the crystal. However, these scans reproduce nicely the spatial distribution of the domains and their spectral response with a contrast reversal at a certain wavelength.

On another sample with a nondeformed stripelike domain structure, as shown in

Figure 10.13: *Contrast reversal in the 2nd-harmonic signal on a $BaTiO_3$ sample due to different wavelengths. The dashed lines correspond to the domain distribution known from PFM measurements (see figure 10.4).*

the PFM images depicted in figure 10.4, we performed scans at two selected wavelengths, namely 16.7 μm and 17.2 μm. Figure 10.13 depicts both scans separately as well as a combined image showing half of either scan to point out the correlation of the two pictures. We can clearly observe the stripelike domain structure as measured by PFM. As a good pin point in the pictures we take the needle in the lower left corner of the scans (marked red in figure 10.13c). The PFM measurements show that this needle is the end of a c domain. At 16.7 μm this c domain needle is brighter than the surrounding a domains, while at 17.2 μm the contrast is reversed.

Again the optical contrast is not simply reversed between the two wavelengths but also shows some displacement at the domain walls. At 16.7 μm we can clearly distinguish two levels of the optical signal: high signal corresponding to the c domains (for example the needle) and low signal for the a domains. At 17.2 μm the borders are blurred. The signal changes only slowly across the domain walls. Again, most likely the penetration depth of the near-field interaction is the reason for this blurring.

Scans at selected amplitudes

As already examined by means of line-scan near-field spectra in section 10.4, also the amplitude of the cantilever oscillation influences the contrast between a and c domains. A change of this amplitude changes the mean distance between the tip and the sample and therefore changes the resonance of the coupled system. For smaller amplitudes we expect the optical signal to be smaller, but the resolution to be increased [Wur99, Tau05].

Figure 10.14 shows measurements performed with an amplitude of about 40 nm – like in the above measurements – in comparison with data obtained at half the amplitude. We measured the 3rd-harmonic signal at 17.2 μm on one and the same sample region. Again we chose the same sample area containing the c domain needle (marked red in figure 10.14c), but we chose a smaller scan range. Because of
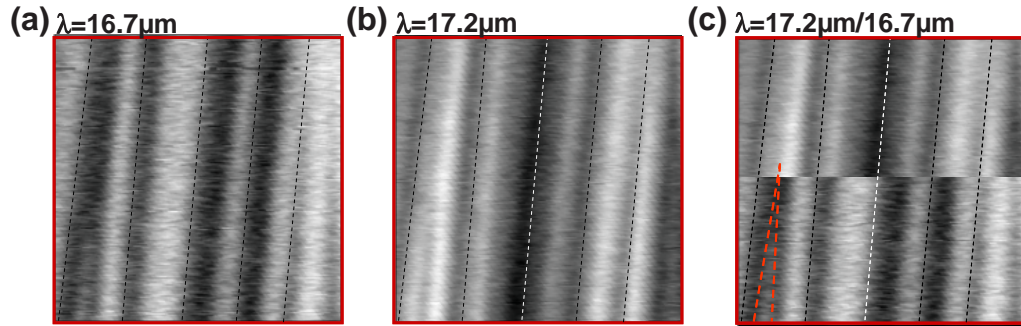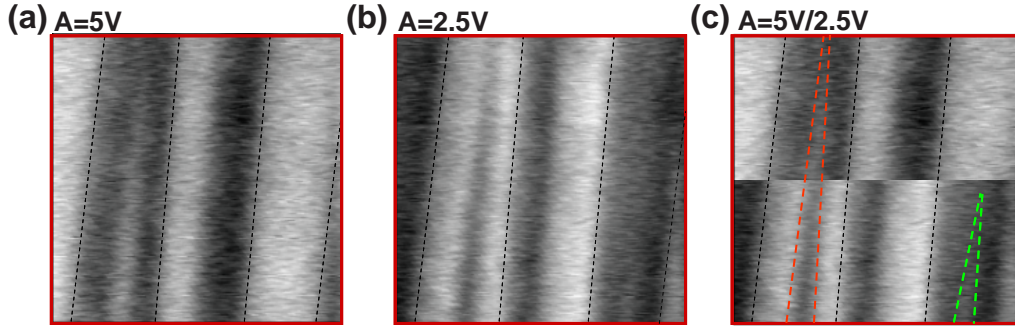
Figure 10.14: *Contrast reversal in the 2nd-harmonic signal on a BaTiO$_3$ sample due to different amplitudes. The dashed lines correspond to the domain distribution known from PFM measurements (see figure 10.4).*

the different harmonic, the needle is now bright at an amplitude of 40 nm. When halving the amplitude, we find a clear contrast reversal. This shows that close to a resonance of the tip-sample system, variations of the amplitude during a scan can cause a contrast reversal. This is in contradiction to the common assumption that the amplitude only influences the signal-to-noise ratio and the lateral resolution but not qualitatively the contrast [Tau05], which is however true only for the off-resonant case.

Additionally, we find that the resolution of the optical measurement changes: For the large amplitude the needle seems to end within the picture, while for the small amplitude it is still observable at the upper border of the scan. A repeated scan showed that no drift was present. We believe that the higher resolution at smaller amplitude allows us to image the very narrow domain end, which is not visible at larger amplitudes. Also note that the resonance frequency of the near-field-coupled tip-sample system is shifted and therefore the intensity as well as the contrast have changed. An additional feature can be observed in the lower right corner: At large amplitudes we observe a broad bright area, while for smaller amplitudes, within the dark area, we observe a bright line, which was identified by PFM as the end of an *a* domain needle (marked green in figure 10.14c). This confirms that the spatial resolution in near-field microscopy is higher if a smaller modulation amplitude is chosen, as discussed in [Wur99, Tau05].

In conclusion, scans of the sample at selected wavelengths clearly show the domain distribution via a purely optical contrast. As expected from theory and from the above spectral investigations, we observe a contrast reversal at a certain wavelength. At selected wavelengths, a contrast reversal can also be observed for different amplitudes corresponding to different distances between tip and sample. Additionally, smaller distances offer a higher resolution of the lateral scan, which will be discussed in the following section.

10.6   Resolution in s-SNOM

The resolution of the distance-dependent near-field spectra is discussed for $LiNbO_3$ in section 9.5. The spectral width of the FEL is the same in the wavelength regimes used for $BaTiO_3$ and for $LiNbO_3$. This spectral resolution of about $\Delta\lambda = 100$ nm corresponds for $BaTiO_3$ to a difference in the dielectric constant of $\Delta\varepsilon = 0.15$.

In the line-scan near-field spectra we observe in addition to the wavelength dependence of the signal, a correlation to the domain distribution along a line on the sample surface. For the 2nd-harmonic signal and p-polarized light (see figure 10.9), we observe clearly the striped domain structure with a mean period of 1 μm. It is difficult to define the lateral resolution, as the near-field has a certain penetration depth and thus we image an average of the domain structures in the sample at different distances from the sample surface. The 90° domain wall has an angle of 45° with respect to the sample surface (see 10.1a) and hence the domain distribution is shifted for different depths. We can estimate the resolution to be better than 300 nm. The resolution does not depend on the wavelength, as expected from theory. The resolution is mainly limited by the tip radius, but also by the distance h between tip and sample and the amplitude A of the cantilever oscillation. The tip radius defines the lateral size of the nanoscopic light source as well as the strength and the decay length of the near-field, while the distance h determines the illuminated area on the sample. Additionally, the distance h defines the penetration depth of the near-field as well as the response of the sample, i.e., the strength and spectral position of the resonance. The amplitude A controls the mean distance h as well as the z modulation, which determines the higher-harmonic generation. In conclusion, a smaller tip-radius and a smaller distance provide a higher lateral resolution in s-SNOM.

In figure 10.15a,c we depict two-dimensional scans of $BaTiO_3$ demodulated at the 2nd harmonic using $\lambda = 17.2$ μm and two different oscillation amplitudes of the cantilever. The needle-shaped domains with a width below 200 nm are clearly resolved for $A = 20$ nm. The cross sections along lines 1 and 2 are depicted in figure 10.15b and 10.15d, respectively. Line 1 crosses a needle-shaped c domain on the left-hand side of the scan area, which is bright for $A = 40$ nm (fig. 10.15a) and dark for $A = 20$ nm (fig. 10.15c). From PFM measurements (see figure 10.4), we know the domain to be roughly 180 nm wide at the position of line 1. This needle can be barely observed for $A = 40$ nm, while it is clearly mapped for $A = 20$ nm. At line 2 (fig. 10.15d) we cross the same c domain needle at a different position, where it has a width of about 1 μm, and additionally we cross the end of an a domain needle being about 150 nm wide according to the PFM data. This second needle is only resolved for $A = 20$ nm, appearing to be around 315 nm wide. From this observation we deduce that our s-SNOM resolves structures as small as 150 nm with a resolution of about 85 nm, corresponding to $\lambda/200$. This resolution depends strongly on the distance between tip and sample and can be increased further by using smaller amplitudes.
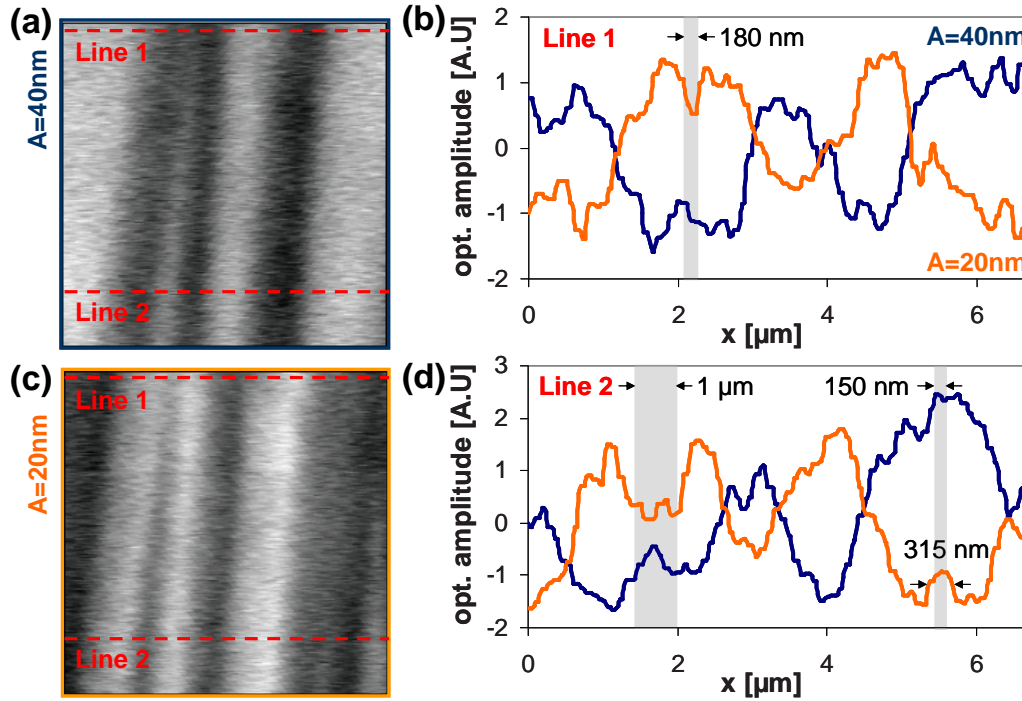
Figure 10.15: *Illustration of the lateral resolution in s-SNOM. (a),(c) show the optical amplitude as measured in two-dimensional scans at $\lambda = 17.2$ μm with different cantilever amplitudes $A = 40$ nm and $A = 20$ nm respectively. (b) and (d) show cross sections along the dashed lines in the scan images. The smallest structure resolved is about 150 nm wide and is imaged with a resolution of around 85 nm (see text).*

10.7   Summary

By the measurements on BaTiO₃, we were able to confirm the validity of our method for another sample material and hence for another wavelength range. Thereby, we extended the measurements to a more complex sample system showing a well-known domain distribution. In addition to the spectroscopic examinations using distance-dependent near-field spectra, we measured the spatial distribution of the near-field signal on the sample. We scanned along a single line on the sample surface while changing the wavelength. With this method we were able not only to identify the domains but also to find the characteristic wavelength of contrast reversal. Additionally, we performed two-dimensional scans across the sample surface at selected wavelengths. We found the wavelengths of maximal contrast and of contrast reversal and performed near-field scans with a resolution of about 85 nm at $\lambda = 18$ μm, corresponding to $\lambda/200$.

11   Conclusion: Experiment

With our unique s-SNOM setup we combine several scanning probe microscopy methods allowing the examination of topographic, electrical, and optical properties of the sample. This allows us not only to image all these properties in situ, but also to minimize any cross talk from mechanical or electrical interaction to the near-field signal. For the optical examination we have two separate setups, one for visible and a second one for the IR regime.

At visible wavelengths, we reported basic examinations on a test sample showing a contrast between different materials, namely gold and glass. Measurements of the distance dependence confirmed the suppression of the far-field signal by the method of higher-harmonic demodulation. In the IR regime we used a free-electron laser as a precisely tunable light source. We excited ferroelectric samples close to their phonon resonances, which allowed the near-field-coupled tip-sample system to be excited resonantly. Several imaging techniques were used to study the basic properties of the near-field signal.

On a single-domain single crystal of ferroelectric $LiNbO_3$ we examined the elementary behavior of the near-field signal close to the resonance by measuring distance-dependent near-field spectra. These measurements are in good agreement with the theoretical calculations for all higher-harmonic signals. By rotating the single-domain sample, we demonstrated the dependence of the near-field signal on changes of the in-plane components of the dielectric tensor of the sample. This influence has been predicted by theory, but has never been proven before experimentally.

Measurements at different polarizations of the incident light showed a systematic change of the signal. It is obvious that for the resonant excitation of the tip-sample system also the component of the electric field parallel to the sample surface contributes the the near-field signal. With measurements at different polarizations we can couple to different components of the dielectric tensor, leading to complementary information.

By measurements on a multi-domain single crystal of ferroelectric $BaTiO_3$, we proved the validity of our method for another wavelength regime and for another sample material. The distance-dependent near-field spectra showed basically the same behavior as the spectra on the first sample material, but were shifted to a different wavelength range. The data were again in good agreement with the theoretical spectra from the dipole model. Additionally, on the multi-domain sample, we were

able to examine the near-field signal on different domains where the dielectric tensor is oriented differently. On this sample we do not only have changes in the plane of the sample surface but also of the perpendicular component. Distance-dependent spectra were measured on different domain types and for different polarizations of the incident light.

As the multi-domain sample offers the opportunity to scan over an area with several domains, we introduced the additional method of line-scan near-field spectra. Using this method, we scanned along line on the sample surface while changing the wavelength of the incident light. For selected wavelengths we see a contrast between different kinds of domains which reverses at a characteristic wavelength. Systematic investigations for various harmonics, different polarizations, and selected distances between tip and sample were done and showed a consistent behavior. Finally we imaged the domain distribution of the sample at selected wavelengths. We observed a contrast reversal at a characteristic wavelength as well as at a certain distance between tip and sample. The domain distribution was clearly identified with a resolution of $\lambda/200$.

12   Conclusions and Outlook

This work combines the theoretical description of near-field optical microscopy on anisotropic dielectrics with the experimental examination of anisotropic ferroelectrics.

In the theoretical part we extended the known dipole model to anisotropic samples. For these samples we expect – in addition to the well-known material contrast – an anisotropy contrast between sample regions with different orientations of the dielectric tensor. For nonresonant excitation of the tip-sample system, this contrast is observable for selected tip shapes, but is characterized by a rather small scattering cross section. Hence, we concluded that it is necessary to excite the tip-sample system at one of its resonances, by resonant excitation of either the tip or the sample. For the tip-induced resonance, the scattering cross section is successfully enhanced, but the corresponding anisotropy contrast is yet rather small. Only for sample-induced resonances we expect an enhancement of both, the scattering cross section as well as the anisotropy contrast.

In order to measure the rather small anisotropy contrast, we designed a setup which is a unique combination of atomic force microscopy, Kelvin probe force microscopy, and near-field observation. We reduced any possible artifacts due to mechanical or electrostatic cross-talk by using a frequency-modulated distance control with an additional amplitude controller as well as a third controller minimizing the electrostatic interaction between tip and sample. In the visible wavelength regime, we performed basic studies on our system such as the discrimination of near-field from far-field contributions to the signal by higher-harmonic demodulation. At IR wavelengths we used the free-electron laser at Forschungzentrum Dresden-Rossendorf as a continuously tunable light source, thereby for the first time combining a FEL with a near-field microscope. In order to study the basic properties of the anisotropy contrast, we excited ferroelectric samples close to their phonon resonances. On two different samples – lithium niobate and barium titanate, both excited resonantly at different wavelengths –, we found the resonances of the near-field-coupled system at the predicted spectral positions.

On lithium niobate we studied the principle spectral behavior of the near-field signal on anisotropic materials, as these single-domain crystals are as close as possible to the ideal sample system of our calculations. In so-called distance-dependent near-field spectra we measured characteristic fingerprints for different polarizations

of the incident light as well as different orientations of the sample. With these measurements we proved for the first time the impact of in-plane anisotropy on the near-field signal. As the anisotropy of the sample is homogeneous across the crystal, a direct measurement of the anisotropy contrast was not possible with this sample, but only the comparison between different orientations.

The second sample, a multi-domain barium titanate single crystal, shows domains with the anisotropy axis oriented either parallel or perpendicularly to the sample surface. On both types of domains, we performed analogous spectral examinations as for lithium niobate. Additionally, we performed lateral scans in combination with spectroscopy and found a clear anisotropy contrast, which is maximized for resonant excitation. As the two domains show resonances at different wavelengths, we observed a contrast reversal between the two wavelengths in several higher harmonics. By performing 2-dimensional scans at selected wavelengths, we were able to measure the domain distribution with a clear contrast between the different domains, which reverses at a certain distance between tip and sample and for a characteristic wavelength. In these scans we achieved a lateral resolution of $\lambda/200$.

In the near future, we plan to study the resolution limit of this method by downscaling the domain size. Additionally, we will directly study the in-plane anisotropy contrast on bismuth ferrite showing the appropriate domain structure. Up to now this was not possible, because these samples show resonances at around 25 μm, which was out of the accessible wavelength range. As these samples are multiferroic, we plan to study the response of ferroelectric and ferromagnetic domains, heading towards addressing the different types with the proper wavelengths and thus separating them in the optical image.

Additionally, we have started examining specially designed tips with nanoparticles of arbitrary size and shape attached to the tip end. By controlling the scattering behavior of the tip with this technique, we are able to achieve a higher resolution and a better reproducibility. Furthermore, it may become possible to examine anisotropic samples with nonresonant excitation at visible wavelengths.

The extension of the detection system for IR wavelengths to interferometric detection is under construction. This method allows the separation of optical amplitude and optical phase at arbitrary wavelengths, which provides complementary information about the sample response.

Furthermore, the examination of other sample systems showing resonances in the IR regime is planned. In order to examine the local spectral behavior of organic samples, we will extend our method to surface-enhanced infrared absorption spectroscopy. On ion-implanted structures, we will study systematically the penetration depth of the near-field for different scan parameters and at different wavelengths. Finally, we are excited by latest developments in the field of metamaterials, allowing e.g. transmission of the near-field information over distances of several micrometers with the superlensing effect of metamaterials.

Appendix A   Reflection at Anisotropic Materials

For isotropic samples the reflection coefficients are well known as the Fresnel coefficients:

$$
\begin{aligned}
r_s &= \frac{\cos\gamma - \sqrt{n^2 - \sin^2\gamma}}{\cos\gamma + \sqrt{n^2 - \sin^2\gamma}} \\
r_p &= \frac{n^2\cos\gamma - \sqrt{n^2 - \sin^2\gamma}}{n^2\cos\gamma + \sqrt{n^2 - \sin^2\gamma}}
\end{aligned}
\tag{A.1}
$$

with the incident angle γ and the relative index of refraction n given by the ratio of the index of refraction of the sample n_s and the surrounding material n_m

$$
n = \frac{n_s}{n_m} \ . \tag{A.2}
$$

The s- and p-polarized components of the reflected field P_p, P_s can be calculated by

$$
\begin{aligned}
P_p &= r_p A_p \\
P_s &= r_s A_s \ .
\end{aligned}
\tag{A.3}
$$

with A_p, A_s the p- and s-polarized components of the electric-field vector of the incident light.

For anisotropic samples the formulae are more complex. For uniaxial anisotropy there are two refracted beams - the ordinary (o) and the extraordinary (eo) beams. There are four reflection coefficients, connecting the incident s- and p-polarized field vectors to the reflected ones:

$$
\begin{aligned}
P_p &= r_{pp} A_p + r_{ps} A_s \\
P_s &= r_{sp} A_p + r_{ss} A_s \ .
\end{aligned}
\tag{A.4}
$$

The coefficients were calculated for the general case by Szivessy in 1928 [Szi28].

The calculation is based on the so-called method of "uniradial oscillation azimuths". For each crystal axis, there is one certain polarization α (angle between the incident plane and the electric-field vector) and amplitude A of the incident

light, which, at a certain incident angle, will produce only one refracted beam with the amplitude 1. Calling these incident polarizations, due to the produced refracted beams, α_o for the ordinary and α_{eo} for the extraordinary one and the corresponding incident amplitudes A_o and A_{eo}, the resulting reflected polarizations ρ_o, ρ_{eo} and the amplitudes of the reflected wave P_o and P_{eo} we get the s- and p-components of the incident and reflected wave with

$$
\begin{aligned}
A_{s,o/eo} &= A_{o/eo} \sin \alpha_{o/eo} \\
A_{p,o/eo} &= A_{o/eo} \cos \alpha_{o/eo} \\
P_{s,o/eo} &= P_{o/eo} \sin \rho_{o/eo} \\
P_{p,o/eo} &= P_{o/eo} \cos \rho_{o/eo}
\end{aligned}
\tag{A.5}
$$

Thus the reflection coefficients are given by

$$
\begin{aligned}
r_{pp} &= \frac{1}{d} \left(-P_{o,p} A_{eo,s} + P_{eo,p} A_{o,s} \right) \\
r_{sp} &= \frac{1}{d} \left(+P_{o,p} A_{eo,p} - P_{eo,p} A_{o,p} \right) \\
r_{ps} &= \frac{1}{d} \left(-P_{o,s} A_{eo,s} + P_{eo,s} A_{o,s} \right) \\
r_{ss} &= \frac{1}{d} \left(+P_{o,s} A_{eo,p} - P_{eo,s} A_{o,p} \right)
\end{aligned}
\tag{A.6}
$$

with

$$
d = \left(A_{o,s} A_{eo,p} - A_{o,p} A_{eo,s} \right) \; .
\tag{A.7}
$$

The equation system for calculating the components A_i, P_i and α_i, ρ_i with $i = e, eo$ is

$$
\begin{aligned}
(A_i \cos \alpha_i + P_i \cos \rho_i) \sin \gamma &= \cos \eta_i \sin r_i \\
(A_i \sin \alpha_i - P_i \sin \rho_i) \sin \gamma \cos \gamma &= \sin \eta_i \sin r_i \cos r_i \\
(A_i \sin \alpha_i + P_i \sin \rho_i) \sin^2 \gamma &= \sin \eta_i \sin^2 r_i \\
(A_i \cos \alpha_i - P_i \cos \rho_i) \cos \gamma \sin^2 \gamma &= (\cos \eta_i \cos r_i + \tan \zeta_i \sin r_i) \sin^2 r_i
\end{aligned}
\tag{A.8}
$$

and

$$
\begin{aligned}
\cot \alpha_i &= \cos (\gamma - r_i) \cot \eta_i + \frac{\sin^2 r_i \tan \zeta}{\sin (\gamma + r_i) \sin \eta_i} \\
\cot \rho_i &= \cos (\gamma + r_i) \cot \eta_i + \frac{\sin^2 r_i \tan \zeta}{\sin (\gamma - r_i) \sin \eta_i} \; .
\end{aligned}
\tag{A.9}
$$

with
γ the incident angle between incident $\mathbf{k}$ vector and the positive z axis,
η_i the polarization of the refracted beams,
r_i the refraction angles between the $\mathbf{k}$ vector of the refracted beam and the negative z axis ,
ζ_i the angle between the wave normal of the refracted beam and its Poynting vector.

The calculation of these parameters for uniaxial crystals in general are described in the following.

For a uniaxial crystal the refractive indices are given by

$$\begin{aligned} n_1 = n_2 &= n_a \\ n_3 &= n_c \end{aligned} \tag{A.10}$$

In order to solve the equation system A.8 we need to calculate a set of parameters (A_i, α_i, P_i, ρ_i, η_i, r_i and ζ_i with $i = o, eo$) for the ordinary (o) and the extraordinary (eo) refractive wave. First we describe the orientation of the crystal relative to the incident plane (xz). The refractive indices of the sample are given by:

$$\frac{1}{n_{ik}^2} = \frac{\alpha_i \alpha_k + \beta_i \beta_k}{n_a^2} + \frac{\gamma_i \gamma_k}{n_c^2} \tag{A.11}$$

with $i, k = 1, 2, 3$ and

$$\begin{aligned} \alpha_1 &= \cos\xi \cos\varepsilon & \alpha_2 &= \sin\xi \cos\varepsilon & \alpha_3 &= -\sin\varepsilon \\ \beta_1 &= -\sin\xi & \beta_2 &= \cos\xi & \beta_3 &= 0 \\ \gamma_1 &= \cos\xi \sin\varepsilon & \gamma_2 &= \sin\xi \sin\varepsilon & \gamma_3 &= \cos\varepsilon \end{aligned} \tag{A.12}$$

with

with $\quad \varepsilon \quad$ the angle between the optical axis and the z axis and

$\quad \xi \quad$ the angle between optical axis and x axis in the xy plane.

The angles r_i between the refracted beams and the negative z axis can be calculated by solving

$$f(r_i) = \left(\left(n_m^2 \cdot \sin^2\gamma - n_a^2 \right) \cdot \tan^2 r_i + n_m^2 \sin^2\gamma \right) \cdot \left(d_0 \tan^2 r_i + d_2 \right) \equiv 0 \tag{A.13}$$

with

$$\begin{aligned} d_0 &= n_m^2 \sin^2\gamma \cdot \left(n_a^2 + \left(n_c^2 - n_a^2 \right) \cdot \sin^2\varepsilon \cos^2\xi \right) - n_a^2 n_c^2 \tag{A.14} \\ d_2 &= n_m^2 \sin^2\gamma \cdot \left(n_c^2 \cos^2\varepsilon + n_a^2 \sin^2\varepsilon \right) \, . \end{aligned}$$

The corresponding polarizations η_i of the refracted waves are given by

$$\cot\eta_i = \frac{\left(\frac{1}{n^2 \sin^2\gamma} - \frac{1}{n_{22}^2} \right) \cdot \tan^2 r_i - \frac{1}{n_{22}^2}}{\left(\frac{1}{n_{12}^2} - \frac{\tan^2 r_i}{n_{23}^2} \right) \cdot \sqrt{1 + \tan^2 r_i}} \tag{A.15}$$

For the refracted ordinary wave the refractive index n_i is equal to the refractive constant

$$n_o = n_a \, , \tag{A.16}$$

the wave normal is parallel to the Poynting vector

$$\zeta_o = 0 \tag{A.17}$$

and the refraction angle r_0 is not dependent on the orientation of the crystal

$$r_o = \arctan \frac{n_m \cdot \sin \gamma}{\sqrt{n_a^2 - n_m^2 \sin^2 \gamma}} \tag{A.18}$$

The polarization η_o is given by the normal of the plane that includes the optical axis as well as the wave normal.

For the refracted extraordinary wave the refractive index n_{eo} depends on the angle b between the wave normal and the optical axis

$$\frac{1}{n_{eo}^2} = \frac{\cos^2 b}{n_a^2} + \frac{\sin^2 b}{n_c^2} \ . \tag{A.19}$$

The wave normal is not parallel to the Poynting vector. The angle ζ_{eo} between the two vectors is dependent on the refractive constants n_{ik} and the angle b between the wave normal and the optical axis of the crystal:

$$\tan \zeta_{eo} = \arctan \frac{(n_c^2 - n_a^2) \sin b \cos b}{n_c^2 \cos^2 b + n_a^2 \sin^2 b} \tag{A.20}$$

The refraction angle r_{eo} depends on the orientation of the crystal

$$r_{eo} = \arctan \sqrt{-\frac{d_2}{d_0}} \tag{A.21}$$

with d_0 and d_2 as described in equation A.14. The polarization η_{eo} is given by a vector perpendicular to the wave normal and lies in the plane which includes the optical axis as well as the wave normal.

For the special case of a uniaxial crystal with the optical axis being normal (c domain) or parallel to the sample surface (a domain) along the x axis ($\delta = 90°$) or the y axis ($\delta = 0°$), the parameters of the refracted and the reflected light are given in table A.1. The resulting reflection coefficients are given in section 6.3 (equations 6.21, 6.22, and 6.23).

	c domain	a domain	
		$\delta = 0°\ (a_y)$	$\delta = 90°\ (a_x)$
ε	$0°$	$90°$	$90°$
ξ	arbitrary	$90°$	$180°$
α_1	$\cos\xi$	0	0
α_2	$\sin\xi$	0	0
α_3	0	-1	-1
β_1	$-\sin\xi$	-1	0
β_2	$\cos\xi$	0	-1
β_3	0	0	0
γ_1	0	0	-1
γ_2	0	1	0
γ_3	1	0	0
n_{11}	n_a	n_a	n_c
n_{22}	n_a	n_c	n_a
n_{33}	n_c	n_a	n_a
$n_{12}=n_{21}$	0	0	0
$n_{13}=n_{31}$	0	0	0
$n_{23}=n_{32}$	0	0	0
ζ_o	0	0	0
$\tan\zeta_{eo}$	$\frac{(nc^2-na^2)\sin r_{eo}\cos r_{eo}}{\cos^2 r_{eo}n_c^2+\sin^2 r_{eo}n_a^2}$	0	$\frac{(nc^2-na^2)\sin r_{eo}\cos r_{eo}}{\sin^2 r_{eo}n_c^2+\cos^2 r_{eo}n_a^2}$
d_0	$n_a^2(\sin^2\gamma - n_c^2)$	$n_a^2(\sin^2\gamma - n_c^2)$	$n_c^2(\sin^2\gamma - n_a^2)$
d_2	$n_c^2\sin^2\gamma$	$n_c^2\sin^2\gamma$	$n_a^2\sin^2\gamma$
$\tan r_o$	$\frac{\sin\gamma}{\sqrt{n_a^2-\sin^2\gamma}}$	$\frac{\sin\gamma}{\sqrt{n_a^2-\sin^2\gamma}}$	$\frac{\sin\gamma}{\sqrt{n_a^2-\sin^2\gamma}}$
$\tan r_{eo}$	$\frac{n_c\sin\gamma}{n_a\sqrt{n_c^2-\sin^2\gamma}}$	$\frac{\sin\gamma}{\sqrt{n_c^2-\sin^2\gamma}}$	$\frac{n_a\sin\gamma}{n_c\sqrt{n_a^2-\sin^2\gamma}}$
b	r_{eo}	$90°$	$90°-r_{eo}$
η_o	$90°$ (s)	$0°$	$90°$
η_{eo}	$0°$ (p)	$90°$	$0°$
α_o	$90°$ (s)	$0°$	$90°$
α_{eo}	$0°$ (p)	$90°$	$0°$
ρ_o	$90°$ (s)	$0°$	$90°$
ρ_{eo}	$0°$ (p)	$90°$	$0°$
r_{pp}	eq. 6.21	eq. 6.22	eq. 6.22
r_{sp}	0	0	0
r_{ps}	0	0	0
r_{ss}	eq. 6.21	eq. 6.22	eq. 6.22

Table A.1: *Parameters of refraction and reflection for a uniaxial crystal with the optical axis perpendicular (c domain) or parallel to the sample surface (a domain) in the plane of incidence ($\delta = 90°$) or perpendicular to it ($\delta = 0°$). For simplicity we assume the dielectric constant of the surrounding medium to be $n = 1$.*

References

[Abb73] E. Abbe. *Beiträge zur Theorie des Mikroskops und der mikroskopischen Wahrnehmung.* M. Schultze's Archiv für mikroskopische Anatomie **IX**, 413–468 (1873).

[Abb83] E. Abbe. *Die Beziehung zwischen Apertur und Vergrößerung beim Mikroskop (The Relation of Aperture and Power in the Microscope).* Journal of the Royal Society (2) **II**, 300–309, 460–473, **III**, 790–812 (1882, 1883).

[Abp98] M. Abplanalp, L. M. Eng, and P. Günter. *Mapping the domain distribution at ferroelectric surfaces by scanning force microscopy.* Applied Physics A **66**, S231–S234 (1998).

[Abr66] S. C. Abrahams, J. M. Reddy, and J. L. Bernstein. *Ferroelectric Lithium Niobate. 3. Single Crystal X-Ray Diffraction Study at 24° C.* Journal of Physics and Chemistry of Solids **27**, 997–1012 (1966).

[Akh02] B. B. Akhremitchev, Y. Sun, L. Stebounova, and G. C. Walker. *Monolayer-Sensitive Infrared Imaging of DNA-Stripes Using Apertureless Near-Field Microscopy.* Langmuir **18** (14), 5325–5328 (2002).

[Ale89] S. Alexander, L. Hellemans, O. Marti, J. Scheir, V. Elings, P. K. Hansma, M. Longmire, and J. Gurley. *An atomic-resolution atomic-force microscope implemented using an optical lever.* Journal of Applied Physics **65** (1), 164–167 (1989).

[Ash72] E. A. Ash and G. Nicholls. *Super-resolution Aperture Scanning Microscope.* Nature **237**, 510–512 (1972).

[Aub03] S. Aubert, A. Bruyant, S. Blaize, R. Bachelot, G. Lerondel, S. Hudlet, and P. Royer. *Analysis of the interferometric effect of the background light in apertureless scanning near-field optical microscopy.* Journal of the Optical Society of America B **20** (10), 2117–2124 (2003).

[Auc98] O. Auciello, J. F. Scott, and R. Ramesh. *The Physics of Ferroelectric Memories.* Physics Today **51** (7), 22–27 (1998).

[Bac94]   R. Bachelot, P. Gleyzes, and A. C. Boccara. *Near field optical microscopy by local perturbation of a diffraction spot.* Microscopy, Microanalysis, Microstructures **5**, 389–397 (1994).

[Bac98]   R. Bachelot, G. Wurtz, and P. Royer. *An application of the apertureless scanning near-field optical microscopy: Imaging a GaAlAs laser diode in operation.* Applied Physics Letters **73** (23), 3333–3335 (1998).

[Bar67]   A. S. Barker and R. Loudon. *Dielectric Properties and Optical Phonons in LiNbO$_3$.* Physical Review **158** (2), 433–445 (1967).

[Bar96]   J. Barenz, O. Hollricher, and O. Marti. *An easy-to-use non-optical shear-force distance control for near-field optical microscopes.* Review of Scientific Instruments **67** (5), 1912–1916 (1996).

[Bek05]   A. Bek, R. Vogelgesang, and K. Kern. *Optical nonlinearity versus mechanical anharmonicity contrast in dynamic mode apertureless scanning near-field optical microscopy.* Applied Physics Letters **87**, 163115–1–3 (2005).

[Bek06]   A. Bek, R. Vogelgesang, and K. Kern. *Apertureless scanning near field optical microscope with sub-10 nm resolution.* Review of Scientific Instruments **77**, 043703–1–11 (2006).

[Bet86]   E. Betzig, A. Lewis, A. Harootunian, M. Isaacson, and E. Kratschmer. *Near-field scanning optical microscopy (NSOM).* Biophysical Journal **49**, 269–279 (1986).

[Bet91]   E. Betzig, J. K. Trautman, T. D. Harris, J. S. Weiner, and R. L. Kostelak. *Breaking the Diffraction Barrier: Optical Microscopy on a Nanometric Scale.* Science **251**, 1468–1470 (1991).

[Bet92]   E. Betzig and J. K. Trautman. *Near-Field Optics: Microscopy, Spectroscopy, and Surface Modification Beyond the Diffraction Limit.* Science **257**, 189–195 (1992).

[Bil06]   L. Billot, M. Lamy de la Chapelle, D. Barchiesi, S.-H. Chang, S. K. Gray, J. A. Rogers, A. Bouhelier, P.-M. Adam, J.-L. Bijeon, G. P. Wiederrecht, R. Bachelot, and P. Royer. *Error signal artifact in apertureless scanning near-field optical microscopy.* Applied Physics Letters **89**, 023105–1–3 (2006).

[Bin82]   G. Binnig and H. Rohrer. *Scanning tunneling microscopy.* Helvetica Physica Acta **55**, 726–735 (1982).

[Bin86]   G. Binnig, C. F. Quate, and C. Gerber. *Atomic Force Microscope.* Physical Review Letters **56** (9), 930–933 (1986).

[Bla03]   S. Blaize, S. Aubert, A. Bruyant, R. Bachelot, G. Lerondel, P. Royer, J.-E. Broquin, and V. Minier. *Apertureless scanning near-field optical microscopy for ion exchange channel waveguide characterization.* Journal of Microscopy **209** (3), 155–161 (2003).

[Blu96]   H. Bluhm, R. Wiesendanger, and K.-P. Meyer. *Surface structure of ferroelectric domains on the triglycine sulfate (010) surface.* Journal of Vacuum Science and Technology B: Microelectronics and Nanometer Structures **14** (2), 1180–1183 (1996).

[Boh98]   C. F. Bohren and D. R. Huffman. *Absorption and scattering of light by small particles.* Wiley, New York (1998).

[Bre05]   M. Brehm, H. G. Frey, R. Guckenberger, R. Hillenbrand, D. Kazantsev, F. Keilmann, N. Ocelic, and T. Taubner. *Consolidating Apertureless SNOM.* Journal of the Korean Physical Society **47**, S80 (2005).

[Bre06a]   M. Brehm, A. Schliesser, and F. Keilmann. *Spectroscopic near-field microscopy using frequency combs in the mid-infrared.* Optics Express **14** (23), 11222–11233 (2006).

[Bre06b]   M. Brehm, T. Taubner, R. Hillenbrand, and F. Keilmann. *Infrared Spectroscopic Mapping of Single Nanoparticles and Viruses at Nanoscale Resolution.* Nano Letters **6** (7), 1307–1310 (2006).

[Bru07]   Bruker Optics GmbH, Ettlingen, Germany. *www.brukeroptics.com* (2007).

[Buk97]   S. J. Bukofsky and R. D. Grober. *Video rate near-field scanning optical microscopy.* Applied Physics Letters **71** (19), 2749–2751 (1997).

[Ceb06]   M. Cebula. *Phasengeregelte homodyne Interferometrie für s-SNOM.* Diploma thesis, TU Dresden (2006).

[Che02]   O. Cherniavskaya, L. Chen, V. Weng, L. Yuditsky, and L. E. Brus. *Quantitative Noncontact Electrostatic Force Imaging of Nanocrystal Polarizability.* Journal of the American Chemical Society (2002).

[Cor07]   Corning Inc., Corning, NY, USA. *www.corning.com* (2007).

[Cou89]   D. Courjon, K. Sarayeddine, and M. Spajer. *Scanning Tunneling Optical Microscopy.* Optics Communications **71** (1,2), 23–28 (1989).

[Cry07]   Crystal Technology Inc., Palo Alto, CA, USA. *www.crystaltechnology.com* (2007).

[Dür86]   U. Dürig, D. W. Pohl, and F. Rohner. *Near-field optical-scanning microscopy.* Journal of Applied Physics **59** (10), 3318–3327 (1986).

[DuP07]   DuPont, USA. *www.dupont.com* (2007).

[Dur99]   C. Durkan, M. E. Welland, D. P. Chu, and P. Migliorato. *Probing domains at the nanometer scale in piezoelectric thin films.* Physical Review B **60** (23), 16198–16204 (1999).

[DW06]   Y. De Wilde, F. Formanek, R. Carminati, B. Gralak, P.-A. Lemoine, K. Joulain, J.-P. Mulet, Y. Chen, and J.-J. Greffet. *Thermal radiation scanning tunnelling microscopy.* Nature **444**, 740–743 (2006).

[EGG07]   EG&G Division of URS Corp., Gathersburg, MD, USA. *www.urscorp.com* (2007).

[Eng98a] L. M. Eng, Abplanalp, and P. Günter. *Ferroelectric domain switching in tri-glycine sulphate and barium titanate bulk single crystals by scanning force microscopy.* Applied Physics A **66**, S679–S683 (1998).

[Eng98b] L. M. Eng, H.-J. Güntherodt, G. Rosenman, A. Skliar, M. Oron, M. Katz, and D. Eger. *Nondestructive imaging and characterization of ferroelectric domains in periodically poled crystals.* Journal of Applied Physics **83** (11), 5973–5977 (1998).

[Eng99a] L. M. Eng, M. Bammerlin, C. Loppacher, M. Guggisberg, R. Bennewitz, R. Lüthi, E. Meyer, T. Huser, H. Heinzelmann, and H.-J. Güntherodt. *Ferroelectric Domain Characterisation and Manipulation: A Challenge for Scanning Probe Microscopy.* Ferroelectrics **222**, 153–163 (1999).

[Eng99b] L. M. Eng, H.-J. Güntherodt, G. A. Schneider, U. Köpke, and J. Muñoz Saldaña. *Nanoscale reconstruction of surface crystallography from three-dimensional polarization distribution in ferroelectric barium-titanate ceramics.* Applied Physics Letters **74** (2), 233–235 (1999).

[Eng00]   L. M. Eng and H.-J. Güntherodt. *Scanning Force Mircoscopy and Near-Field Scanning Optical Microscopy of Ferroelectric and Ferroelastic Domain Walls.* Ferroelectrics **236**, 35–46 (2000).

[Eng07]   L. M. Eng. Privat communication (2007).

[Fel04]   F. Felten, G. A. Schneider, J. Muñoz Saldaña, and S. V. Kalinin. *Modeling and meeasurement of surface displacements in BaTiO₃ bulk material in piezoresponse force microscopy.* Journal of Applied Physics **96** (1), 563–568 (2004).

[Fis81]   U. C. Fischer and H. P. Zingsheim. *Submicroscopic pattern replication with visible light.* Journal of Vacuum Science and Technology **19** (4), 881–885 (1981).

[Fis85]   U. C. Fischer. *Optical characteristics of* 0.1 *μm circular apertures in a metal film as light sources for scanning ultramicroscopy.* Journal of Vacuum Science and Technology B: Microelectronics and Nanometer Structures **3** (1), 386–390 (1985).

[Fis88]   U. C. Fischer, U. T. Dürig, and D. W. Pohl. *Near-field optical scanning microscopy in reflection.* Applied Physics Letters **52** (4), 249–251 (1988).

[Fis02]   U. Fischer, J. Heimel, H.-J. Maas, M. Hartig, S. Hoeppener, and H. Fuchs. *Latex bead projection nanopatterns.* Surface and Interface Analysis **33**, 75–80 (2002).

[Fow89]   G. R. Fowles. *Introduction to Modern Optics.* Dover Publications, New York (1989).

[Fra94]   K. Franke, J. Besold, W. Haessler, and C. Seegebarth. *Modification and detection of domains on ferroelectric PZT films by scanning force microscopy.* Surface Science Letters **302**, L283–L288 (1994).

[FZD07]   Forschungszentrum Dresden-Rossendorf, Dresden, Germany. *www.fz-rossendorf.de* (2007).

[Gie97]   F. J. Giessibl. *Forces and frequency shifts in atomic-resolution dynamic-force microscopy.* Physical Review B **56** (24), 16010–16015 (1997).

[GL99]   T. Gutjahr-Löser, W. Krieger, H. Walther, and J. Kirschner. *Ferrimagnetic resonance excitation by light-wave mixing in a scanning tunneling microscope.* Journal of Applied Physics **86** (11), 6331–6334 (1999).

[Gra06]   S. Grafström. *Reflectivity of a stratified half-space: the limit of weak imhomogeneity and anisotropy.* Journal of Optics A: Pure and Applied Optics **8**, 134–141 (2006).

[Gru96]   A. Gruverman, O. Auciello, and H. Tokumoto. *Scanning force microscopy for the study of domain structure in ferroelectric thin films.* Journal of Vacuum Science and Technology B: Microelectronics and Nanometer Structures **14** (2), 602–605 (1996).

[Gru97a]   A. L. Gruverman, J. Hatano, and H. Tokumoto. *Scanning Force Microscopy Studies of Domain Structure in BaTiO3 Single Crystals.* Japan Journal of Applied Physics **36**, 2207–2211 (1997).

[Gru97b]   A. L. Gruverman, S. A. Prakash, S. Aggarwal, R. Ramesh, O. Auciello, and H. Tokumoto. *Nanoscale Investigation of Polarization Retention Loss in Ferroelectric Thin Films via Scanning Force Microscopy.* Materials Research Society, Dezember 1-5 (1997).

[Güt92]   P. Güthner and K. Dransfeld. _Local poling of ferroelectric polymers by scanning force microscopy._ Applied Physics Letters **61** (9), 1137–1139 (1992).

[Haf90]   C. Hafner. _The Generalized Multipole Technique for Computational Electromagnetics._ Artech House, Boston (1990).

[Haf93]   C. Hafner. _Post-Modern Electromagnetics: Using Intelligent MaXwell Solvers._ Wiley, Chichester (1993).

[Ham98]   H. F. Hamann, A. Gallagher, and D. J. Nesbitt. _Enhanced sensitivity near-field scanning optical microscopy at high spatial resolution._ Applied Physics Letters **73** (11), 1469–1471 (1998).

[Ham07]   Hamamatsu Photonics K.K., Tokyo, Japan. _www.hamamatsu.com_ (2007).

[Hid96]   T. Hidaka, T. Maruyama, M. Saitoh, N. Mikoshiba, M. Shimizu, T. Shiosaki, L. A. Wills, R. Hiskes, S. A. Dicarolis, and J. Amano. _Formation and observation of 50 nm polarized domains in $PbZr_{1-x}Ti_xO_3$ thin film using scanning probe microscope._ Applied Physics Letters **68** (17), 2358–2359 (1996).

[Hil00]   R. Hillenbrand and F. Keilmann. _Complex Optical Constants on a Subwavelength Scale._ Physical Review Letters **85** (14), 3029–3032 (2000).

[Hil01a] R. Hillenbrand. _Nahfeldoptische Amplituden- und Phasenkontrastmikroskopie zur nanoskopischen optischen Abbildung von Materialkontrast und optisch resonanten Partikeln._ Dissertation, TU München (2001).

[Hil01b] R. Hillenbrand, B. Knoll, and F. Keilmann. _Pure optical contrast in scattering-type scanning near-field microscopy._ Journal of Microscopy **202** (1), 77–83 (2001).

[Hil02a] R. Hillenbrand and F. Keilmann. _Material-specific mapping of metal/ semiconductor/ dielectric nanosystems at 10nm resolution by back-scattering near-field optical microscopy._ Applied Physics Letters **80**, 25–27 (2002).

[Hil02b] R. Hillenbrand, T. Taubner, and F. Keilmann. _Phonon-enhanced light-matter interaction at the nanometre scale._ Nature **418**, 159–162 (2002).

[Hil03]   R. Hillenbrand, F. Keilmann, P. Hanarp, D. S. Sutherland, and J. Aizpurua. _Coherent imaging of nanoscale plasmon patterns with a carbon nanotube optical probe._ Applied Physics Letters **83** (2), 368–370 (2003).

[Hil04]   R. Hillenbrand. _Towards phonon photonics: scattering-type near-field optical microscopy reveals phonon-enhanced near-field interaction._ Ultramicroscopy **100**, 421–427 (2004).

[Hip50]   A. v. Hippel. *Ferroelectricity, Domain Structure, and Phase Transitions of Barium Titanate.* Reviews of Modern Physics **22** (3), 221–237 (1950).

[Hon01]   S. Hong, J. Woo, H. Shin, J. U. Jeon, Y. E. Pak, E. L. Colla, N. Setter, E. Kim, and K. No. *Principle of ferroelectric domain imaging using atomic force microscopy.* Jounral of Applied Physics **89** (2), 1377–1386 (2001).

[Hra02]   J. Hranisavljevic, N. M. Dimitrijevic, G. A. Wurtz, and G. P. Wiederrecht. *Photoinduced Charge Separation Reactions of J-Aggregates Coated on Silver Nanoparticles.* Journal of the American Chemical Society **124** (17), 4536–4537 (2002).

[Hu99]   G. D. Hu, J. B. Xu, and I. H. Wilson. *Domain imaging and local piezoelectric properties of the (200)-predominant $SrBi_2Ta_2O_9$ thin film.* Applied Physics Letters **75** (11), 1610–1612 (1999).

[Hub97]   C. Hubert, J. Levy, A. C. Carter, W. Chang, S. W. Kiechoefer, J. S. Horwitz, and D. B. Chrisey. *Confocal scanning optical microscopy of $Ba_xSr_{1-x}TiO_3$ thin films.* Applied Physics Letters **71** (23), 3353–3355 (1997).

[Hub98]   C. Hubert and J. Levy. *Nanometer-scale imaging of domains in ferroelectric thin films using apertureless near-field scanning optical microscopy.* Applied Physics Letters **73** (22), 3229 – 3231 (1998).

[Hub99]   C. Hubert and J. Levy. *New optical probe of GHz polarization dynamics in ferroelectric thin films.* Review of Scientific Instruments **70** (9), 3684–3687 (1999).

[Hub00]   C. Hubert and J. Levy. *Mesoscopic Microwave Dispersion in Ferroelectric Thin Films.* Physical Review Letters **85** (9), 1998–2001 (2000).

[Hub05]   A. Huber, N. Ocelic, D. Kazantsev, and R. Hillenbrand. *Near-field imaging of mid-infrared surface phonon polariton propagation.* Applied Physics Letters **87**, 081103–1–3 (2005).

[Hub06]   A. Huber, N. Ocelic, T. Taubner, and R. Hillenbrand. *Nanoscale Resolved Infrared Probing of Crystal Structure and of Plasmon-Phonon Coupling.* Nano Lett. **6** (4), 774–778 (2006).

[Ino94]   Y. Inouye and S. Kawata. *Near-field scanning optical microscopy with a metallic probe tip.* Optics Letters **19** (3), 159–161 (1994).

[Iso07]   Isometsomet Corp., Springfield, VA, USA. *www.isomet.com* (2007).

[Jac83]   J. D. Jackson. *Klassische Elektrodynamik, 2.Auflage.* Walter de Gruyter, Berlin, New York (1983).

[Jac98]   H. O. Jacobs, P. Leuchtmann, O. J. Homan, and A. Stemmer. *Resolution and contrast in Kelvin probe force microscopy*. Journal of Applied Physics **84** (3), 1168–1173 (1998).

[Jon62]   F. Jona and G. Shirane. *Ferroelectric Crystals*. Pergamon Press, Oxford, London, Frankfurt am Main (1962).

[Jud07]   Judson Technologies, LLC, Montgomeryville, PA, USA. *www.judsontechnologies.com* (2007).

[Kal04]   T. Kalkbrenner, U. Håkanson, and V. Sandoghdar. *Tomographic Plasmon Spectroscopy of a Single Gold Nanoparticle*. Nano Letters **4** (12), 2309–2314 (2004).

[Kar95]   K. Karrai and R. D. Grober. *Piezoelectric tip-sample distance control for near field optical microscopy*. Applied Physics Letters **66** (14), 1842–1844 (1995).

[Kei04]   F. Keilmann and R. Hillenbrand. *Near-field microscopy by elastic light scattering from a tip*. Philosophical Transactions of the Royal Society of London A **362**, 787–805 (2004).

[Kel98]   L. Kelvin. *Contact Electricity of Metals*. Philos. Mag. **46**, 82 (1898).

[Kin07]   Kyocery Kinseki Corp., Tokyo, Japan. *http://global.kyocera.com* (2007).

[Kit98]   S. Kitamura and M. Iwatsuki. *High-resolution imaging of contact potential difference with ultrahigh vacuum noncontact atomic force microscope*. Applied Physics Letters **72** (24), 3154–3156 (1998).

[Kit05]   C. Kittel. *Introduction to Solid State Physics*. Wiley, New York (2005).

[Kni76]   D. J. E. Knight and P. T. Woods. *Application of nonlinear devices to optical frequency measurement*. Journal of Physics E: Scientific Instruments **9**, 898–916 (1976).

[Kno98]   B. Knoll and F. Keilmann. *Scanning microscopy by mid-infrared near-field scattering*. Applied Physics A **66**, 477 – 481 (1998).

[Kno99a]   B. Knoll. *Abtastende Nahfeldmikroskopie mit Infrarot- und Mikrowellen*. Dissertation, TU München (1999).

[Kno99b]   B. Knoll and F. Keilmann. *Mid-infrared scanning near-field optical microscope resolves 30 nm*. Journal of Microscopy **194** (2/3), 512–515 (1999).

[Kno99c]   B. Knoll and F. Keilmann. *Near-field probing of vibrational absorption for chemical microscopy*. Nature **399**, 134–137 (1999).

[Kno00]   B. Knoll and F. Keilmann. *Enhanced dielectric contrast in scattering-type scanning near-field optical microscopy.* Optics Communications **182** (4-6), 321–328 (2000).

[Kog97]   J. Koglin, U. Fischer, and H. Fuchs. *Material contrast in scanning near-field optical microscopy at 1-10 nm resolution.* Physical Review B **55** (12), 7977–7984 (1997).

[Kre71]   E. Kretschmann. *Die Bestimmung optischer Konstanten von Metallen durch Anregung von Oberflächenplasmaschwingungen.* Zeitschrift für Physik **241**, 313–324 (1971).

[Lab00]   M. Labardi, S. Patane, and M. Allegrini. *Artifact-free near-field optical imaging by apertureless microscopy.* Applied Physics Letters **77** (5), 621–623 (2000).

[Lah96]   A. Lahrech, R. Bachelot, P. Gleyzes, and A. C. Boccara. *Infrared-reflection-mode near-field microscopy using an apertureless probe with a resolution of λ/600.* Optics Letters **21** (17), 1315–1317 (1996).

[Lei03]   C. H. Lei, A. Das, M. Elliott, and J. E. Macdonald. *Conductivity of macro-molecular networks measured by electrostatic force microscopy.* Applied Physics Letters **83** (3), 482–484 (2003).

[Lev00]   J. Levy, C. Hubert, and A. Trivelli. *Ferroelectric polarization imaging using apertureless near-field scanning optical microscopy.* Journal of Chemical Physics **112** (18), 7848–7855 (2000).

[Lew84]   A. Lewis, M. Isaacson, A. Harootunian, and A. Muray. *Development of a 500 Å Spatial Resolution Light Microscope.* Ultramicroscopy **13**, 227–232 (1984).

[Ley07]   Leysop Ltd., Basildon, England. *www.leysop.com* (2007).

[Lid92]   D. Lide. *CRC Handbook of Chemistry and Physics.* CRC Press Inc, Boca Rato, FL, USA (1992).

[Lin77]   M. Lines and A. Glass. *Principles and Applications of Ferroelectrics and Related Material.* Clarendon Press, Oxford (1977).

[Lin96]   I. Lindell, K. I. Nikoskinen, and M. J. Flykt. *Electrostatic image theory for an anisotropic half-space slightly deviating from transverse isotropy.* Radio Science **31** (6), 1361–1368 (1996).

[Lin97]   I. Lindell, K. Nikoskinen, and A. Viljanen. *Electrostatic image method for the anisotropic half space.* IEE Proceedings Science Measurement and Technology **144** (4), 156–162 (1997).

[Lop98]   C. Loppacher, M. Bammerlin, F. Battiston, M. Guggisberg, D. Müller, H. R. Hidber, R. Lüthi, E. Meyer, and H.-J. Güntherodt. *Fast digital electronics for application in dynamic force microscopy using high-Q cantilevers.* Applied Physics A **66**, S215–S218 (1998).

[Lop00a] C. Loppacher. *Nichtkontakt-Rasterkraftmikroskopie mit digitalem Phasenreglerkreis.* Dissertation, Universität Basel (2000).

[Lop00b] C. Loppacher, R. Bennewitz, O. Pfeiffer, M. Guggisberg, M. Bammerlin, S. Schär, V. Barwich, A. Baratoff, and E. Meyer. *Experimental aspects of dissipation force microscopy.* Physical Review B **62** (20), 13674–13679 (2000).

[Lop04]   C. Loppacher, U. Zerweck, and L. M. Eng. *Kelvin probe force microscopy of alkali chloride thin films on Au(111).* Nanotech. **15**, S9–S13 (2004).

[Mad98]   A. Madrazo, R. Carminati, M. Nieto-Vesperinas, and J.-J. Greffet. *Polarization effects in the optical interaction between a nanoparticle and a corrugated surface: implications for apertureless near-field microscopy.* Journal of the Optical Society of America A **15** (1), 109–119 (1998).

[Mag01]   N. Maghelli, M. Labardi, S. Patane, F. Irrera, and M. Allegrini. *Optical near-field harmonic demodulation in apertureless microscopy.* Journal of Microscopy **202** (1), 84–93 (2001).

[Mar88]   Y. Martin, D. W. Abraham, and H. K. Wickramasinghe. *High-resolution capacitance measurement and potentiometry by force microscopy.* Applied Physics Letters **52** (13), 1103–1105 (1988).

[Mar96]   Y. Martin, F. Zenhausern, and H. K. Wickramasinghe. *Scattering spectroscopy of molecules at nanometer resolution.* Applied Physics Letters **68** (18), 2475–2477 (1996).

[Mar97]   Y. Martin, S. Rishton, and H. K. Wickramasinghe. *Optical data storage read out at 256 Gbits/in.^{2}.* Applied Physics Letters **71** (1), 1–3 (1997).

[Mat07]   MaTeck GmbH, Jülich, Germany. *www.mateck.de* (2007).

[McD98]   E. B. McDaniel, S. C. McClain, and J. W. P. Hsu. *Nanometer scale polarimetry studies using a near-field scanning optical microscope.* Applied Optics **37** (1), 84–92 (1998).

[Mel07]   Melles Griot, Carlsbad, CA, USA. *www.mellesgriot.com* (2007).

[Mer54]   W. J. Merz. *Domain Formation and Domain Wall Motions in Ferroelectric $BaTiO_3$ Single Crystals.* Physical Review **95** (3), 1103–1105 (1954).

[Mey88a] G. Meyer and N. M. Amer. *Erratum: Novel optical approach to atomic force microscopy [Appl. Phys. Lett 53, 1045 (1988)].* Applied Physics Letters **53** (24), 2400–2402 (1988).

[Mey88b] G. Meyer and N. M. Amer. *Novel optical approach to atomic force microscopy.* Applied Physics Letters **53** (12), 1045–1046 (1988).

[Mey92] E. Meyer. *Atomic Force Microscopy.* Progress in Surface Science **41** (1), 3–43 (1992).

[Mic04] P. Michel, F. Gabriel, E. Grosse, P. Evtushenko, T. Dekorsy, M. Krenz, M. Helm, U. Lehnert, W. Seidel, R. Wünsch, D. Wohlfarth, and A. Wolf. *First Lasing of the ELBE Mid-IR FEL.* Proceedings of the 26th International FEL Conference, Trieste 8–13 (2004). *http://accelconf.web.cern.ch/AccelConf/f04/papers/MOAIS04/MOAIS04.pdf, www.fzd.de.*

[Mie08] G. Mie. *Beiträge zur Optik trüber Medien, speziell kolloidaler Metallösungen.* Annalen der Physik **4** (25), 25–445 (1908).

[Min07] Minicircuits, Brooklyn, NY, USA. *www.minicircuits.com* (2007).

[Mur95] H. Muramatsu, N. Chiba, K. Homma, K. Nakajima, T. Ataka, S. Ohta, A. Kusumi, and M. Fujihira. *Near-field optical microscopy in liquids.* Applied Physics Letters **68** (24), 3245–3247 (1995).

[Nan07a] Nanonics Imaging Ltd., Jerusalem, Israel. *www.nanonics.co.il* (2007).

[Nan07b] Nanosensors™, NanoWorld AG, Neuchatel, Switzerland. *www.nanosensors.com* (2007).

[nan07c] Nanosurf AG, Liestal, Switzerland. *www.nanosurf.com* (2007).

[New07] Newport Corp. Irvine, CA, USA. *www.newport.com* (2007).

[Non91] M. Nonnenmacher, M. P. O'Boyle, and H. K. Wickramasinghe. *Kelvin probe force microscopy.* Applied Physics Letters **58** (25), 2921–2923 (1991).

[Non92] M. Nonnenmacher, M. P. O'Boyle, and H. K. Wickramasinghe. *Surface investigations with a Kelvin probe force microscope.* Ultramicroscopy **42-44**, 268–273 (1992).

[Nov97] L. Novotny, R. X. Bian, and X. S. Xie. *Theory of Nanometric Optical Tweezers.* Physical Review Letters **79** (4), 645–648 (1997).

[Nov06] L. Novotny and B. Hecht. *Principles of Nano-Optics.* Cambridge University Press, New York (2006).

[Oce04]   N. Ocelic and R. Hillenbrand. *Subwavelength-scale tailoring of surface phonon polaritons by focused ion-beam implantation.* Nature materials **3**, 606–609 (2004).

[Oce06]   N. Ocelic, A. Huber, and R. Hillenbrand. *Pseudoheterodyne detection for background-free near-field spectroscopy.* Applied Physics Letters **89**, 101124–1–3 (2006).

[Omi07]   Omicron Nanotechnology GmbH, Taunusstein, Germany. *www.omicron-instruments.com* (2007).

[Orl00]   X. K. Orlik, M. Labardi, and M. Allegrini. *Nanometer-scale observation of ferroelectric domains using an apertureless naer-field optical microscope.* Applied Physics Letters **77** (13), 2042–2044 (2000).

[Ott04]   T. Otto, S. Grafström, H. Chaib, and L. M. Eng. *Probing the nanoscale electro-optical properties in ferroelectrics.* Applied Physics Letters **84** (7), 1168–1170 (2004).

[Pen00]   J. B. Pendry. *Negative Refraction Makes a Perfect Lens.* Physical Review Letters **85**, 3966–3969 (2000).

[Poh84]   D. Pohl, W. Denk, and M. Lanz. *Optical stethoscopy: Image recording with resolution l/20.* Applied Physics Letters **44** (7), 651–653 (1984).

[Pol07]   Polytec GmbH, Waldbronn, Deutschland. *www.polytec.com* (2007).

[Ram02]   L. Ramoino, M. Labardi, N. Maghelli, L. Pardi, and M. Allegrini. *Polarization-modulation near-field optical microscope for quantitative local dichrosim mapping.* Review of Scientific Instruments **73** (5), 2051–2056 (2002).

[Ras05]   M. B. Raschke, L. Molina, T. Elsaesser, D. H. Kim, W. Knoll, and K. Hinrichs. *Apertureless Near-Field Vibrational Imaging of Block-Copolymer Nanostructures with Ultrahigh Spatial Resolution.* ChemPhysChem **6** (10), 2197–2203 (2005).

[Rem54]   J. P. Remeika and W. M. Jackson. *A Method for Growing Barium Titanate Single Crystals.* Journal of the American Chemical Society **76** (3), 940–941 (1954).

[Ren04]   J. Renger, S. Grafström, L. M. Eng, and V. Deckert. *Evanescent wave scattering and local electric field enhancement at ellipsoidal silver particles in the vicinity of a glass surface.* Journal of the Optical Society of America A **21** (7), 1362–1367 (2004).

[Ren05] J. Renger, S. Grafström, L. M. Eng, and R. Hillenbrand. *Resonant light scattering by near-field-induced phonon polaritons.* Physical Review B **71**, 75410–1–7 (2005).

[Ren06] J. Renger. *Excitation, Interaction, and Scattering of Localized and Propagating Surface Polaritons.* Phd thesis, TU Dresden (2006).

[Sar91] D. Sarid. *Scanning Force Microscopy.* Oxford, New York (1991).

[Sau90] F. Saurenbach and B. D. Terris. *Imaging of ferroelectric domain walls by force microscopy.* Applied Physics Letters **56** (17), 1703–1705 (1990).

[Sch05a] F. Schlaphof. *Kraftmikroskopische Untersuchungen dünner ferroelektrischer Filme.* Phd thesis, TU Dresden (2005).

[Sch05b] A. Schliesser, M. Brehm, and F. Keilmann. *Frequency-comb infrared spectrometer for rapid, remote chemical sensing.* Optics Express **13** (22), 9029–9038 (2005).

[Sch05c] S. C. Schneider, S. Grafström, and L. M. Eng. *Scattering near-field optical microscopy of optically anisotropic systems.* Physical Review B **71**, 115418–1–5 (2005).

[Sch07a] S. C. Schneider, S. Grafström, and L. M. Eng. *Far-field studies in s-SNOM at visible and IR wavelengths.* planned (2007).

[Sch07b] S. C. Schneider, S. Grafström, and L. M. Eng. *Towards artifact free s-SNOM at visible and IR wavelenghts.* planned (2007).

[Sch07c] S. C. Schneider, J. Seidel, S. Grafström, L. M. Eng, S. Winnerl, D. Stehr, and M. Helm. *Impact of optical in-plane anisotropy on near-field phonon polariton spectroscopy.* Applied Physics Letters **90** (13), 143101–1–3 (2007).

[Sei01] J. Seidel, S. Grafström, C. Loppacher, S. Trogisch, F. Schlaphof, and L. M. Eng. *Near-field spectroscopy with white-light illumination.* Applied Physics Letters **79** (14), 2291–2293 (2001).

[Ser80] J. L. Servoin, F. Gervais, A. Quittet, and Y. Luspin. *Infrared and Raman responses in ferroelectric perovskite crystals: Apparent inconsistencies.* Physical Review B: Comments and Addenda **21** (5), 2038–2041 (1980).

[Smo99] I. I. Smolyaninov, C. H. Lee, and C. C. Davis. *Near-field second harmonic imaging of lead zirconate titanate piezoceramic.* Applied Physics Letters **74** (14), 1942–1944 (1999).

[Smo01a] I. I. Smolyaninov, H. Y. Liang, C. H. Lee, and C. C. Davis. *Local crystal analysis using near-field optical second harmonic microscopy: Application to thin ferroelectric films.* Journal of Applied Physics **89** (1), 206–211 (2001).

[Smo01b] I. I. Smolyaninov, H. Y. Liang, C. H. Lee, C. C. Davis, V. Nagarajan, and R. Ramesh. *Near-field second harmonic imaging of the c/a/c/a poly-domain structure of epitaxial $PbZr_xTi_{1-x}O_3$ thin films.* Journal of Microscopy **202** (1), 250–254 (2001).

[Son07] Sony Computer Entertainment Inc. *www.playstation.com* (2007).

[Spe92] M. Specht, J. D. Pedarning, W. M. Heckl, and T. W. Hänsch. *Scanning Plasmon Near-Field Microscope.* Physical Review Letters **68** (4), 476–479 (1992).

[Stä96] M. Stähelin, M. A. Bopp, G. Tarrach, A. J. Meixner, and I. Zschokke-Gränacher. *Temperature profile of fiber tips used in scanning near-field optical microscopy.* Applied Physics Letters **68** (19), 2603–2605 (1996).

[Sta07] Stanford Research Systems, Inc., Synnyvale, California. *www.thinksrs.com* (2007).

[Syn28] E. H. Synge. *A Suggested Method for extending Microscopie Resolution into the Ultra-Microscopic Region.* Philosophers Magazine **6**, 356–362 (1928).

[Szi28] G. Szivessy. *Kristalloptik* in *Licht als Wellenbewegung,* vol. XX of *Handbuch der Physik,* edited by H. Geiger and K. Scheel. Verlag Julius Springer, Berlin (1928).

[Tal96] C. E. Talley, G. A. Cooksey, and D. R. C. *High resolution fluorescence imaging with cantilevered near-field fiber optic probes.* Applied Physics Letters **59** (25), 3809–3811 (1996).

[Tau03] T. Taubner, R. Hillenbrand, and F. Keilmann. *Performance of visible and mid-infrared scattering-type near-field optical microscopes.* Journal of Microscopy **210** (3), 311–314 (2003).

[Tau04a] T. Taubner, R. Hillenbrand, and F. Keilmann. *Nanoscale polymer recognition by spectral signature in scattering infrared near-field microscopy.* Applied Physics Letters **85** (21), 5064–5066 (2004).

[Tau04b] T. Taubner, F. Keilmann, and R. Hillenbrand. *Nanomechanical Resonance Tuning and Phase Effects in Optical Near-Field Interaction.* Nano Letters **4** (9), 1669–1672 (2004).

[Tau05]   T. Taubner, F. Keilmann, and R. Hillenbrand. *Effect of Tip Modulation on Image Contrast in Scattering-Type Near-Field Optical Microscopy.* Journal of the Korean Physical Society **47**, S213–S216 (2005).

[Tau06]   T. Taubner, D. Korobkin, Y. Urzhumov, G. Shvets, and R. Hillenbrand. *Near-Field Microscopy Through a SiC Superlens.* Science **313**, 1595 (2006).

[Tay97]   R. S. Taylor, K. E. Leopold, M. Wendman, G. Gurley, and V. Elings. *Bent-fiber near-field scanning optical microscopy probes for use with commercial atomic-force microscopes.* SPIE **3009**, 119–129 (1997).

[Ter90]   B. D. Terris, J. E. Stern, D. Rugar, and H. J. Mamin. *Localized charge force microscopy.* Journal of Vacuum Science and Technology A **8** (1), 374–377 (1990).

[Tho07]   Thorlabs GmbH, Dachau, Germany. *www.thorlabs.com* (2007).

[Tik00]   O. Tikhomirov, B. Red'kin, A. Trivelli, and J. Levy. *Visualization of 180° domain structures in uniaxial ferroelectrics using confocal scanning optical microscopy.* Journal of Applied Physics **87** (4), 1932–1936 (2000).

[Tip94]   P. A. Tipler. *Physik.* Spektrum Akademischer Verlag, Heidelberg, Berlin (1994).

[Vei02]   M. Veithen and P. Ghosez. *First-principle study of the dielectric and dynamical properties of lithium niobate.* Physical Review B **65**, 214302–1–12 (2002).

[Was03]   R. Waser. *Nanoelectronics and Information Technology.* Wiley-CH, Weinheim (2003).

[Wea91]   J. M. R. Weaver and D. W. Abraham. *High resolution atomic force microscopy potentiometry.* Journal of Vacuum Science and Technology B: Microelectronics and Nanometer Structures **9** (3), 1559–1561 (1991).

[Wen07]   M. T. Wenzel, M. Cebula, S. C. Schneider, S. Grafström, and L. M. Eng. *Improved nanoparticle tips for scattering scanning near-field optical microscopy.* In preparation (2007).

[Wes85]   J. Wessel. *Surface-enhanced optical microscopy.* J. Opt. Soc. Am. B **2** (9), 1538 (1985).

[Wik07]   *www.wikipedia.org* (2007).

[WiT07]   Witec GmbH, Ulm, Germany. *www.witec.de* (2007).

[Wol91]   O. Wolter, T. Bayer, and J. Greschner. *Micromachined silicon sensors for scanning force microscopy.* Journal of Vacuum Science and Technology B: Microelectronics and Nanometer Structures **9** (2), 1353–1357 (1991).

[Wur98]   G. Wurtz, R. Bachelot, and P. Royer. *A reflection-mode apertureless scanning near-field optical microscope developed from a commercial scanning probe microscope.* Review of Scientific Instruments **69** (4), 1735–1743 (1998).

[Wur99]   G. Wurtz, R. Bachelot, and P. Royer. *Imaging a GaAlAs laser diode in operation using apertureless scanning near-field optical microscopy.* The European Physical Journal Applied Physics **5**, 269–275 (1999).

[Wur03]   G. A. Wurtz, J. S. Im, S. K. Gray, and G. P. Wiederrecht. *Optical Scattering from Isolated Metal Nanoparticles and Arrays.* The Journal of Physical Chemistry B **107** (51), 14191–14198 (2003).

[Xie01]   A.-F. Xie, B.-Y. Gu, G.-Z. Yang, and Z.-B. Zhang. *Image of near-field second-harmonic generation for inversely poled mesoscopic $LiNbO_3$ domains.* Physical Review B **63**, 054104–1–6 (2001).

[Zen94]   F. Zenhausern, M. O´Boyle, and H. Wickramasinghe. *Apertureless near-field optical microscope.* Applied Physics Letters **65** (13), 1623–1625 (1994).

[Zen95]   F. Zenhausern, Y. Martin, and H. Wickramasinghe. *Scanning Interferometric Apertureless Microscopy: Optical Imaging at 10 Angstrom Resolution.* Science **269**, 1083–1085 (1995).

[Zer02]   U. Zerweck. *Kraft-Distanz-Spektroskopie und Kelvinpotential an Monolagen organischer Moleküle.* Diploma thesis, TU Dresden (2002).

[Zer05]   U. Zerweck, C. Loppacher, T. Otto, S. Grafström, and L. M. Eng. *Accuracy and resolution limits of Kelvin probe force microscopy.* Physical Review B **71**, 125424–1–9 (2005).

[Zgo94]   M. Zgonik, P. Bernasconi, M. Duelli, R. Schlesser, and P. Günter. *Dielectric, elastic, piezoelectric, electro-optic, and elasto-optic tensors of BaTiO3 crystals.* Physical Review B **50** (9), 5941–5949 (1994).

Own Publications

Papers

Ch. Loppacher, F. Schlaphof, **S. Schneider**, U. Zerweck, S. Grafström, L.M. Eng, A. Roelofs, and R. Waser. *Lamellar ferroelectric domains in PbTiO$_3$ grains imaged and manipulated by AFM.* Surface Science **532-535**, 483-487 (2003).

S.C. Schneider, S. Grafström, and L.M. Eng. *Scattering scanning near-field optical microscopy of optically anisotropic systems.* Physical Review B **71** (1), 115418-115422 (2005).

S. Winnerl, D. Stehr, O. Drachenko, H. Schneider, M. Helm, W. Seidel, P. Michel, **S. Schneider**, J. Seidel, S. Grafström, L.M. Eng, T. Roch, G. Strasser, T. Maier, M. Walther. *FELBE Free-Electron Laser: Status and Application for Time Resolved Spectroscopy Experiments.* Proceedings paper in Conference Digest, Joint 31st International Conference on Infrared and Millimeter Waves and 14th International Conference on Terahertz Electronics (IRMMW-THz), 159-159 (2006).

S. Schneider, J. Seidel, S. Grafström, L.M. Eng, S. Winnerl, D. Stehr, and M. Helm. *Impact of optical in-plane anisotropy on near-field phonon polariton spectroscopy.* Applied Physics Letters **90** (14), 143101-143103 (2007).

S.C. Schneider, L.M. Eng, M. Cebula, O. Mieth, T. Härtling, J. Seidel, S. Grafström, S. Winnerl, D. Stehr, and M. Helm. *Near-field Spectroscopy on Anisotropic Single Crystals.* In preparation, (2007).

M.T. Wenzel, M. Cebula, **S.C. Schneider**, S. Grafström, and L.M. Eng. *Improved nanoparticle tips for scattering scanning near-field optical microscopy.* In preparation, (2007).

S.C. Schneider, S. Grafström, and L.M. Eng. *Constant tip scattering near-field optical microscope for visible and IR wavelenghts.* Planned, (2007).

M. Cebula, **S.C. Schneider**, S. Grafström, and L.M. Eng. *Quasiheterodyne detection for near-field optical microscopy at arbitrary wavelengths.* Planned, (2007).

Conference contributions

Talks

S. Schneider, Ch. Loppacher, U. Zerweck, S. Grafström, and L.M. Eng. *Optischer Nahfeldkontrast in anisotropen Dielektrika.* Annual Meeting of the Deutsche Physikalische Gesellschaft - spring meeting of the Division Condensed Matter (DPG-2004). March 8th to 12th 2004, Regensburg, Germany.

S.C. Schneider, S. Grafström, and L.M. Eng. *Scattering scanning near-field optical microscopy on anisotropic dielectrics.* Annual Meeting of the Deutsche Physikalische Gesellschaft - spring meeting (DPG-2005). March 4th to 9th 2005, Berlin, Germany.

S.C. Schneider, J. Seidel, S. Grafström, Ch. Loppacher, M. Cebula, L.M. Eng, S. Winnerl, D. Stehr, and M. Helm. *Scattering scanning near-field optical microscopy on anisotropic dielectric using a free electron laser light source.* Annual Meeting of the Deutsche Physikalische Gesellschaft - spring meeting of the Division Condensed Matter (DPG-2006). March 27th to 31th 2006, Dresden, Germany.

S.C. Schneider, J. Seidel, M. Cebula, S. Grafström, Ch. Loppacher, L.M. Eng, S. Winnerl, D. Stehr, and M. Helm. *Near-field inspection of phonon resonance in ferroelectric using a free electron laser.* The 9th International Symposium on Ferroic Domains and Micro- to Nanoscopic Structures (ISFD-9). June 26th to 30th 2006, Dresden, Germany.

S. Winnerl, D. Stehr, O. Drachenko, H. Schneider, M. Helm, W. Seidel, P. Michel, **S. Schneider**, J. Seidel, S. Grafström, L.M. Eng, T. Roch, G. Strasser, T. Maier, M. Walther. *FELBE Free-Electron Laser: Status and Application for Time Resolved Spectroscopy Experiments.* Joint 31st International Conference on Infrared and Millimeter Waves and 14th International Conference on Terahertz Electronics (IRMMW-THz). September 18th to 22th 2006, Shanghai, China.

Posters

Ch. Loppacher, F. Schlaphof, **S. Schneider**, U. Zerweck, S. Grafström, L.M. Eng, A. Roelofs, J. Rodríguez Contreras, H. Kohlstedt, and R. Waser. *Domain imaging and manipulation in ferroelectric thin films by piezoresponse force microscopy.* 7th Intl. Conf. on Nanometer-scale Science and Technology (NANO-7) & 21st Europ. Conf. on Surface Science (ECOSS-21). June 24th to 28th 2002, Malmö, Sweden.

S. Schneider, S. Grafström, Ch. Loppacher, U. Zerweck, L.M. Eng. *Apertureless Scanning Near-Field Optical Microscopy on Anisotropic Dielectric Systems.* Annual Meeting of the Deutsche Physikalische Gesellschaft and DPG - spring meeting of the Division Condensed Matter (DPG-2003). March 24th to 28th 2003, Dresden, Germany.

S.C. Schneider, S. Grafström, L.M. Eng. *Scattering scanning near-field optical microscopy of anisotropic dielectrics.* The 8th International Conference on Near-field Nano Optics & Related Techniques (NFO-8). September 5th to 9th 2004, Seoul, Korea.

S.C. Schneider, S. Grafström, L.M. Eng. *Scattering scanning near-field optical microscopy of anisotropic dielectrics.* Second International Conference on Surface Plasmon Photonics (SPP-2). May 21st to 26th 2005, Graz, Austria.

S. Grafström, J. Renger, **S. Schneider**, and L. M. Eng. *The Role of Polaritons in Scattering Near-field Optical Microscopy.* Fall meeting of the Materials Research Society MRS. November 28th to December 2nd 2005, Boston, USA.

S.C. Schneider, J. Seidel, M. Cebula, S. Grafström, Ch. Loppacher, L.M. Eng, S. Winnerl, D. Stehr, and M. Helm. *Nanoscale Near-Field Phonon Resonance Anisotropy Inspection Using a Free Electron Laser.* 9th International conference on near-field optics, nanophotonics and related techniques (NFO-9). September 10th to 15th 2006, Lausanne, Switzerland.

M. Cebula, **S. Schneider**, and L. Eng. *Phase-controlled Homodyne Interferometric Detection for s- SNOM.* Annual Meeting of the Deutsche Physikalische Gesellschaft and DPG - spring meeting of the Division Condensed Matter (DPG-2007). March 26th to 30th 2007, Regensburg, Germany.

S.C. Schneider, S. Grafström, L.M. Eng. *Sample-enhanced scattering SNOM on anisotropic samples.* Third International Conference on Surface Plasmon Photonics (SPP-3). June 17th to 22th 2007, Dijon, France.

Acknowledgments

I thank all the people who supported me while I was working on this thesis.

First of all I want to thank Professor Lukas Eng as my supervisor who challenged me with this demanding topic. You always found the right words to motivate me and to get me back on the right track of the thesis. Thank you also for having always an open ear for problems and suggestions.

Many thanks go to Stefan Grafström for endless scientific and personal discussions. It will always be surprising for me how one person can know the answer to (nearly) everything. Also, thank you very much for helping me with the linguistic(al) trials and tribulations of this work.

I want to thank my referees, Professor Jeremy Levy and Professor Ramamoorthy Ramesh for evaluating my work - I hope you enjoy reading it.

Furthermore, I thank my supervisors at Argonne National Laboratory, Gary Wiederrecht and Stephen Streiffer, for giving me the opportunity to work at Argonne and for the fruitful discussions. I thank Gregory Wurtz, Renaud Bachelot, and Alexandre Bouhelier, whom I had the luck to work with at Argonne, for insights into the French way of near-field microscopy. It was a valuable time at Argonne for my work and for me personally.

For them supporting my work at the Forschungszentrum Dresden-Rossendorf, I thank Stefan Winnerl, Dominik Stehr, and Manfred Helm for so many discussions and help with the realization of the setup at the FEL. I want to thank the whole FELBE team for running the ship for us and for adjusting the FEL even at three o'clock in the morning.

I thank the coworkers who supported me during the 24-hours shifts at the FEL: Jan Seidel, Stefan Grafström and Lukas Eng - the best combined group of pundits and euphorics ever measuring with a near-field microscope in combination with an FEL - as well as Christian Loppacher, Thomas Härtling, Marc Tobias Wenzel, Marcus Cebula, Alexander Haußmann and Oliver Mieth. Thank you very much for spending day and night in the lab and for accepting sleep deprivation and insanity at five o'clock in the morning. Moreover, I thank Elke Beyreuther and René Kullock for the transport of the Super-Sunny.

I wish to thank everyone of the Scanning Probe Microscopy and Manipulation Group for being creative and crazy, calm and nuts, deliberate and rash, funny and

serious, boring and exciting, altogether for being a hilarious bunch of people.

I thank the whole IAPP for being so open-minded and friendly people and for teaching me table soccer. I will not unlearn this in my whole life - awesome!

I thank the people who accompanied me during my studies, mainly Matthias "Frontzl" Frontzek, Andreas "Petzi" Petzold, and later Oliver "Ollhorst" Mieth. Thank you for so much fun, party, and most of all for all the coffee.

This brings me to the "Bierstube", the place where I celebrated social life besides the lab at the university. Thank you Chrischan, Sandy, Phillip, Kerstin, Johannes, Mandy, Ina, Andi, Ronny, Enno, Wolfram, Frontzl, and the whole rest. Raise the cups! ;0)

Outside the university it was my boyfriend Daniel who supported me during my whole studies. Thank you for bringing me back to earth when I was too deep into science, for pushing me forward, and for bearing all the stress.

Particularly, I thank my family for believing and trusting in me. Lucky me, having the best parents and the best brother of the world. It means so much to me to know that you stand behind me no matter whether I succeed or fail. Thank you!

Erklärung

Die vorliegende Arbeit wurde am Institut für Angewandte Physik/Photophysik der Technischen Universität Dresden unter wissenschaftlicher Betreuung von Prof. Dr. Lukas M. Eng durchgeführt.

Hiermit bestätige ich, dass ich diese Dissertation ohne unzulässige Hilfe Dritter und ohne die Benutzung anderer als der angegebenen Hilfsmittel angefertigt habe. Die aus fremden Quellen direkt oder indirekt übernommenen Gedanken sind als solche kenntlich gemacht. Die Arbeit wurde bisher weder im Inland noch im Ausland in gleicher oder ähnlicher Form einer anderen Prüfungsbehörde vorgelegt.

Ein früheres erfolgloses Promotionsverfahren hat nicht stattgefunden.
Ich erkenne die Promotionsordnung der Technischen Universität Dresden an.

Dresden, den 19. April 2007